Decay tagging of neutron-deficient ^{73,74}Sr

Jack Henderson

Ph.D.

University of York
Physics

July 2014

Abstract

Decay tagging of neutron-deficient ^{73,74}Sr

The isospin dependence of the nuclear interaction was probed using energy differences between analogue excited states across the A=74 isobaric triplet. The first spectroscopy of transitions between states in the proton-dripline nuclide, ^{74}Sr was performed using the highly-selective recoil-beta tagging technique with the JUROGAM II + RITU + GREAT setup at the University of Jyväskylä. Considerable experimental development was required to acheive the requisite level of sensitivity. This included the development of a phosphor-sandwich detector, a finely segmented doublesided silicon-strip detector (DSSD) and a charged-particle veto array (UoYtube).

The $2_1^+ \rightarrow 0_1^+$ and $4_1^+ \rightarrow 2_1^+$ transitions were identified through a combination of time and energy gates, and the implementation of a charged-particle veto. A beta-decay half-life was also extracted, in good agreement with a complementary measurement performed at RIKEN. Comparison with Skyrme Hartree-Fock calculations indicates that ^{74}Sr is approximately 1-MeV less bound than previously supposed, implying that both observed excited states are two-proton unbound. Through comparison with published data from the A=74 isobar, triplet-energy differences (TEDs) were determined, indicating a continued need for an additional isotensor, J=0, 100-keV isospin-nonconserving (INC) interaction component, consistent with that found to be required at lower masses. The implication of this result is that such an INC component is mandated across the nuclear landscape, regardless of local nuclear structure effects.

Additionally, candidates for the beta-delayed proton decay of ^{73}Sr$\rightarrow^{73}$Rb$\rightarrow^{72}$Kr were observed using the same experimental setup. The lowest energy proton detected is consistent with that which might be expected for the decay of the ground state in ^{73}Rb, allowing for the first measurement of the proton separation energy, S_p. This value is of considerable astrophysical interest since ^{73}Rb is considered to be a waiting point in the rp process.

Contents

List of Figures

List of Tables

Acknowledgements

I will begin by thanking my supervisor, Dave, for providing both an interesting and varied Ph.D. project, whilst affording me plenty of opportunity to collect airmiles and see the world. The other academics at York have also been a constant source of support. In particular, Bob and Mike have been of great help throughout the course of my Ph.D., always being willing to give comments, advice and corrections.

The remainder of the Nuclear Group at York also deserve a lot of credit for putting up with me. The horsemen of the postdocalypse (in no particular order): Paul, Lianne, Gemma, Phil & James, for providing advice, alcohol and abuse, as and when required. Tom, for providing constant corrections on my misunderstanding of this "isospin" thing. The rest of you, for being always receptive to the words "pub", "lunch" and "tea".

The group in Jyväskylä were part of what made my Ph.D. such an enjoyable experience, making me feel welcome since day one and allowing me the opportunity to really get to grips with the facility. In particular, Panu deserves serious thanks, walking me through the facility from when I first arrived and offering assistance with the analysis throughout. Also in need of thanks are Cath for always being willing to help correct my understanding of the experimental setup, and Chris for making my stay in Finland truly enjoyable.

Back in York, I reserve a special thanks for Matt and Su, for feeding and otherwise looking after Anna whilst I was away, keeping a weight off my mind. A degree of thanks must also go the University rugby club, for providing a welcome distraction from my Ph.D. and an outlet for any academia-related frustrations.

Of course I must thank my parents, Ruth and Jonathan, without whom none of this would've been possible, and my sisters, Beth, Anna and Lynn. Finally, my time in York has been made all the more special by my fiancé Anna, who has helped keep me relatively sane throughout.

Ta.

Declaration of Authorship

This thesis is submitted for the degree of Doctor of Philosophy in accordance with the regulations of the University of York. The work described herein has not been submitted for any other degree or qualification, except where explicitly indicated otherwise in Chapter 4.

The experimental work was performed at, and in collaboration with, the University of Jyväskylä, Finland. The work enhancing the senstivity of the recoil-beta tagging technique was performed in collaboration with P. Ruotsalainen of the University of Jyväskylä. The investigation of neutron-deficient strontium isotopes was carried out by the author under the supervision of Dr. D. G. Jenkins.

The following papers containing work included in this thesis have been - or will shortly be - submitted for publication:

- J. Henderson *et al.*, Enhancing the sensitivity of recoil-beta tagging, *Journal of Instrumentation* **8** P04025 (2013)
- J. Henderson *et al.*, Spectroscopy on the proton drip-line: First observation of excited states in ^{74}Sr, *In preparation* (2014)

Jack Henderson

Chapter 1

Introduction and motivations

Ook

The Librarian - Discworld
Terry Pratchett

The primary aim of the work described in this thesis was the γ- and β-decay spectroscopy of the exotic, neutron-deficient nuclide, ^{74}Sr. The region of the nuclear landscape involved is shown in Fig. 1.1. One can immediately see that the nuclide of interest lies at an extreme of the nuclear chart, a single proton away from the proton drip-line.

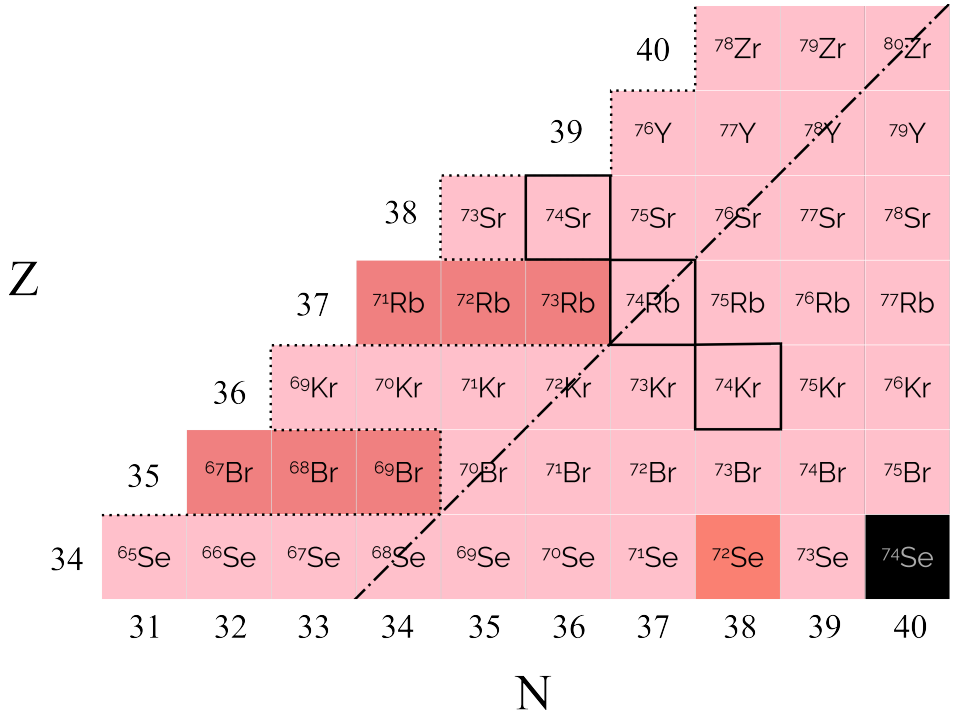

FIGURE 1.1: The nuclear landscape in the region of interest for the present work. The dotted line indicates the proton drip-line, whilst the dotted-dashed line represents the $N = Z$ line. Colours indicate the decay modes of the nuclei, pink nuclei β decay, dark-pink nuclei proton decay and black nuclei are stable.

Due to the very exotic nature of ^{74}Sr a highly-selective technique known as recoil-beta tagging (RBT) was used, and will be described in Chapter 2. The experiment was performed

at the University of Jyväskylä (JYFL) where the RBT technique was first developed [1]. The experimental setup available at the commencement of the work will be introduced in Chapter 3. Despite the highly-selective nature of the RBT technique, some additional experimental developments were required in order to make such a neutron-deficient nuclide as ^{74}Sr experimentally accessible. These developments will be introduced in Chapter 4. The experiment and analysis will be described in Chapter 5 with the interpretation discussed in Chapter 6. In the present chapter, the motivations for the work will be outlined. In order to provide a more comprehensive description, included with these motivations will be a brief discussion of some nuclear modelling techniques and concepts.

1.1 Isospin

The concept of isospin was introduced by Heisenberg in 1932 [2] and considers the proton and neutron as different isospin projections of the same particle, the nucleon. As formalised by Wigner [3], the isospin quantum number, T, of both the proton and neutron is $1/2$ with a projection for the neutron of $T_z = +1/2$ and for the proton of $T_z = -1/2$. An $N = Z$ nucleus will therefore trivially have an isospin projection, T_z, of 0.

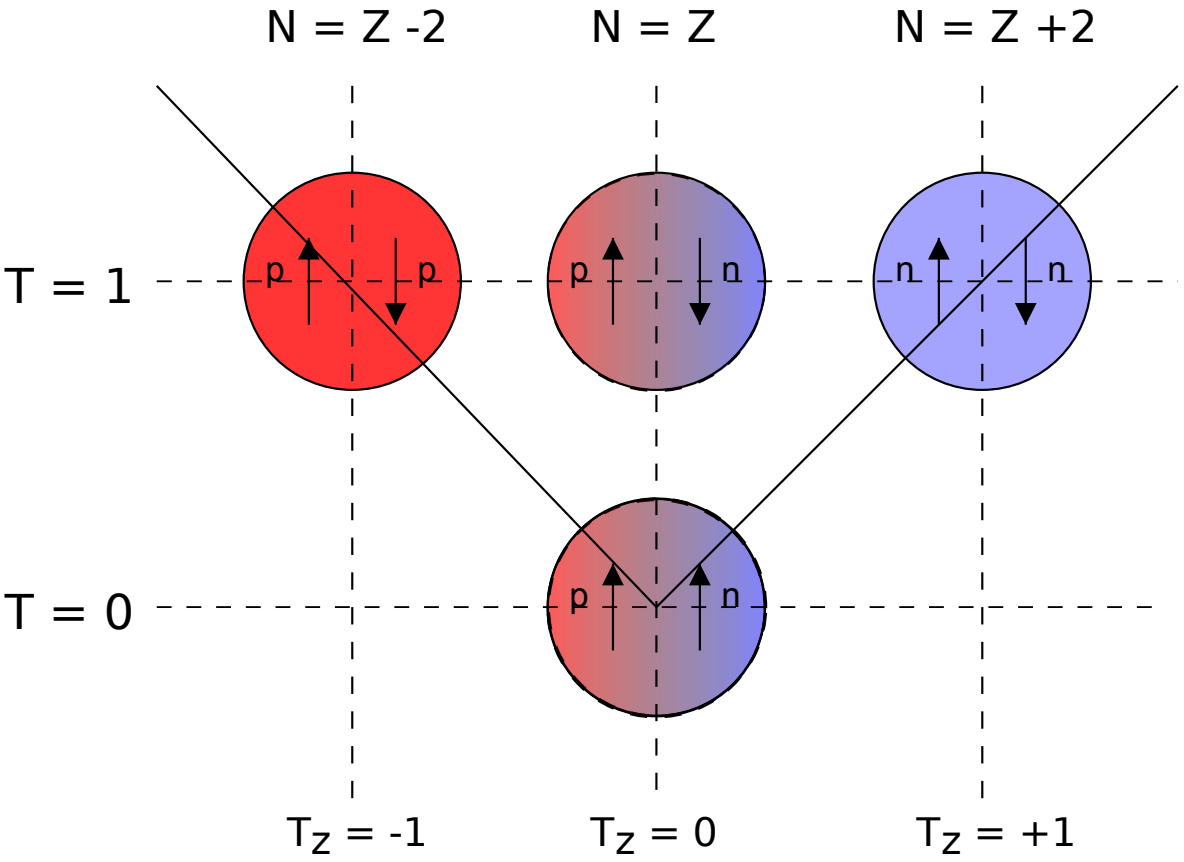

FIGURE 1.2: An illustration of isospin in the deuteron system. This can be extended to all odd-odd nuclei in the $N = Z$ region. Arrows indicate the relative spins of the nucleons. Protons have $T_z = -1/2$ and neutrons $T_z = 1/2$. Solid lines indicate the lowest possible isospin of the nuclei, which typically corresponds to the isospin of the ground state.

The idea of isospin symmetry is rooted in the similarity - once Coulomb effects are eliminated - of interactions between constituent nucleons in the nucleus, regardless of the individual nucleons' isospin projections. One therefore assumes naïvely that the nuclear forces between all pairs of nucleons are equal and that the nuclear Hamiltonian is independent of isospin [3]. This section will explore the consequences of this fundamental assumption of isospin independence.

Consider first the simplest example, that of the $A = 2$ isobar, which can be understood through the illustration given in Fig. 1.2. For the $T_z = 0$, $N = Z$ projection, the nucleon spins can be either parallel or anti-parallel, while for the $T_z = \pm 1$ projections, aligned spins are forbidden by the Pauli exclusion principle which demands an antisymmetric wavefunction. The $T = 0$ configuration therefore corresponds to the nucleon spins being aligned, while the $T = 1$ configuration has the nucleon spins anti-aligned. In the $A = 2$ isobar, only the $T = 0$, $T_z = 0$ case is bound, being the ground state of the deuteron, while the $T = 1$ configurations are all unbound.[1] The $T_z = -1, 0, +1$ members of an isobar are known collectively as an isobaric triplet.

One can extend the analogy with the deuteron to higher mass isobaric triplets centered on an odd-odd $N = Z$ nucleus by considering the nucleus as nucleon-nucleon pairs atop an even-even $N = Z$ "core". For those cases, one would expect to see common $T = 1$ states in all members of the isobaric triplet, associated with excitations relative to the anti-aligned nucleon-nucleon pair, whilst $T = 0$ states would only exist within the $T_z = 0$ nucleus. The initial assumption of the isospin independence of the nuclear force would have it that, after the elimination of electromagnetic effects, all $T = 1$ states will have the same energy within the nuclear potential. It should be noted that the deuteron analogy is an oversimplified picture and, in reality, couplings between states of the same T cause shifting of levels. The analogy to the deuteron for isobaric triplets centered on an odd-odd $T_z = 0$ nucleus is used because it allows for a simple illustration of isospin concepts. Similar arguments can be used for $T_z = \pm 1/2$ pairs, and triplets centered on an even-even $T_z = 0$ nucleus.

From the assumption of isospin symmetry the nuclear force can be probed by examining the energies of states across an isobar. This is experimentally complicated in the general case, since typically the ground-state band in a nucleus is of the lowest isospin quantum number. For example, one would typically expect the ground state band of a $T_z = 0$ nucleus to be of $T = 0$ configuration, of a $T_z = \pm 1$ nucleus to be of a $T = 1$ configuration, etc. However, for isobars of $A \gtrsim 50$, it is found that the ground-state bands of odd-odd $T_z = 0$, $N = Z$ nuclei are of the $T = 1$ configuration, providing a unique opportunity to probe the nuclear force in this region. Indeed, it is a feature of odd-odd $T_z = 0$ nuclei, $T = 1$ states lie lower with respect to the Fermi surface than in the even-even case.

[1] These consist of the diproton ($T_z = -1$), the first excited state of deuteron ($T_z = 0$) and the dineutron ($T_z = +1$).

Experimental isospin investigations across triplets can be separated into two methods. Firstly, an examination of the binding energy of a nucleus allows the absolute energy of the ground-state to be extracted. With the assumption of isospin independence, these ground-state energies should be identical across an isobar once electromagnetic contributions are accounted for. Any remaining discrepency is known as a Coulomb displacement energy (CDE). Secondly, after normalising to the ground-state of the $T = 1$ band, one can examine the differences in energies of excited states in the band which should again be the same once electromagnetic contributions are eliminated. In this case any remaining discrepency is known as a Coulomb energy difference (CED). The second of these two methods will be the subject of this work and shall now be discussed in more detail, however the underlying principles are the same for the interpretation of both techniques.

1.1.1 Coulomb energy differences

The Coulomb energy difference between two analogous states of spin J in nuclei of isospin number T is defined as:

$$CED_J = E^*_{J,T,T_{z<}} - E^*_{J,T,T_{z>}}, \tag{1.1}$$

where $T_{z<}$ is the isospin projection of the more neutron-deficient nucleus and $T_{z>}$ of the more neutron-rich nucleus. Since differences between the energies of analogous excited states (known as isobaric analogue states, or IASs) are dominated by electromagnetic interactions, CEDs are particularly sensitive to small structural changes. Pairing differences also need to be taken into account.

Nuclides which have interchanged neutron and proton numbers are known as mirror nuclei and parenthesise the $N = Z$ line. Since the proton and neutron numbers are exchanged, pairing effects are cancelled out, making mirror energy differences (MEDs) sensitive only to electromagnetic effects, specifically to the isospin symmetry of the nuclear force. MEDs are therefore referred to as isovector energy differences, and for $T = 1$ states are defined as:

$$MED_J = E^*_{J,T,T_z=-1} - E^*_{J,T,T_z=+1}. \tag{1.2}$$

One is also able to define an triplet energy difference (TED) across an isobaric triplet:

$$TED_J = E^*_{J,T,T_z=-1} + E^*_{J,T,T_z=+1} - 2E^*_{J,T,T_z=0}. \tag{1.3}$$

In a TED, the difference between the average of the like-nucleon (pp and nn) interactions and the neutron-proton (np) interaction is probed. Whereas single-particle terms are still

important for MEDs, they are cancelled in TEDs making the latter sensitive only to electromagnetic effects and any other isospin non-conserving (INC) interaction. TEDs are isotensor energy differences, being sensitive only to the isospin-dependence of the nuclear force. This makes them an ideal probe of the nature of the nuclear force, while CEDs and MEDs are more suited as probes of changes in nuclear structure effects across an isobar.

In order to properly interpret energy differences between IASs, one needs to compare with calculated energy differences resulting from the Coulomb interaction and other INC interactions. These calculations are performed using the nuclear shell model, which will now be discussed.

1.2 The nuclear shell model

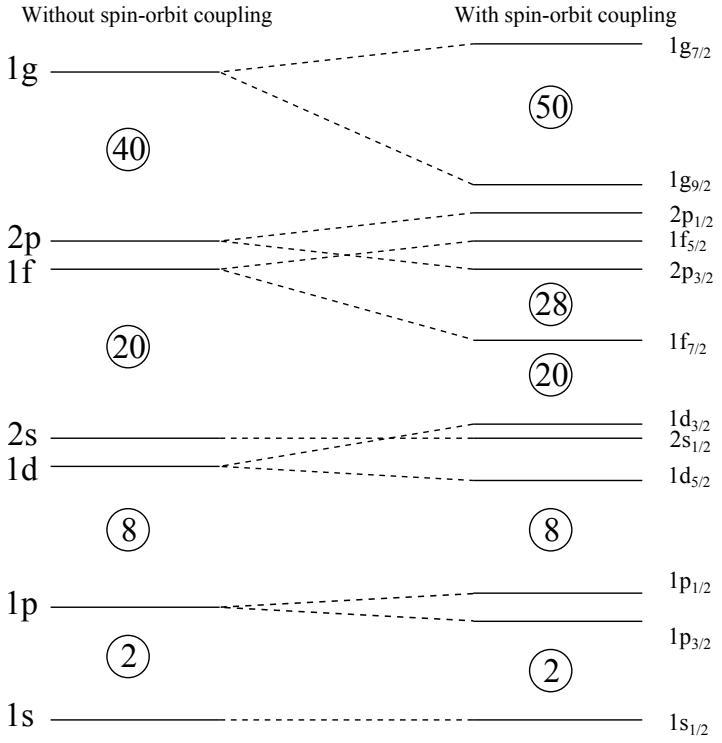

FIGURE 1.3: An illustration of the effect of adding a strong spin-orbit component to the shell model. The left-hand levels are those calculated using a realistic potential with no spin-orbit component whilst the right hand levels are those when a strong spin-orbit component is added. The emergence of additional magic numbers 28 and 50, and the suppressing of the magic number 40, was the first indicator that such an interaction was required. Note that the level splitting is not to scale.

A significant interpretative development in nuclear physics came with the (independent) introduction of the nuclear shell model by Haxel, Jensen and Seuss [4], and Goeppert-Mayer [5]. The development of the nuclear shell model was rooted in the realisation that the introduction of a strong spin-orbit interaction - and the consequent splitting of orbitals - accurately reproduced observed "magic numbers" of protons and neutrons as shown in Fig. 1.3. The

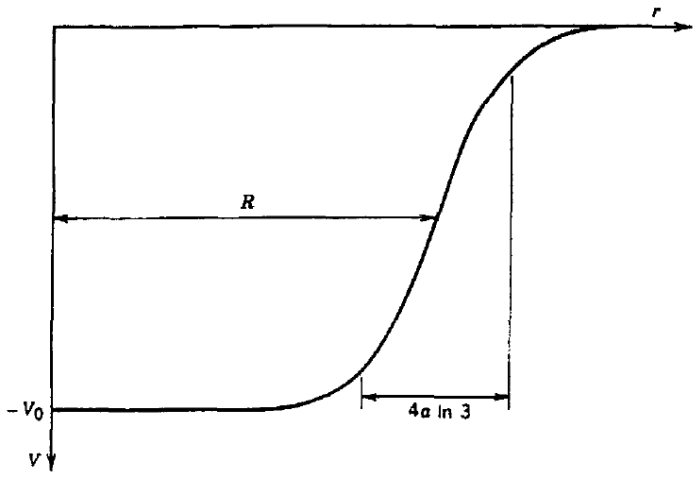

FIGURE 1.4: The Woods-Saxon potential. V_0 is the depth of the potential well, R is the mean radius and a describes the skin thickness, such that $4aln(3)$ is the radial distance over which the potential goes from $0.9V_0$ to $0.1V_0$ [7].

shell model has since evolved away from purely describing the nuclear binding energy in the vicinity of closed shells and, with the advent of large-scale computing, is now able to tackle nuclear structure problems far from such regions.

The nuclear shell model is an independent-particle model. In other words, the nucleons are treated as moving within a mean field, independently of neighbouring particles. Additional components - including the Coulomb interaction - arising from nucleon-nucleon interactions are included through a pertubative, *residual interaction*. The shell-model Hamiltonian therefore becomes:

$$H = H_0 + H_{res}, \tag{1.4}$$

where H_0 is the mean-field Hamiltonian, and H_{res} is the small, pertubative residual Hamiltonian. The Hartree-Fock method (see Section 1.5.1 for more details) can then be used to obtain the wavefunction with minimised energy. An example of a realistic mean-field potential is the Woods-Saxon [6] potential, as shown in Fig. 1.4 and described by

$$V(r) = -\frac{V_0}{1 + exp\left(\frac{(r-R_0)}{a}\right)}. \tag{1.5}$$

Here, V_0 describes the depth of the potential well, R_0 describes the mean radius and a the skin thickness.

The many-body nature of the nucleus means that, even with the mean-field approximation to the nucleus, calculations explicitly involving all constituent nucleons quickly become computationally impractical. The shell-model problem is somewhat simplified if one considers the

nucleus as consisting of valence nucleons orbiting an effectively inert, doubly-magic "core". The problem is further simplified through truncation of the valence space. This is typically achieved by only considering a limited number of shell-model orbitals above the inert core. For example, in the region of the present work, one might consider an inert, ^{56}Ni (28 protons, 28 neutrons) core, with a truncated valence space, consisting of the $p_{3/2}f_{5/2}p_{1/2}g_{9/2}$ orbitals (see Fig. 1.3). With these steps, the valence space of the problem is dramatically reduced, making the diagonalisation of the necessary matrix elements possible. A consequence of this simplification however is that the residual interaction can no longer be derived from fundamental interaction data such as nucleon-nucleon scattering. As a result, phenomonological effective interactions are used. These effective interactions tend to be limited in their scope, typically being targeted towards a single region of the nuclear landscape.

In the region of interest for the present work (the pfg shell in Fig. 1.3) there was, until recently, a dearth of experimentally-reliable effective interactions. In order to develop a reliable effective interaction, one has to not only account for the shell of interest but also the higher-lying shells. For example, in the case of the upper pf shell, one must also account for the $g_{9/2}$ shell. This is even true for the $f_{7/2}$ shell, where one might naïvely assume the shell gap at 28 would reduce the effect of the pf shell above. In recent years however, the JUN45 effective interaction [8] was introduced. Particularly in the $N = Z$ region of the nuclear landscape this new interaction allows reliable shell-model calculations in the upper fp shell, especially as the influence of the $g_{9/2}$ shell begins to grow.

Using large-scale shell model calculations with state-of-the-art interactions, one may therefore probe CEDs, MEDs and TEDs theoretically as well as experimentally. A significant advantage of using energy differences (as opposed to absolute energy levels) is that errors in the absolute excitation energy calculated using the shell model are relatively unimportant as long as they are consistent across the isobar. It is important however to have a good understanding of the shell-model components which contribute to the calculated energy differences.

1.2.1 Relevant shell-model components

Radial term

In the shell model, one considers valence nucleons alongside an inert core. It is important, however, to remember that this inert core is still charged and therefore exerts a Coulomb effect on valence protons, which must be accounted for. The contribution from the core can be derived by assuming a uniformly charged sphere of radius R_C [9], resulting in,

$$E_C = \frac{3}{5}\frac{Z(Z-1)e^2}{R_C}, \tag{1.6}$$

with the absolute energy difference between states,

$$\Delta E_C = E_C(Z_>) - E_C(Z_<). \tag{1.7}$$

This effect dominates for CDEs, but is largely washed out when considering CEDs since the energies are normalised to the ground-states. As a result of the change in orbital radius along a rotational band, a small contribution remains for CEDs [10]. This change in orbital radius arises from changes in the occupation of participating orbitals. For example, in $f_{7/2}$-shell nuclei, occupation of p orbitals decreases along a rotational band. Assuming the orbital radii are identical for both IAS, the resulting contribution to the CED is therefore

$$\Delta E_{CED} = \Delta E_C(J) - \Delta E_C(0). \tag{1.8}$$

This contribution is accounted for in the shell model through the addition of a V_{cr} term to the residual interaction,

$$V_{cr}(J) = 2T\alpha_r \left(\frac{m_\pi(g.s.) + m_\nu(g.s.)}{2} - \frac{m_\pi(J) + m_\nu(J)}{2} \right). \tag{1.9}$$

Here, α_r is a constant, which is derived empirically from data for the $A = 42$ isobar, and m_π and m_ν are the occupation numbers for radius-driving orbitals for protons and neutrons, respectively.

Single-particle terms

In addition one must also account for the change in spatial overlap between the valence nucleons and the core of charge Z_{cs}. This contribution can be shown to be [9],

$$E_{ll} = \frac{-4.5 Z_{cs}^{13/12}[2\ell(\ell+1) - N(N+3)]}{A^{1/3}(N+\frac{3}{2})} \text{ keV}, \tag{1.10}$$

where N is the principal quantum number.

One also needs to correct for the relativistic electromagnetic spin-orbit force. This force results from the Larmor precession of the nucleons with respect to the nuclear force because of their magnetic moments, and from the Thomas precession of the protons due to their charge [11, 12]. The electromagnetic spin-orbit potential, V_{ls} can be generalised to:

$$V_{ls} = (g_s - g_l)\frac{1}{2m_N^2 c^2}\left(\frac{1}{r}\frac{\mathrm{dV}_C}{\mathrm{d}r}\right)\vec{l}\cdot\vec{s}. \tag{1.11}$$

Here, g_s and g_l are the gyromagnetic factors, V_C is the Coulomb potential, and m_N is the mass of the nucleon. Using the formalism of Nolen and Schiffer [12], this equates to an approximate energy splitting contribution of:

$$E_{ls} \simeq (g_s - g_l)\frac{1}{2m_N^2c^2}\left(\frac{-Ze^2}{R_C^3}\right)\langle\vec{l}\cdot\vec{s}\rangle. \tag{1.12}$$

Here $\langle\vec{l}\cdot\vec{s}\rangle = l/2$ or $-(l+2)/2$ for the case of $j = l + s$ or $j = l - s$, respectively.

Multipole Coulomb term

The Coulomb multipole (V_{CM}) termdescribes the difference in energy required to realign pairs of nucleons dependent upon the individual isospin projections and the coupled spin of the pair. In the case of a proton pair, realignment results in a change in spatial separation and consequently, a change in the Coulomb energy between the pair. The realignment of neutron-neutron and neutron-proton pairs, on the other hand, results in no such change in the Coulomb energy. This effect is accounted for through Coulomb matrix elements (CMEs). The importance of this J dependent term is shown in Fig. 1.5, which indicates the probability distribution of the relative distance between two like-particles in the $f_{7/2}$ shell [13].

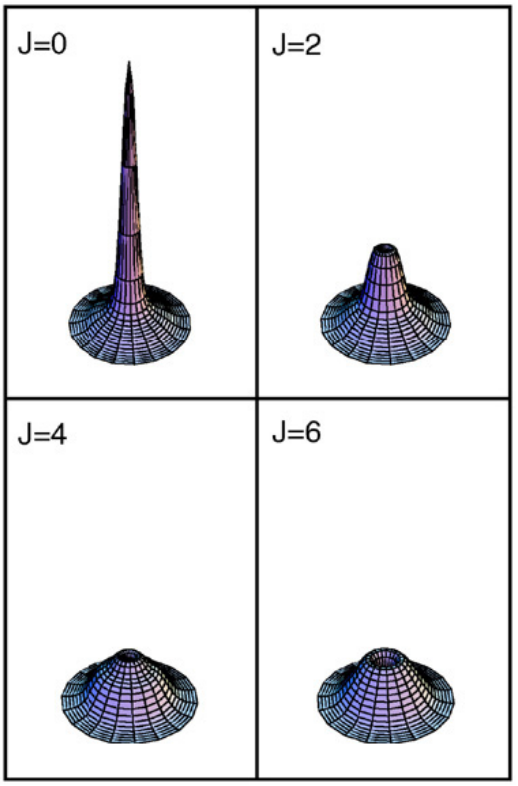

FIGURE 1.5: Illustration of the importance of the V_{CM} term. Shown are the probability distributions for the relative distance between two like-particles in the $f_{7/2}$ shell for a variety of coupled angular momenta. The V_{CM} term accounts for the additional repulsion between proton pairs as a result of this J dependent spatial overlap.

V_B term

The additional isospin non-conserving components to the shell model investigated in the present work are then included in the form of an additional term, V_B, which is determined empirically. The systematic measurement of this V_B term has been the primary goal of recent studies into INCs.

1.3 Previous measurements

In recent years, a great deal of experimental effort has been put into extracting both MEDs and TEDs, with particularly the $f_{7/2}$ shell being extensively studied. A commonly used example of mirror symmetry is shown in Fig. 1.6, with measurements of the $T_z = \pm 1/2$ pair, ^{51}Fe and ^{51}Mn. The similarities between the excited states is immediately apparent, with the MEDs shown in the plot on the right-hand side.

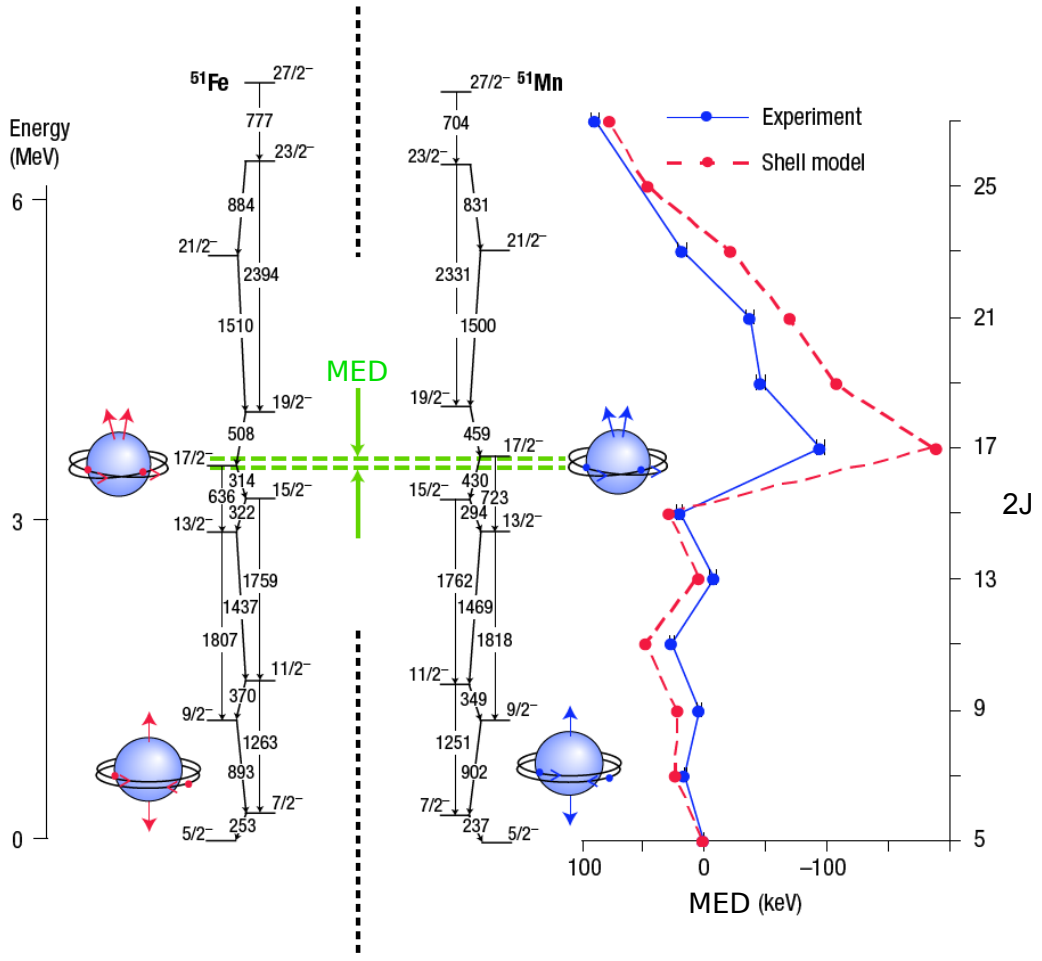

FIGURE 1.6: MED information for the $T_z = \pm 1/2$ pair, ^{51}Fe and ^{51}Mn. Adapted from Ref. [13].

More recently, sophisticated shell-model calculations have made comparisons between theoretical predictions and experimental data possible in the more exotic regions surrounding the $N = Z$ line. This has allowed for in-depth studies into the exact nature of the nuclear force and, particularly, the contributions from isospin breaking terms.

A study by Zuker *et al.* [14] attempted to incorporate the INC components mentioned in Section 1.2.1 and to quantify any remaing INC components. V_C - containing all Coulomb

interaction contributions - was calculated in a harmonic-oscillator basis for different values of J. These values are shown in the first line of Tab. 1.1. By subtracting V_C from the experimental MED and TED data for the $A = 42$ isobar, one is left with an estimate of the isovector (second line) and isotensor (third line) energies respectively. These contributions are significant, being of similar magnitude to the contributions from the Coulomb interaction.

TABLE 1.1: Coulomb (V_C), isovector (MED-V_C) and isotensor (TED-V_C) energies [14]. V_C was calculated in a harmonic-oscillator basis. MED and TED data were taken from the $A = 42$ isobar.

	$J = 0$	$J = 2$	$J = 4$	$J = 6$
V_C (keV)	81.60	24.60	6.40	-11.40
MED-V_C (keV)	5.38	92.55	4.57	-47.95
TED-V_C (keV)	116.76	80.76	2.83	42.15

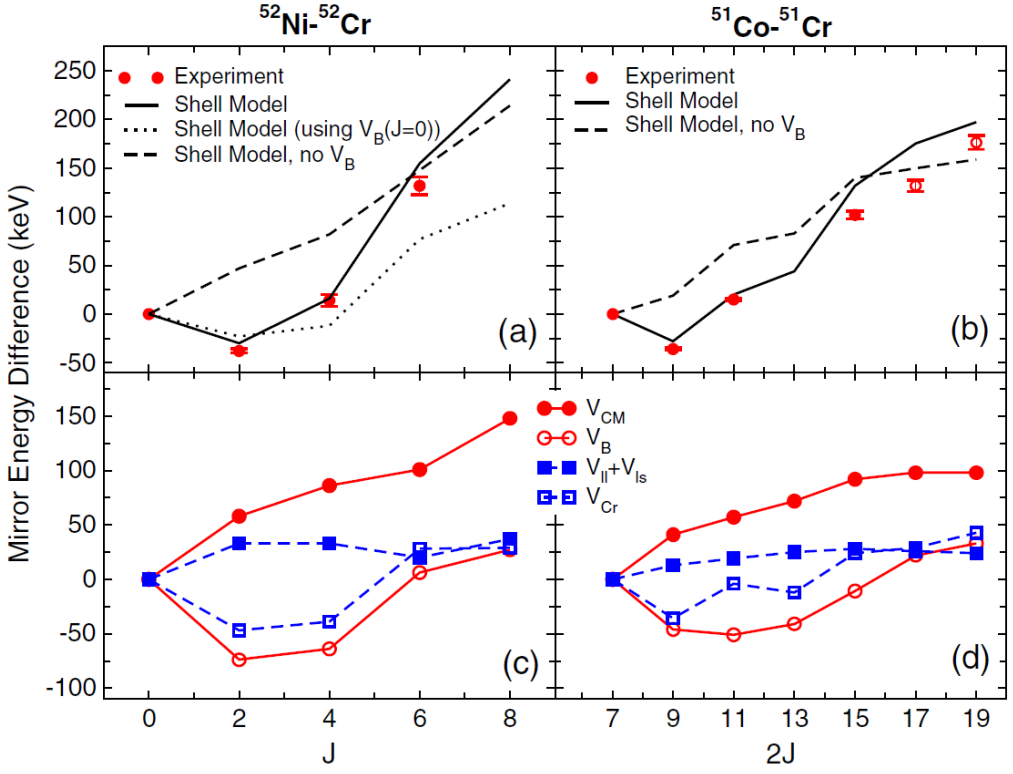

FIGURE 1.7: MEDs extracted from data for the mirror nuclei, ^{52}Ni and ^{52}Cr (top left) and ^{51}Co and ^{51}Cr (top right). Shell model calculations without (dashed line) and with (solid line) the additional INC term as described in the text. The different components of the shell model are shown in the lower panels.

A study by Davies *et al.* [15] in the $f_{7/2}$ shell, investigated MEDs between the $T_z = \pm 2$ nuclei, ^{52}Ni and ^{52}Cr, and those between the $T_z = \pm 3/2$ nuclei ^{51}Co and ^{51}Cr. The results are shown in Fig. 1.7. In agreement with the previous results [14, 16], it was found that Coulomb isospin-breaking terms were insufficient to reproduce the experimental data within the calculations. It was again found in the isovector case that an additional 100-keV repulsive term is required at $J = 2$ for the proton-proton interaction in order for the data to be accurately reproduced, as shown by the shell-model calculations plotted in Fig. 1.7.

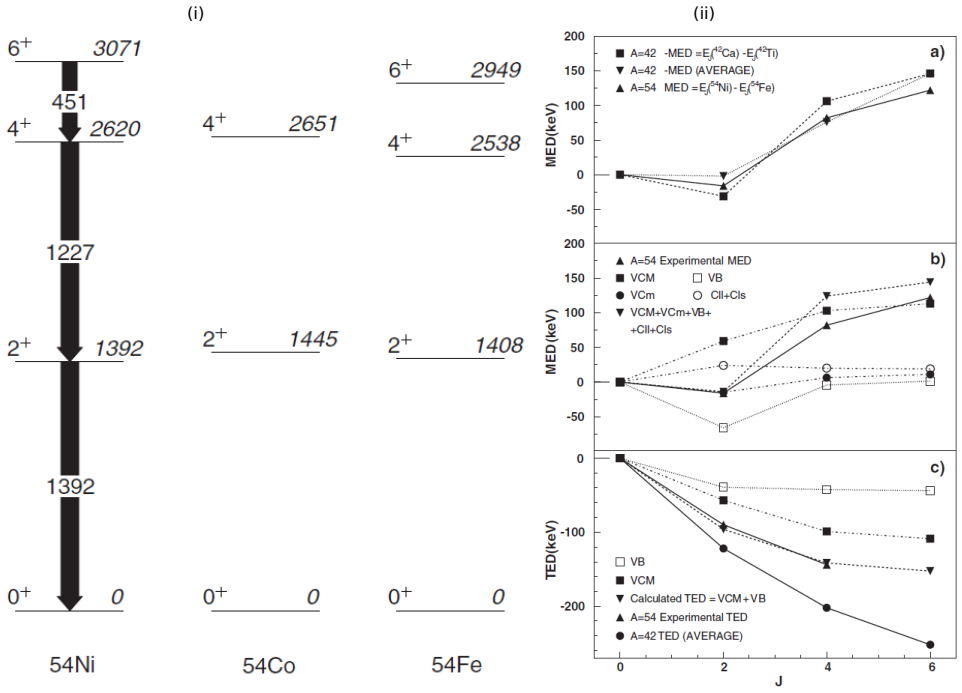

FIGURE 1.8: (i) Deduced level scheme for the $A = 54$ isobaric triplet. (ii) MED and TED for the $A = 54$ isobar as deduced in Ref. [17] along with calculated contributions from the various shell-model components. It is found that an additional $\sim$ 100-keV interaction is required to accurately reproduce the TED data.

The requirement for additional INC terms has also been reinforced in the isotensor TED data. A study by Gadea *et al.* [17] measured both MEDs and TEDs across the $A = 54$ isobaric triplet and provides a useful comparison between the two measurements. The deduced level scheme is given in Fig. 1.8 (i). Note that due to the experimental difficulty of populating $T = 1$ states in the $T_z = 0$ nucleus ^{54}Co, only states up to $J^\pi = 4^+$ were identified. The limits the scope of the measured TEDs, whereas the MED information was available up to $J^\pi = 6^+$.

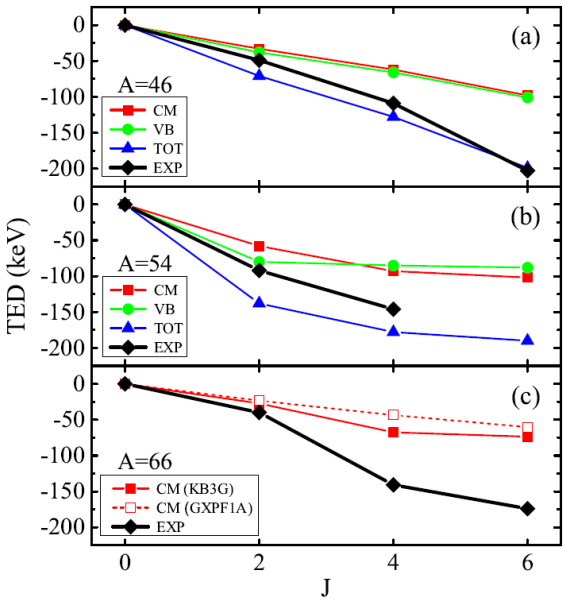

FIGURE 1.9: $A = 66$ isobar TED data (c), with $A = 46$ (a) and $A = 54$ (b) data shown for comparison [18]. Calculated shell-model energy differences without the additional 100-keV INC interaction are shown for two different effective interactions, neither of which accurately reproduces the data.

MED and TED information for the $A = 54$ isobaric triplet are given in Fig. 1.8 (ii). Here, (a) shows the MED data for $A = 54$ compared with $A = 42$. Note that the sign changefor the MED is included to account for cross conjugation. Fig. 1.8 (ii) (b) shows the components of the calculated MED$_J$ while

Fig. 1.8 (ii) (*c*) shows the components of the calculated TED. Due to the nature of TEDs, as discussed earlier, all single particle effects cancel, meaning only V_{CM} and V_B components are required. An additional isotensor component is found to be necessary, although a magnitude of ~ 50 keV is found to be sufficient, rather than the ~ 100 keV found in Ref. [14].

Until recently, MED and TED studies were largely limited to the $f_{7/2}$ shell and below. With recent experimental developments, notably the use of recoil-beta tagging as in the present work, investigations have progressed into the fp shell. At the commencement of this work, the $A = 66$ isobar represented the highest mass at which MED and TED data were available. A recent study by Ruotsalainen *et al.* [18], utilising the same recoil-beta tagging technique as with the present work, provided $A = 66$ TED and MED data up to $J^\pi = 6^+$, where previous data was limited to the first-excited 2^+ state [19]. The TED are shown in Fig. 1.9, alongside the $A = 46$ and $A = 54$ isobars for comparison.

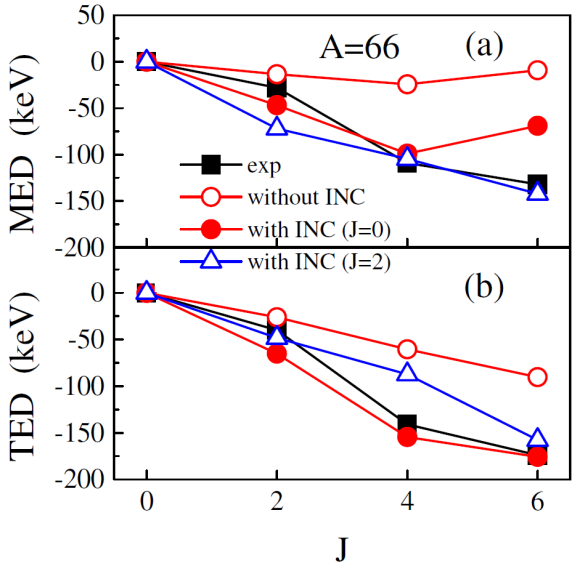

FIGURE 1.10: Shell-model calculations for the $A = 66$ isobar from Ref. [20]. The use of an additional 100-keV $J = 0$ and a 100-keV $J = 2$ INC are investigated. It is found that the $J = 0$ INC component best reproduces the data for the $A = 66$ isobar.

No V_B element is shown in Fig. 1.9 (c) because, as yet, there are insufficient data to establish its magnitude through systematic studies. Whilst the magntiude of any additional INC component is not shown, it is immediately apparent that standard isospin-nonconserving V_C components is not sufficient to reproduce the TED trend. It should be noted however that the shell-model calculations for the $A = 66$ isobar in Ref. [18] are simplistic in nature and do not include, for example, the $g_{9/2}$ orbital.

A theoretical study of MEDs and TEDs in the $A \sim 70$ region was recently completed by Kaneko *et al.* [20]. The state-of-the-art JUN45 interaction was used in a $pf_{5/2}g_{9/2}$ valence space. A new diagonalisation method was used to allow the large-scale valence space to be studied [21, 22]. The Coulomb multipole term, V_{CM}, was used with a Coulomb monopole term, ε_{ll} and spin-orbit term, ε_{ls} also included. $J = 0$ and $J = 2$ couplings for the additional INC interaction were considered. As can be seen in Fig. 1.10, TED data for the $A = 66$ isobar were best reproduced with the addition of a $J = 0$ INC interaction.

The $J = 0$ INC terms are defined as:

$$\begin{aligned} V_{pp} &= \beta_{pp} V_{pp}^{J=0}, \\ V_{nn} &= \beta_{nn} V_{nn}^{J=0}, \\ V_{pn} &= \beta_{pn} V_{pn}^{J=0}, \end{aligned} \tag{1.13}$$

where $V_{pp}^{J=0}$, $V_{nn}^{J=0}$ and $V_{pn}^{J=0}$ are the pp, nn and pn pairing interactions, respectively. It is found that values of $\beta_{pp} = 200$ keV, $\beta_{nn} = -100$ keV and $\beta_{pn} = 0$ keV best fit the data given in Ref. [18].

Further to determining the strengths of INC components of interactions, Ref. [20] provides predictions of MEDs, TEDs and other nuclear-structure effects in the $A \sim 70$ region with INC components as determined for the $A = 66$ isobar. Fig. 1.11 shows predicted TEDs for the $A = 70$, $A = 74$ and $A = 78$ isobars in (b), (c) and (d), respectively, as well as the individual components of the interaction. The TED for the $A = 66$ isobar is also shown for completeness. Single-particle effects, ε_{ls} and ε_{ll} are found to either cancel out or be negligibly small, as would be expected from previous discussion of TEDs.

Experimental studies of TEDs in the $A = 70$ region will provide vital information on the validity of these calculations, giving further insight into the nature of the nuclear force as the $g_{9/2}$ shell increases in influence. As well as MED and TED predictions, Ref. [20] also reinforces previous studies, which predicted significant shape-coexistence in the $T_z = -1$ nucleus, ^{70}Kr. Due to problems with beam contamination, a direct study of ^{70}Kr was not possible at the time of this work, however a measurement of the $A = 74$ isobaric triplet would further probe the region of interest, allowing for testing of these theoretical predictions.

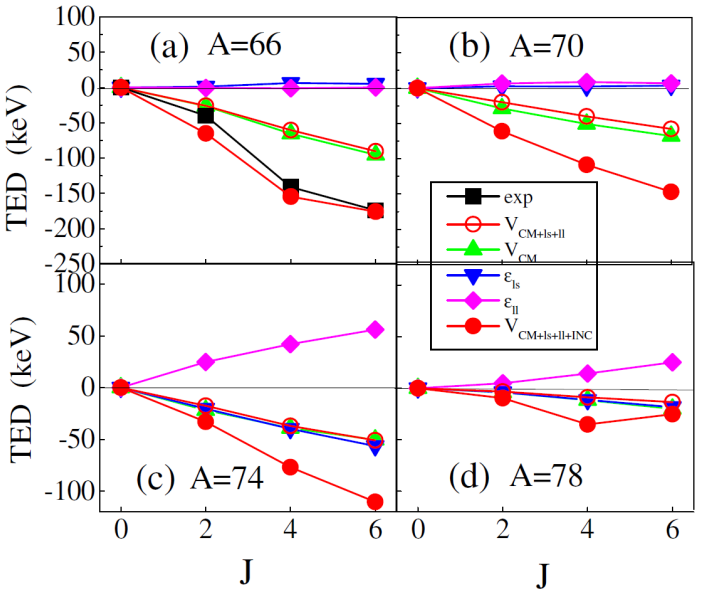

FIGURE 1.11: Calculated TEDs for (a): $A = 66$, (b): $A = 70$, (c): $A = 74$ and (d): $A = 78$ [23] using the same interaction as in Fig. 1.10, with a $J = 0$ INC component.

An important consideration for the present work is that the $A = 74$ isobar lies in a region of enhanced collectivity. This region was recently found to begin at ^{72}Kr through the measurement of the large $B(E2)$ which are symptomatic of such enhanced collectivity [24]. This sharp increase in collectivity represents a major nuclear structure change. Extracting TEDs

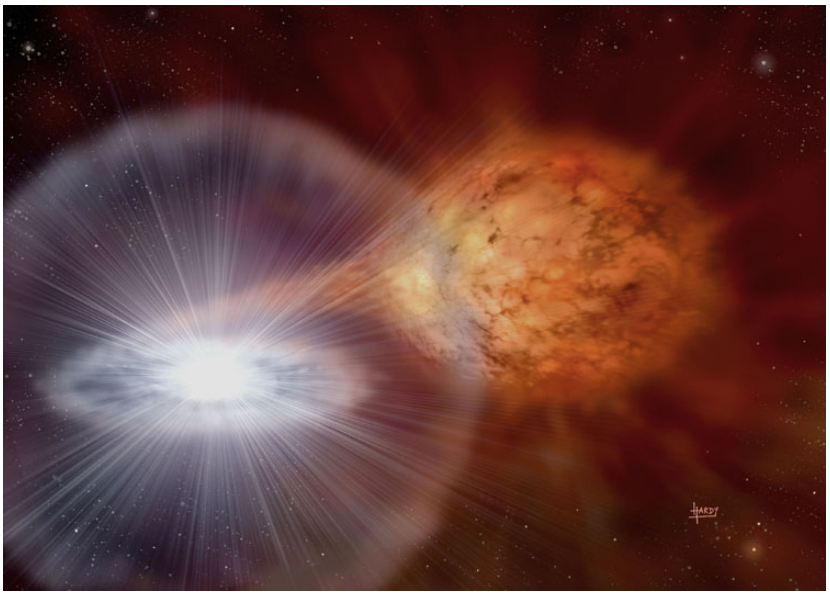

FIGURE 1.12: An artist's impression of an X-ray burst environment [25]. Matter can be seen to be accreting from the partner onto the neutron star.

in this region is therefore of high interest since they will allow for studying the structure dependence of any INCs.

1.4 The astrophysical rp-process

Investigations in the $N \sim Z$ region also have astrophysical implications. The rp-process occurs in the vicinity of the $N = Z$ line, with rapid proton-capture chains and subsequent β decays allowing for the seeding of heavy elements in the $A \sim 100$ region. The rp-process requires a high temperature ($\gtrsim 1$ GK) environment with a large proton flux to progress.

1.4.1 X-ray bursts

The astrophysical phenomena best able to provide the necessary conditions for the rp-process are X-ray bursts. The accretion of matter from a partner star onto a neutron star in a binary system results in a gravitational energy release at temperatures corresponding to X-ray energies. In the case of a more massive partner ($> 5M_{\odot}$, a **h**igh **m**ass **X**-ray **b**inary, HMXB), the matter tends to be "funneled" along magnetic field lines, resulting in localised accretion at the magnetic poles of the neutron star. This - combined with a neutron star of high rotational frequency - results in an X-ray pulsar [26].

In the case of a low-mass partner star ($< 1.5M_{\odot}$, a **l**ow **m**ass **X**-ray **binary**, LMXB) and a neutron star with a weak magnetic field, the accreted matter is not funneled onto the poles. Instead, matter is accreted by a process known as Roche lobe overflow. The Roche lobe of a

star in a binary system describes the region of space inside which material is gravitationally bound. In Roche lobe overflow, the matter lies outside of the lobe and can be accreted onto the partner. This process is not localised - as was the case with HMXB - rather, the matter is accreted fairly uniformly from the accretion disk.

Matter accreted in LMXB is fused to form helium, however temperatures are not sufficient to fuse the produced helium. Instead, the helium sinks into the neutron star. The helium eventually reaches sufficient temperature and pressure to undergo the triple-α process, resulting in thermonuclear runaway [27]. This causes the explosive burning of surface hydrogen and helium, resulting in a high proton flux which allows the rp-process to progress. An artist's impression [25] of the astrophysical environment in which an X-ray burst may occur is shown in Fig. 1.12.

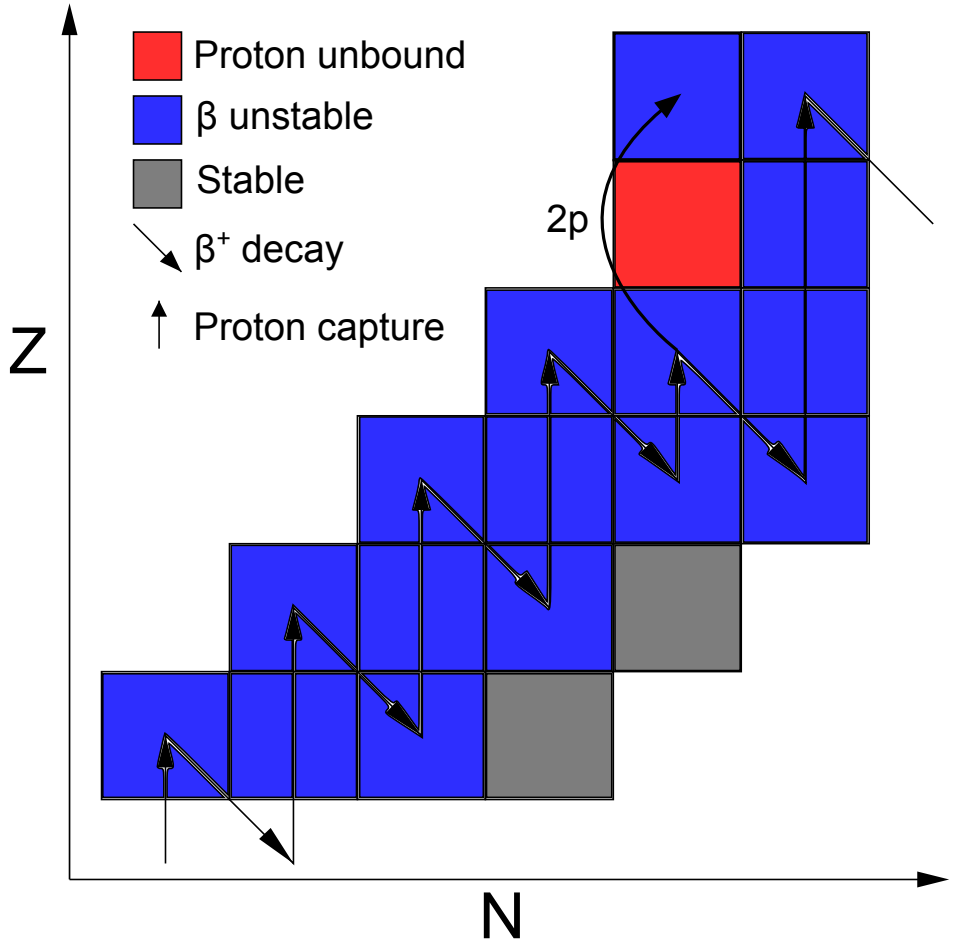

FIGURE 1.13: An illustration of the rp-process. Rapid, consecutive proton captures result in a progression to higher masses. When proton capture becomes inhibited due to the daughter nucleus being proton unbound, the process must progress either through a β-decay - which can be very slow - or the near prompt capture of two consecutive protons.

1.4.2 Nuclear physics considerations

The rate at which the rp-process progresses depends on competition between proton-capture reactions, (p,γ), photodissociating reactions, (γ,p), and β^+ decay. Proton capture will proceed until the γ-ray flux is sufficiently intense that the (γ,p) reaction dominates, or until the β^+-decay lifetime is short enough to compete with the capture process. Beta-decay lifetimes are therefore clearly of great interest for rp-process studies, with level densities and proton-separation energies (S_p) also important.

At higher masses ($A \gtrsim 70$), proton-separation energies and β^+-decay lifetimes are not experimentally verified and result in large uncertainties for the rp-process. In particular, proton-unbound nuclides are known to exist in this region, such as ^{69}Br and ^{73}Rb. These nuclides result in waiting points for the rp-process as proton capture onto ^{68}Se and ^{72}Kr populates unbound states which tend to proton decay, meaning a β decay is required before the process can continue. The capture of two protons in quick succession can bypass this waiting point, as shown in Fig. 1.13, however this process is extremely sensitive to the proton-separation energy of the unbound nuclide.

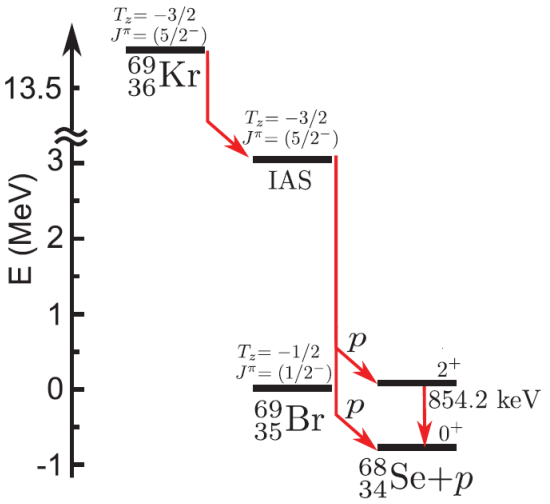

FIGURE 1.14: Schematic describing β-delayed proton decay of ^{69}Br [28]. The Fermi β-decay of ^{69}Kr populates the $T = 3/2$ IAS in ^{69}Br, which proton decays.

Beta-delayed proton emission provides a unique method of probing the proton-separation energy. The use of such decays from ^{65}Se and ^{69}Kr as a Trojan horse for the study of states in ^{65}As and ^{69}Br respectively was presented by Rogers *et* al. [28]. The Fermi β-decay of the parent nucleus goes strongly into the IAS of the daughter, as shown in Fig. 1.14 which then emits a proton to decay into states in the granddaughter.

Proton emission following a Fermi-allowed β decay provides limited information on excited states in the daughter nucleus, however Gamow-Teller β-decays from the parent nucleus are also possible (see Chapter 2 for details of Gamow-Teller decays). Beta decays have a strong Q-value dependence and as such, Gamow-Teller decays would be expected to populate allowed low-lying states preferentially. In the case of ^{69}Br, the angular momentum difference, $\Delta l = 2$ forbids Gamow-Teller transitions between the ground states of ^{69}Kr and ^{69}Br, however the analagous decay between ^{73}Sr and ^{73}Rb has $\Delta l = 1$. One might therefore expect a Gamow-Teller β-decay component into the ground state of ^{73}Rb, the proton decay of which would allow for the extraction of S_p for ^{73}Rb.

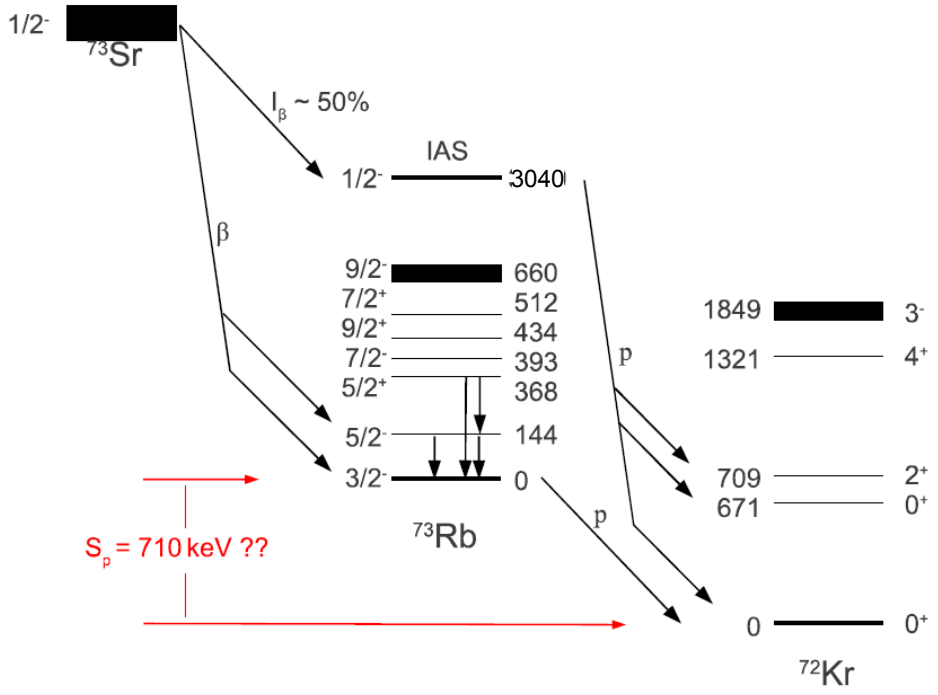

FIGURE 1.15: The anticipated decay scheme for ^{73}Sr [30]. About 50% of the ^{73}Sr decay branch goes via Fermi decay to the IAS in ^{73}Rb, with the remaining 50% going by Gamow-Teller decay to low-lying states, including the ground state. The estimated S_p value comes from CDE calculations.

In 1993, Batchelder *et al.* [29] made the first measurement of the beta-delayed proton decay of ^{73}Sr. Due to experimental limitations, this study was only able to observe proton decays above a threshold energy of about 2.5 MeV. As a result, only the Fermi decay to the IAS in ^{73}Rb was reported, with a 3.75 MeV-proton line observed corresponding to its prompt decay. The decay branch to the IAS is predicted to be about 50%, with the remainder of the strength going by Gamow-Teller decays to the low-lying states in ^{73}Rb. The observation of the beta-delayed proton decays associated with the Gamow-Teller branch to the ground state of ^{73}Rb will provide a direct observation of S_p. A schematic of the predicted β-delayed proton decay scheme of ^{73}Sr is shown in Fig. 1.15. The S_p is predicted on the basis of CDE calculations.

1.5 β-decay lifetime calculations

β-decay properties of even-even nuclides in the neutron-deficient, medium-mass ($50 \lesssim A \lesssim 100$) region have been calculated in recent years using a deformed Skyrme Hartree-Fock methodology with Bardeen-Cooper-Schrieffer (BCS) pairing correlations and the quasiparticle random-phase-approximation (QRPA) [31]. Of particular interest in these calculations is the extraction of Gamow-Teller strengths ($B(GT)$s) for rp-process nuclides, however they are also powerful for the calculation of the β-decay lifetime. The underlying theory of the individual

components to the calculation will be discussed for completeness, before the conclusions reached in the study are introduced.

1.5.1 Skyrme Hartree-Fock potentials

The Hartree-Fock method is a mean-field approach used to model nuclear structure. To determine the nuclear ground-state one begins with an initial, trial wavefunction. In order to accurately model the fermions in the nuclear many-body system, which must obey the Pauli exclusion principle, one requires that this trial nuclear ground-state wavefunction is antisymmetric, and is therefore constructed using a Slater determinant. Variations upon this trial ground-state wavefunction are made in order to minimise the Hartree-Fock energy until a self-consistent convergence is reached. In other words, the method searches for the Slater determinant which minimises the expectation value for the effective Hamiltonian.

The Skyrme interaction [32, 33] is an effective interaction based on Dirac δ functions, with both two- and three-body components,

$$V_{\text{Skyrme}} = \sum_{i<j} V(i,j) + \sum_{i<j<k} V(i,j,k). \tag{1.14}$$

The two-body component is given by

$$\begin{aligned} V(1,2) = {} & t_0 \left(1 + x_0 P^\sigma\right) \delta\left(\mathbf{r}_1 - \mathbf{r}_2\right) + \frac{1}{2} t_1 \left[\delta\left(\mathbf{r}_1 - \mathbf{r}_2\right) \mathbf{k}^2 + \mathbf{k}^2 \delta\left(\mathbf{r}_1 - \mathbf{r}_2\right)\right] \\ & + t_2 \mathbf{k} \delta\left(\mathbf{r}_1 - \mathbf{r}_2\right) \mathbf{k} + i W_0 \left(\boldsymbol{\sigma}^{(1)} + \boldsymbol{\sigma}^{(2)}\right) \mathbf{k} \times \delta\left(\mathbf{r}_1 - \mathbf{r}_2\right) \mathbf{k}, \end{aligned} \tag{1.15}$$

where $\mathbf{k}$ is the relative momentum operator, $\boldsymbol{\sigma}^{(1)}$ and $\boldsymbol{\sigma}^{(2)}$ are the spin matrices, and t_n, x_0 and W_0 are experimentally derived variables. The three-body component is given by

$$V(1,2,3) = t_3 \delta(\mathbf{r}_1 - \mathbf{r}_2) \delta(\mathbf{r}_2 - \mathbf{r}_3). \tag{1.16}$$

For the case of even-even nuclei which have saturated spin, this three-body component can be reduced to

$$V_\rho(1,2) = \frac{1}{6} t_3 \left(1 + P^\sigma\right) \delta\left(\mathbf{r}_1 - \mathbf{r}_2\right) \rho\left(\frac{1}{2}\left(\mathbf{r}_1 + \mathbf{r}_2\right)\right), \tag{1.17}$$

where the resultant interaction can be seen to be density dependent and two body. The aforemention, empirically derived parameters in Equations 1.15 and 1.17 are then fitted to

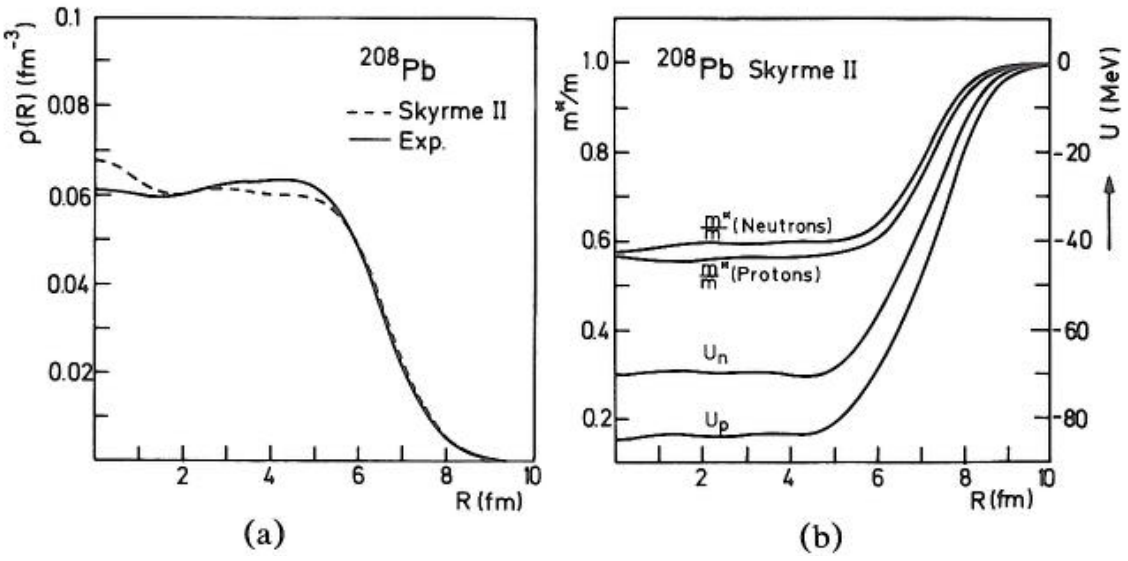

FIGURE 1.16: Calculated using a Hartree-Fock approach with a Skyrme II interaction [35] for ^{208}Pb: (a) Charge density, calculated vs. experimental. (b) Effective mass for protons and neutrons, m^*/m and nuclear potential, $U(r)$. Note that the proton potential does not include the Coulomb term [34].

a set of experimental data. It should be noted that the "three-body" interaction is often considered to be representative of the ρ-dependence of the effective interaction because it is larger than the physical three-body interactions within nuclei, which are known to be weaker [34].

Due to the density dependence of the Skyrme interaction, one cannot construct the Hartree-Fock in the same variational manner, since this relies on a linear Hamiltonian. Instead, the expectation value of the Skyrme interaction is calculated and given with respect to a Slater determinant. The fact that the Skyrme interaction is constructed from δ functions allows the energy to be expressed in terms of an energy density, which is itself a function of the nucleon density, kinetic energy density and spin-orbit densities. By summing over all occupied single-particle states, this energy can be calculated [35].

One of the major benefits of combining the Hartree-Fock method with the Skyrme potential is that it allows the simulataneous calculation of the binding energies, nuclear radii and single-particle energies, where density independent forces would be limited to the nuclear radii and single-particle energies. This is because, in the case of the Skyrme interaction, an additional, negative "rearrangement" term is included, allowing for the fitting to all three observables. An example of the nuclear charge distribution, ρ_R, is given in Fig. 1.16 (a) whilst the effective mass, m^*/m and average nuclear potential, $U(r)$, is shown in Fig. 1.16 (b), created using the Skyrme II interaction [35]. The above introduction was based on a spherical Skyrme Hartree-Fock potential, however it is also possible to extend the model to derformed potentials, such as those expected in the $N \sim Z$, $A > 72$ region of the nuclear landscape [36].

1.5.2 BCS pairing

It is well-established that pairing correlations are important for determining nuclear structure properties. As a result it is necessary to include such correlations when one considers a mean field, such as that created from the Skyrme Hartree-Fock approach, in order to account for the so-called "pairing gap", Δ. One solution is known as the Bogolyubov transformation, in which the self-consistent mean field of the Hartree-Fock approach and the pairing correlations are considered simultaneously, achieved by transforming the fermion particle operators into quasiparticle operators [37]. More explicit discussion of the Hartree-Fock-Bogolybov method is beyond the scope of this work.

An alternative method [38, 39] is to use the specific case of the Bogolyubov transformation in which the quasiparticle state is analagous to the BCS wavefunction [40]. This is only valid in the case of a time-reversal-invariant system. Using the methodology outlined in reference [34],

$$|BCS\rangle = \prod_{k>0} (u_k + v_k a_k^+ a_{\bar{k}}^+) \, |-\rangle \, . \tag{1.18}$$

Here v_k and u_k are the parameters to be varied, while for each state $k > 0$ a conjugate state of $\bar{k} < 0$ also exists and the entire single-particle space is generated from the states $\{k, \bar{k}\}$. v_k^2 and u_k^2 define the probability of a pair state $(k, \bar{k})$ being occupied or not being occupied, respectively, such that the corresponding energy has a minimum. It should be noted that the two parameters are not independent since

$$|u_k|^2 + |v_k|^2 = 1. \tag{1.19}$$

An important additional consideration is that, in that form given in Equation 1.18, $|BCS\rangle$ is a superposition of different numbers of pairs and consequently the number of particles is no longer invariant. Since the particle number in nuclear physics is small (when compared to solid-state physics, for example), this can have a significant effect. One therefore limits the variation of the trial wavefunctions (u_k and v_k in Equation 1.18) to the case where the particle number, N, satisfies

$$\langle BCS| \, \hat{N} \, |BCS\rangle = 2 \sum_{k>0} v_k^2 = N. \tag{1.20}$$

From these equations and assuming a fixed pairing gap, one can derive relations for the occupation parameters, v_k and u_k,

$$v_k^2 = \frac{1}{2}\left(1 \pm \frac{\tilde{\varepsilon}_k}{\sqrt{\tilde{\varepsilon}^2 + \Delta_k^2}}\right)$$
$$u_k^2 = \frac{1}{2}\left(1 \pm \frac{\tilde{\varepsilon}_k}{\sqrt{\tilde{\varepsilon}^2 + \Delta_k^2}}\right). \tag{1.21}$$

In the BCS approximation these parameters are then simply considered factors and multiplied to the single-particle wavefunction, ψ, extracted from the Hartree-Fock approach.

1.5.3 QRPA

Where HF+BCS calculations can reproduce nuclear ground and single-particle states, they are not able to recreate nuclear excitations arising from the collective motion of many nucleons. The random-particle phase approximation (RPA) is therefore used to describe collective excitations in magic nuclei, achieved by considering small amplitude oscillations as particle-hole (ph) correlations. This is achieved through the use of ph creator and destructor operators.

RPA is extended for general use far from closed shells through the quasirandom-particle phase approximation (QRPA), in which pairing correlations are also considered. The result is that, through the ph-operator, one is able to create equations which can be solved to extract collective multi-particle multi-hole excitations.

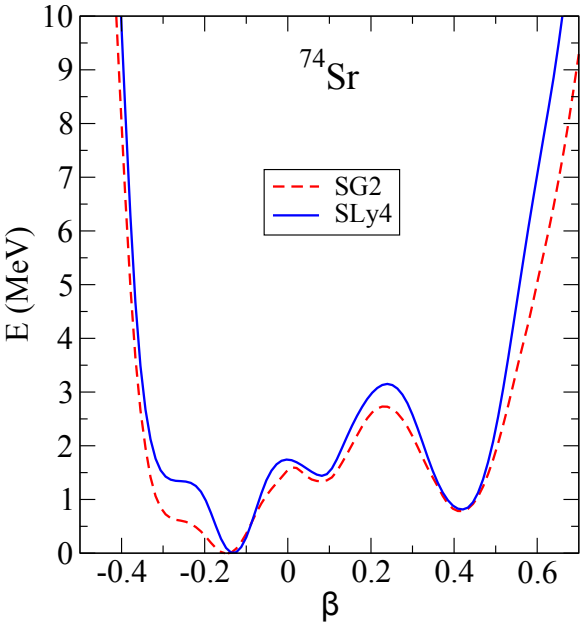

FIGURE 1.17: Potential surfaces extracted from a deformed Skyrme Hartree-Fock + BCS for ^{74}Sr [31]. The potential surfaces for both the SLy4 [41] and SG2 [42] Skyrme forces are shown.

1.5.4 Calculated β-decay properties

In the work described in Ref. [31], the Skyrme force SLy4 [41] was used with the Hartree-Fock approach to create a self-consistent mean-field. This allowed the extraction of the single-particle energies, wavefunctions and occupation probabilities for even-even nuclei. The Hartree-Fock equation was

solved using the method described in reference [36] to account for deformation. Pairing between like nucleons was included using the BCS approximation with fixed gap parameters, Δ, for both protons and neutrons. These were determined from experimental data.

The potential surfaces with respect to the quadrupole deformation parameter,

$$\beta = \sqrt{\frac{\pi}{5}} \frac{Q_0}{A\langle r^2 \rangle}, \tag{1.22}$$

are shown in Fig. 1.17 for ^{74}Sr for both the SLy4 and the SG2 Skyrme forces.

The proton-neutron phonon operator was developed using the QRPA and was used to account for Gamow-Teller (GT) components to the β decay (see Section 2.2.2). The GT strength, $B_{if}(\mathrm{GT})$ was normalised by an effective quenching value, determined from experimental data. Since Fermi β-decays are isospin conserving, their strength, $B_{if}(\mathrm{F})$, is dominated by transitions between IAS. The excitation energy of the IAS in the daughter was given by,

$$E_{IAS} = \Delta M_i - \Delta M_f + 0.7824 - \Delta E_C \text{ MeV}. \tag{1.23}$$

The Coulomb displacement energy, ΔE_C between IAS was accounted for empirically by

$$\Delta E_C = 1.4144(Z_i + Z_f)/(2A^{1/3}) - 0.9127 \text{ MeV}. \tag{1.24}$$

The resultant half-life was calculated as a sum over the available energies (defined by the Q-value of the decay) and weighted by phase-space factors, $\Phi_{if}^{\beta^+/OEC}$,

$$T_{1/2}^{-1} = \frac{1}{D} \sum_{0<E_f<Q_{EC}} \left[B_{if}(\mathrm{GT}) + B_{if}(\mathrm{F})\right] \Phi_{if}^{\beta^+/OEC}. \tag{1.25}$$

Here, Q_{EC} is the Q-value resulting from the electron capture and relates to the Q-value of the β^+-decay by,

$$Q_{EC} = Q_{\beta^+} + 2m_e. \tag{1.26}$$

The calculated half-lives are shown in Fig. 1.18 for those nuclides where experimental information was available. At the time these calculations were performed, no experimental value for Q_{EC} was available for the decay of ^{74}Sr. A value $Q_{EC} = 11.2$ MeV was used, which was extracted from systematics. Using this, a half-life of 54 ms was extracted [43] using the model outlined.

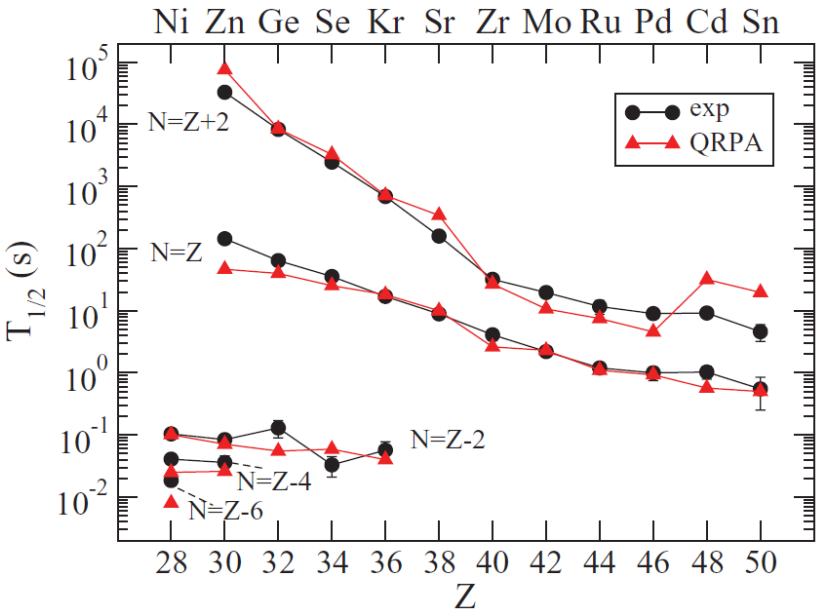

FIGURE 1.18: Experimental half-lives vs calculated-half lives from QRPA calculations for those nuclides where experimental data was available [31].

The $Q(EC)$ value is a significant source of error in these calculations. For example, in reference [23], shell-model calculations using two different effective interactions (GXPF1A and JUN45) are performed, complete with an INC component. The consequent proton (S_p) and two-proton (S_{2p}) separation energies calculated in the region of interest are shown in Fig. 1.19. The $Q_{syst}(EC)$ value used in the Skyrme Hartree-Fock calculations corresponds to $S_{2p} = 1.45$ MeV, in reasonable agreement with the GXPF1A calculations. On the other hand, were the $S_{2p} = 0.41$ MeV value calculated using JUN45 to prove closer to the truth, one would expect the ^{74}Sr half-life to be about a factor of two shorter than predicted.

		70Sr	71Sr	72Sr	73Sr	74Sr	75Sr					74Zr	75Zr	76Zr	77Zr	78Zr	79Zr		
		−0.21	−0.12	1.11	0.96	2.16	1.87					0.61	−0.65	−0.06	−0.21	1.03	1.52		
		−3.52	−2.23	−1.15	0.15	1.26	3.99					−3.56	−3.02	−2.00	−0.81	0.39	3.46		
	68Rb	69Rb	70Rb	71Rb	72Rb	73Rb	74Rb			72Y	73Y	74Y	75Y	76Y	77Y	78Y			
	−3.14	−3.32	−2.11	−2.26	−0.81	−0.90				−3.85	−0.40	−2.37	−1.94	−0.61	−0.64				
	−3.24	−2.18	−1.13	0.14	0.52	3.94				−4.50	−4.55	−1.98	−0.44	0.64	3.82				
66Kr	67Kr	68Kr	69Kr	70Kr	71Kr	72Kr			70Sr	71Sr	72Sr	73Sr	74Sr	75Sr	76Sr				
−0.26	−0.11	1.13	0.98	2.41	1.81				−0.48	−0.65	0.72	0.39	1.50	1.24					
−3.25	−1.90	−0.74	0.36	1.81	4.30				−4.37	−3.11	−2.00	−1.34	0.41	3.36					
									69Rb	70Rb	71Rb	72Rb	73Rb	74Rb					
									−3.89	−2.46	−2.71	−1.73	−1.10						
									−3.16	−1.72	−0.45	−0.07	3.74						

FIGURE 1.19: Proton and two-proton separation energies from shell-model calculations utilising the GXPF1A (left) and JUN45 (right) shell-model effective interactions. The latter interaction file predicts that ^{74}Sr should be considerably less well-bound than assumed from systematics.

1.6 Scope of the present work

To summarise, the primary aim of the present work is to observe low-lying excited states in the $T_z = -1$ nuclide ^{74}Sr and to extract TEDs for the $A = 74$ isobar, which will represent the highest mass for which such values have been calculated. This will allow for the evaluation of INCs for shell-model calculations in the upper-fp shell, where the influence of the $g_{9/2}$ shell will be more significant than in any previous studies. The extracted TEDs will also allow for the first assessment of INCs in a highly-collective region of the nuclear landscape, allowing for an evaluation of their structure dependence.

As an additional motivation, at the commencement of the present work, no experimentally extracted β-decay half-life for ^{74}Sr was available. During the course of the work a complementary experiment was performed to measure this value. This result will be alluded to and is used to optimise the work described herein. The evaluation of the β-decay half-life, used in concert with the Skyrme Hartree-Fock + BCS + QRPA calculations discussed previously will be used to assess how bound the ^{74}Sr nucleus is, particularly as one probes higher-lying excited states.

A final source of motivation is the measurement of β-delayed protons from the decay of ^{73}Sr, which will likely be produced with a low cross section in the reaction used to produce ^{74}Sr. This will allow for the determination of the proton separation energy, S_p, of ^{73}Rb, a value which is of astrophysical interest in the rp-process.

Chapter 2

Experimental technique

> It is well known that a vital ingredient of success is not knowing that what you're attempting can't be done.
>
> Terry Pratchett - Equal Rites

In order to achieve the aims set out in Chapter 1, the recoil-beta tagging (RBT) method was employed. This relatively new technique is an extension of the well-established recoil-decay tagging (RDT) method and allows for the extraction of low cross-section channels from reactions high in contaminants. This chapter will explain the need for such a sensitive technique before introducing RDT and RBT to the reader. In order to provide a complete discussion, some comments on nuclear transitions, decays and reactions will also be included. Additionally, a brief mention of alternative methods will be presented.

2.1 Nuclear reactions and the cross-section problem

Historically, experiments aiming to probe the neutron-deficient region of the nuclear landscape have tended to utilise a type of nuclear reaction known as fusion evaporation. Fusion-evaporation reactions are compound-nuclear reactions; all the nucleons in the incident and target nuclei are involved. The beam nucleus is incident on a target nucleus with sufficient energy to overcome the Coulomb barrier, resulting in the creation of a compound nucleus in a highly excited state. In order to de-excite, massive particles - typically protons, neutrons and α particles - are emitted until the remaining excitation energy is sufficiently low as to hinder particle emission. At this point, statistical γ rays are emitted. Initially these γ rays originate from the continuum and are of very low energy, but eventually discrete excited states are populated. These subsequently de-excite to the ground state, usually via the yrast states, as shown in Fig. 2.1. Whilst de-excitation via yrast states dominates, non-yrast states can also be populated.

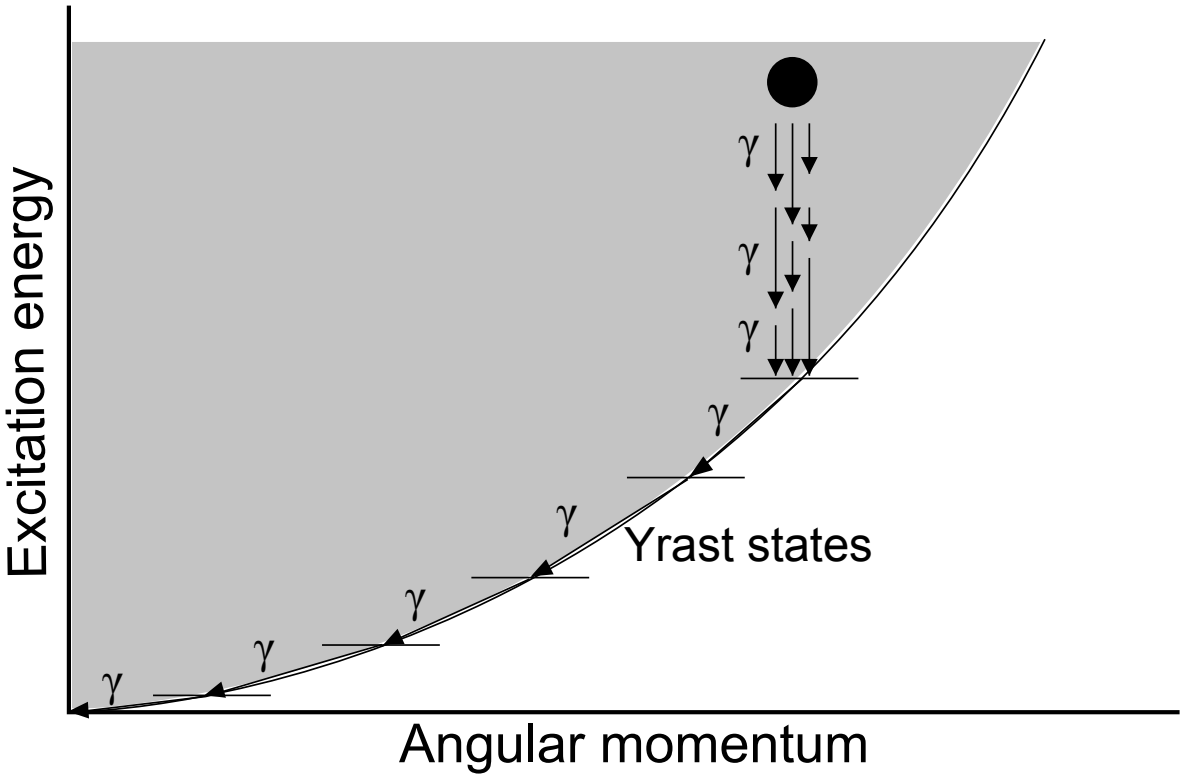

FIGURE 2.1: The γ-ray emission process following fusion evaporation. The statistical γ rays emitted from the compound nucleus tend to populate the yrast states, however non-yrast states can also be populated.

Due to the large number and statistical nature of the de-excitations in compound nuclear reactions the final states populated are largely independent of the initial state of the beam and target nuclei. There remain preferential alignments with respect to the beam axis due to the angular momentum imparted to the compound nucleus.

There is, of course, an energy dependence on reaction channels. As the energy of the incident nucleus increases, so does the excitation energy of the compound nucleus resulting in a larger number of massive particles being emitted. An illustration of fusion-evaporation cross-sections for neutron evaporation-channels is shown in Fig. 2.2 to demonstrate this.

Near the valley of stability, pure neutron-evaporation channels dominate as a result of the Coulomb barrier hindering the emission of charged particles. As one aims to populate nuclides in the neutron-deficient region of the nuclear landscape however, the relatively weakly-bound nature of the protons in the nucleus means that proton-evaporation channels begin to compete and eventually dominate over the neutron-evaporation channels. The pure neutron-evaporation channels are those of interest in the vicinity of the proton drip-line, one must therefore deal with cross sections for the channel of interest of the order of 100 nb for a total evaporation cross-section of 100 mb. The challenge of extracting such weak channels required the development of highly selective techniques, one of which, recoil-decay tagging (RDT), will now be discussed further.

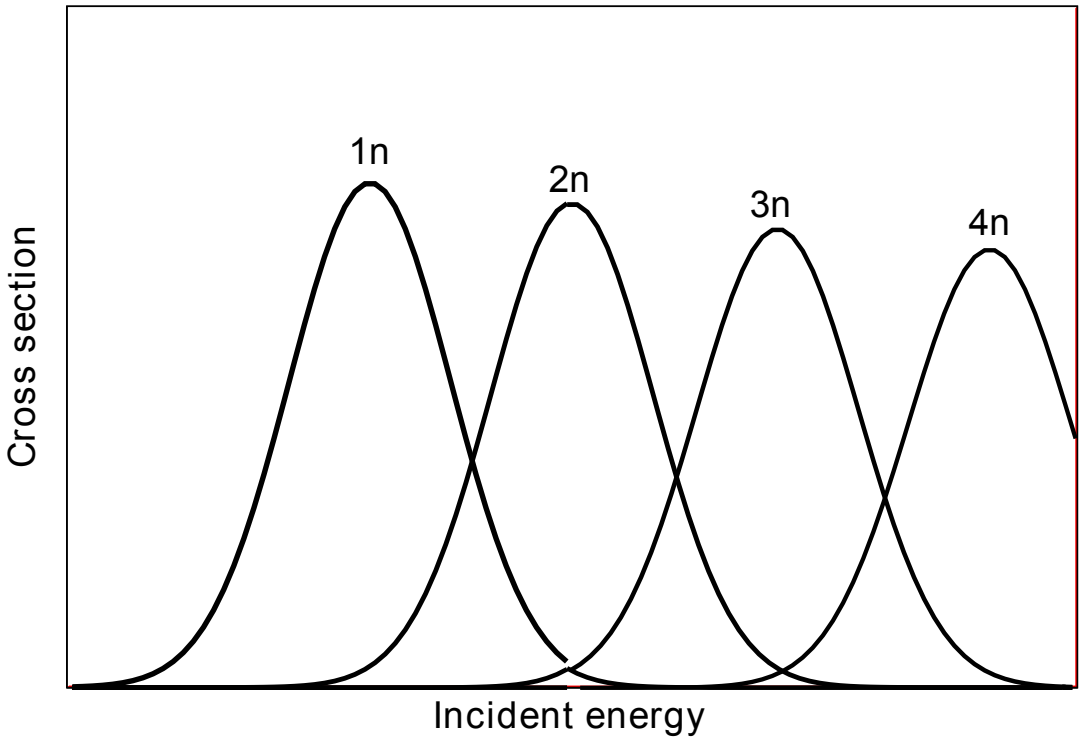

FIGURE 2.2: An illustration of the dependence of cross sections for given reaction channels on the energy of the incident particle in fusion evaporation.

As the name suggests, RDT uses the characteristic decay properties of nuclides in order to unambiguously select a given reaction channel. The principal steps in RDT are as follows:

- Produce the nucleus of interest, typically in a fusion-evaporation reaction.
- Perform spectroscopy of prompt γ decays at the target position.
- Implant the reaction products, including contaminants, in a charged-particle detector
- Identify the characteristic decay of the nucleus of interest using charged-particle detector and/or ancillary detectors.
- Correlate the decay with the implantation and hence select the spectroscopic information corresponding to the reaction channel of interest.

A brief introduction of relevant nuclear decays and transitions will now be presented.

2.2 Nuclear decays and transitions

It is a general principle in physics that, if a transition between a higher- and lower-energy state is not forbidden, it will take place. In nuclear physics, these take two broad forms:

transitions (decays) between different nuclei, and internal decays between different allowed states in the same nucleus. The former are made up predominantly of α, β and proton decay, while the latter consist of γ-ray transitions and electron internal-conversion. This section will introduce the three most common forms, α-, β- and γ-decay, in order to provide the necessary information to understand the RDT technique and more specifically, recoil-beta tagging (RBT).

Transitions probabilities, λ_{if}, between initial state, i and final state, f can be understood through Fermi's Golden Rule,

$$\lambda_{if} = \frac{2\pi}{\hbar}|M_{if}|^2\rho_f, \tag{2.1}$$

where ρ_f is the density of final states and M_{if} is the matrix element describing the transition,

$$M_{if} = \int \psi_i V \psi_i \mathrm{d}v. \tag{2.2}$$

Here, ψ_i and ψ_f are the initial- and final-state wavefunctions, respectively, and V is the operator describing the transition.

2.2.1 Alpha decay

Alpha decay is a two-body emission which is particularly common for nuclei with $A > 150$. As it is a two-body process, the emitted α particle has a characteristic energy,

$$T_\alpha = \frac{Q}{1 + {}^{m_\alpha}/_{m_X}}, \tag{2.3}$$

where Q is the Q value of the decay and m_α and m_X are the masses of the α particle and daughter nucleus, respectively.

Since the charged α particle is bound inside the nucleus, it must tunnel through the nucleus's potential barrier in order to be emitted, as illustrated in Fig. 2.3. This results in α-decay lifetimes being heavily dependent on the Q value of the reaction, since this relates closely to the width, Δr, and relative height of the Coulomb potential through which the α particle must tunnel. This relationship is known as the Geiger-Nuttal rule [44].

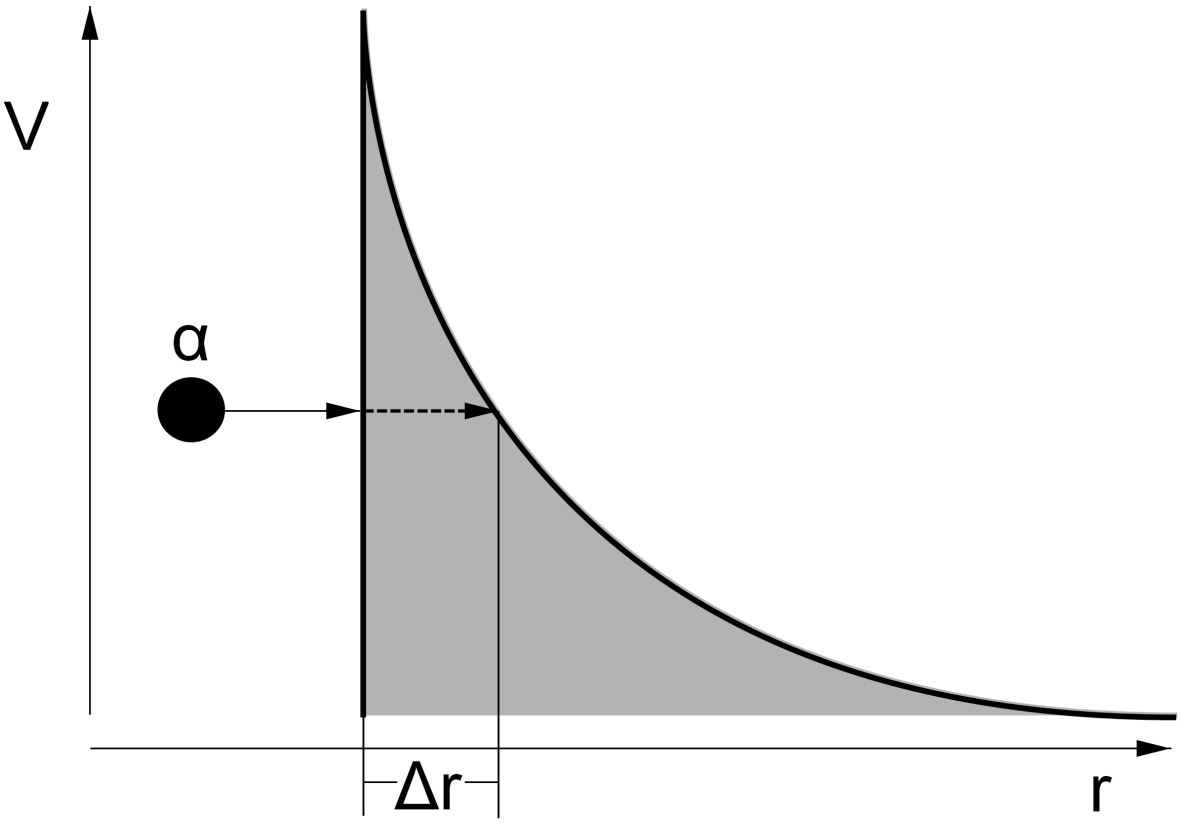

FIGURE 2.3: Illustration of an α-particle inside a nuclear Coulomb barrier

2.2.2 Beta decay

Beta decays come in three forms, β^-, β^+ and electron capture (EC),

$$\begin{aligned} X_{(Z,N)} &\rightarrow X_{(Z+1,N-1)} + \beta^- + \bar{\nu}_e \\ X_{(Z,N)} &\rightarrow X_{(Z-1,N+1)} + \beta^+ + \nu_e, \\ X_{(Z,N)} + e^- &\rightarrow X_{(Z-1,N+1)} + \nu_e, \end{aligned} \tag{2.4}$$

respectively. Where α decay is two body, β^- and β^+ decays are three body. As a result, while emitted α particles have a characteristic energy, β particles emitted in $\beta^\pm$ decay can take a continuum of energies up to the β-decay Q value, since the emitted neutrino also takes a portion of the emitted energy. An example of the spectrum of β-particle energies expected from a β decay of a given Q value is shown in Fig. 2.4, and is described by

$$N(T_e) = \frac{C}{c^5}\left(T_e^2 + 2T_e m_e c^2\right)^{1/2}(Q - T_e)^2\left(T_e + m_e c^2\right). \tag{2.5}$$

Alternatively, one can rearrange Equation 2.5 with respect to $(Q - T_e)$,

$$(Q - T_e) \propto \sqrt{\frac{N(p)}{p^2 F(Z', p)}}. \tag{2.6}$$

This relationship allows one to create what is known as a Fermi-Kurie plot, an example of which is shown in Fig. 2.5 [45]. This plot intersects the x-axis at the Q value of the β decay. The deviation from proportionality at low energy arises from low-energy scattering within the electron source [7]. Given sufficient experimental energy resolution, deviations from proportionality at high energy on the Fermi-Kurie distribution would allow the extraction of m_{ν_e}. This places strong upper limit on m_{ν_e}, as such a deviation is not observed in β-decay measurements.

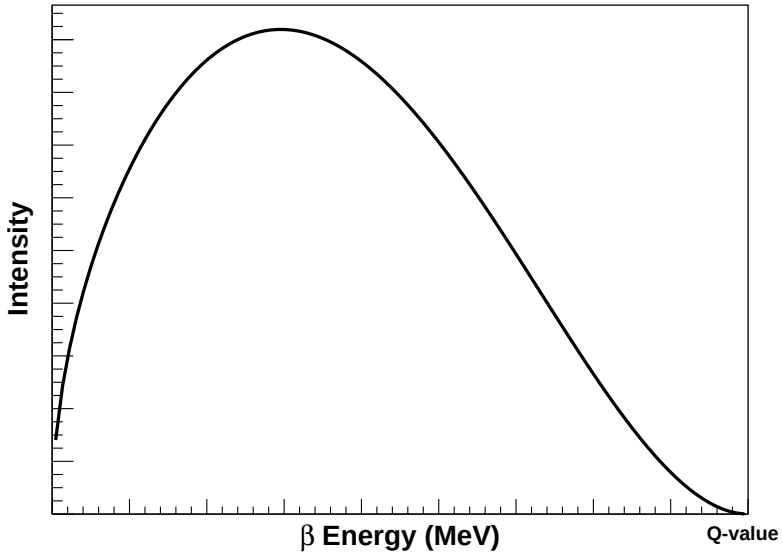

FIGURE 2.4: An illustration of the expected spectrum of energies for a β particle emitted in the β decay for a given Q value.

The transition probability for β decay is often referred to in terms of the $ft_{1/2}$ of the transition, where f is the Fermi integral,

$$f(Z', E_0) = \frac{1}{(m_e c)^3 (m_e c^2)^2} \int_0^{p_m ax} F(Z', p) p^2 (E_0 - E_e)^2 dp, \tag{2.7}$$

which has been tabulated for values of the daughter proton number, Z' and the maximum electron energy, E_0. This gives a relation between the halflife of the decay, $t_{1/2}$, and the transition matrix element introduced in Fermi's Golden Rule, $|M_{fi}|$,

$$ft_{1/2} = 0.693 \frac{2\pi^3 \hbar^7}{g^2 m_e^5 c^4 |M_{fi}|^2}. \tag{2.8}$$

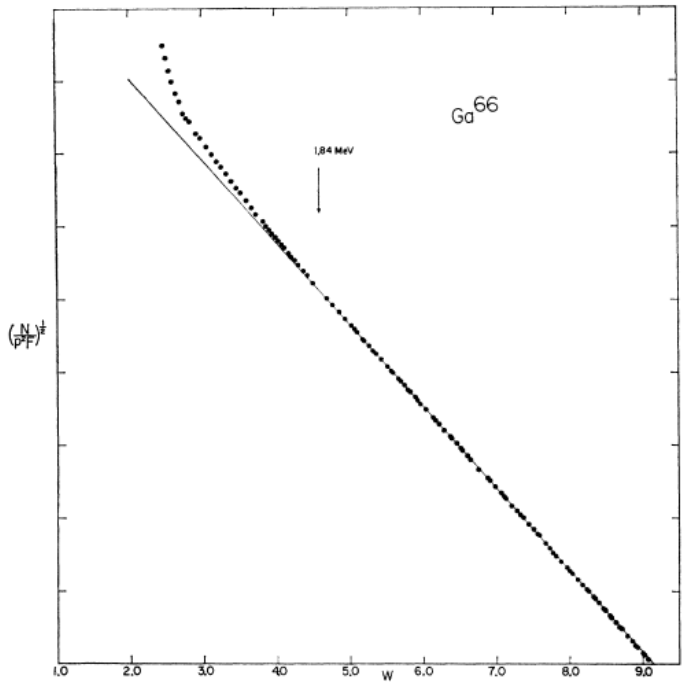

FIGURE 2.5: Fermie-Kurie plot for the superallowed, $0^+ \rightarrow 0^+$, β^+ decay of ^{66}Ga. N/p^2F is plotted against the total energy, $W = T_e + m_e c^2$ [**?**].

Due to large variations in β-decay halflives, the quoted value is often the log ft of the transition rather than the value given in Equation 2.8. Fast β decays with log ft values between three and four are known as superallowed decays, and result from large intial- and final-state overlap, such as decays between analagous 0^+ states in the initial and final nuclei. By convention, β decays are split using two characteristics, by orbital angular momentum changes into allowed and forbidden types[1], and by spin changes of the decaying nucleon into Fermi and Gamow-Teller types. Allowed transitions are those in which no orbital angular momentum is transferred by the emitted fermions, so $\Delta L = 0$. If the spins of the two emitted fermions are antialigned, there is no change in the nuclear spin ΔJ, which is known as a Fermi decay. If the spins are aligned ($S = 1$) on the other hand, the nuclear spin can change by an

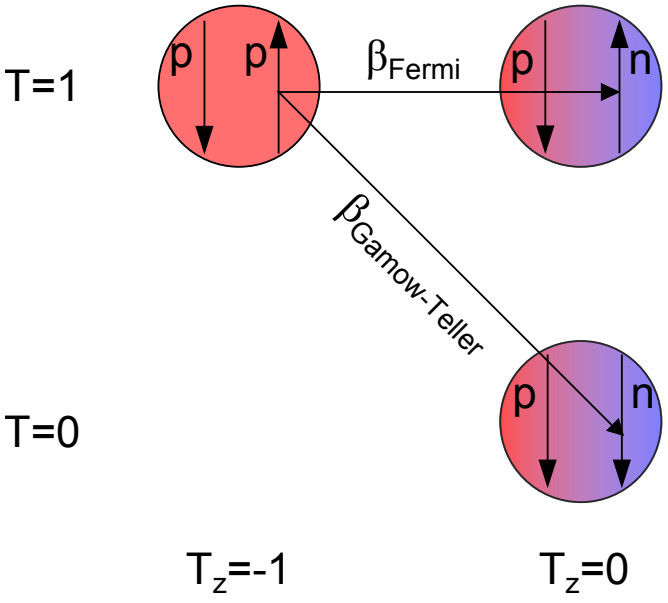

FIGURE 2.6: Isospin conservation in β-decay

[1]It is worth noting here that "forbidden" transitions are not actually forbidden.

angular-momentum vector of length 1, so ΔJ can be either 0 or 1, known as a Gamow-Teller decay. Forbidden transitions are those for which orbital angular momentum is transferred, allowing for larger changes in nuclear angular momentum and changes in parity. These too can be of the Fermi and Gamow-Teller types, but are not relevant for the remainder of the present work. Typical expected $\log ft$ values for different classifications of β decay are shown in Table 2.1, while a schematic of known $\log ft$ values for allowed transistions is given in Fig. 2.7 [46].

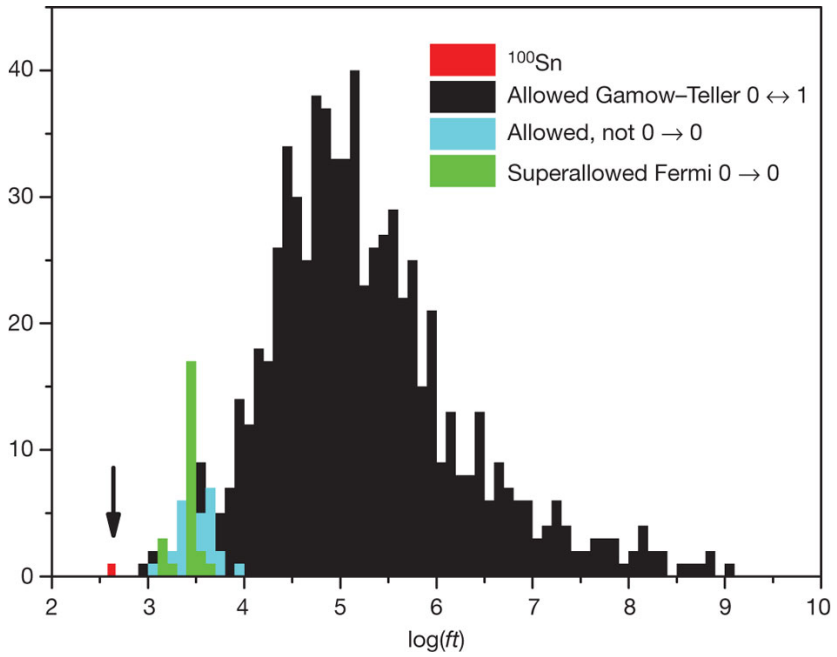

FIGURE 2.7: Known $\log ft$ values for allowed β-decays. It can be seen that allowed Fermi transitions tend to have much lower $\log ft$ values, although there are some noteable exceptions, such as the subject of Reference [46], from which this figure was taken.

TABLE 2.1: Typical $\log ft$ value for β-decay classifications [47].

Transition classification	$\log ft$
Superallowed	2.9-3.7
Allowed	4.4-6.0
First forbidden	6-10
Second forbidden	10-13
Third forbidden	> 15

The reader may note that the red point (^{100}Sn) in Fig. 2.7 corresponds to both the lowest $\log ft$ value, and also a Gamow-Teller transition - a combination one might not usually expect. Generally, the Gamow-Teller strength is fractured across multiple, well-separated 1^+ states in the daughter nucleus (known as the Gamow-Teller giant resonance). Since β decays can only populate states which are energetically allowed, this typically has the effect of dramatically reducing the observed Gamow-Teller strength in β-decay. As a result of the doubly magic nature of ^{100}Sn, a considerably larger β-decay energy window is available - making more states accessible, whilst the majority of Gamow-Teller strength is funnelled through a single,

well-populated state. This has the effect of making a far large proportion of the total Gamow-Teller strength available, resulting in the extremely low log ft value observed [46].

Using the deuteron case as in Section 1.1, it can also be seen from Fig. 2.6 that Fermi β decays are isospin conserving, whereas Gamow-Teller decays are not. This property can be used to investigate isospin mixing, whereby a state of a given J^π is actually a superposition of states of different T [48].

2.2.2.1 β-delayed proton decay

β-delayed particle emission has been observed since the earliest days of nuclear physics, with β-delayed α decay observed by Rutherford and Wood in 1916 [49]. The fact that β decays are able to populate excited states in the daughter nucleus allows for decay processes to occur which might otherwise be energetically forbidden. β-delayed particle emissions become common far from stability, with a combination of high β-decay Q value and low particle separation energy.

β-delayed particle emission is a two step process. As such, one can treat the decay branch by considering the product of a β-decay into a given state, and that state's subsequent particle emission - taking into account competing decay branches, such as γ decats in the proton emitting nucleus. The β decay strength of a given branch can be determined using the description provided previously in this section.

In the case of proton emission, one can use a similar description as that given for α decay in Section 2.2.1, where one considers the probability of a proton tunnelling in order to escape the nucleus. Importantly, one must not only consider the Coulomb barrier, but also the centrifugal barrier arising from the orbital angular momentum of the emitted proton. The β-delayed proton strength is therefore dependent upon the β-decay strength and the barrier penetrability of the particle emitting state. The barrier penetrability is given by

$$P(E_k) = \frac{1}{1 + \exp \frac{E_B - E_k}{\omega_B}}, \tag{2.9}$$

for a parabolic barrier [50], where E_k is the energy of the emitted particle (i.e. S_p), E_B is the barrier height and ω_B is the barrier width.

2.2.3 Gamma decay

Alpha and β decays represent a transition between two nuclei. Gamma decays, on the other hand, are transitions between internal states within the same nucleus. These occur when the nucleus emits a γ ray in order to de-excite from a higher-lying state. Another route

by which a nucleus can de-excite is by the excitation and emission of an atomic electron, known as electron internal conversion. Whilst γ-ray emission is the most common method of transition and dominates in most cases, in certain cases - for example in the extreme case of a transition between a ground state and first-excited state both of $J^\pi = 0^+$ - internal conversion can dominate. For the present work however, internal conversion is not a significant factor and will not be discussed further.

Internal transitions can be described as being either electric or magnetic in nature. Since these two forms have opposite parity, they result in different selection rules,

$$\begin{aligned} \pi(ML) &= (-1)^{L+1}, \\ \pi(EL) &= (-1)^{L}. \end{aligned} \tag{2.10}$$

Angular distributions of electromagnetic radiation are described by Legendre polynomials, which are themselves described on the multipolarity of the transition, thereby providing an observable by which the relative angular momenta of internal states can be determined. In addition, the transition probabilities depend on the electromagnetic nature of the transition, with electric transitions generally being stronger than the magnetic transition of the same multipolarity, whilst the transition with the lowest order multipole will tend to dominate.

Crude estimates, known as Weisskopf estimates (see Tab. 2.2), are used for electromagnetic transitions of a given multipolarity and electromagnetic nature. These estimates are based on a single proton making a transition from one state to another. By comparing the observed transition probabilty to these Weisskopf estimates, one can understand how well-matched the initial and final states of the transition are, as discussed previously with Fermi's Golden Rule. The extraction of the reduced transition matrix element, $B(EL)$, provides information on the nature of the excitations in a nucleus. For example, collective excitations, such as rotations or vibrations, are characterised by particularly large $B(E2)$ reduced transition matrix elements. As a result of these features,γ decays provide a wealth of observables which allow one to understand the nature of excitations in a given nucleus.

TABLE 2.2: Weisskopf estimates for electric and magnetic γ-ray transitions with varying multipolarity [7].

$\lambda(E1)$	$1.0 \times 10^{14} A^{2/3} E^3$
$\lambda(E2)$	$7.3 \times 10^{7} A^{4/3} E^5$
$\lambda(E3)$	$34 A^2 E^7$
$\lambda(E4)$	$1.1 \times 10^{-5} A^{8/3} E^9$
$\lambda(M1)$	$5.6 \times 10^{13} E^3$
$\lambda(M2)$	$3.5 \times 10^{7} A^{2/3} E^5$
$\lambda(M3)$	$16 A^{4/3} E^7$
$\lambda(M4)$	$4.5 \times 10^{-6} A^2 E^9$

2.3 Recoil-decay tagging

Whilst powerful, RDT is not without limitations. In order for correlations between decay and implantation to be clean, there can be no further implantation in the charged-particle detector after an implantation and before its subsequent decay, placing a limit on the implantation rate related to the lifetime of the decay. The rate limit can be tempered with the use of a position-sensitive implantation detector, since both spatial- and temporal-correlation requirements can be used to associate an implantation with the resultant decay. The rate is then limited by the implantation rate for each spatially-resolvable area of the implantation detector.

The characteristic energy of the α-particle emitted in the α decay of a given nucleus makes it ideal for RDT. Additionally, the short range of α particles in matter means that they will typically deposit their energy entirely within the implantation detector, reducing the need for any auxiliary detectors. The first example of RDT, a study of ^{180}Hg performed in 1986 [51], used the characteristic α-decay of ^{180}Hg as a tag and since the introduction of the RDT technique, the use of an α-particle tag has been by far the most common.

An extension to the standard RDT technique is to additionally tag on the decay of the daughter nucleus. In combination, the use of two or more characteristic decays to perform an α-particle tag results in extremely clean spectra, allowing for the observation of γ decays in even lower cross-section reaction channels.

Another form of the RDT technique is recoil-isomer tagging. From the values in Tab. 2.2 it is apparent that the lifetimes of states decaying by γ emission are heavily dependent on the angular momentum transfer, the energy difference between states and the required parity change. In particular, long lived internal states, known as isomers, might occur, for example due to a requirement for large angular momentum transfer (spin isomers) or between states which lie at a very low relative excitation energy (shape isomers).

In the cases where the isomeric lifetime is both sufficiently long for the nucleus to pass through a recoil separator and sufficiently short for a significant proportion of de-excitations to occur in coincidence with the recoil implantation, one can employ the recoil-isomer tagging technique [52]. In recent years this technique has become widely used, particularly in the $100 \lesssim A \lesssim 200$ region, where isomeric states which satisfy the aforementioned conditions are common.

Additionally, in transuranium elements, recoil-fission tagging can be used. A recent example of this was the study of ^{256}Rf, where the characteristically short fission-decay lifetime allowed for the unambiguous selection of the channel of interest [53]. It is therefore apparent that, for $A \gtrsim 100$, RDT represents a powerful technique for the unambiguous identification and selection of weakly populated channels of interest.

2.3.1 The Schmidt lifetime extraction method

Whilst the characteristic energy of a decay is typically sufficient for the unambiguous selection of a nuclide in the RDT technique, a further degree of selectivity can be achieved through the decay lifetime, τ. Since the decay is used to tag on the nuclide, it is straightforward to extract a decay curve from the time difference, Δt, between the implantation and its corresponding decay. From this it is trivial to extract the characteristic lifetime of the decay. This provides a further variable by which the unambiguous tag can be confirmed.

As previously discussed, RDT is a powerful technique because it allows for the extraction of low cross-section reaction channels. It is therefore not uncommon for a tagged decay to contain insufficient statistics for a decay lifetime to be extracted reliably with the standard method of fitting an exponential decay, especially in cases where a long-lived background cannot be eliminated.

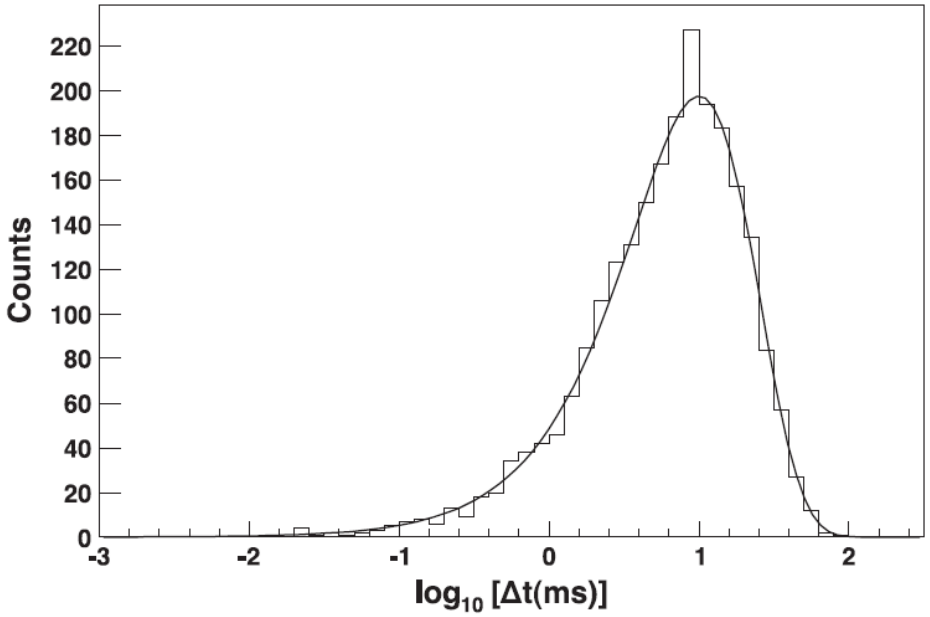

FIGURE 2.8: $\log(\Delta t)$ of ^{256}Rf, taken from [53]. The peak of the distribution corresponds to the lifetime of the nuclide.

An alternative lifetime-extraction method to the typical exponential fit has been developed by K-H. Schmidt *et al.* [54, 55] for cases with poor statistics. Instead of plotting linear Δt, one considers the logarithm, $\log(\Delta t)$. For a radioactive decay, the linear decay time frequency distribution is given by

$$\frac{\mathrm{d}n}{\mathrm{d}t} = -n\lambda e^{-\lambda t}, \tag{2.11}$$

where λ is the decay constant, $1/\tau$. In contrast, for the Schmidt method the logarithmic decay time distribution is used:

$$\frac{\mathrm{d}n}{d(\log t)} = -n\lambda e^{\log t} e^{-\lambda e^{\log t}}. \tag{2.12}$$

Fitting Equation 2.12 to the logarithmic-decay-time distribution results in a curve such as that shown in Fig. 2.8, taken from the work of Greenlees *et al.* [53] in which recoil-fission tagging was used to extract information on the superheavy nuclide, ^{256}Rf. The peak in the distribution corresponds to the lifetime of the nuclide.

TABLE 2.3: Expected properties of radioactive decay, from Ref. [55]

Events, n	Expected standard deviation $\sigma_{\Theta_{\mathrm{exp}}}$	Lower limit of $\sigma_{\Theta_{\mathrm{exp}}}$	Upper limit of $\sigma_{\Theta_{\mathrm{exp}}}$
1	0	-	-
2	0.58	0.04	1.83
3	0.55	0.19	1.91
4	0.50	0.31	1.92
5	0.47	0.41	1.90
6	0.44	0.48	1.89
7	0.42	0.52	1.87
8	0.40	0.58	1.85
9	0.38	0.62	1.84
10	0.37	0.65	1.82
11	0.35	0.67	1.81
12	0.34	0.70	1.79
13	0.33	0.72	1.77
14	0.32	0.73	1.77
15	0.31	0.75	1.76
16	0.30	0.77	1.75
17	0.30	0.78	1.74
18	0.29	0.79	1.73
19	0.28	0.80	1.72

With the standard method of fitting an exponential curve to the linear timing data, it is non-trivial to determine whether the data correspond to the radioactive decay of a single nuclide, or whether there are contributions from multiple nuclides of comparable half-lives. Using the Schmidt method, the standard deviation of the data provides a metric by which this distinction can be made [55]. The lower and upper limits as quoted by Schmidt are given in Tab. 2.3. Should the experimental standard deviation lie below the lower limit, the data can be rejected with an error below 5% to have originated from a radioactive decay and are likely to originate from a random background. On the other hand, should the experimental standard deviation lie above the upper limit, one can reject the data as having an error of below 5% of belonging to the decay of a single nuclide and are likely to originate from some combination of decays from multiple radioactive species.

2.4 Recoil-beta tagging

Given the prevalance of β-emitting nuclei, it is perhaps not surprising that a recoil-beta tagging (RBT) extension to the RDT technique was developed. The technique is not without experimental difficulties which will be laid out in the following section, along with the methods used to overcome them and some discussion of previous experiments carried out using the RBT technique.

2.4.1 Experimental difficulties

The fact that a β particle can be emitted with a range of energies (as discussed previously) makes placing a characteristic tag on a β decay purely on energetic grounds non-trivial. Additionally, where more massive α particles and protons stop relatively quickly in matter, depositing all of their kinetic energy in a small region, β particles scatter readily and have a much longer range. This means that stopping a β particle in the standard charged-particle detectors used for protons and α particles is impractical and that more complete detection methods are required. Their long range does however provide a key method of distinction between β particles and heavier charged particles, as one might expect β particles to penetrate through a thin detector and into another backing it, where heavier particles would be expected to stop in the thin detector.

Finally, one must consider the lifetime of β decays which can be long, even far from stability. When using the RDT technique, short decay-correlation times are advantageous as one is able to maximise the likelihood that a detection is the result of a decay, rather than a false correlation due to a background event. For longer lifetimes, longer correlation times are required to maximise statistics, which results in higher random false-correlation rates.

2.4.2 Proof of principle

The RBT technique was originally demonstrated by Steer *et al.* [1] at JYFL, identifying the nucleus ^{74}Rb. The experimental difficulties outlined previously were overcome through a combination of experimental ingenuity and the physics of the local nuclear landscape.

As discussed in Section 1.1, odd-odd, $N = Z$ nuclei above $A \sim 50$ have $T = 1$, $J^{\pi} = 0^{+}$. As a result, β decays between ground states across the isobaric triplet are Fermi and superallowed in nature. Half-lives of odd-odd, $N = Z$ nuclei in the region are consequently of the order of 100 ms, allowing for relatively short correlation times.

Additionally, as one approaches the proton drip-line, Q_{β^+} increases meaning that the β^+ end-point energy can be as high as 10 MeV. Consequently, while no discrete energy can be used as an unambiguous tag, one may make a characteristic high-energy requirement.

Finally, by using an auxilliary detector as well as the standard implantation detector, it was possible to identify these high-energy β particles. The fact that this auxilliary detector lies behind the implantation detector with respect to the beam direction meant that there could be no false identification of high-energy recoils as β particles.

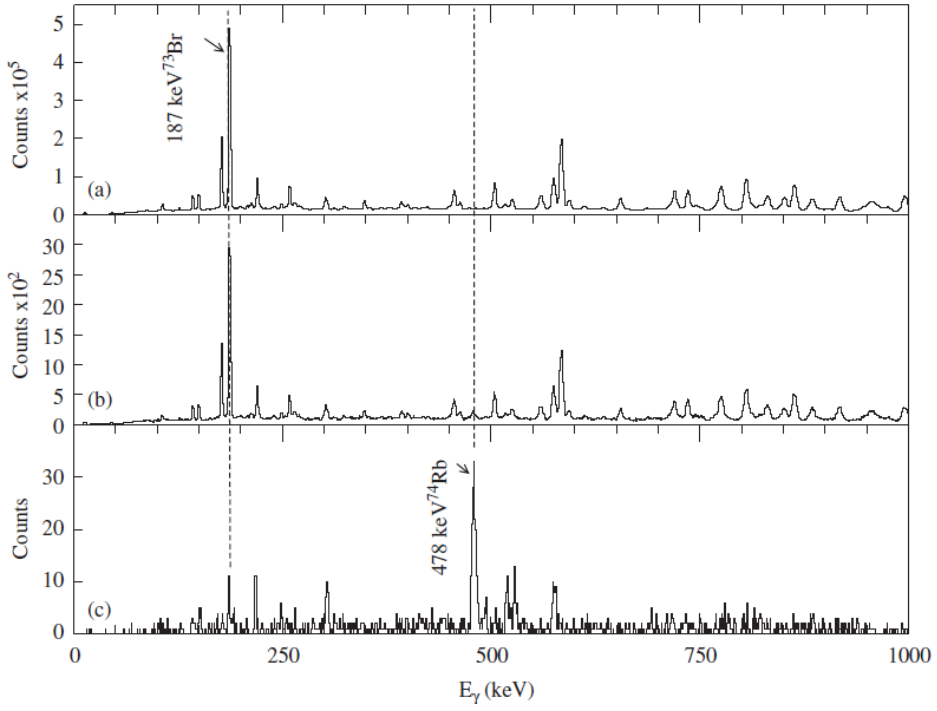

FIGURE 2.9: RBT proof of principle performed at JYFL. In (a), all γ rays in coincidence with a fusion-evaporation recoil are shown with no requirement for a subsequent decay. In (b), a decay-time gate is included, with the channel of interest - ^{40}Ca(^{36}Ar,pn)^{74}Rb - become apparent above background. Finally, in (c), a requirement that the detected β particle is of high energy is included, with the channel of interest now dominating the spectrum.

Steer *et al.* were able to isolate the γ rays associated with the $N = Z$ nuclide, ^{74}Rb, despite a low cross section relative to contaminant reaction channels. The method by which this was achieved is shown in Fig. 2.9. Fig. 2.9 (a) shows a recoil-gated spectrum, the dominant contamination channel corresponds to the evaporation of $3p$ into ^{73}Br. Fig. 2.9 (b) requires a subsequent detection within 100 ms of the recoil implantation, resulting in a peak at the energy corresponding to the decay of the first excited state in ^{74}Rb becoming apparent. Finally, Fig. 2.9 (c) requires a β particle of energy 3-10 MeV being detected within 100 ms of implantation, causing the ^{74}Rb channel of interest to dominate the spectrum.

2.4.3 Further studies

Following the successful demonstration of RBT, the technique has been used on a number of occasions to extract low cross-section channels. These experiments have been performed at two facilities, with the majority taking place at the Univeristy of Jyväskylä (JYFL) and one experiment at Argonne National Laboratory (ANL).

The first experiment following the proof of principle used RBT to make the first observations of excited states in the $N = Z$ nuclide, ^{78}Y [56]. Following that, an in-depth study of excited states in the $N = Z$ nuclide ^{66}As was carried out [57], resulting in the first observations of a number of new states, as well as the reassignment of the $T = 1$, $J^{\pi} = 6^{+}$ state. An experiment utilising a charged-particle evaporation veto (see Chapter 4 for more details) was then performed, resulting in improved sensitivity and allowing for the first observation of the first-excited 4^{+} and 6^{+} states in ^{66}Se [18]. These results were alluded to in Section 1.3. All of the experimental studies mentioned above were carried out at JYFL.

At ANL, an experiment was performed using RBT to identify new excited states in the $N = Z$ nuclide ^{62}Ga [58]. Here, only an implantation detector was used, with the requirement that a β particle was detected within 400 ms of the recoil implantation. The absense of a high-energy requirement on the β particle was made possible by the use of a mass-resolving spectrometer, dramatically reducing the flux from the $3p$ channel, which was the primary source of contamination.

2.5 Alternative techniques

In order to achieve the goals described in Chapter 1 two alternative methods can be used, both of which require the use of a radioactive-ion beam (RIB) facility. The first involves the knockout of nucleons from a more massive RIB whilst the second involves the Coulomb excitation (CoulEx) of the nuclide of interest after it is produced at a RIB facility.

2.5.1 Knockout reactions

In a knockout reaction, as the name suggests, one aims to remove one or more nucleons from a nucleus in order to produce the nuclide of interest. For example, in the case of the nuclide of interest in the present work, one might look to remove two neutrons from the $N = Z$ nucleus, ^{76}Sr. This is typically achieved by impinging a high-energy beam onto a high-density, low-Z target, such as ^{9}Be. A low-Z target is preferred so as to reduce Coulomb contributions to the interaction.

The states populated in knockout reactions depend on the nucleons removed. It is important to remember that, ignoring secondary excitations, no states will be populated beyond those that can be created by replacing particles with holes in the initial nucleus. Knockout reactions have previously been used to populate excited states in $T_z = -1$ nuclides, for example in ^{66}Se [19].

In order to produce a ^{76}Sr secondary beam to knockout nucleons from, one must first fragment a considerably higher mass beam and separate the residues. Generally, in the $A < 70$ region, this primary beam will be ^{78}Kr, however this is unsuitable for the production of Sr isotopes due to the higher Z. As a result, a ^{124}Xe beam would have to be used, significantly reducing the cross section and consequently requiring more beam time. With time at suitable radioactive-beam facilities at a premium, the requirement for large amounts of beam time is prohibitive, making the use of more accesible, stable-beam facilities an attractive alternative, particularly if the aims are equally achievable at such facilities.

2.5.2 Coulomb excitation

In a Coulomb-excitation (CoulEx) reaction a charged projectile interacts with the target nucleus through the exchange of virtual photons resulting in the excitation of the nucleus and the inelastic scattering of the projectile. Due to the long range of the electromagnetic force, this interaction can occur at lower energies than would be required to overcome the Coulomb barrier. Consequently, if one selects a sufficiently low beam energy, one can discount the nuclear force as contributing to the interaction. Multiple virtual photon exchange is also possible, resulting in multi-step excitations to higher lying excited states.

The purely electromagnetic nature of CoulEx reactions performed well below Coulomb barrier energies allow for the extraction of a number of important experimental observables as well as the excitation energy of states. Of particular interest for studies of isospin, the reaction cross-section to a given excited state is closely related to the reduced matrix elements ($B(EL)$) of the transition. This also means that, for a strongly collective excitations with their characteristically large $B(E2)$ values, CoulEx will strongly populate the collective states.

Far from stability, CoulEx measurements are performed in inverse kinematics, whereby the traditional “target” and “projectile” nuclides are exchanged and the nuclide of interest is impinged onto the CoulEx target. In the case of ^{74}Sr, the production of a beam of sufficient intensity ($> 10\ \mathrm{s}^{-1}$) proved complicated, making the use of RBT a more suitable alternative.

Chapter 3

Experimental situation prior to the commencement of this work

> Any sufficiently advanced technology is indistinguishable from magic.
>
> Arthur C. Clarke

The RDT technique as discussed in Sec. 2.3 has three broad experimental requirements:

- Gamma-ray and conversion-electron spectroscopy at the target position
- The separation of fusion products from beam-like products[1]
- The identification of specific decay modes

The technique is widely used at JYFL. In this chapter, the general experimental setup of the laboratory will be discussed along with a brief introduction to relevant detector types. Additionally, the data-acquisition system at JYFL will be described. A discussion of changes made specific to the RBT technique setup will be carried out in subsequent chapters.

3.1 Particle detection methods

3.1.1 Scintillation detectors

Scintillation detectors are named for their scintillating properties, whereby they exhibit luminescence upon interaction with ionising radiation. Solid scintillators come in two forms: organic (plastic) and inorganic[2].

[1] Fission products also need to be separated for $A > 180$

[2] Liquid scintillators are also used - notably for neutron detection - however they are not relevant to the present work.

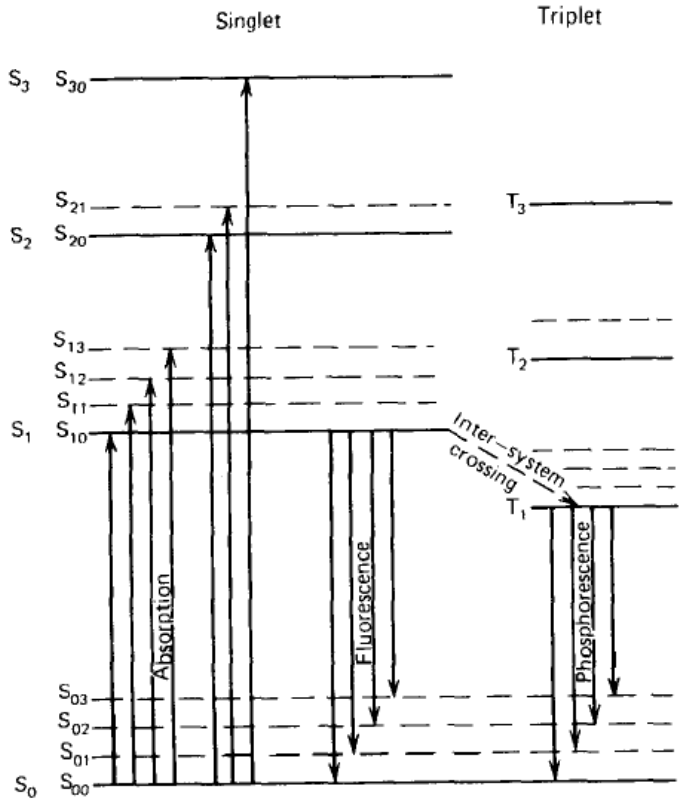

FIGURE 3.1: Singlet (S) and triplet (T) electronic and vibrational states in an organic scintillator. Notation: $S_{\text{electronic, vibrational}}$ [59].

In an organic scintillator, the luminescence arises from transitions within a single molecule. This means that organic scintillators can be used largely independent of the state of the material. Upon interaction, electrons are excited from the lowest lying electron ground state to a higher lying electronic state. This will typically fluoresce promptly back to one of the vibrational electronic ground states as seen in Fig. 3.1. The energy of the fluoresced photon will not equal the energy of the excitation unless the electron returns to the vibrational ground state, which means that organic scintillators are largely transparent to their own luminescence.

In contrast, inorganic scintillation arises from the crystalline lattice structure of the inorganic material. This band structure is shown in Fig. 3.2. In pure crystalline material, electrons can only exist in the valence and conduction bands. The excitation of electrons between these two bands is not particularly problematic in terms of the required energy, however photon de-excitation is slow and of too-high an energy to result in the emission of visible light. With the addition of impurities, states lying between these two bands can be created, known as *activator states*. These states make the de-excitation of electrons more efficient and allow for photon emissions in the energy range of visible light whilst limiting self-absorption.

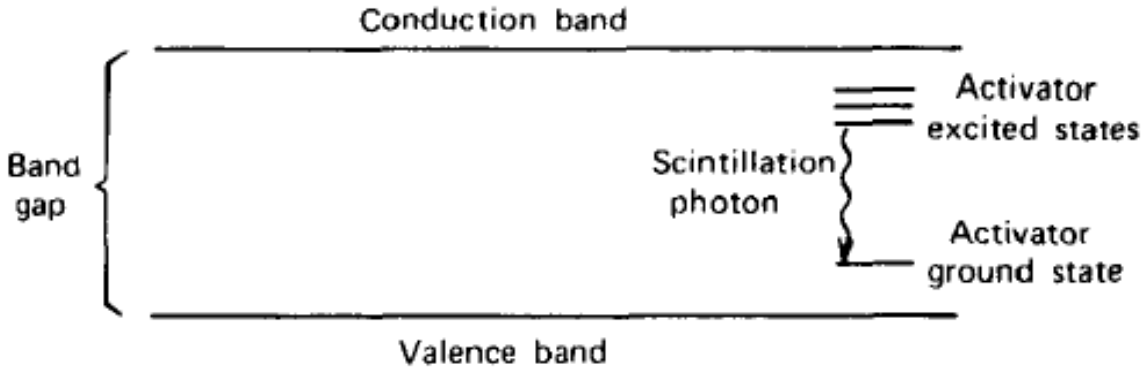

FIGURE 3.2: Inorganic scintillator band structure [60].

An ionising particle interacting with an inorganic scintillator will create numerous electron-hole pairs. The resulting free electrons will be captured by activator sites before de-exciting and emitting a photon of visible wavelength. A further advantage of the inclusion of activator impurities is that they make the scintillator material largely transparent to the luminescence, helping reduce reabsorption.

3.1.2 Semiconductor detectors

One of the intrinsic limitations of scintillation detectors is their typically poor energy resolution[3]. Semiconductor detectors generally have superior resolution due to having a larger number of signal-carriers (electrons and holes) per interaction. A semiconductor is a crystalline material with a small enough band-gap to allow the excitation of electrons from the valence into the conduction band, as shown in Fig. 3.3. This small band gap - typically of the order of an eV - results in large numbers of charge carriers being created when ionising radiation interacts with the lattice.

In order to increase the charged carrier density, semiconductor detectors are normally doped with donor or acceptor impurities, providing additional free electrons and holes, respectively. The charge carriers are caused to drift towards the collection regions by applying a bias across the material. The timing resolution of semiconductor detectors are related to the velocity of this drift, which is in turn related to the intrinsic electron and hole mobilities in the material. The two most common semiconductor detectors used in nuclear physics are Si and Ge, generally for charged-particle and γ-ray spectroscopy, respectively.

3.1.3 Ionisation chambers

The final type of detector relevant to this work is the ionisation chamber; specifically the proportional counter. Whereas scintillation and semiconductor detectors are typically solid,

[3]There are some notable exceptions however, such as LaBr3

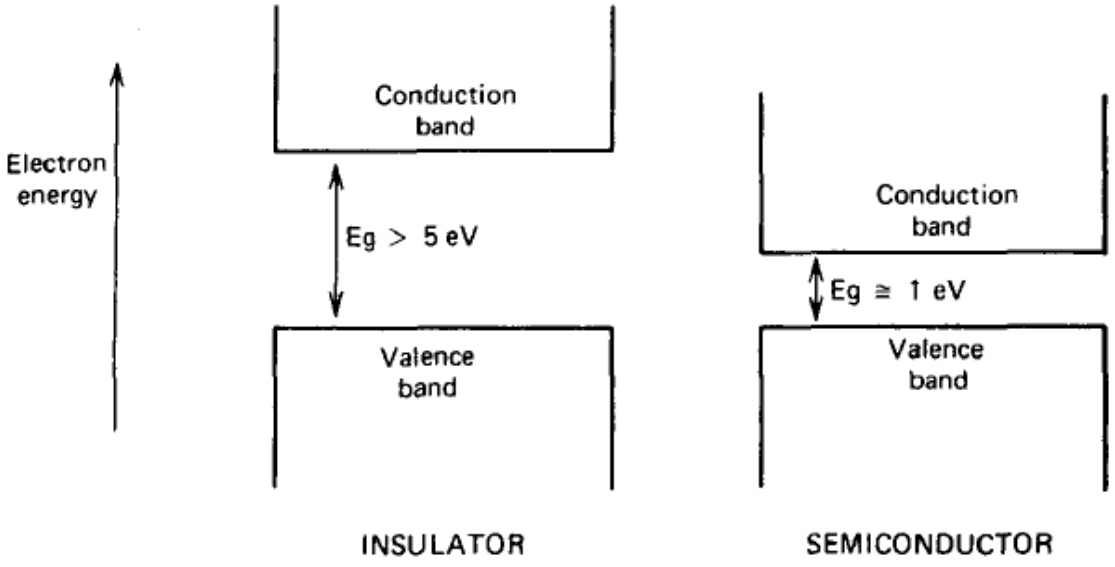

FIGURE 3.3: Semiconductor band gaps [60] compared to those of an insulating material.

an ionisation chamber uses a gas as the interacting medium. As the ionising particle traverses the medium it ionises the gas, creating electron-hole pairs. These are then drawn towards the electrodes, with signals induced from the instant they are created until they are collected.

Signals induced only from the electron-hole pairs created in the ionisation process are typically very small, making their extraction non-trivial. In order to increase the amplitude of the pulse induced upon the electrodes, a voltage can be applied across the detection region. The effect of this voltage on the pulse amplitude is shown in Fig. 3.4. Above the region of ion saturation, where recombination is suppressed, the size of pulse can be seen to be proportional to the energy deposited in the medium. In this region, electrons are imparted sufficient energy from the bias across the detector to ionise secondary electron-hole pairs. This region is known as the proportional region with large signals that can be easily related to the energy deposited in the detector.

The energy resolution from proportional counters is not as good as that can be achieved with a semiconductor detector, however due to the sparse nature of the medium, very good timing resolution can be achieved. In addition, the low density of the medium allows particles to pass completely through a detector whilst only depositing a small fraction of their energy, proportional to - amongst other things - the Z of the incident particle. This makes ionisation chambers ideal for timing measurements and the extraction of ΔE measurements for particle identification.

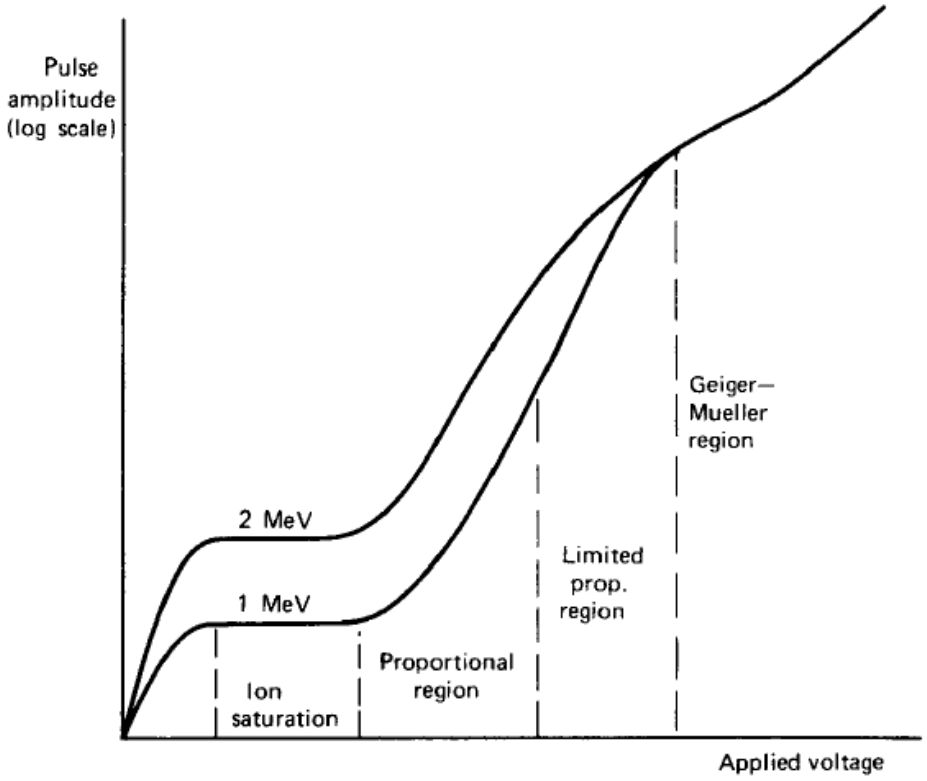

FIGURE 3.4: The dependence of pulse amplitude in an ionisation chamber on the applied voltage, with different operation regions indicated [60]

3.2 Gamma-ray spectroscopy

As described in Sec. 2.2.3, de-excitations between excited states in nuclei typically proceed in one of two fashions, either through the emission of an atomic electron (electron internal-conversion) or the emission of a photon[4]. In the $N = Z$ region, the transitions of interest are dominated by γ-ray emission and so electron internal-conversion spectroscopy will not be discussed.

3.2.1 Gamma-ray spectroscopy

Since γ rays are uncharged, they interact discontinuously with matter. Three main processes exist: photoelectric absorption, Compton scattering and pair production. Fig. 3.5 shows the energy dependence of the three interaction types in NaI.

[4]There are other routes by which the nucleus can de-excite. For example, if the transition energy is greater than 1.022 MeV, it can decay by pair-production.

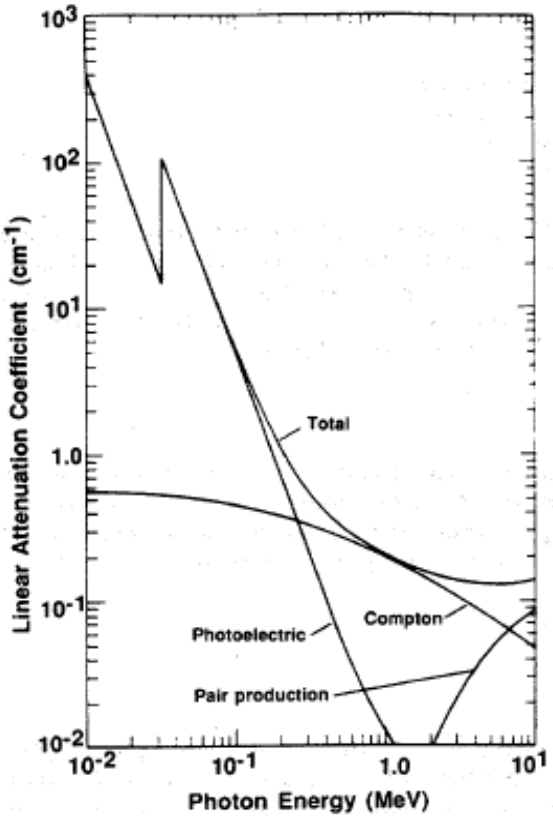

FIGURE 3.5: Linear attentuation coefficient of NaI with individual contributions from photoelectric absorption, Compton scattering and pair production shown [61].

3.2.1.1 Photoelectric absorption

Photoelectric absorption is where the photon completely transfers its energy to an atomic electron (which is known as a photoelectron), causing it to be ejected from the atom. The energy of the photoelectron is dependent on the binding energy of the atomic electron, E_b and the energy, $h\nu$, of the incident γ ray:

$$E_{e^-} = h\nu - E_b \tag{3.1}$$

Since the photoelectric effect requires atomic electrons, it is unsurprisingly dependent on the proton number, Z. It is also strongly energy dependent, with absorption considerably more likely for low energy γ rays. The transition probability, τ, depends on various factors but generally:

$$\tau \propto \frac{Z^n}{E_\gamma^{3.5}}, \tag{3.2}$$

where n varies between four and five depending upon the γ-ray energy. Due to this energy dependence, photoelectric absorption is only significant if $E_\gamma \lesssim 1$ MeV.

3.2.1.2 Compton scattering

In the case of Compton scattering, the incident γ ray scatters off an atomic electron, imparting some of its energy to that electron an ejecting it from the atom. The scattering angle, θ, can take any value, with the remaining γ-ray energy, E'_γ related to θ and the intial γ-ray energy, E_γ, by:

$$E'_\gamma = \frac{E_\gamma}{1 + \frac{E_\gamma}{m_0 c^2}\left(1 - cos(\theta)\right)} \tag{3.3}$$

Compton scattering also depends on the number of atomic electrons and therefore varies linearly with the Z of a material. There is also an energy dependence, with the scattering cross-section reducing slowly with increasing energy.

3.2.1.3 Pair production

At high energies ($E_\gamma > 1.022$ MeV) photons can form an electron-positron pair. This interaction must take place in the vicinity of a Coulomb field in order to conserve momentum. All kinetic energy is then distributed between the electron and positron. The energies at which pair production is particularly relevant are higher than those that will be discussed in this thesis, with photoelectric absorption and Compton scattering the dominant interaction mechanisms.

3.2.2 HPGe arrays

High-purity germanium (HPGe, abbreviated to Ge in this work) arrays are common in modern nuclear facilities, enabling high-resolution γ-ray spectroscopy. Semiconductor detectors are required to be ultrapure to maximise the depth of the depletion region. Techniques to purify Ge to the necessary levels have been developed[5] allowing for relatively high-volume detector crystals to be depleted. The relevant material properties of Ge are listed in Tab. 3.1.

Due to the low band-gap of Ge, detectors are cooled down to liquid-nitrogen temperatures (77 K) to prevent thermal excitations inducing a signal. The low band-gap results in a very good energy resolution for Ge detectors, with full-width half maxima (FWHMs) of less than 2 keV achievable for γ rays with energies of approximately 1 MeV. It is this property which

[5]Similar purities are not yet achievable for Si

TABLE 3.1: Properties of intrinsic Ge, taken from [60]

Atomic number	32
Density (300 K)	5.32 g/cm^2
Atoms	4.41×10^{22} cm^{-3}
Forbidden energy gap (300 K)	0.665 eV
Forbidden energy gap (0 K)	0.746 eV
Electron mobility (77 K)	3.6×10^4 cm^2/V·s
Hole mobility (77 K)	4.2×10^4 cm^2/V·s
Energy per electron-hole pair (77 K)	2.96 eV

makes Ge detector arrays invaluable, as the high resolution allows for γ-ray energy peaks with centroids differing by only a few keV to be distinguished.

3.2.2.1 Compton suppression

The discontinuous nature of γ-ray interactions with matter, specifically via Compton scattering, means that it can often take multiple interactions before all of the γ-ray energy is transferred to the matter. Should one of those interactions occur outside of the detection medium, a false energy reading will be observed, where trivially, $E_{\text{meas}} < E_\gamma$. This results in what is known as a Compton background.

To help eliminate these scattered events, Compton-suppressing vetoes are used. A scintillator with high γ-ray detection efficiency is placed between Ge detector elements, and events in these scintillators are used as a veto for neighbouring Ge events. Bismuth germanate (BGO) detectors are widely used for this purpose due to its high Z and hence, large stopping power. The relevant material properties are shown in Tab. 3.2, with an example of a Compton-suppressed ^{60}Co spectrum shown in Fig. 3.6. Since no spectroscopy information is extracted from the scintillator, the poor energy resolution is not problematic, while the high specific gravity results in a high efficiency which makes the material ideal for use as a γ-ray veto.

TABLE 3.2: Properties of bismuth germanate (BGO) scintillation material, taken from [60]

Specific gravity	7.13
Refractive index	2.15
Decay time	0.30 μs
Abs. Light Yield	8200 photons/MeV
Energy resolution (511 keV)	16 %

In addition to a BGO veto, clover Ge detectors are often used. These consist of a number of Ge detector elements arranged in a close geometry. Multiple detections from different crystals in the same clover can then be reconstructed in order to give the full γ-ray energy. The level of segmentation within a clover can vary signficantly, for example the Segmented Germanium Array (SeGA) has 32-fold segmentation [63]. In recent years, the Advanced Gamma Tracking Array (AGATA) [64] and the Gamma-Ray Energy Tracking In-beam Nuclear Array

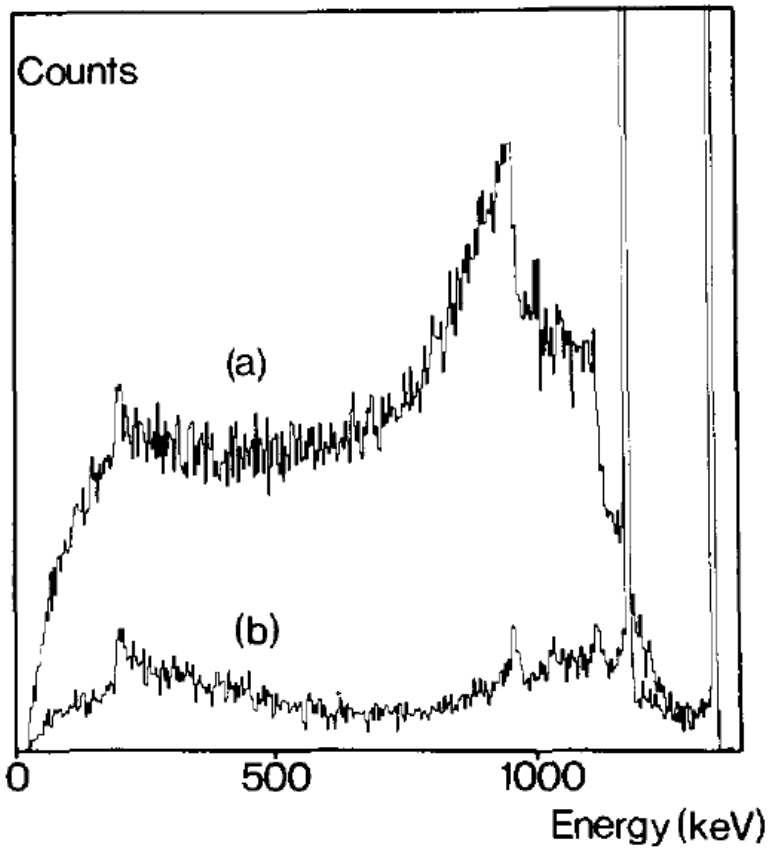

FIGURE 3.6: A ^{60}Co γ-ray spectrum both without (a) and with (b) BGO Compton suppression [62].

(GRETINA) [65] Ge arrays have been developed, providing unprecedented spatial resolution and allowing accurate reconstruction of γ-ray events by tracking them through the detector.

3.2.2.2 JUROGAM II

JUROGAM II and its predecessor JUROGAM have been operating along with the RITU recoil separator at JYFL since 2003. Made up of ex-EUROBALL detectors, JUROGAM consisted of 43 HPGe detectors, with Compton suppression provided using BGO vetoes. The 43 JUROGAM detectors were all of Phase I [66] and GASP [67] type.

JUROGAM was upgraded in 2008 to form JUROGAM II. Twenty-four EUROGAM II composite clover detectors with four-fold segmentation [68] are arranged in two rings of twelve around the target position, straddling 90°, with two rings containing 15 Phase-I [66] and GASP [67] detectors upstream. BGO Compton suppression is again used. Fig. 3.7 shows the original JUROGAM array in position along with RITU and GREAT, which will be described below.

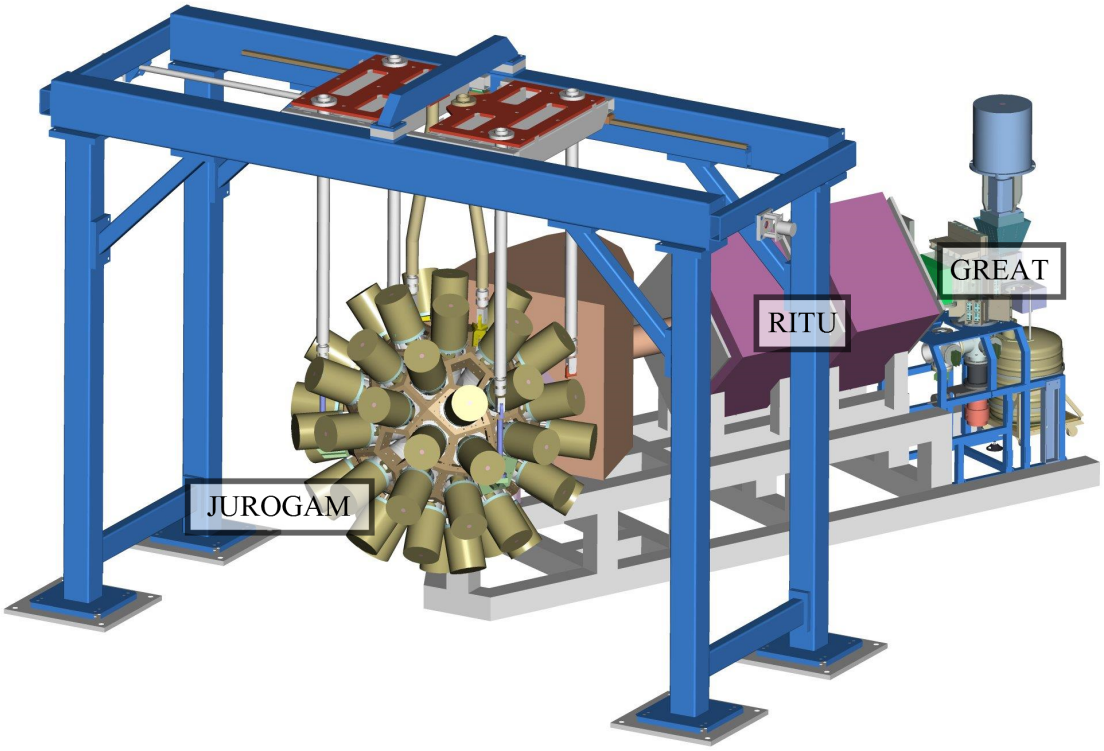

FIGURE 3.7: JUROGAM in position with RITU and GREAT. JUROGAM II now lies in the position of JUROGAM, with its 24 clover detectors straddling 90°.

3.3 Recoil separation

Recoil separators are a widely-used tool in contemporary nuclear physics. Through various combinations of electrostatic and magnetic dipoles, and other elements such as achromatic degraders and Wein filters[6], separators allow for the precise selection of reaction products. Separators such as the FMA [69] at Argonne National Laboratory are in use worldwide, enhancing the selectivity of recoils to allow for in-beam spectroscopic and decay studies.

The principle behind a recoil separator is rather straightforward. The application of a transverse electrostatic or magnetic field to a charged particle in motion will cause it to deviate from its original trajectory by an amount proportional to its mass, charge and velocity, as given by the Lorentz force,

$$\mathbf{F} = q[\mathbf{E} + (\mathbf{v} \times \mathbf{B})]. \tag{3.4}$$

Here $\mathbf{F}$ is the resultant force on the charged particle, q is the charge of the particle, $\mathbf{E}$ is the applied electric-field, $\mathbf{v}$ is the velocity of the charged particle and $\mathbf{B}$ is the magnetic field.

[6]Both achromatic degraders and Wein filters are beyond the scope of this work

Through careful selection of **E** and **B**, one is able to selectively bring a particle onto the focal plane, with position dependence on mass, velocity and charge.

The focal point of a recoil is therefore dependent upon the charge state of that particle. Since for any given interaction, a range of charge states can be produced, this would appear to place a fundamental limit on the transmission efficiency of any recoil separator, as only a few of those charge states can be brought onto the separator focal plane. For particularly high energy beams (∼100 MeV/u), this problem is overcome courtesy of the completely ionised nature of the beam.

3.3.1 The RITU gas-filled separator

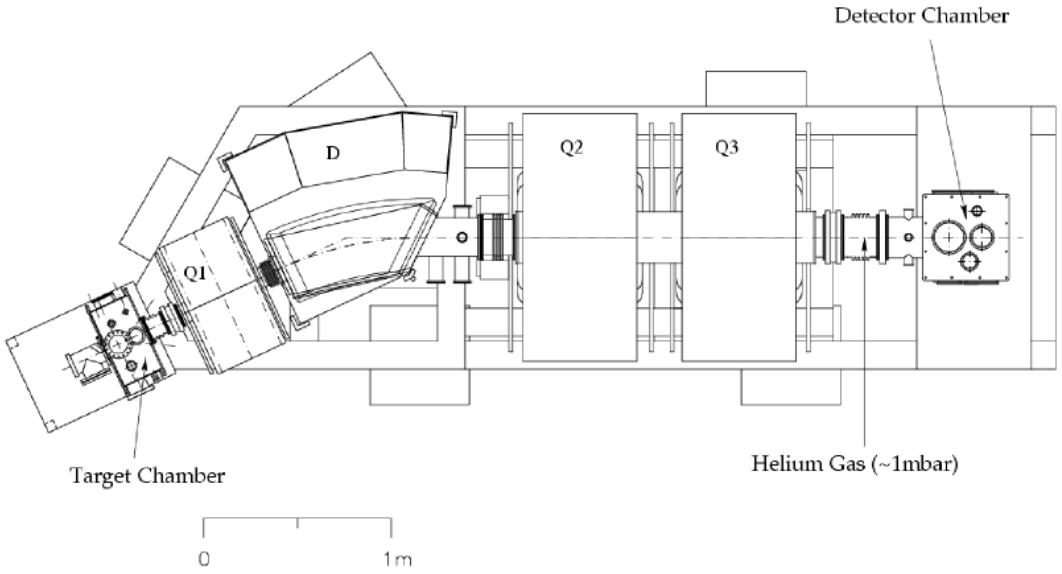

FIGURE 3.8: Schematic of the RITU recoil separator [70]. The dipole and quadrupoles are labelled D and Q, respectively.

Gas-filled separators were developed in order to provide higher transmission by equilibrating the charge states of incoming ions. Through interactions with the gas - 100 to 1000 interactions per metre for a gas pressure of 1 mbar [71] - the ions' charge states equalise. This allows the focusing of multiple incoming charge states onto a common focal point.

The magnetic rigidity of a magnetic field quantifies the effect of a given magnetic field on a charged particle of momentum p and charge q as

$$B\rho = p/q, \tag{3.5}$$

where ρ is the radius of curvature of the particle in the magnetic field B.

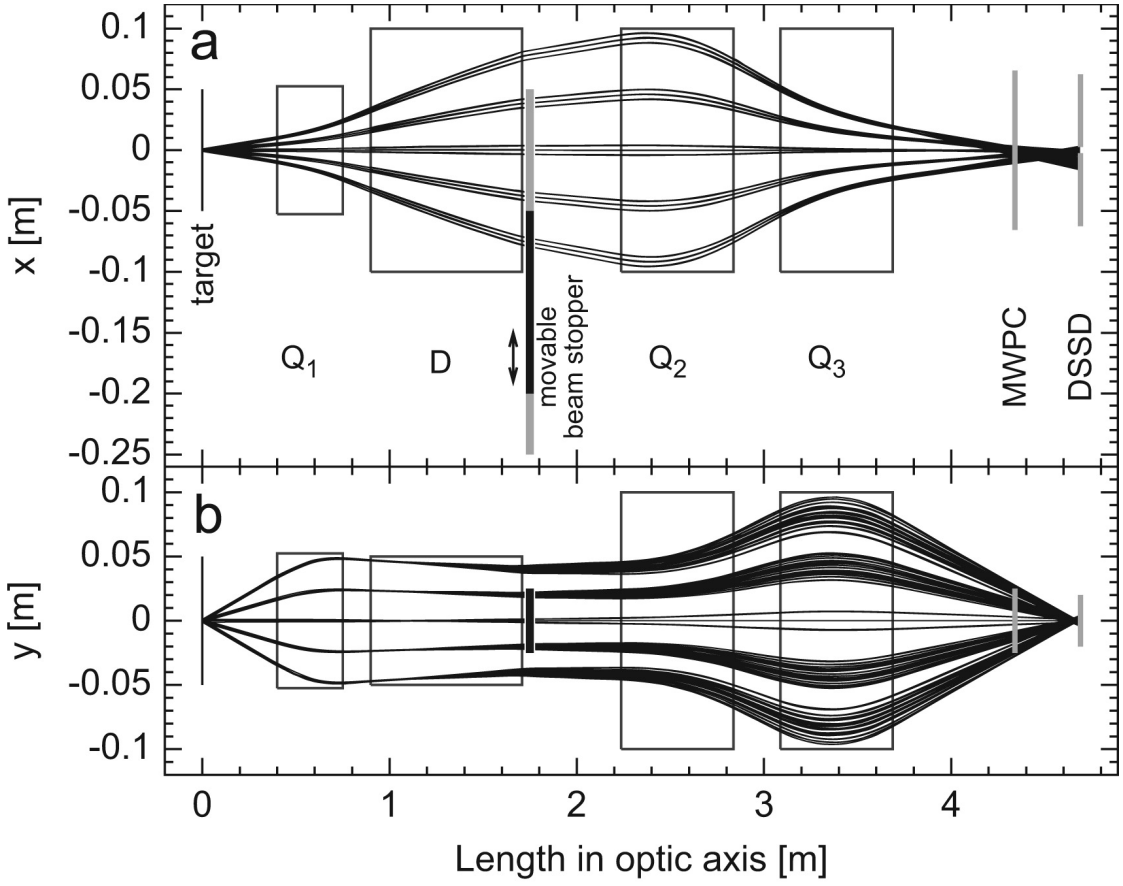

FIGURE 3.9: Ion transmission through the RITU separator [72].

As shown in [71], for an average charge state $\bar{q}$, this can then be written as

$$B\rho = 0.0227A(v/v_0)/\bar{q} \text{ Tm}, \tag{3.6}$$

where A is the mass number of the ion, v is the velocity of the ion and v_0 is the Bohr velocity ($v_0 = 2.19 \times 10^6$ m/s). Using the assumption made by Bohr [73] regarding the scattering of fission products and the Thomas-Fermi atomic model, one can then approximate

$$B\rho = 0.0227A/Z^{1/3} \text{ Tm}, \tag{3.7}$$

where Z is the proton number. This demonstrates that, at least to first order, the magnetic rigidity is independent of the charge state and velocity upon entering the gas. Removing these elements from the assumptions regarding Eq. 3.4, one can conclude that, to first order,

a gas-filled separator separates products only by mass. Only magnetic field elements are used in gas-filled separators, because electrostatic deflectors cannot be safely operated in the gas pressures (∼1 mbar) used.

TABLE 3.3: RITU specifications. Taken from [72].

Max. magnetic rigidity	2.2 Tm
Total mass	17,500 kg
Horizontal/vertical acceptance	±25 / ± 85 mrad
Dispersion	10 mm/(1% in $B\rho$)
Dipole radius of curvature	1850 mm
Dipole maximum field	1.2 T
Dipole deflection angle	25°
Dipole gap	100 mm
Dipole entrance and exit angles	0°, −25°
Q_1 gap diameter	105 mm
Q_1 max. gradient	13.5 T/m
Q_1 optical length	350 mm
$Q_{2,3}$ gap diameter	200 mm
$Q_{2,3}$ max. gradient	6.0 T/m
$Q_{2,3}$ optical length	600 mm
Total optical length	4.8 m

The **R**ecoil **I**on **T**ransport **U**nit (RITU) gas-filled separator [70] was developed at JYFL for the separation of scattered beam from recoiling nuclei in heavy-element studies (see Fig. 3.8). The design was an extension of the more typical DQQ (dipole-quadrupole-quadrupole) configuration at the time of construction, with an additional quadrupole magnet included before the dipole to make for a $Q_1DQ_2Q_3$ configuration. The addition of the quadrupole before the dipole allows for the vertical focussing of the reaction products before they pass through the dipole, effectively increasing the separator's angular acceptance. Ion trajectories in the RITU separator are shown in Fig. 3.9 and some general properties of the seperator are given in Tab. 3.3.

The RITU separator has been shown to be a strong tool for investigations of heavy isotopes [75] in combination with a wide range of spectrometers, to be discussed later in this chapter. Through consideration of Eq. 3.7 one can determine the relative separation achieveable with RITU. If the scattered beam separation is defined as the ratio of the recoil rigidity to the beam rigidity,

$$\text{Scattered beam separation} = \frac{B\rho_{recoil}}{B\rho_{beam}} = \frac{A_{recoil}Z_{beam}^{1/3}}{A_{beam}Z_{recoil}^{1/3}}, \tag{3.8}$$

one can quantify the separation for different beam and recoil combinations.

For the high-mass regions that RITU was designed for, such as ^{256}Rf [53], ^{208}Pb targets are used in combination with relatively light beams, such as ^{50}Ti in the ^{256}Rf example. For such a

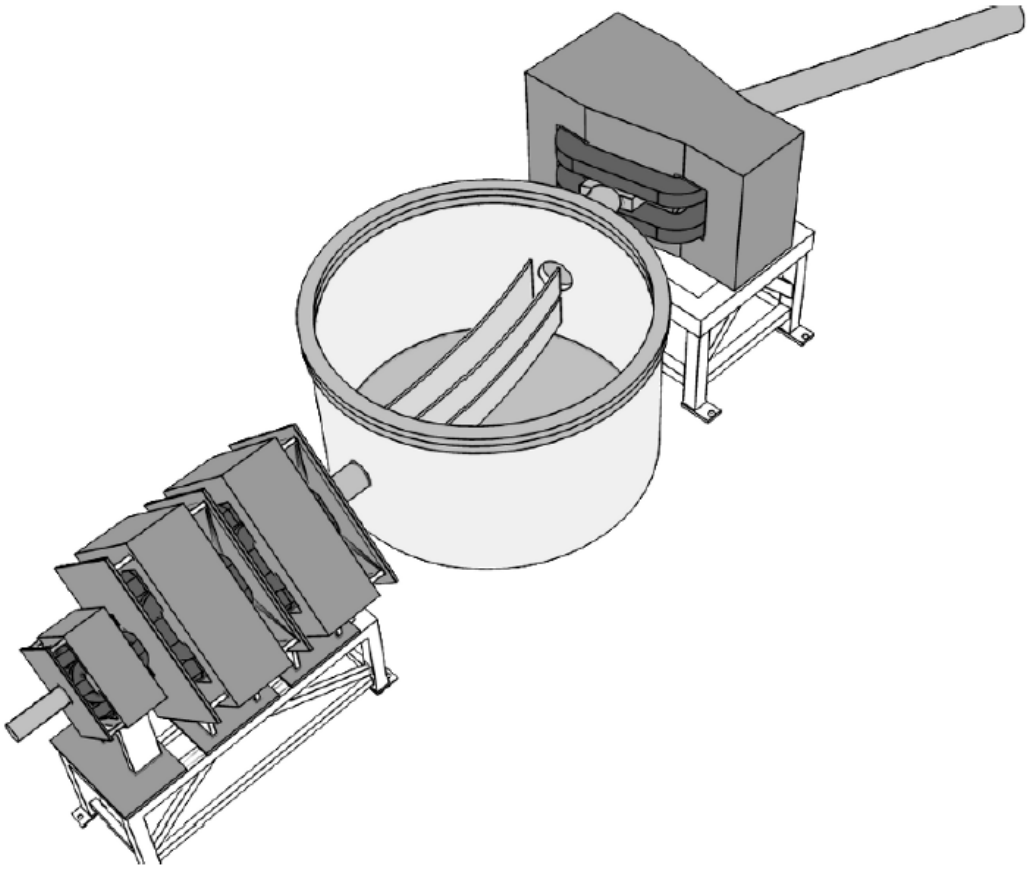

FIGURE 3.10: Artist's impression of the MARA seperator [74]

beam and recoil combination, the scattered beam separation would be approximately 3.1. By comparison, recoil-beta tagging studies are at relatively low mass ($A < 100$), with typically ^{40}Ca targets and, as a proportion of the recoil mass, higher mass beams. For example, in studies of ^{66}As, a ^{28}Si beam might be impinged on a ^{40}Ca target [57]. This beam and recoil combination would result in a scattered beam separation of 1.8.

3.3.2 The MARA vacuum-mode separator

Whereas gas-filled separators are prevented from incorporating electrostatic deflectors due to their instability in a gaseous environment, vacuum separators have no such limitation. As such, electromagnetic vacuum-mode seperators can be constructed using a combination of electric- and magnetic-dipoles to seperate reaction products. Where the rigidity of a magnetic dipole is as shown in Eq. 3.5, the rigidity of an electric dipole is given by

$$E\rho = pv/q, \tag{3.9}$$

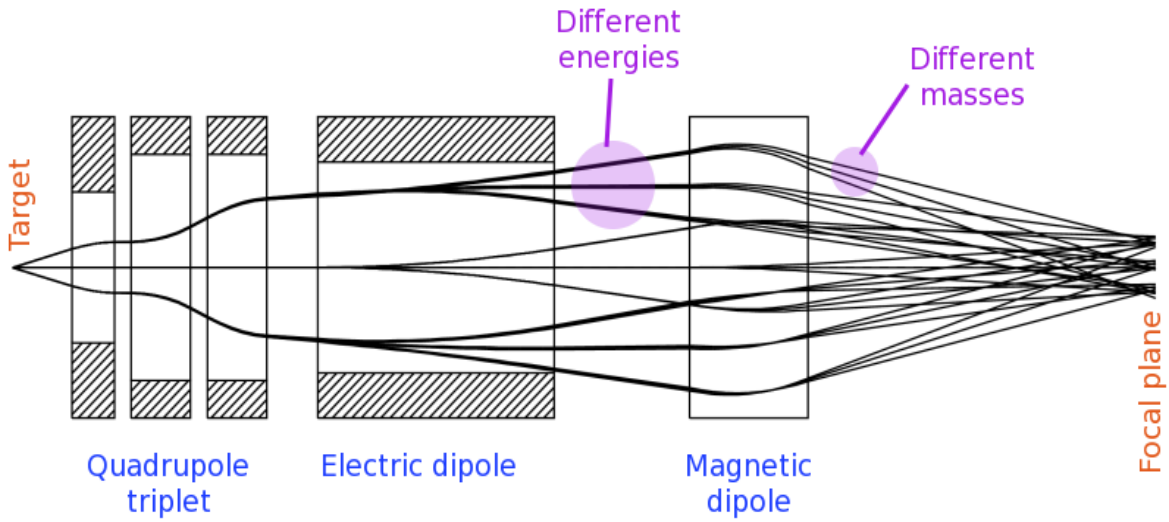

FIGURE 3.11: MARA transmission

where E is the electric field, p is the momentum and ρ, v and q are again the radius of curvature, the ion velocity and the charge state respectively. Where the velocities are non-relativistic, classical assumptions can be made and Eq. 3.9 can be expressed in terms of the ion's kinetic energy, E_k:

$$E\rho = E_k/q. \tag{3.10}$$

By making the same non-relativistic assumption for Eq. 3.5, one can also obtain the magnetic rigidity in terms of E_k:

$$B\rho = \sqrt{2E_k m}/q. \tag{3.11}$$

An artist's impression of the **M**ass **A**nalysing **R**ecoil **A**pparatus [76] under construction at JYFL is shown in Fig. 3.10. The seperator has a $\mathrm{QQQD}_E\mathrm{D}_M$ configuration, combining electrostatic and magnetic dipoles. By careful selection of distances between the electrostatic deflector and the magnetic dipole, and the magnetic dipole and the focal plane, the kinetic energy dependence in Eq. 3.10 and 3.11 can be cancelled, leaving only a mass dependence on

the focal plane position. The energy dispersion from the electrostatic dipole and the mass dispersion from the magnetic dipole is shown in Fig. 3.11.

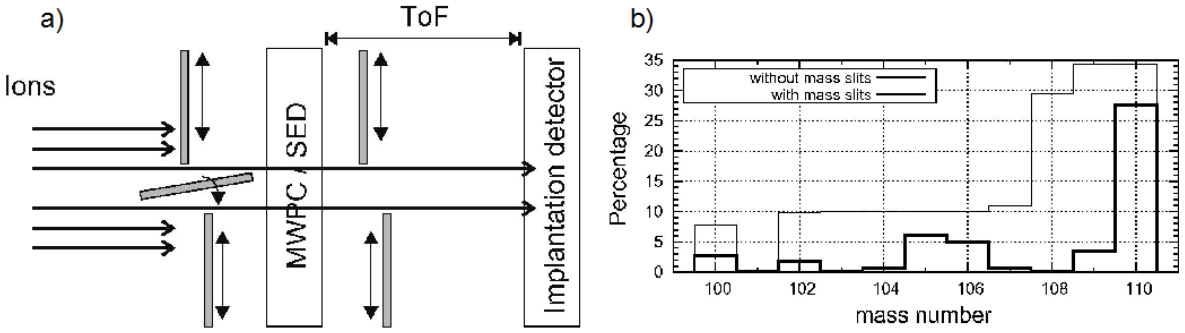

FIGURE 3.12: a) A schematic showing the MARA slits, b) A simulation showing the reduction in background isobars from the inclusion of the MARA slits [76].

Slits will be placed on the approaches of the focal plane to further improve mass selection (see Fig. 3.12 (a)). These slits will be used to select certain charge states of the target isobar by their impinged position on the focal plane. As can be seen in Fig. 3.12 (b) this can dramatically reduce the transmission of neighbouring isobars for only a slight reduction in the transmission of the target isobar.

3.4 Charged-particle spectroscopy

3.4.1 Recoil selection

While a large proportion of recoil selection is performed by the electromagnetic dipoles of a recoil separator, further refinement can be achieved using charged-particle detectors. When traversing a medium, a heavy charged particle[7] loses energy through inelastic collisions with atomic electrons. Since heavy charged particles are considerably more massive than electrons, significant deviations in the trajectory through the medium do not typically result from these collisions.

The Bethe-Bloch formula describes the energy loss of charged particles in a medium and gives the following proportionality:

$$-\frac{dE}{dx} \propto z^2, \tag{3.12}$$

where z is the charge state of the incident particle. As long as the energy dissipated in the detection medium is low enough that velocity changes are not significant, one can differentiate between ions of different charge.

[7] A heavy charged particle being anything of proton mass or higher

Additionally there is a trivial dependence on the time-of-flight (ToF) of an ion and its mass for a given energy. By combining ΔE and ToF measurements, the selection of recoils of interest can be improved. As discussed previously, ionisation chambers are particularly good at performing both measurements due to rapid signal collection and the low density of the medium and for this reason they are widely used for recoil identification.

3.4.2 Decay spectroscopy

Performing charged-particle spectroscopy with the intention of extracting decay information, there are generally three important observables: the identification of the emitted particle, the energy of the emitted particle and the lifetime of the decay. In the case of recoil-decay tagging, the recoil of interest is generally sufficiently long-lived that timing resolutions are not a primary concern[8].

Particle identification can be achieved using ΔE measurements in concert with the measurement of the total energy to provide sufficient information to differentiate between, for example, protons and α particles. With recoil-α and proton tagging however, particle identification is not typically required, as these decays emit particles with a characteristic energy, allowing for the differentiation between competing channels purely on the basis of the detected energy.

Due to the lower mass of β particles, their trajectory through a medium is altered significantly by each collision (whereas protons and α particles maintain largely the same trajectory even as they interact). Combined with the continuum of energies that β particles take after a decay, particle identification using ΔE measurements is no longer particularly sensitive. The large range of β particles in a medium when compared to protons and α particles of the same energy allows some differentiation however. Whilst a proton or α particle might be fully stopped in a detector, a β particle is liable to deposit some energy but will still punch through. By combining a reasonably thick (500 μm) detector with a thicker detector behind it and requiring coincident events between both detectors, one can actively select β particles.

The workhorse of decay spectroscopy in contemporary nuclear physics is the silicon strip detector (SSD). The arrangement of a series of strips on a doped, depleted silicon wafer allows for one-dimensional position sensitivity along with the excellent energy resolution of silicon semiconductor detectors. The width of these strips is referred to as the *strip pitch*. By applying a similar strip structure on the reverse side of the wafer one can achieve two-dimensional position sensitivity, known as a double-sided silicon strip detector (DSSD[9]).

[8] There are exceptions. For example, in certain α-tagging cases the daughter nucleus is very short lived, making timing resolutions more important.

[9] The initialisation DSSSD is also used.

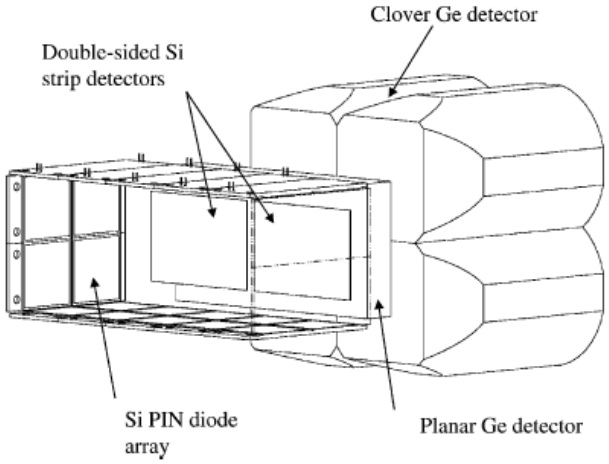

FIGURE 3.13: The GREAT spectrometer

3.4.3 The GREAT spectrometer

The gamma recoil electron alpha tagging (GREAT) spectrometer [77] was designed to fulfill all of the requirements of decay spectroscopy for RDT and has been used with great success for such studies since its installation. It consists of a multiwire proportional counter (MWPC), a pair of DSSDs, a planar Ge detector, a Si PIN diode array and a clover Ge detector, the arrangement for which is shown in Fig. 3.13. The MWPC is not shown but lies in front of the PIN diode array and DSSDs. The PIN diodes are used for low-energy electron studies and are not relevant for the present work and will not be discussed. The clover Ge detector works under the same principles as those included in the JUROGAM II array and will also not be discussed.

3.4.3.1 GREAT MWPC

A multiwire proportional counter is identical to a proportional counter except that grids of electrodes are suspended in the gas. This makes the detector position sensitive and also speeds up charge collection. As discussed previously, ionisation chambers are ideal for recoil identification and it is for this purpose that the GREAT MWPC is used. Isobutane is separated by Mylar foils from the helium in RITU and the vacuum in which the rest of the GREAT detectors operate. By combining the ΔE and ToF measurements, recoil identification is improved. ToF measurements are made using a time to amplitude converter (TAC) between the MWPC and DSSDs, because of the short flight-distance between the detectors.

3.4.3.2 GREAT DSSDs

As can be seen in Fig. 3.13, the two GREAT DSSDs are mounted side-by-side to provide the maximum focal plane coverage. These DSSDs serve dual purposes. Recoils transmitted

through RITU and MWPC are implanted into the DSSDs. As already mentioned the Si-MWPC TAC provides ToF information, whilst the DSSD provides an implantation pixel which allows for later correlations between decays. The second purpose is for the detection of the decays themselves. Upon decaying, energy will be deposited into a pixel of the DSSD which can then be reverse-correlated to identify recoils. For recoil-α and proton tagging, the DSSD also provides the characteristic decay energy information which allows the highly-selective tag to be made.

3.4.3.3 GREAT planar Ge detector

The GREAT planar Ge detector abutts the pair of DSSDs with a separation of 10 mm. It is double sided in the same manner as a DSSD with an active area of 120 mm x 60 mm, a thickness of 15 mm and a strip pitch of 5 mm. It was originally designed for the spectroscopy of X rays and low-energy γ rays. With the RBT tagging technique however it was used for the detection of high energy β-particles, effectively forming a ΔE-E telescope, as discussed in Section 2.4.2.

3.5 The total data readout system

The final aspect of the experimental setup is the data-acquisition system, commonly known as a DAQ. For the simplest example of a single-channel system, the DAQ is responsible for extracting the observables, generally the signal intensity - corresponding to the energy - and the time of the interaction. In more complicated, multi-channel DAQs, the DAQ is responsible for collating the data in such a way that coincident events can be identified.

Traditionally, DAQs relied on triggering which would determine whether an event should be acquired by the DAQ. For example, an experiment might be intended to measure particle-γ ray coincident events, with a Si detector for particle detection combined with a Ge array for γ ray detection. Here, one might decide to set a particle-γ trigger, with a requirement for both detections in the Si and the Ge within a certain time window before triggering.

Upon triggering, the DAQ will accept all events within a the time window, including events which precede the trigger. At this point, the DAQ is effectively non-responsive, introducing a system wide dead-time before a further event can trigger the detectors. Due to this, triggers are typically set to be particularly selective in order to maximise selectivity. For example, the high-efficiency Ge array, Gammasphere, operates at peak efficiency when a four-fold trigger is used (that is, when four Ge events are required in order to activate the trigger).

The fact that the RDT method requires a delayed coincidence method results in dead-time limitations. In order to reduce these limitations, a novel triggerless total data readout system

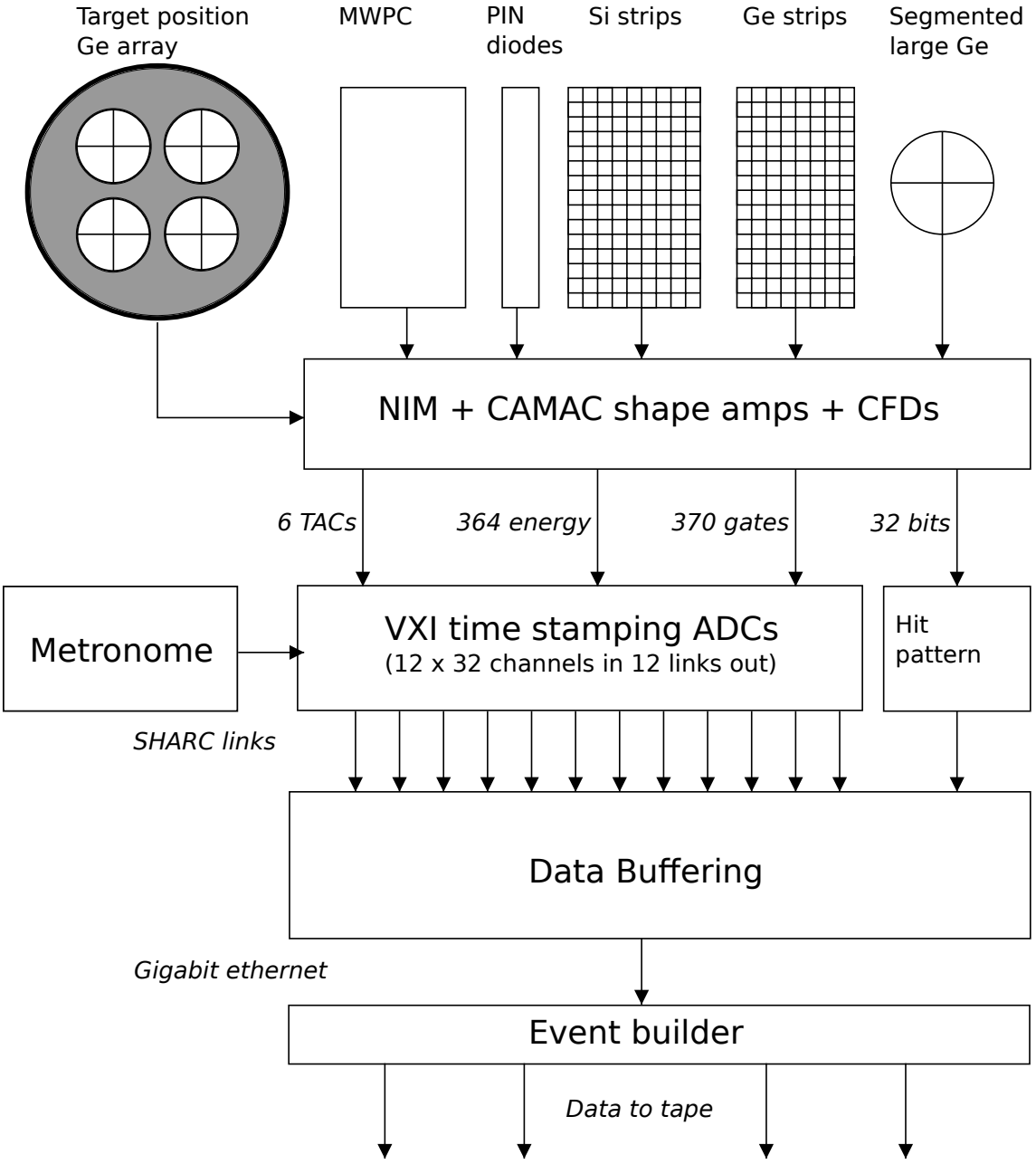

FIGURE 3.14: A schematic of the TDR system, adapted from Ref. [78]

(TDR) was developed [78], the schematics of which are shown in Fig. 3.14. Every event is stamped and then collected together in software with spatial and temporal correlations used to eliminate false events.

Compared to this, running a RDT experiment with a conventional DAQ a trigger width of 5 μs might be used, with a delayed-coincidence requirement at the focal plane in order to account for the time of flight through RITU. For rate of 5 kHz in the DSSD and a 35 μs gate, a dead-time of 18% was calculated by Lazarus *et al.* [78], rising to 35% for a DSSD rate of 10 kHz with longer gates resulting in more dead time. By comparison, due to the processing power now available the TDR acquisition system can deal with DSSD rates of 10 kHz without

dead time becoming a significant problem, since each channel is read out independently, with the limitation on rates resulting mainly from the processing power at the system's disposal.

Chapter 4

Detector development - UoYtube, phoswich and new DSSD

> Never promise more than you can perform.
>
> Publilius Syrus

Note: The contents of this chapter, up to and including Section 4.2.3 were performed in collaboration of P. Ruotsalainen of JYFL. The work was published by the author in Ref. [79] and discussed in P. Ruotsalainen's thesis [80].

The RBT studies of ^{74}Rb [1], ^{78}Y [56] and ^{66}As [57] at JYFL, whilst fruitful, also served to highlight the need for increased sensitivity of the RBT method. Subsequent attempts to utilise the technique with particularly weak channels (specifically $2n$) further demonstrated this, with β selectivity not strong enough to suppress strong backgrounds and with low cross-sections and detector efficiencies conspiring to hinder the double-RBT technique (similar to the double-α tagging technique mentioned in Section. 2.3). In order to improve channel selectivity, one has four effective options:

- Improve pixellation of DSSD to reduce the rate of random correlations
- Detect evaporated charged particles to allow unwanted multi-charged particle channels to be vetoed from the correlation analysis
- Improve identification and discrimination of high-energy β particles relative to low-energy β particles and background γ rays
- Implement mass selection of recoils

All of these improvements were made during the course of the present work, with the exception of mass-selection of recoils which requires an entirely new recoil separator. The MARA vacuum-mode recoil separator (see Sec. 3.3.2 and Ref. [76]) is presently under construction

at JYFL, and when it becomes available it will be interesting to see how it would allow the RBT methodology to be further developed.

4.1 New detector elements

4.1.1 Phoswich detector for high-energy β-particle selection

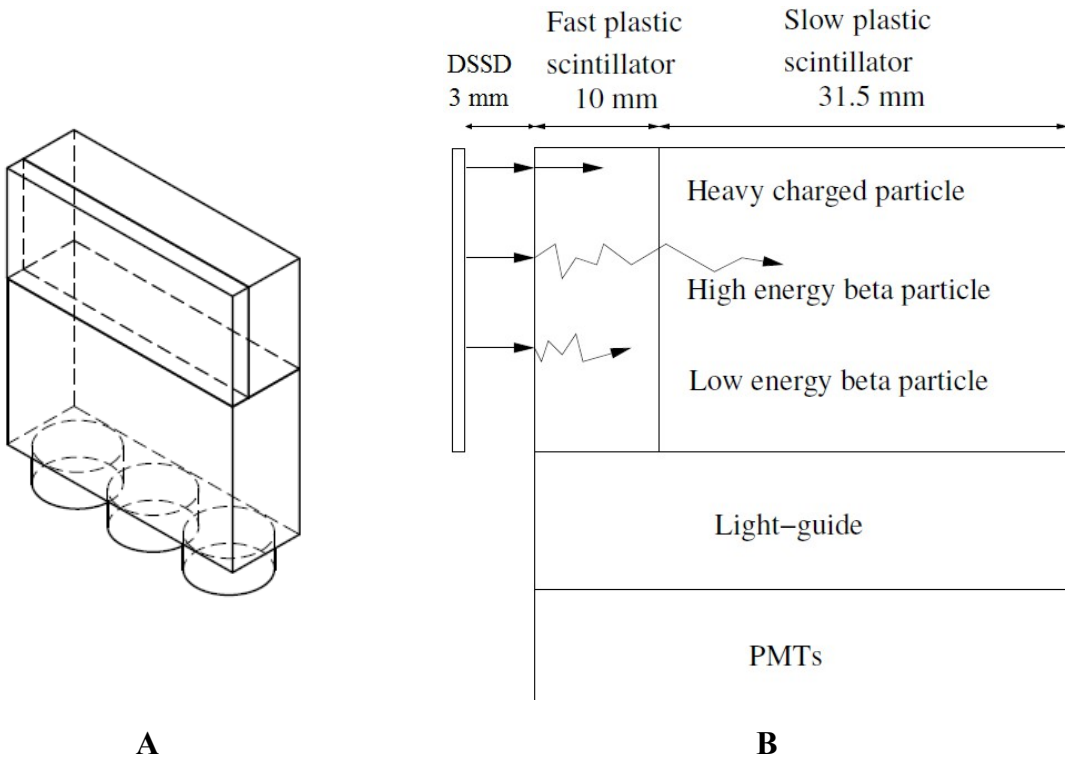

FIGURE 4.1: The phoswich detector setup. A) A schematic of the phoswich. B) The phoswich detector method. A 10 mm fast-response plastic scintillator (BC-404) is coupled with a 31.5 mm slow-response plastic scintillator (BC-444). A light guide directs the outputs from the two scintillator materials into three photomultipliers. As shown in B), heavy charged particles and low-energy β particles are stopped within the fast plastic scintillator, whilst high-energy β particles penetrate through the fast plastic scintillator and also deposit energy in the slow plastic scintillator. Gamma rays will typically only interact in one of the elements.

In developing the RBT methodology from the initial demonstration, the planar-Ge detector was replaced with a plastic scintillator detector. The plastic scintillator was fast and a good signal could be obtained for high-energy β particles. A phosphor-sandwich (phoswich) detector is an attractive replacement for this simple detector as a better means of discriminating different types of ionising radiation. Such detectors are widely used for particle identification [81, 82]. They are typically made up of two or more blocks of scintillator material with

different timing properties. Through the analysis of pulse shapes, one can identify where the interaction occurred within the detector, allowing for their use as ΔE-E devices.

In order to better characterise high-energy β particles for the RBT application, the simple plastic scintillator was replaced with a phoswich detector (see Fig. 4.1) comprising a 10-mm thick fast-response plastic scintillator (BC-404) optically coupled to a 31.5-mm thick slow-response plastic scintillator (BC-444)[1]. The respective time constants of the two plastic scintillators are 1.8 ns and 285 ns [83], with tests of the phoswich showing a total pulse length of ∼80 ns and ∼700 ns, respectively. These are then attached to a light guide below the scintillators which couples to three 10-stage Hamamatsu photomultiplier tubes. The phoswich is placed into the original position of the planar-Ge detector, with the fast plastic abutting the DSSD. High-energy β particles will deposit energy continuously along their track, penetrating to the slow-plastic scintillator at the rear. In contrast, β particles with energies lower than 2-3 MeV will only deposit energy in the front fast plastic. The variation in the 2-3 MeV threshold depends on the incident angle of the β particle. Gamma rays interact discontinuously and would typically register only in one of the two sections, generally in the slow element due to the larger size.

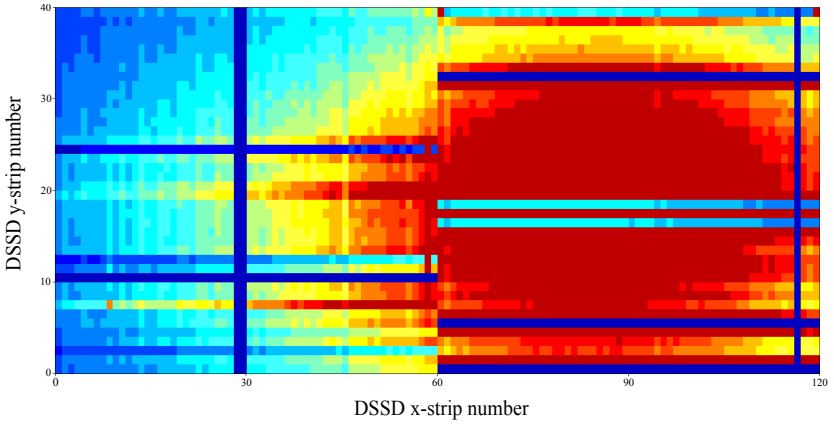

FIGURE 4.2: Typical pixel map for the original GREAT configuration of two DSSDs when studying the ^{40}Ca(^{28}Si,pn)^{66}As reaction with low rates in blue and higher rates in yellow→red. The left hand DSSD can be seen to be effectively redundant with the majority of recoils being incident on the right-hand DSSD.

4.1.2 Higher-pixellated DSSD

In the original RBT work, the two side-by-side 700-μm thick GREAT DSSDs (Sec. 3.4.3.2) were used for implantation and decay measurements at the focal plane of the RITU separator. As mentioned in Section 3.3.1, RITU performance is not optimised for studies at and below the $A = 100$ mass region and it was difficult to separate the fusion-evaporation residues from scattered beam. The consequence of this was that the residues could only effectively be implanted into one of the two DSSDs and the second DSSD was essentially redundant,

[1]These shall henceforth be refered to as fast and slow plastic, respectively

as illustrated in Fig. 4.2. These original DSSDs each had dimensions of 60 x 40 mm^2, with a strip pitch of 1 mm. The board on which the DSSDs were mounted has been replaced with a new board containing a single 500 μm-thick DSSD, of type BB13, designed by Micron Semiconductor Ltd [84]. This new DSSD has dimensions of 60 x 60 mm^2 and a strip pitch of 0.48 mm in both the x and y directions. The new DSSD therefore represents a reduction of pixel area by a factor of four compared to the previous device. The DSSD is positioned so as to be centered on the region of high intensity on the old DSSD, as shown by the intense region in Fig. 4.2.

4.1.3 Charged particle veto box - UoYtube

The chief contamination in RBT studies in the proton rich $A \sim 70$ region arises from multiple charged-particle evaporation channels, while the channel leading to the odd-odd $N = Z$ nucleus is typically pn evaporation, or $2n$ evaporation for production of $N = Z - 2$ nuclei. Detecting evaporated charged particles with high efficiency can be used to reduce contamination for both the pn and $2n$ fusion evaporation channels. A veto barrel detector called UoYtube (the **U**niversity **o**f **Y**ork **tube**) was constructed, comprising 96 CsI(Tl) detectors arranged on six faces of a hexagonal barrel (see Fig. 4.3). Each CsI(Tl) crystal had an area of 20 x 20 mm^2 and was 2-mm thick. The scintillation light was collected with S3590-08 PIN diodes from Hamamatsu with the photodiode output coupled to Mesytec preamplifiers. The preamplifier signal goes through a gain and offset box to ensure the signal is within range for the data-acquisition system. Signals are then interpreted with a moving-window deconvolution algorithm [85] in Lyrtech ADCs.

4.2 In-beam tests

Two in-beam tests were conducted: the first to evaluate the performance of UoYtube and the second to study the new DSSD and phoswich detector. For both tests, recoils were identified using RITU coupled to the GREAT focal-plane spectrometer. Gamma rays emitted at the target position were detected by the JUROGAM II array. For both tests described below, the 5 upstream Phase-I type detectors were not mounted.

A ^{28}Si beam provided by the University of Jyväskylä K130 cyclotron at an energy of 75 MeV was impinged upon a ^{nat}Ca target of thickness 0.65 mg/cm^2. A ^{nat}C charge reset foil of thickness 0.03 mg/cm^2 was directly behind the target. The channel of interest for the following tests was ^{40}Ca(^{28}Si,pn)^{66}As as it had been successfully used with the RBT technique and the cross sections were known to be high enough for tests to be completed with short run times. Beam intensities were maintained at between 2-7 pnA. These intensities corresponded to

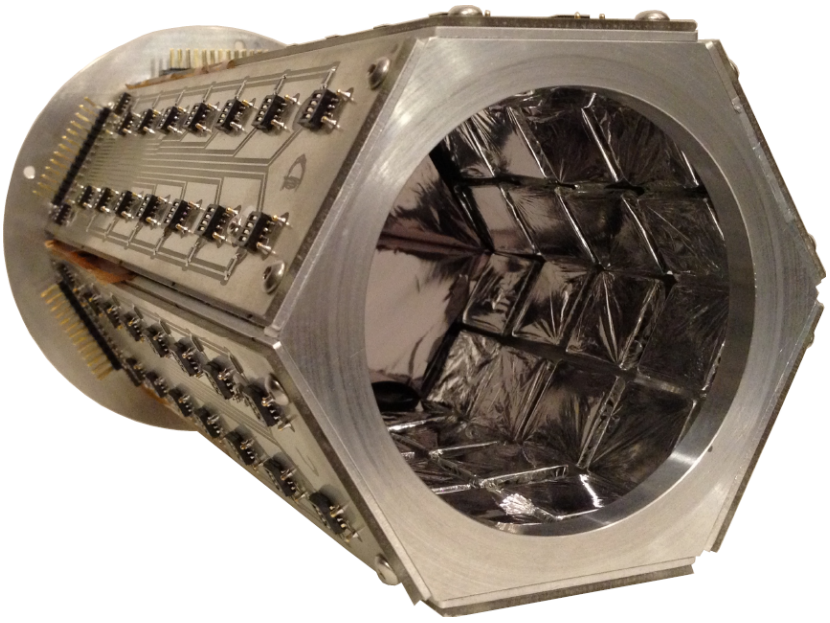

FIGURE 4.3: Photograph of the original UoYtube charged particle veto box. 96 CsI(Tl) crystals are arranged around the 6 sides of the box which has a hexagonal cross-section. 2.5-μm thick Ni foils were applied to all surfaces, with 9-μm thick Ta foils at forward angles to stop scattered beam.

DSSD rates of between 3-10 kHz. Good separation of beam and recoils was found for a RITU gas pressure of 1.2 mbar.

The remainder of the setup was made up of the GREAT MWPC and, for the UoYtube test, the GREAT DSSD and segmented planar Ge detector. Recoils were selected using ΔE-ToF and E-ToF, extracted from the GREAT spectrometer as described in Section 3.4.3. The UoYtube test had a duration of 2 days, the phoswich/DSSD test duration was also 2 days with an additional 1.8 days running with the new DSSD in combination with the planar-Ge detector. Data acquistion was handled by the JYFL total data readout system (TDR) (Sec. 3.5 and Ref. [78]).

4.2.1 Test of the UoYtube

The UoYtube veto-box was mounted at the target position in the Light Ion Spectrometer Array (LISA) target chamber [87]. This chamber was designed for the mounting of Si detectors for fast proton- and α-decay studies, and was used because it was large enough to accommodate the UoYtube. The use of the LISA chamber came at the expense of the first JUROGAM II ring - housing 5 Phase-I type detectors - due to the size of the chamber.

Analysis of the UoYtube data was carried out using the Java-based analyser Grain [88], developed at JYFL. Events were passed through ΔE-ToF and E-ToF recoil gates to assess their validity and to eliminate scattered beam implantations. The UoYtube data were also considered, with the requirement that ≤ 1 charged-particle events were seen for the identification of

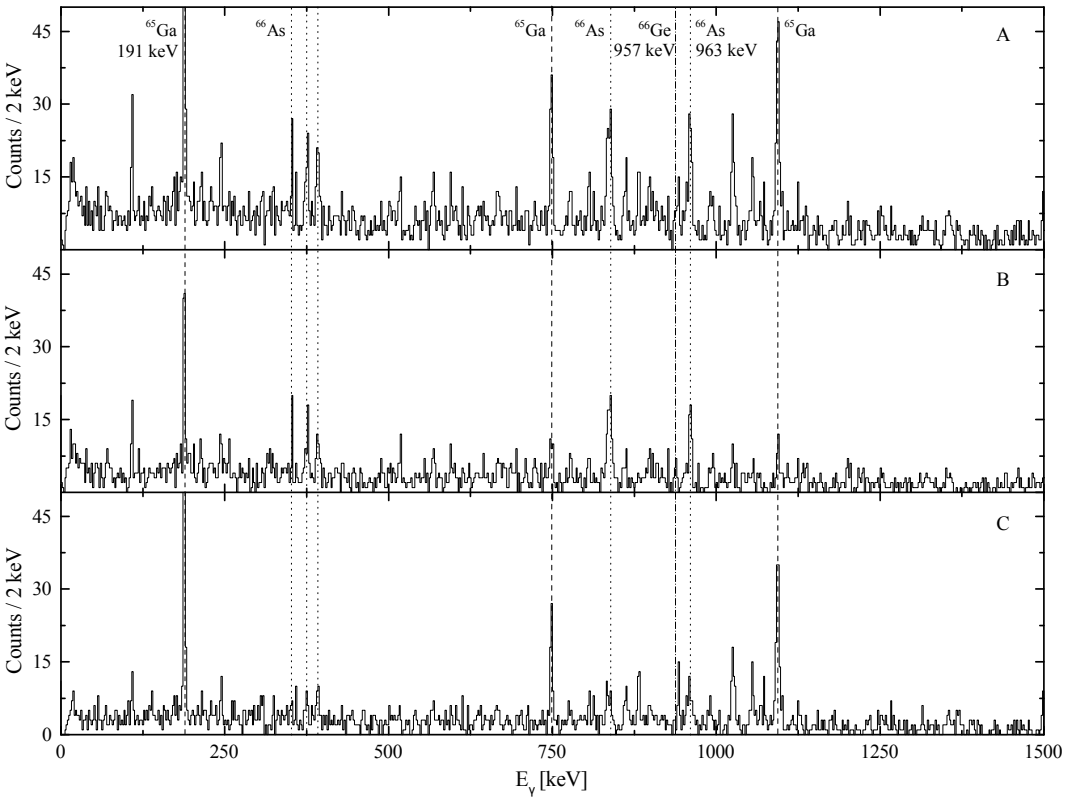

FIGURE 4.4: JUROGAM II γ-ray spectra tagged with a β decay within 300 ms of a recoil implantation for different UoYtube veto conditions. A) shows tagged events with no UoYtube requirements, B) shows tagged events requiring ≤ 1 charged particle detected in the UoYtube whilst C) shows tagged events in which > 1 charged particle events were detected in the UoYtube. All three required a β-particle energy deposition in the planar-Ge detector of ≥ 1.5 MeV. Prominent γ peaks corresponding to the ^{40}Ca(^{28}Si,pn)^{66}As channel are indicated by the dotted lines, γ peaks corresponding to ^{40}Ca(^{28}Si,3p)^{65}Ga are indicated by the dashed lines and the $2^+ \rightarrow 0^+$ transition in ^{66}Ge is indicated by a dotted-dashed line. Energies of those transitions relevant to the analysis described in the text are indicated. Contaminants are reduced by more than a factor of 3 by the vetoing strategy in (B). By placing tighter gates on the UoYtube energy and timing conditions than those used in this figure, it is possible to reduce any loss of ^{66}As events, although the reduction in contaminants is less significant.

^{66}As. Events which did not pass the recoil gates were then assessed using the β-event gates. If they occured within the same pixel and within a given time of a recoil-event, they were assessed to see if they contained valid β events. Valid β events were those that have passed time and energy gates on the DSSD and planar Ge detector. If the β event corresponding to a recoil was deemed valid, the recoil is β tagged.

The 191-keV line, corresponding to the de-excitation of the $5/2_1^-$ state to the ground state of the ^{40}Ca(^{28}Si,3p)^{65}Ga channel was used as a test for the contaminant events. It was found that the inclusion of the UoYtube suppressed the amount of contaminant statistics by more than a factor of three for events in which a single charged particle was detected in the UoYtube. Suppression by a factor of up to twenty was achieved for those events in which no charged particles were detected, depending upon the energy and timing gates on the UoYtube. The simulated efficiency of the UoYtube for the beam and target used is

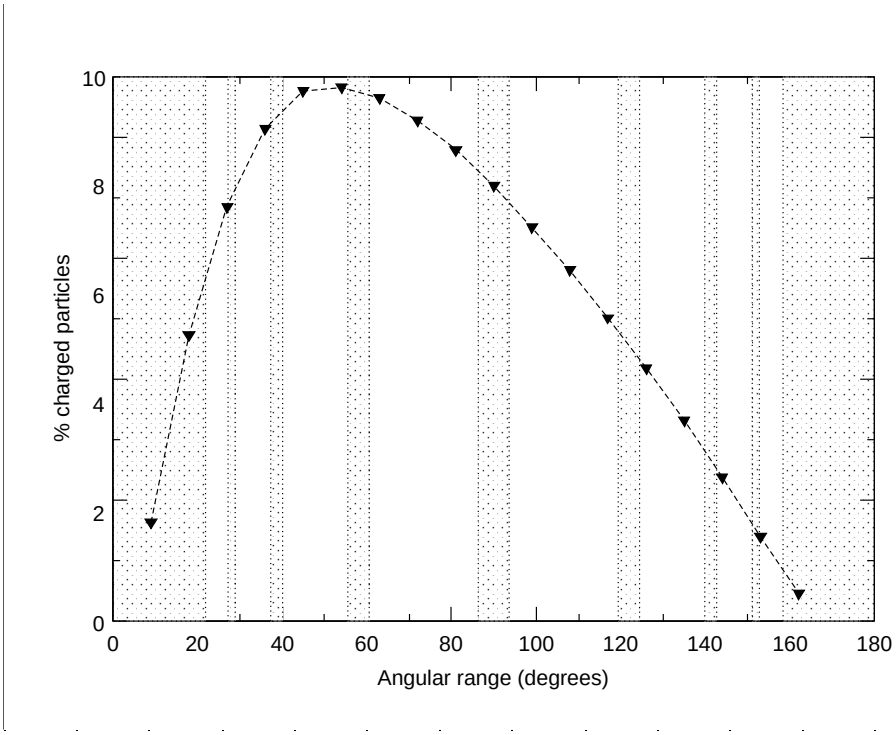

FIGURE 4.5: Angular distributions of emitted α particles and protons for a 75-MeV, ^{28}Si beam impinged on a ^{40}Ca target, taken from the PACE4 code [86]. The dotted regions indicate angles at which the UoYtube is insensitive due to gaps between detector elements. This simulation indicates that 62% of fusion-evaporation charged particles are emitted at angles which the UoYtube is sensitive to.

approximately 62%, as can be seen in Fig. 4.5. This corresponds to a suppression factor for the $3p$ channel of a factor of 18, which corresponds well with the suppression observed in tests. The channels with no charged-particle evaporation are those which are of most interest for studies of $N < Z$ nuclei in the $A \approx 70$ mass region, so the high suppression factor for such channels is vital. Indeed, the identification of excited states in ^{66}Se (the $2n$ channel), was achieved during the test of the UoYtube and will be the subject of a future publication. Due to incomplete angular coverage and other reductions in efficiency, a veto strategy requiring ≤ 1 charged-particle events was found to provide the best contaminant suppression for the pn channel whilst maintaining good statistics, as shown in Fig. 4.4.

4.2.2 Test of the DSSD and phoswich

The new DSSD was mounted in place of the previous pair of DSSDs in the GREAT spectrometer. The phoswich detector was mounted in the original position of the planar-Ge detector. Pulse shapes were recorded for the phoswich detector. It is the intention that, ultimately, pulse shape analysis for the phoswich could be done online using the field-programmable gate array (FPGA) hardware on the Lyrtech cards which would permit higher rates without resulting in large amounts of data (this will be discussed later in the present chapter). In the test, analysis of pulse shapes was carried out offline. The first stage of the analysis is a

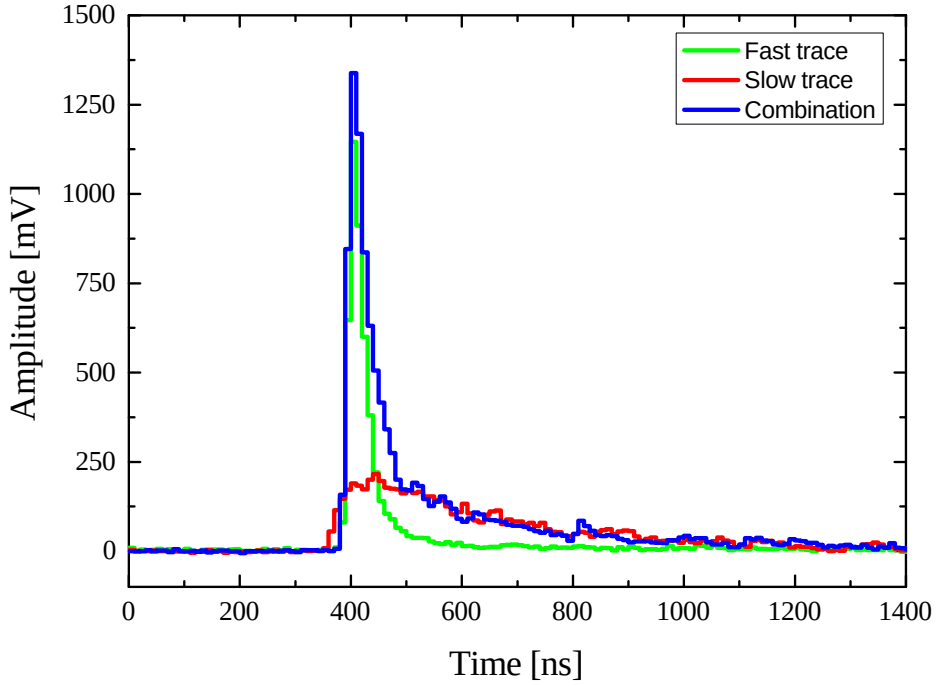

FIGURE 4.6: Typical pulse shapes for interaction in the fast plastic (green), slow plastic (red) and in both elements of the detector (blue).

constant background approximation and subtraction, an average signal height is taken in the region before the pulse and then subtracted throughout the length of the signal. A 100-ns window is then integrated over as the fast element of the pulse, with an integration over the remainder of the pulse used to determine the slow element. Typical pulse shapes recorded for interactions in the fast plastic, slow plastic and the combined system are shown in Fig. 4.6.

Analysis of the data was again carried out using the analyser Grain in the same manner as that described for the UoYtube. Events which are not valid recoils are considered as candidates for β-decay events, and their validity is assessed by passing them through β-selection gates from the phoswich such as that shown in Fig. 4.7. This gate requires that the phoswich signal had strong fast and slow components, corresponding to the β particle punching through the fast phoswich element. A timing gate is also placed on the phoswich/DSSD coincidence. By using the sum of the fast and slow elements of the signal, an alternative β-particle selection method is also possible with the phoswich used in a similar manner to the original planar-Ge detector.

4.2.3 Characterisation of new setup

The UoYtube veto analysis was carried out offline which allowed comparisons to be made between the vetoed and non-vetoed spectra in order to characterise any improvements. Two forms of background were considered: False correlations due to high-rates in the DSSD pixels, and genuine correlations from background channels. The ^{40}Ca(^{28}Si,3p)^{65}Ga channel had the

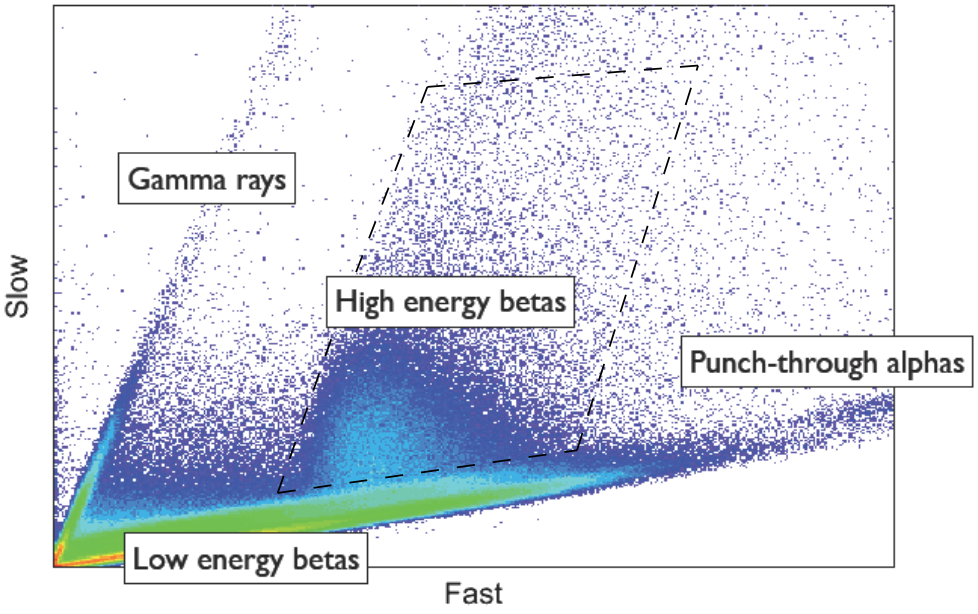

FIGURE 4.7: Slow against fast phoswich signals, where fast signals are those resulting from an integral over the first 100 ns after the trigger, and slow signals are the integral over the remainder of the pulse. High-energy β particles can easily be distinguished as the region protruding above the line corresponding to the purely fast elements. Gamma events are also found in the low-energy fast components, although they are preferentially detected in the slow components due to its larger size. A typical high-energy β particle gate is indicated by the dashed line.

highest cross-section and as a result its influence is largely due to false correlations. Other background events, such as the ^{40}Ca(^{28}Si,2p)^{66}Ge channel were produced with lower cross-sections and were therefore considered to be less falsely correlated. The latter of the two forms of background is used to define the cleanliness of the spectra, which is defined as the ratio between the intensities of the 963-keV γ-rays from ^{66}As and the 957-keV γ-rays from ^{66}Ge.

The cleanliness achieved with the UoYtube setup is shown in Fig. 4.8. It can be seen that the addition of the UoYtube veto reduces the optimal threshold energy for the β-particles - that where the maximum cleanliness is achieved - by approximately 1 MeV. This reduction makes a larger fraction of the β-particle energy distribution available with cleaner correlations, leading in turn to greater and cleaner γ-transition statistics. It must be noted that the use of the UoYtube veto does eliminate good events as well as bad, with at least a 10% reduction in good events for the same threshold energy. This can be even more significant if timing and energy gates are loosened because more uncorrelated target position charged particles are accepted in the gates. However, any loss is more than offset by the increased number of good events which occur above the lower optimal threshold energy.

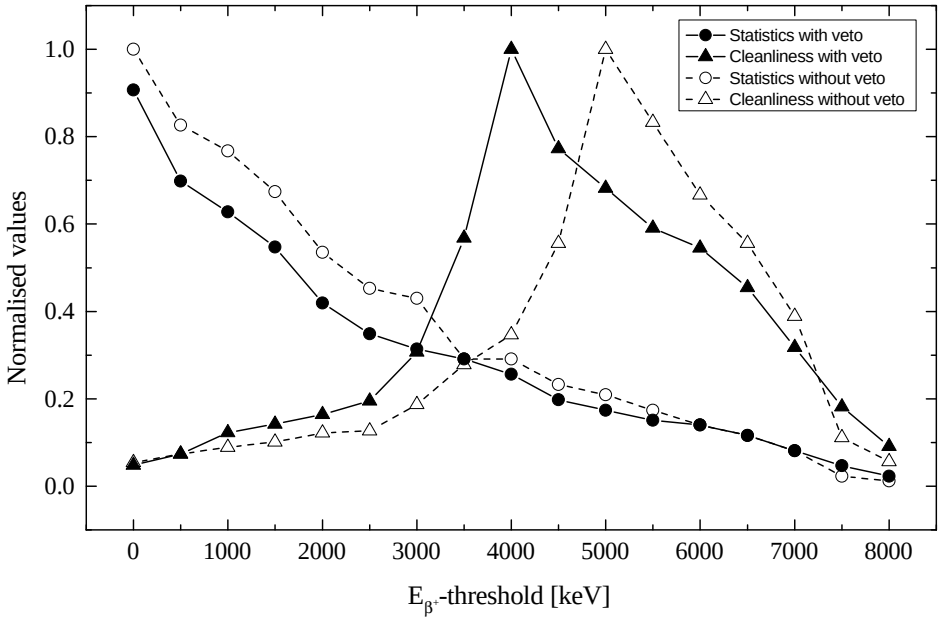

FIGURE 4.8: Normalised cleanliness (triangles) and amount of statistics (circles) for the UoYtube setup without a vetoing strategy (unfilled points) and with a requirement that ≤ 1 charged particle is detected in the UoYtube (filled points). Cleanliness here is defined as the ratio of intensities of the 963-keV γ-ray peak corresponding to the $2^+ \rightarrow 0^+$ transition in ^{66}As and the 957-keV peak corresponding to the $2^+ \rightarrow 0^+$ transition in ^{66}Ge. The number of statistics is the number of events corresponding to the 963-keV transition. Tighter energy and timing gates were used in this figure than those that were used in Fig. 4.4, and statistics were normalised to the non-vetoed data for comparison. The trend indicates a lower β-energy threshold can be used with the UoYtube to achieve maximum cleanliness.

As described previously, β selection with the phoswich can be made in two ways, a selection on the fast element vs the slow element of the signal, or the use of the sum of the fast and slow elements as a threshold energy, in the same manner as for the planar-Ge detector. Fig. 4.9 shows the result of the different techniques. The spectrum in Fig. 4.9 (A) is the raw recoil tagged spectrum, Fig. 4.9 (B) requires that the candidate β particle has an energy over a threshold of approximately 2 MeV, whilst Fig. 4.9 (C) requires that the fast and slow elements lie within a 2D gate defined so as to enclose the high-energy β particles shown in Fig. 4.7. All three spectra have a 200-ms timing requirement. The threshold energy selected for spectrum (B) was chosen in order to be approximately equivalent to the lowest energy accepted by the 2D phoswich gate used in spectrum (C).

It can be seen from Fig. 4.9 that, whilst the use of the pulse shapes from the phoswich does have the effect of reducing the false correlations, it does so at the expense of good events in the 837-keV ^{66}As peak. The 963-keV peak proved too poorly populated in the phoswich tests to be a viable method of characterising the detector. This reduction in good events is due to β particles interacting with a large angle of incidence to the detector and therefore not passing into the slow element. As would be expected, the threshold method in the phoswich test behaves in much the same manner as in the UoYtube test. Importantly however, the

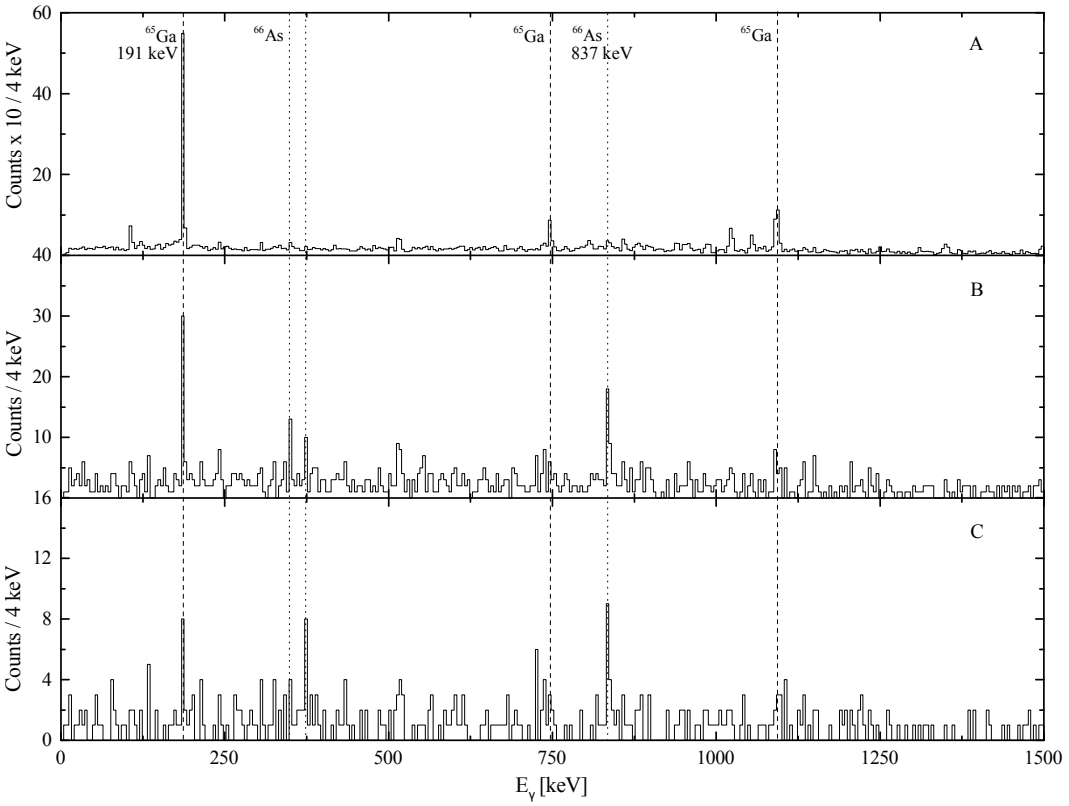

FIGURE 4.9: JUROGAM II γ-ray spectra. A: Raw recoil-tagged spectrum. B: Threshold energy requirement of approximately 2 MeV. C: 2D fast and slow phoswich element gate. A 200-ms timing requirement was used in this case as it gave the best improvement in signal to background ratio. The threshold for B was chosen in order to be equivalent to the lowest energy accepted by the 2D phoswich gate used in C. The dashed lines correspond to the γ decays of excited states in ^{65}Ga, whilst the dotted lines correspond to the decays of excited states in ^{66}As. Transition energies relevant to discussion in the text are indicated. Spectrum C is found to be cleaner than spectrum B but at the expense of good events however, since analysis is carried out entirely offline, the two selection techniques can be used in a complementary fashion.

two techniques are not exclusive and can be used in combination in order to provide a more complete picture.

As a demonstration of the validity of the phoswich gates, the natural log of the timing difference [89] between the recoil event and that of the presumed good β event is plotted and shown in Fig. 4.10 after a constant background subtraction. The centroid of this fit corresponds to the lifetime of the decay, leading to a value of $t_{1/2} = 94 \pm 9$ ms, which lies within the error limits of the known ^{66}As half-life of 95.7 ± 0.3 ms [90]. The number of counts against the time difference on a linear time scale are also shown in the inset of Fig. 4.10.

Two different DSSD tagging strategies are possible in Grain, known as the SINGLE and SQUARE strategies. For the SQUARE strategy, all surrounding pixels in the DSSD are considered when looking for the β decay of a recoil, whereas in the SINGLE strategy, only the implantation pixel is considered. The affect on the γ-spectra of using the SINGLE and SQUARE strategies is shown in Fig. 4.11, with the upper spectrum corresponding to

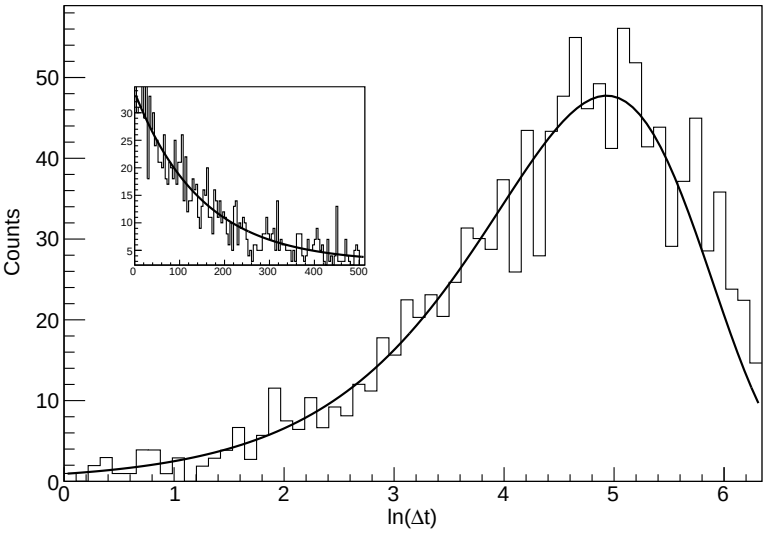

FIGURE 4.10: The natural logarithm of the time difference between implants and β decays for high-energy events selected by the phoswich gate. The shown fit corresponds to $t_{1/2} = 94 \pm 9$ ms. Inset: The time difference on a linear, ms scale. The cut-off occurs at 6.55 (corresponding to 700 ms), after which backgrounds begin to dominate the data.

the SQUARE strategy and the bottom spectrum corresponding to the SINGLE strategy. Analysis of these data shows only a small increase above background in valid ^{66}As events for the larger tagging scheme involving the neighbouring pixels alongside a significant increase in contaminant events. This demonstrates that the single pixel tagging strategy is optimal and also validates the reduction in pixel size, as the increase in background for a larger effective pixel size is significant when compared to the increase in good, ^{66}As events.

The effect of false correlations is also investigated by considering the 191-keV peak resulting from the decay of the second excited state in ^{65}Ga. Here, an index of false correlations is defined as being the ratio between the intensity of the 191-keV decay and the number of β particles accepted in the planar detector. Fig. 4.12 shows this false correlation index for varying threshold for tests of the new DSSD with the planar Ge detector. The SQUARE strategy was used to simulate increased pixel size within the same experiment. Also shown in Fig. 4.12 are two runs taken with the old, less finely segmented, DSSD. Analysis of the data from the higher beam intensity data was challenging, since high rates in the DSSD resulted in a large proportion of events containing false correlations. The lower intensity data from the old DSSD in Fig. 4.12 were taken from the UoYtube runs. For these runs it was found that false correlations were at a more manageable level. It can be seen, therefore, that data from the new DSSD, even at beam intensities which would have caused problems for the older DSSD, are not dominated by false correlations. It then seems reasonable that higher beam intensities of 5-6 pnA are practical for RBT studies with the new DSSD.

For completeness, the cleanliness technique was applied to data obtained using the new DSSD and the planar Ge detector for both the SINGLE and SQUARE strategies. It was found that,

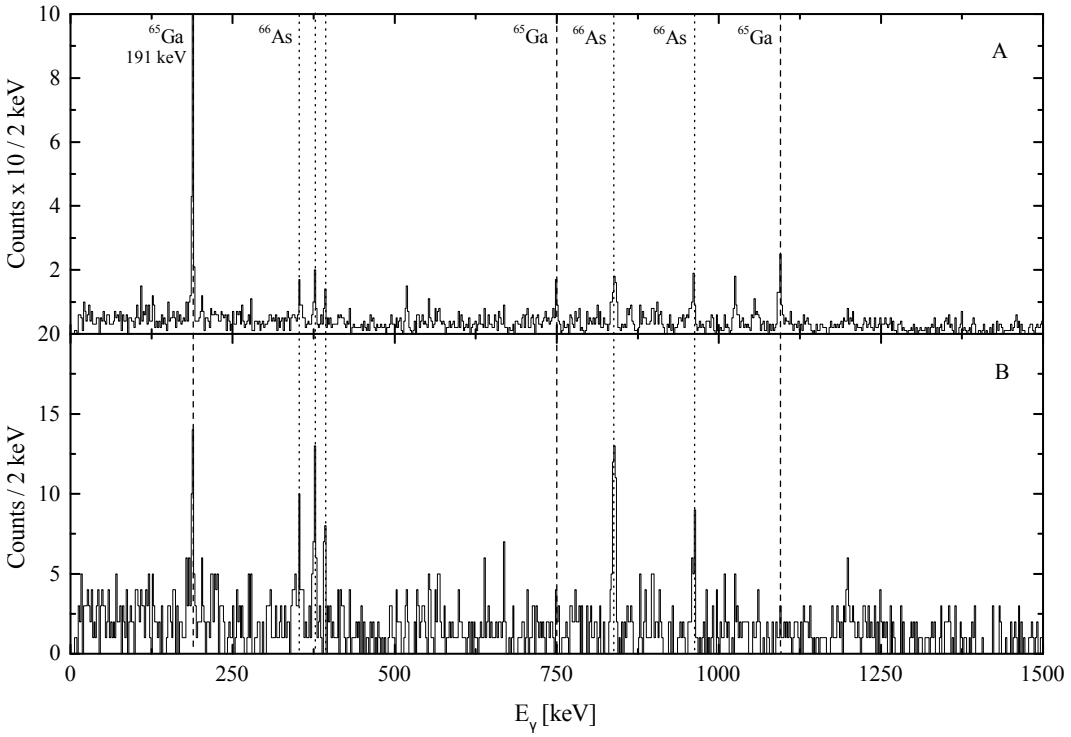

FIGURE 4.11: JUROGAM II γ-ray spectra using two different recoil-to-decay DSSD correlation strategies. The top spectrum uses the SQUARE tagging strategy, whilst the bottom spectrum uses the SINGLE strategy (see text for tagging strategy definitions). While there is a slight increase in the number of genuine ^{66}As events (indicated by the dotted lines) using the SQUARE tagging strategy, it comes at the expense of a significant increase in the 191-keV contaminant lines (indicated by the dashed lines). β-particle energy thresholds were set at 3500 keV.

as would be expected, the reduction in pixel size had no significant effect on the cleanliness of genuine ^{66}Ge correlations because this background channel was not dominated by false correlations. This validates the distinction between the false correlation backgrounds and those originating from genuine β decays and other competing processes.

Finally, tests were carried out using the new DSSD along with the planar Ge detector to investigate how the production rates responded to various beam intensities in order to help determine the optimal intensities for any future runs. It was found that for beam intensities between 3 and 7 pnA, rates increased linearly, as would be expected. This would indicate that false correlation rates were not high enough at these intensities to significantly inhibit the tagging process.

4.3 Further development

While the tests described above demonstrated the improvement to the set-up, they also served to highlight some possible further improvements, foremost among which was the need to increase the UoYtube efficiency and make it compatible with the more general purpose

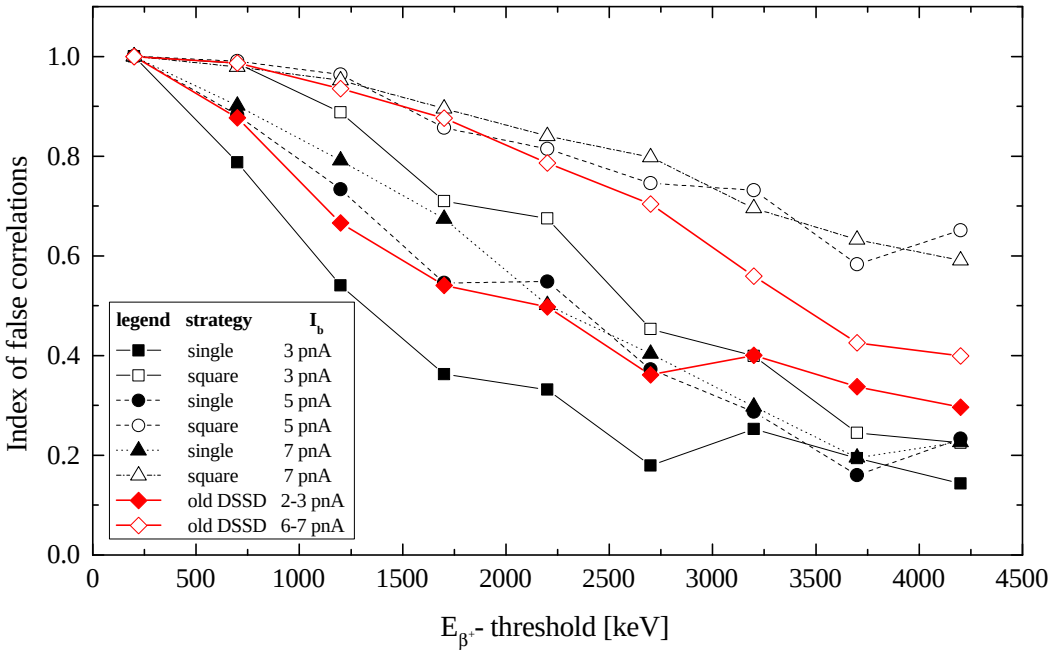

FIGURE 4.12: False correlation index for different tagging strategies (explained in the text) with the new DSSD. Also included are two experimental runs with the old DSSD. The higher intensity run with the old DSSD represents a false correlation index which makes analysis difficult, as false correlations begin to dominate the data, whereas the lower intensity run with the old DSSD resulted in false correlations which were easily manageable. The highlighted relevant region represents the typical β-energy thresholds used in the RBT studies and therefore the region in which improvements are most significant. It can be seen therefore, that the new DSSD with the SINGLE tagging strategy can manage higher beam intensities whilst maintaining manageable false correlations. It should also be noted that for the highest intensity run with the SQUARE tagging strategy, the 191-keV ^{65}Ga γ ray could not be eliminated within the normal threshold ranges, demonstrating the problem of false correlations when individual pixel rates are high. Error bars are excluded for clarity. Errors are less than ± 0.125 for all points within the region of interest.

RITU target chambers. This would make the mounting of the device more straightforward and would allow the use of the five upstream Phase I JUROGAM II detectors, improving the γ-ray detection efficiency of the setup.

In order to achieve these goals, the UoYtube was redesigned. In the original UoYtube design small gaps were included between the CsI(Tl) elements to allow for flexibility when constructing the detector. In the new design, these gaps were removed, making for a more complete solid angle coverage. Simultaneously, the size of the general purpose target chambers necessitated the reduction in length of the tube from the 221 mm of the original design to 185 mm, as well as a slight reduction in the breadth of the detector from 102 mm down to 100 mm.

To accomplish these reductions in size, the number of CsI(Tl) elements on the hexagonal cylinder was reduced to 7x2 on each face. Due to the geometry of the target chamber and the target position with respect to JUROGAM II, these were arranged with 4x2 of the detectors downstream of the target position and 3x2 upstream. Previous calculations [74], as shown

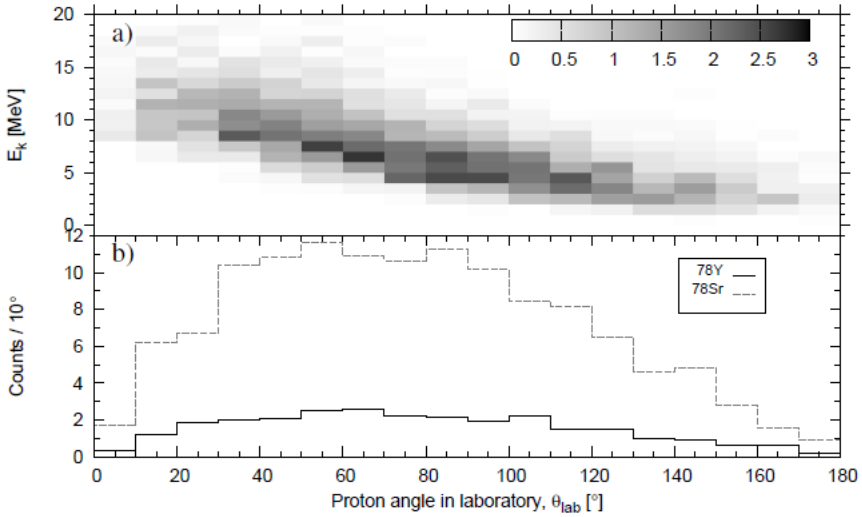

FIGURE 4.13: Fusion evaporation distributions as calculated by J. Saren [74]. The forward-focussed nature of the evaporated particles compensates for the asymmetric detector distribution around the target position.

in Fig. 4.13, demonstrate that the forward-focussed nature of the charged particle emission - even at the relatively modest energies used - compensates for this asymmetry.

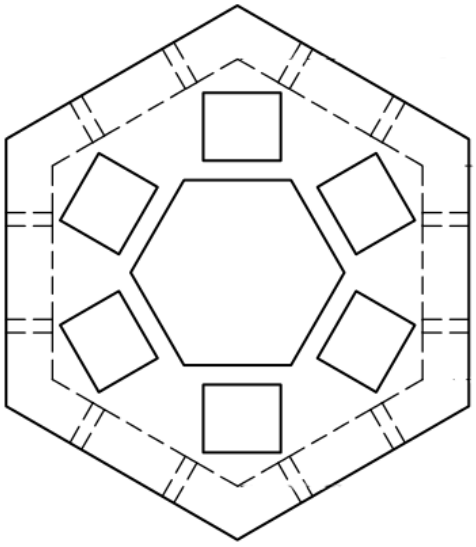

FIGURE 4.14: The endcap design for the new UoYtube array. Six pentagonal detector elements are mounted on each endcap.

Further to a reduction in size, endcaps were designed in order to reduce the opening angles at either end of the tube. These hexagonal sections (see Fig. 4.14) would each contain six pentagonal CsI(Tl) elements, providing more complete angular coverage. This reduces the forward opening angle to 13.24° and the backwards angle to 19.98°. From the PACE calculations in Fig. 4.15, this would represent a coverage of 96.7% of emitted charged particles. Fig. 4.15 also highlights the improvement over the original tube design. Dotted regions indicate laboratory angles for which the old UoYtube design was insensitive due to incomplete

coverage. The dashed region represents the angles for which both designs are insensitive. It can be seen that the new design represents a significant improvement in solid angle coverage over the original UoYtube.

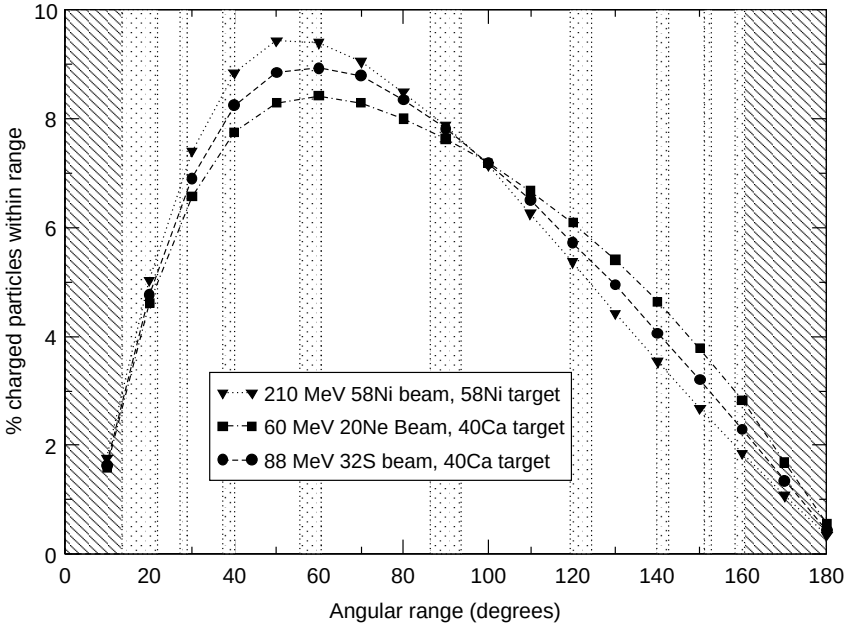

FIGURE 4.15: Fusion evaporated charged particle angular distribution, as calculated with PACE [86]. The improvement over the original design can be seen, with the dashed regions corresponding to angles at which both the new and old designs were insensitive and the dotted regions being angles at which the old design was insensitive.

Since the previous detector system had utilized the LISA chamber, it was possible to make use of the target changing mechanism developed for that chamber. With the new set-up, a new target mechanism had to be devised. With studies on or beyond the $N = Z$ line, ^{40}Ca is the most common target as it is the most massive stable $N = Z$ nuclide. Since ^{40}Ca oxidises rapidly in air, it is vital to minimise the time taken to mount the target and bring the system down to vacuum. To make this possible, the tube was split at approximately the target position. The downstream elements could therefore be mounted on the chamber flange and beam adjustments made with the upstream end unattached. The target could then be rapidly mounted and the system taken down to vacuum. To make this attachment as fast as possible, plugs and sockets were used to attached the upstream and downstream elements. The complete redesign of the UoYtube is shown in Fig. 4.16.

The same Mesytec pre-amplifiers are used as with the original UoYtube, with the same model of PIN diodes (Hammamatsu S3590-08) and the 7x2 CsI(Tl) elements on the plates being made up of the old UoYtube detectors. The pentagonal CsI(Tl) crystals necessary for the endcaps were provided by Hilger-Crystals in the necessary dimensions. The light output from these crystals was guided to the PIN diodes by light-guides made using chemical deposition.

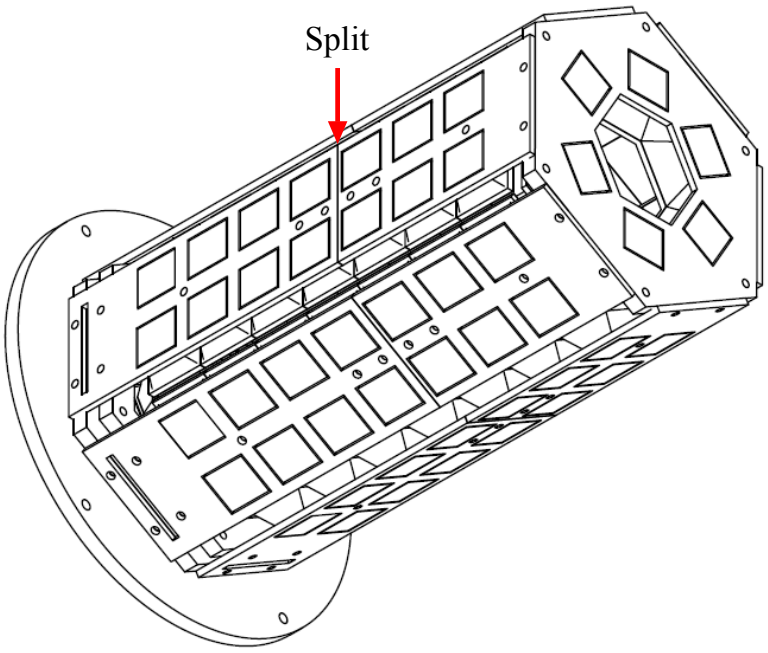

FIGURE 4.16: Design of the alumnium frame for the new UoYtube. The upstream endcap is shown on the right of the image, with the split to allow target mounting occuring between the fourth and fifth rings of detectors when viewed from left to right, indicated by the red arrow.

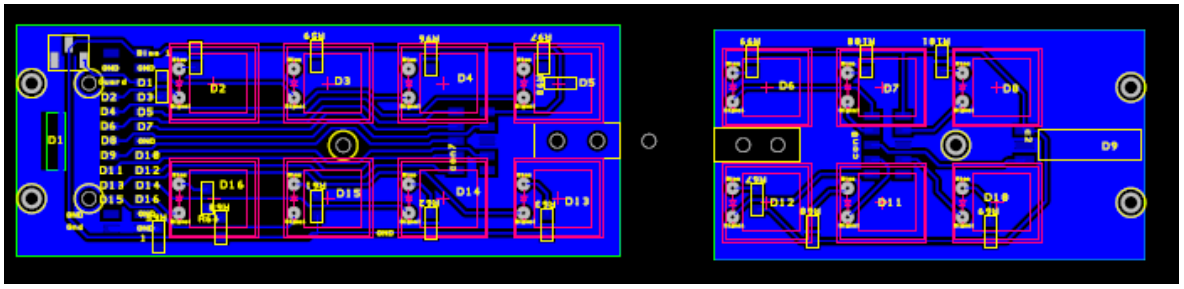

FIGURE 4.17: The layout of the PCB for the redesigned UoYtube [91] with the detector numbering. Singals from detectors D1 and D9 are read from the downstream and upstream endcaps respectively.

Printed circuit boards (PCBs) were developed to be mounted on the aluminium frame design shown in Fig. 4.16. Jumper cables attach the downstream PCBs to those on the upstream section. The 96 signals from the photodiodes are read out in six groups of 16 signals. Each set of 16 comprises one signal from the downstream endcap, the 14 from the tube barrel and one signal from the upstream endcap. The layout of the PCB is shown in Fig. 4.17 [91].

As the redesigned UoYtube is not intended for use with the LISA target chamber, it was also necessary to develop a new chamber capable of reading out the 96 channels that the UoYtube requires. The dimensions of the new chamber were to be exactly the same as those of the more general purpose target chamber used at JYFL. The target chamber was constructed by HiVac and incorporated six, 25-way d-connector type feedthroughs. Fig. 4.18 shows the

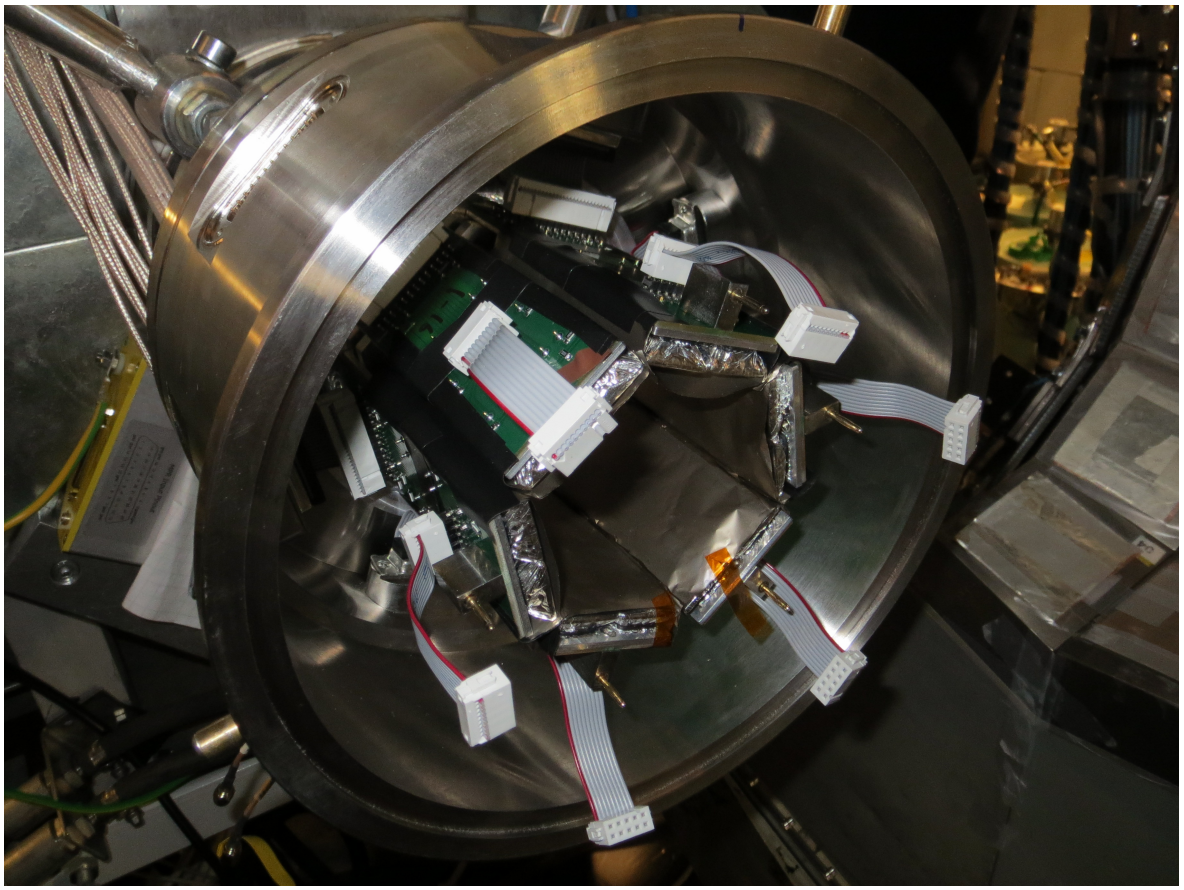

FIGURE 4.18: The downstream portion of the new UoYtube mounted in the new target chamber. The plugs are used to attach the downstream section to the upstream portion of the tube. 10-μm Ni foils used to protect the CsI elements from scattered beam can also be seen.

downstream portion of the new veto array mounted in the new target chamber in preparation for alignment, while Fig. 4.19 shows the complete mounted tube and Fig. 4.20 shows the new target chamber mounted at the center of the JUROGAM II array.

The individual CsI(Tl) crystals are again wrapped in 2.5-μm Mylar foils to aid light collection. These foils can be complemented by additional, high-Z materials in an experimental situation, in order to prevent scattered beam paralysing the detectors. This is particularly important for the downstream detectors. The thicknesses of these heavier foils is determined on a case by case basis, depending on the beam required for a given experiment, in order to maximise reductions in backgrounds from scattered beam and target material, whilst minimising losses due to evaporated charged particles being stopped in the foils.

To allow for the hermetically sealed, welded feedthroughs to be installed on the target chamber in a short time scale, the target chamber built for the redesigned UoYtube was constructed from steel. Due to the higher Z of the constituents of steel, the new chamber has a significant attenuation effect, particularly on low-energy γ rays. This effect was studied in the theses of A. Girka [92] and O. Nevodov [93]. The geometry of the JUROGAM II array means that

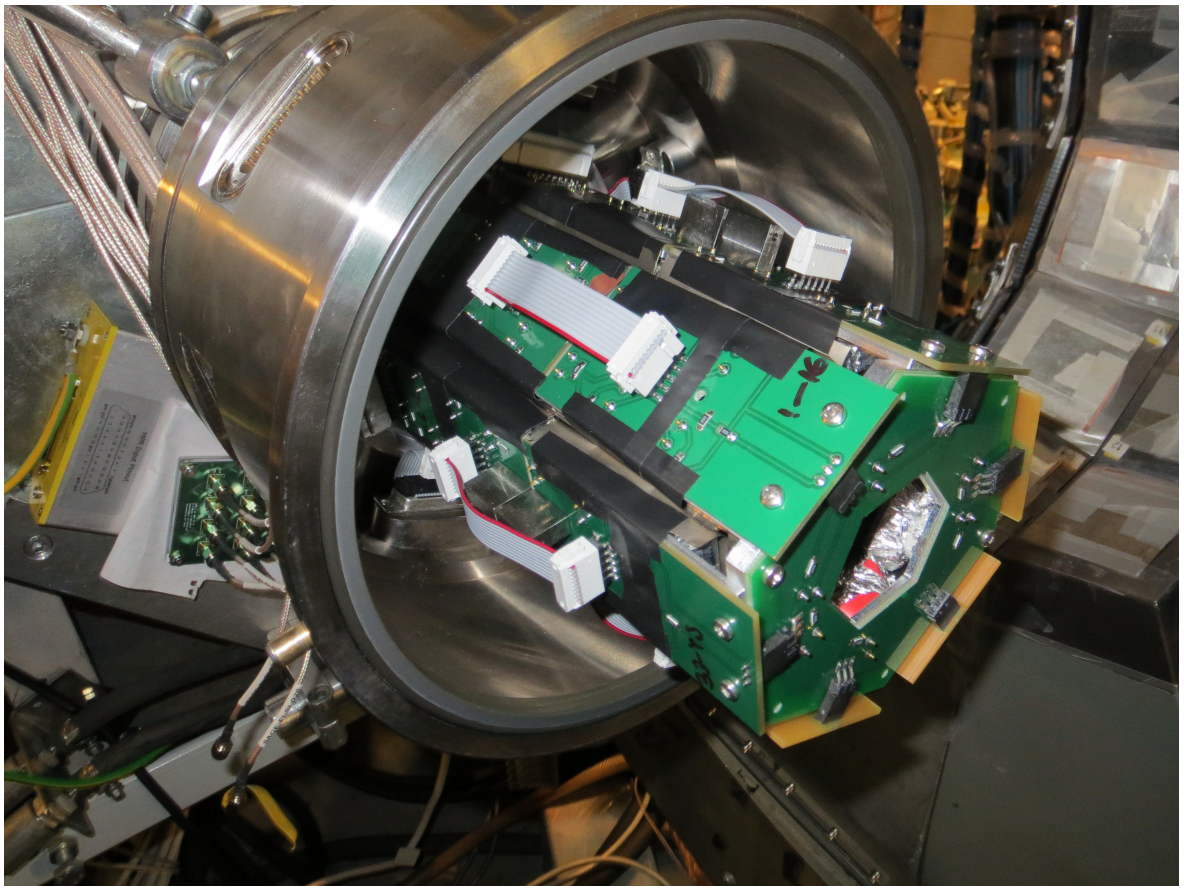

FIGURE 4.19: The complete UoYtube mounted in the target chamber. The jumper cables between the up- and down-stream portions are now attached. These are quick to attach and aid the rapid mounting of the targets within the tube. A 25-way d-connector is also attached.

only the clover detectors are shadowed by the steel of the new target chamber, illustrated in Fig. 4.21, with the clover efficiency shown both with and without the new target chamber. A reduction in peak efficiency of about 25% is observed, although the effect is less pronounced at higher energies, with a reduction of only about 10% at 1 MeV. Similarly, the efficiency data for the JUROGAM II Phase-I detectors with and without the UoYtube are shown in Fig. 4.22. The tube has a significant attenuating effect at low energy, with a reduction in efficiency of about a factor of two. Again, at higher energy the effect is lessened with a reduction of about 30% at 1 MeV.

4.4 UoYtube and MARA

At the time of writing, the redesigned UoYtube has been used for three experiments at JYFL including the work discussed in this thesis, with a single proton detection efficiency of $\sim 75\%$. These experiments have all been performed with the RITU separator, however in the near future, the MARA separator (see Section 3.3.2) will be installed at JYFL, providing isobaric separation.

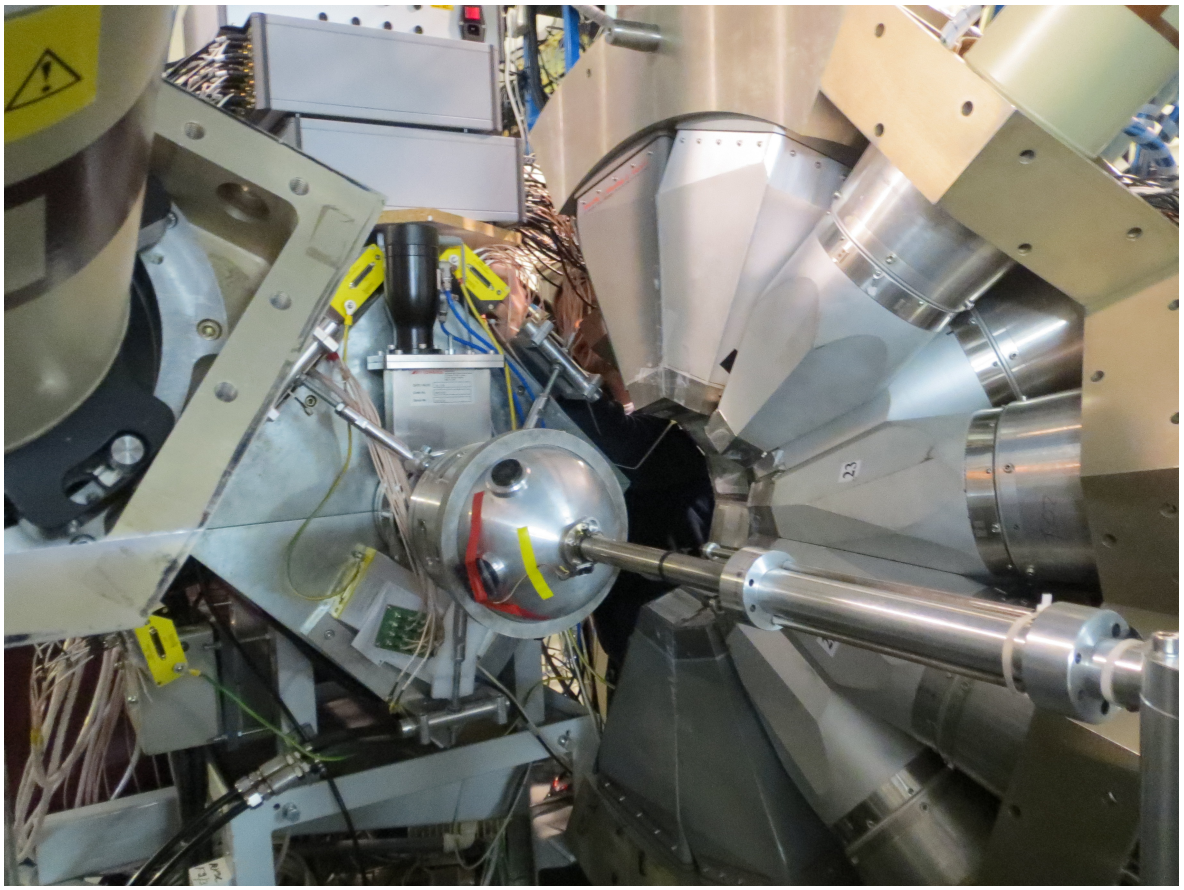

FIGURE 4.20: The new general purpose target chamber at the center of the JUROGAM II array, mounted on the first quadrupole of RITU. Four of the six Mesytec preamplifiers (yellow) can be seen, mutually grounded onto RITU. The gain and offset boxes (grey) can also be seen, mounted on top of the RITU quadrupole.

MARA is expected to provide 28% transmission of the isobar of interest, compared to a transmission of $\sim$ 3% for neighbouring isobars [76]. In concert with the UoYtube, this 90% suppression of unwanted channels could be significantly improved. For example, in a similar case to that discussed in the present work, the $3p$ channel would be suppressed by an additional 98.5% over that achieved with MARA alone, resulting in an absolute suppression of 99.8%.

Additionally, the UoYtube will enable identification of the individual components of the isobar with high efficiency. One can consider individual γ-ray transitions with respect to the number of evaporated charged-particles detected in coincidence with them. This will allow for the separation of transitions within an isobar without the requirement for high-statistics γ-γ coincidence data.

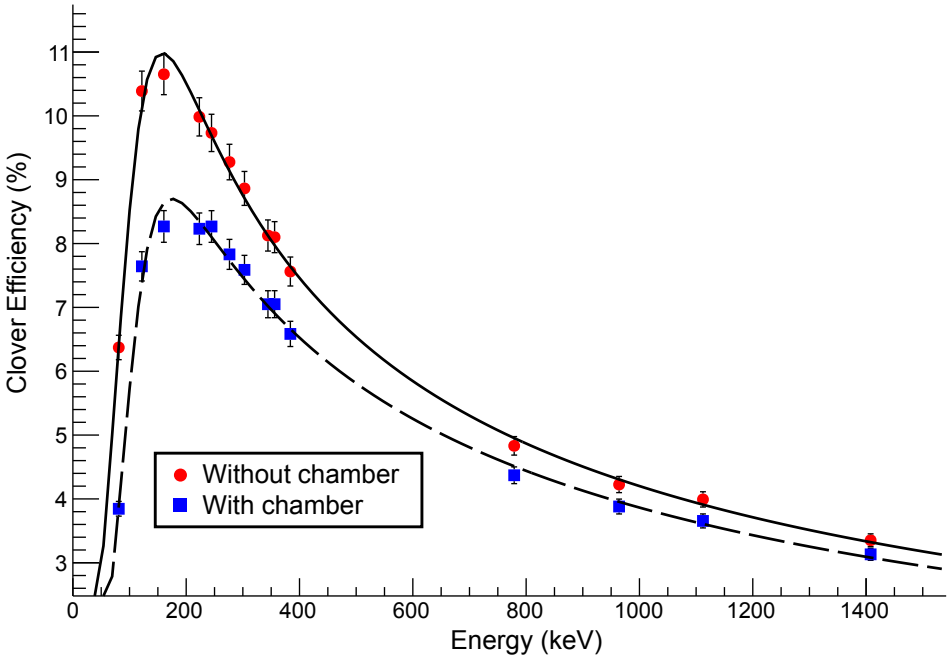

FIGURE 4.21: The efficiency curve of the JUROGAM II clovers shown with (without) the target chamber by the red squares (circles). The chamber can be seen to have a significant effect on the low-energy γ rays, with a reduction in peak efficiency of about 25%.

4.5 UoYtube particle identification

Note: The particle identification tests discussed in this section were performed subsequent to the experiments discussed in later chapters, for which particle identification was not available.

It has been known for many years that the particle-dependent light response of CsI(Tl) makes it suitable for particle identification [94]. This light response manifests itself as a sharper signal decay time for increased ionization density, where the ionization density is the number of ions produced per unit path length in the material. Fig. 4.23 demonstrates this, with pulse heights taken at times of 0.5 μs and 4 μs after the trigger showing a larger "fast" component relative to the "slow" component for alpha particles than protons and electrons.

The varying light response in scintillators arises from the rate of energy deposition from the incident particle. For more massive, higher Z particles, the energy deposition is concentrated in a smaller area, allowing for more exotic excitations of the scintillation material. In the case of inorganic scintillators, such as CsI(Tl), these excitations are known as excitons and tend to be shorter lived than singly free electrons and holes. At different ionization densities, these excitons are populated in different proportions, giving rise to the particle-dependent light response of the scintillation material.

This property has been widely used in arrays such as Microball [95], CHIMERA [96] and Dwarfball [97] through the use of pulse-shape analysis (PSA) techniques similar to those employed for the phoswich detector. The development and implementation of such analysis

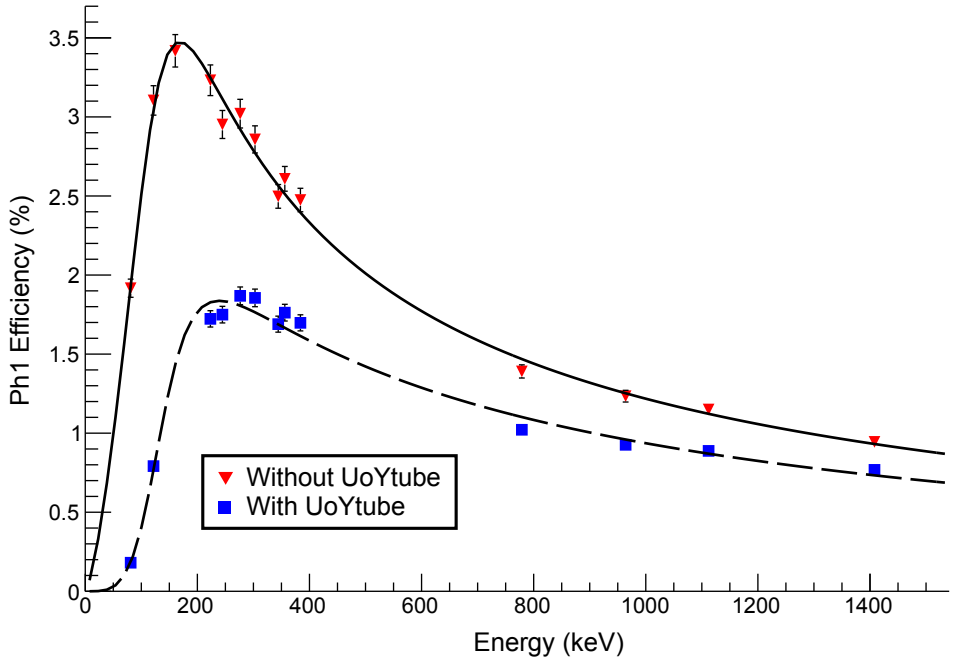

FIGURE 4.22: The efficiency curve of the JUROGAM II Phase-I detectors shown with (without) the UoYtube array by the red squares (triangles). The UoYtube can be seen to have a significant effect on the low-energy γ rays, with a reduction in peak efficiency of about a factor of two. The effect is less pronounced at higher energies with the UoYtube reducing efficiency by about 30% at 1 MeV.

techniques for the UoYtube will allow the accurate identification of α-particle channels which might otherwise be inseparable from proton-evaporation channels. The fact that the analysis techniques for the UoYtube and phoswich will likely be similar is also advantageous, as a single algorithm might be installed in the field-programable gate arrays (FPGAs) of the TDR system (see Section 3.5) and employed for both detectors.

In order to assess the possibility of performing PSA and to develop the necessary algorithms, an experiment was performed at JYFL. Extracting pulse shapes is memory intensive and can cause some problems for the data acquisition system, so they were only taken for one of the six UoYtube boards, representing 16 detectors covering a variety of angles. A ^{47}Ti beam at 157 MeV was extracted from the K130 cyclotron and impinged onto a ^{58}Ni target in order to produce both fusion-evaporated α particles and protons. Recoils were then transmitted through RITU, in order to provide timing information by which recoil-coincident fusion-evaporation products could be identified.

Pulse shapes taken during the experiment are shown in Fig. 4.24, representing the four observed shapes. The black pulse corresponds to a γ ray interacting directly with the photodiode and therefore provides information on their timing response. The green line corresponds to the detection of a proton; it can be seen that the decay of the signal is slow, with the pulse height at the end of the visible signal (about 9 μs) similar to that at its maximum. The blue signal on the other hand is the result of α-particle detection, with faster rise and decay times. Finally the red signal represents the detection of two charged particles in quick succession.

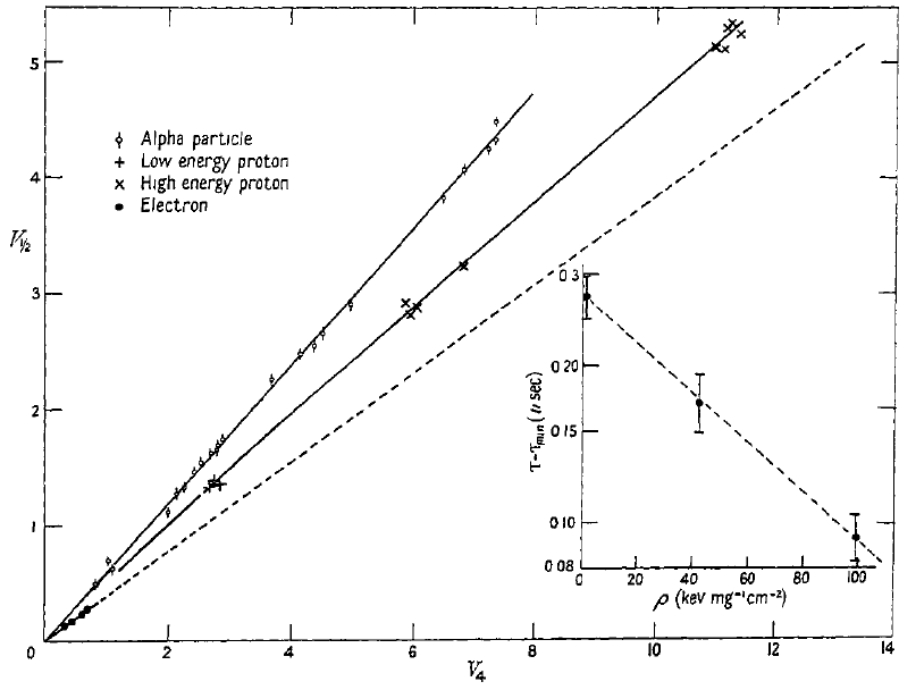

FIGURE 4.23: Light response from "fast" (0.5 μs) and "slow" (4 μs) components of CsI(Tl) signals originating from α particles, protons and electrons [94].

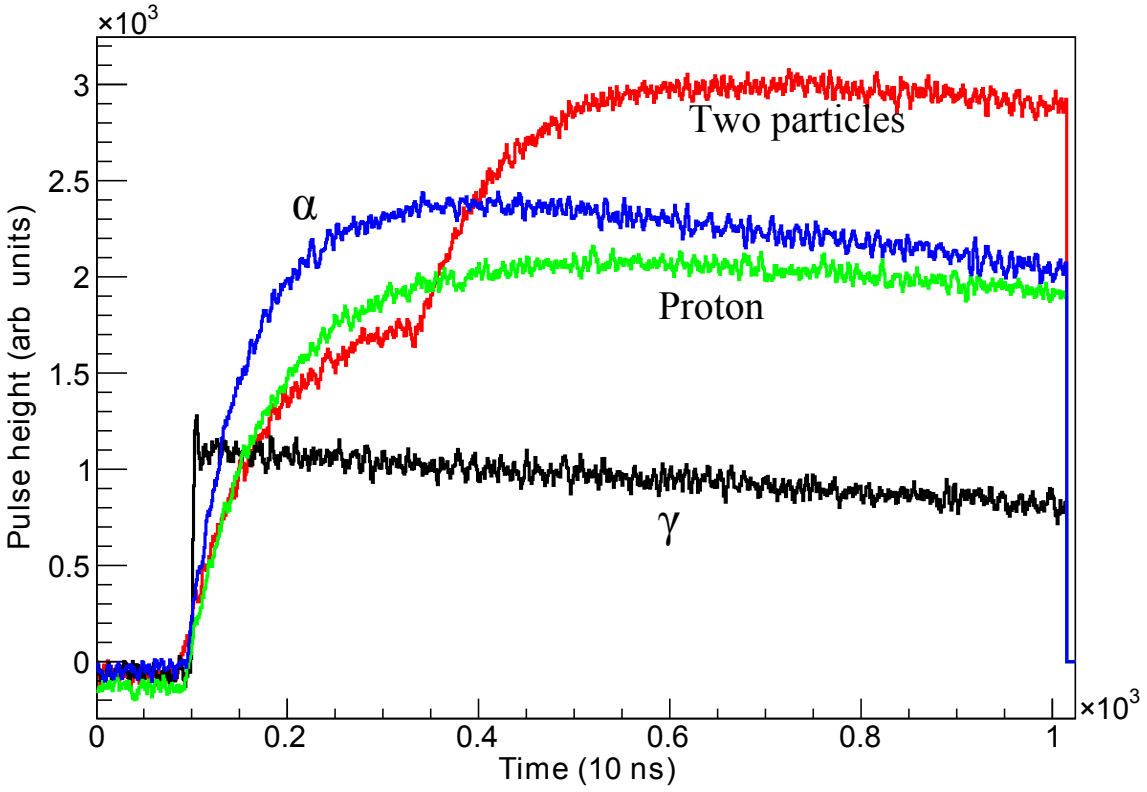

FIGURE 4.24: Traces extracted from the UoYtube for four different detection types: Black - a γ ray interacts directly with the photodiode, Green - a proton in CsI(Tl), Blue - an α particle in CsI(Tl) and red - two charged particle detections in quick succession in CsI(Tl).

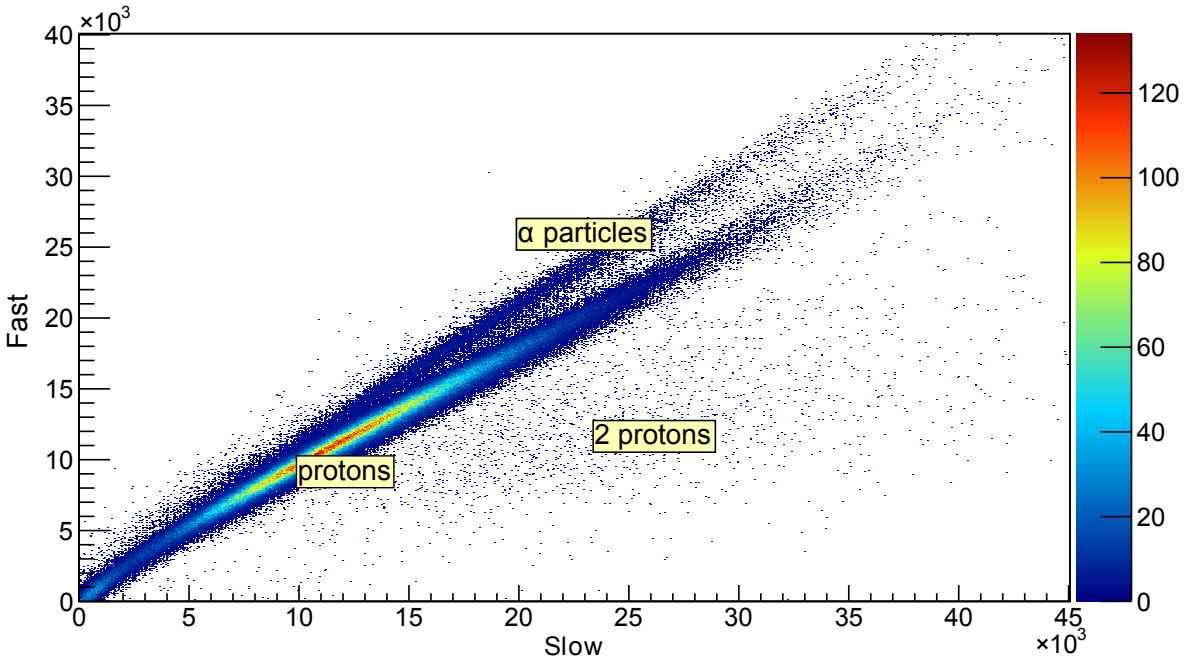

FIGURE 4.25: "Slow" ($4 \rightarrow 9$ μs from trigger time) and "fast" ($0 \rightarrow 3$ μs) elements of the UoYtube signal, labelled with the responsible interaction.

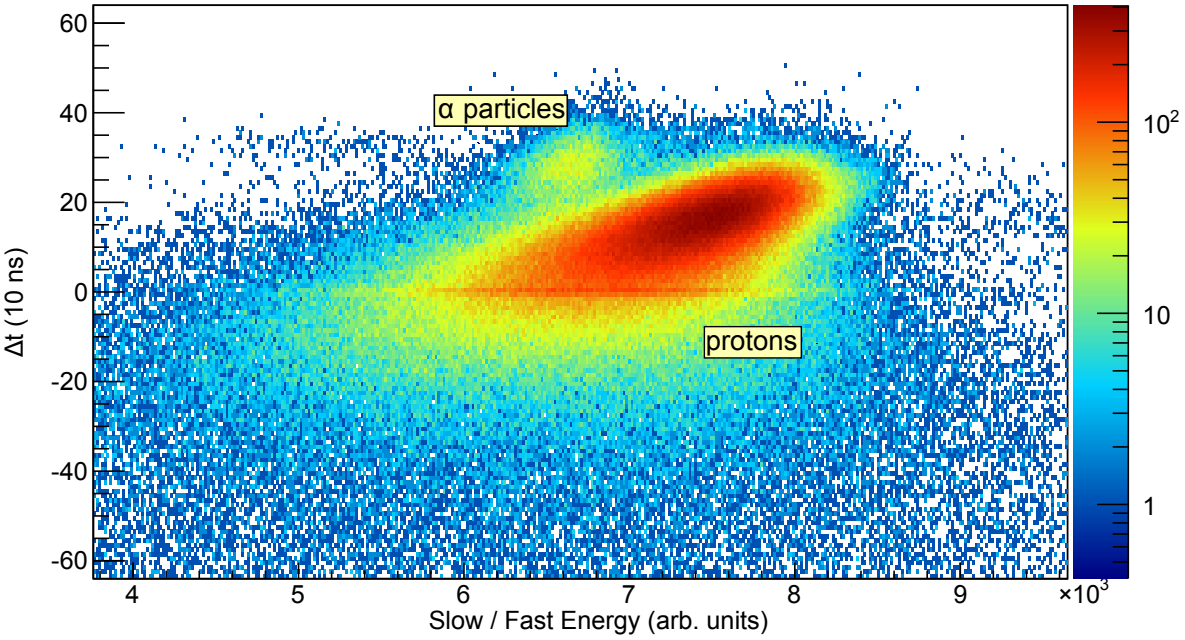

FIGURE 4.26: Slow component of the CsI signal divided by the energy extracted from the MWD algorithm plotted against the time of flight between the UoYtube and implantation detector. The alpha and proton components are highlighted.

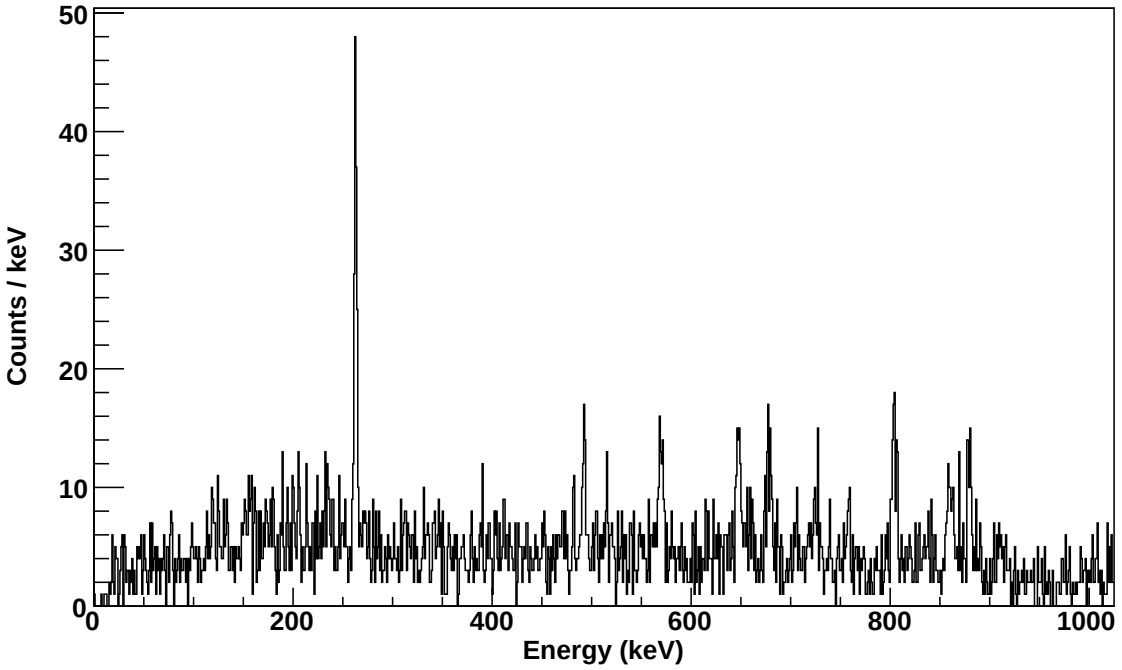

FIGURE 4.27: γ rays gated on the α-particle locus. The dominant transitions originate from the (αp) channel, corresponding to the nuclide ^{99}Pd.

In order to provide a metric for particle identification, a baseline subtracted integral was performed over "slow" ($4 \rightarrow 9$ μs from trigger time) and "fast" ($0 \rightarrow 3$ μs) elements. These are shown plotted against one another in Fig. 4.25. These data have already had an energy vs time UoYtube gate applied in order to determine those which are recoil coincident, which has the additional effect of eliminating the component corresponding to γ rays interacting directly with the photodiode. The three remaining contributions to the data are indicated.

Another method by which the alpha particles can be separated is shown in Fig. 4.26. Here the ratio of the slow component to the energy extracted using a moving window deconvolution algorithm is plotted against the time difference between implantation at the RITU focal plane and the UoYtube detection. Due to α-particle detections resulting in a faster rise time they tend to correspond to a faster time, whilst their decay properties result in a consistent ratio of the slow component to the energy. These properties are manifested in the locus above the proton locus in Fig. 4.26. The two techniques were both tested and proved to have similar identification efficiencies. Importantly, both techniques make use of the same observables and can therefore be performed complementarily, rather than at the expense of each other.

With the addition of particle identification, the UoYtube can also serve as a recoil-selection detector as well as the vetoing purpose for which it was originally designed. To properly characterise this capability, it is important to quantify the α-particle identification efficiency. In the test performed, γ rays associated with α-particle channels were not sufficiently intense as to provide a measure of this efficiency. Instead, the ratio of "accepted" to total particles detected in the 16 UoYtube elements used was calculated and was found to be 2% (that

is, 2% of events detected in the UoYtube passed the α-particle gate). This was then normalised by the expected ratio of produced α particles to protons, extracted from a PACE4 calculation [86]. The calculation predicted that 25% of charged particles produced should be α particles. Additionally, due to the requirement that a focal-plane detection was made [2], the reduced RITU transmission efficiency for α-particle channels was accounted for. This reduction was estimated to be about 25% for the purposes of the calculation. This results in an efficiency estimate for α-particle identification of about 10%. It should be noted that this estimate relies heavily on calculations which, especially far from stability, can vary by large amounts and as such it would be beneficial to estimate the efficiency using γ-spectroscopy in order to provide a complementary measurement. As a demonstration of the validity of the α-particle locus, Fig. 4.27 shows γ rays when a UoYtube gate on α particles is applied. The observed transitions all correspond to α-particle channels, with ^{99}Pd being the dominant channel, corresponding to the evaporation of an α particle and a proton.

[2] Required in order to get accurate timing information

Chapter 5

Experimental details and analysis

I started out with nothing and I've still got most of it left

Seasick Steve

The apparatus in this Chapter is discussed more completely in Chapters 3 and 4.

5.1 Experimental details

A 105-MeV ^{36}Ar beam was provided by the JYFL K130 cyclotron. The beam was impinged onto a 0.66 mg/cm^2 ^{40}Ca target which was backed by a 42 μm/cm^2 $^{\text{nat}}$C foil in order to reset the charge state of the recoiling nucleus. The channel of interest was ^{40}Ca(^{36}Ar,2n)^{74}Sr.

RITU (Section 3.3.1) was used to separate recoils from beam-like products. Recoils were implanted into the finely segmented, 500-μm thick, β-tagging DSSD (Section 4.1.2), providing energy, E. The GREAT MWPC (Section 3.4.3.1) was used to extract ΔE and ToF information. The phoswich (Section 4.1.1) abutted the DSSD for β-particle identification. The UoYtube (Section 4.1.3) target position veto-box was used to suppress unwanted reaction channels. JUROGAM II (Section 3.2.2.2) was used for the detection of γ rays.

5.2 Analysis

To recapitulate, the recoil-beta tagging technique is performed as follows:

- Identify recoils and coincident γ rays.
- Identify candidate decay events.
- Correlate candidate decay events and associated recoils by looking back through a time window Δt from the decay candidate.

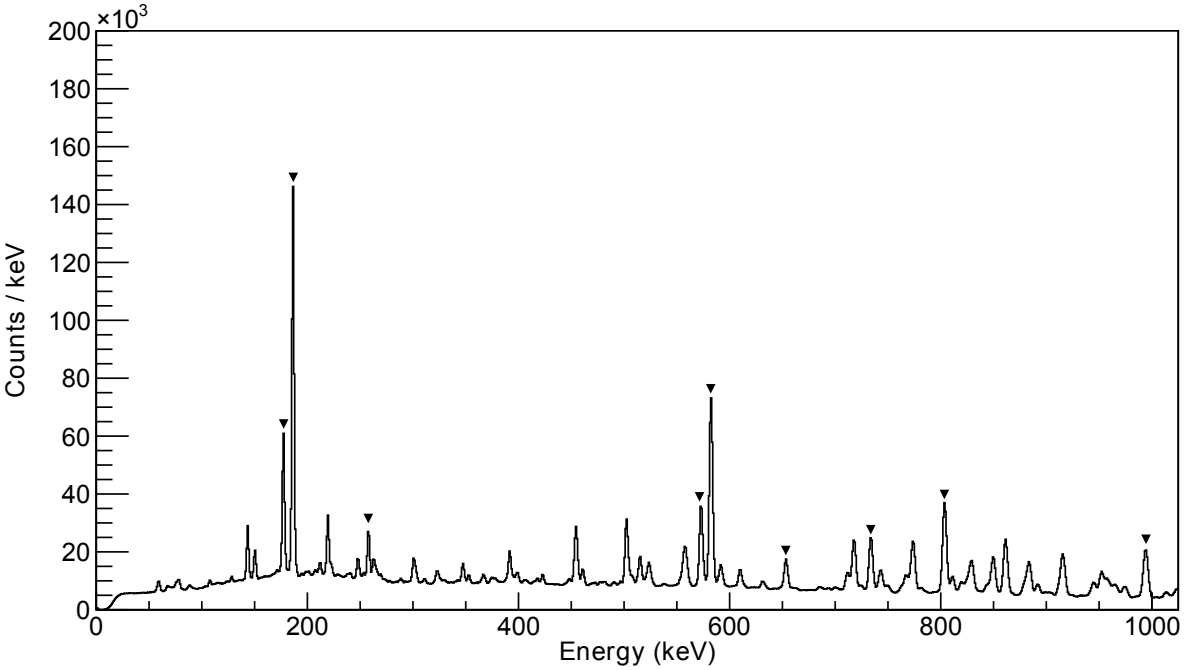

FIGURE 5.1: In-beam JUROGAM II calibration peaks indicated by triangles. All of these γ-ray transitions originate from the primary fusion-evaporation contaminant, ^{73}Br.

- Through high-energy decay requirements, short Δt requirements and charged-particle vetoes at the target position, characteristically identify the decay of interest and its correlated recoil and γ rays.

This section will describe how these steps were carried out. This will be preceded by a description of the calibrations which are required before analysis can take place.

5.2.1 Calibrations

Initial energy calibrations of JUROGAM II were carried out using a ^{152}Eu, ^{133}Ba source placed at the target position. Once an approximate calibration was available with a Doppler correction, JUROGAM II was recalibrated using the in-beam γ-ray energy peaks from ^{73}Br indicated in Fig. 5.1. This method effectively eliminates any uncertainty in the Doppler correction, particularly with respect to the target position. A ^{152}Eu, ^{133}Ba source was used for the purposes of efficiency calibration, as seen in Fig. 5.2. The peak JUROGAM II efficiency was approximately 7% whilst at the energies of interest in the present work, the efficiency is closer to 5%.

The x-side DSSD was calibrated using a triple-α source (^{239}Pu, ^{241}Am and ^{244}Cm) and the y-side using a ^{133}Ba conversion-electron source. This allowed the x-side to be calibrated for energies up to 10 MeV for the purposes of recoil selection and the y-side up to 1 MeV for β-particle selection. Thresholds for both x- and y-sides were set using the ^{133}Ba source to be less than 100 keV to allow for pixel identification for low energy β events in the DSSD.

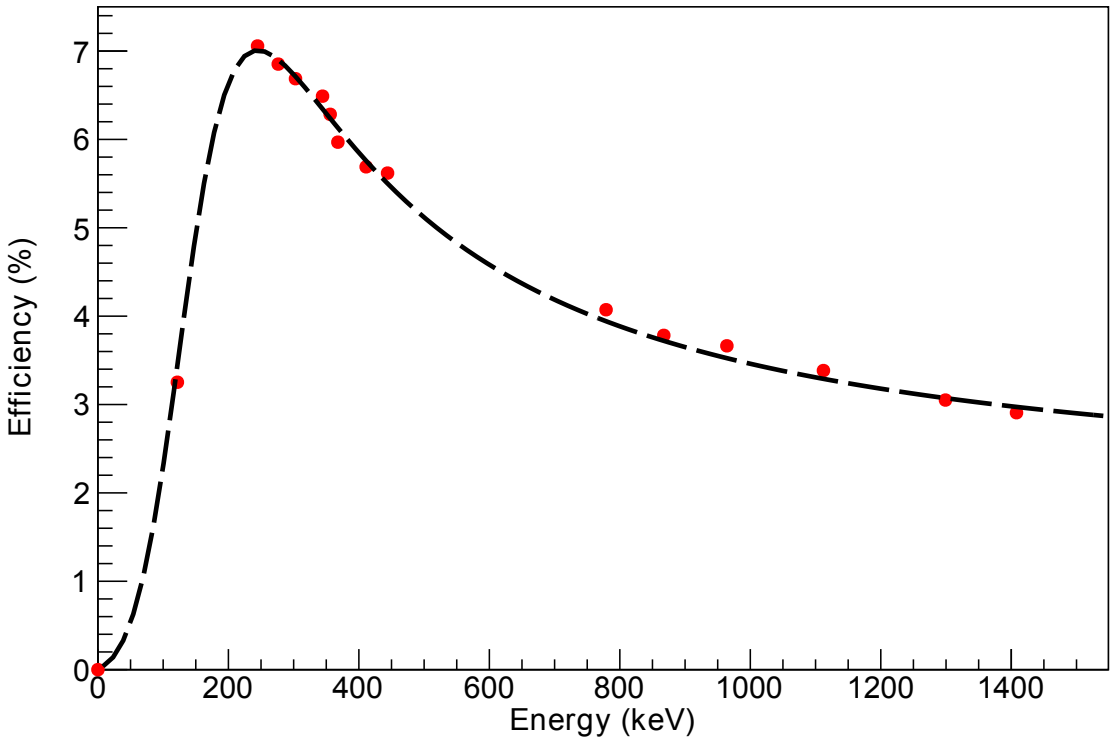

FIGURE 5.2: JUROGAM II efficiency against γ-ray energy for the present work, with the UoYtube and new target chamber in position. The peak efficiency is about 7%, approximately 50% of that generally quoted for JUROGAM II. In the energy range of interest (400 - 600 keV), the measured efficiency is about 5%.

The different calibrations used for the two sides of the DSSD meant that, for low energy events, the x-strip calibrations were often poor. This can be seen in Fig. 5.3, where no distinct $x \sim y$ locus is visible, as would be expected if both sides were well calibrated, although a number of structures are apparent, resulting from the contributions of individual x strips. To correct for this effect, individual x strips were recalibrated for low energies with respect to the (presumed to be) well calibrated y-strips, in order that $E_x = E_y$, as shown in Fig. 5.4. These new energy calibrations are considered valid for all low-energy (< 2 MeV) events.

The UoYtube was not energy calibrated, however the individual detector elements were time aligned relative to one another by the addition of time offsets. All calibrations were monitored throughout and no drift was noticed over the course of the experiment. Three individual JUROGAM II clover segments were not functional, along with two Phase I/GASP type detectors in the array. Eleven DSSD x-strips and four y-strips were not functional. Ten UoYtube detector elements were not functional.

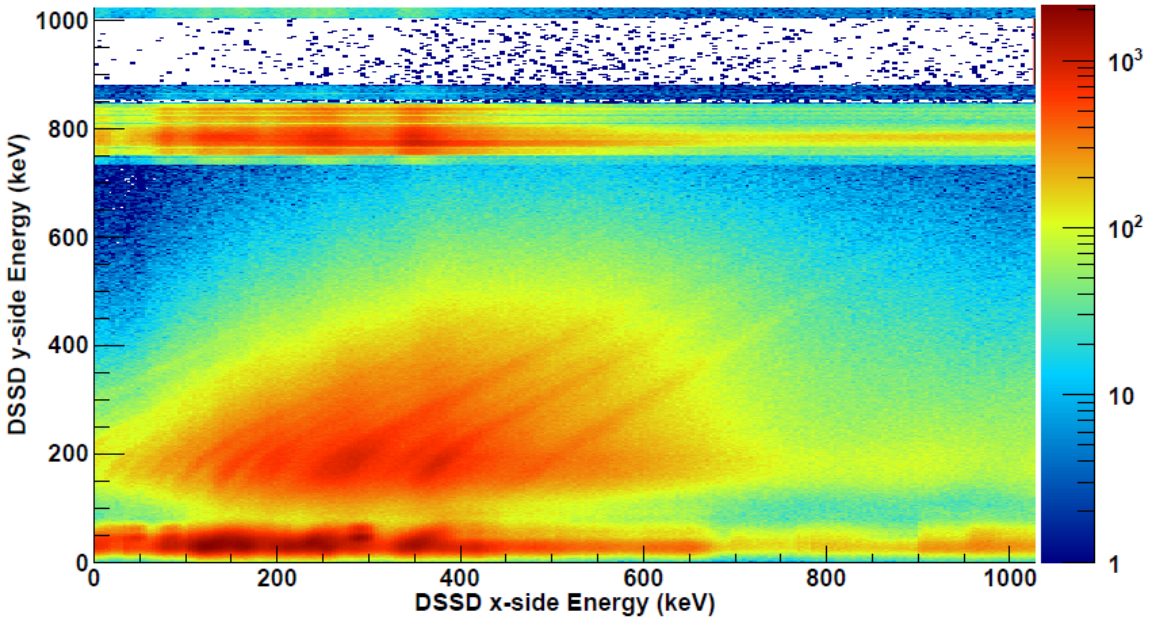

FIGURE 5.3: Low energy DSSD x-strip energy vs y-strip energy, resulting from β-particle detections. Due to poor low-energy calibration in the x strips a wide β-particle energy gate would have to be used, significantly inhibiting selectivity.

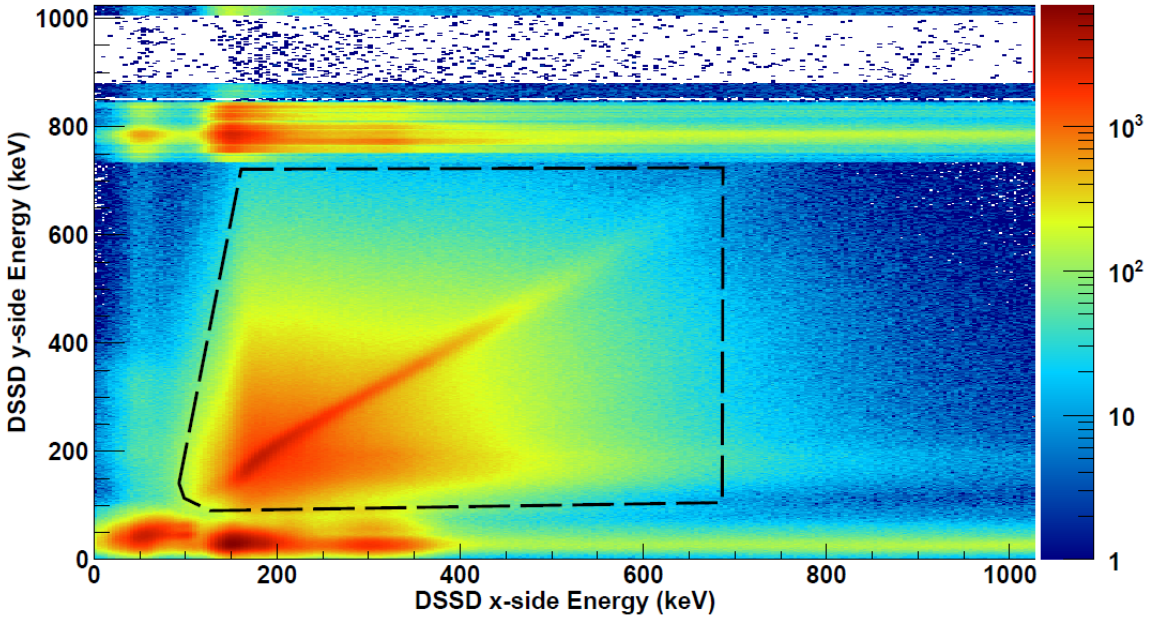

FIGURE 5.4: DSSD x-strip vs y-strip energy with the x-strip energies recalibrated such that $E_x = E_y$, in order to allow the x-strips to be used to select low energy events. With the recalibrated x-side, one can now gate more tightly on the locus at $E_x = E_y$, with a possible initial gate indicated by the dashed line.

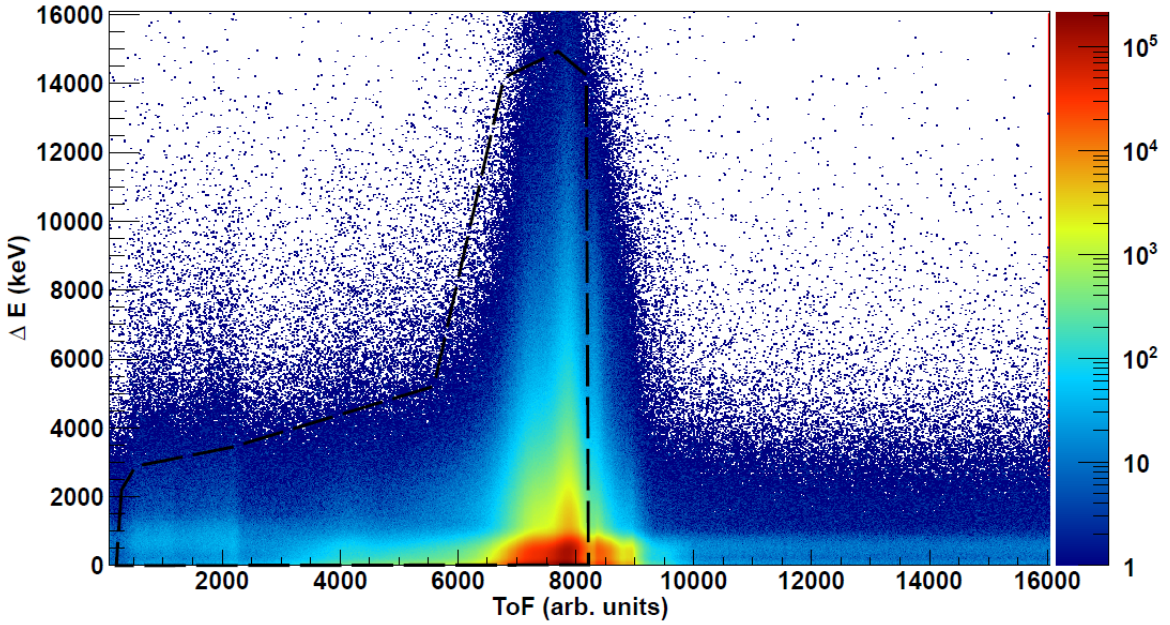

FIGURE 5.5: Energy loss in the MWPC vs ToF between MWPC and DSSD. The dashed line indicates the 2D gate used to validate a recoil. The locus with larger ToF values originates from scattered beam-like particles.

5.2.2 Event selection

Recoils were selected on the basis of DSSD implantation energy, E, measured in the x-strips, energy loss in the MWPC ΔE and the time-of-flight, ToF, between the MWPC and DSSD. The 2D gates for ΔE vs ToF and E vs ToF are shown in Fig. 5.5 and Fig. 5.6 respectively. Coincident γ-ray events were selected on the basis of the time of detection in the Ge detector, t_{Ge}, relative to the implantation time and the ToF, as shown in Fig. 5.7. The consequence of the recoil gating on the JUROGAM II spectrum is shown in Fig. 5.8.

Coincident UoYtube detections were selected based on their energy and time relative to implantation, as shown in Fig. 5.9. The effect of the UoYtube charged particle veto is shown in Fig. 5.10. Using γ-ray peaks associated with the ^{40}Ca(^{36}Ar,3p)^{73}Br channel as an indicator, the UoYtube detection efficiency for a single proton was calculated to be 66% with a $3p$ veto efficiency of 96%.[1] The effect of this veto efficiency, compared to the previous single-proton efficiency of 62% and the potential maximum single-proton efficiency of 75% is shown in Table 5.1.

Events which passed the recoil gates were stored in the GRAIN TAGGER class. Any event which failed to pass the recoil gates and had no associated MWPC signal was considered as a candidate β-decay event. The event was required to in the same pixel within 200 ms of an

[1]When the ten missing UoYtube detector elements are considered this corresponds to a potential, total UoYtube detection efficiency of ∼75% for a single proton.

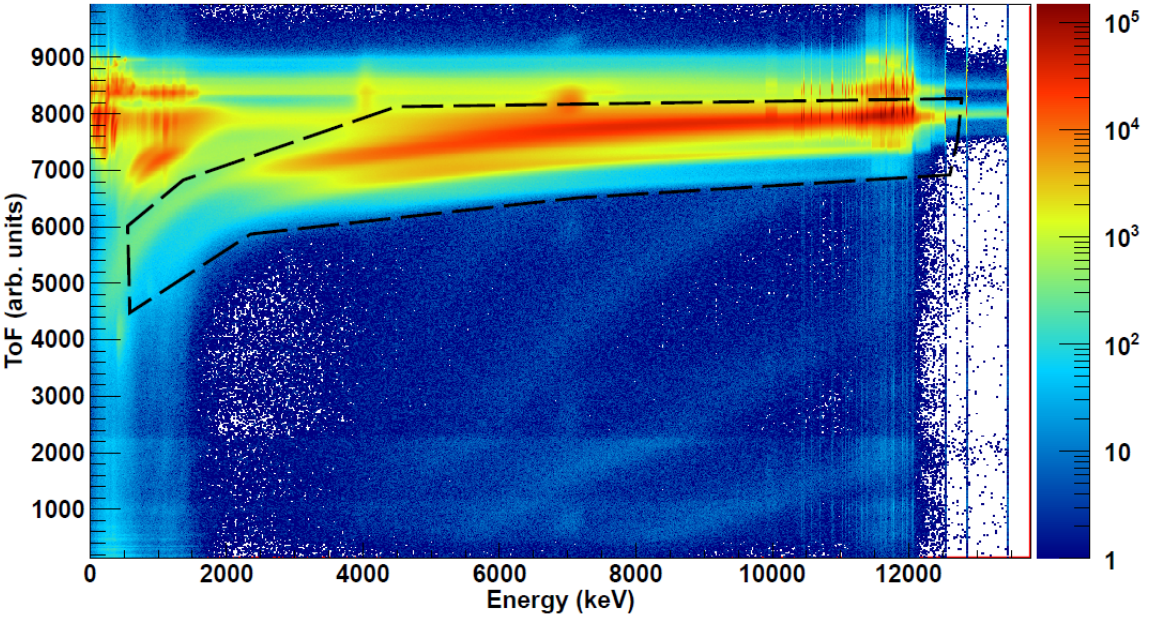

FIGURE 5.6: Implantation energy in the DSSD vs ToF between MWPC and DSSD. The dashed line indicates the 2D gate used to validate a recoil.

Nuclide	Channel	Norm. events	Accepted events (UoYtube efficiency)		
			62%	66%	75%
^{74}Sr	2n	1	1	1	1
^{74}Rb	pn	1370	521	466	343
^{74}Kr	2p	2808	405	325	175
^{73}Kr	2p1n	8484	1225	981	530
^{73}Br	3p	32310	1773	1270	505
^{72}Se	4p	4448	93	59	17

TABLE 5.1: The UoYtube veto suppression for the channels relevant to the present work. UoYtube single-proton detection efficiencies of 62%, 66% and 75% are shown, corresponding respectively to the previous UoYtube design, the efficiency available in the present work, and the maximum efficiency possible with the present design. Numbers of events are normalised to ^{74}Sr and were extracted for the beam kinematics of the present work using the PACE4 code [86].

implantation. Here, the pixel is defined by the x- and y-strips with the highest energy for a given event.

Beta-decay events were required to pass a x- and y-energy DSSD around the locus, as shown in Fig. 5.4, and had to have a significant fast phoswich component as shown by the gate in Fig. 5.11. The total phoswich energy as determined by the algorithm described in Section 4.1.1 could then be used as a lower energy threshold to complete the RBT.[2]

[2]The pulse-shape algorithm had to be used as the PMT signals were too fast for the moving window deconvolution algorithm in the digital electronics to give a meaningful result.

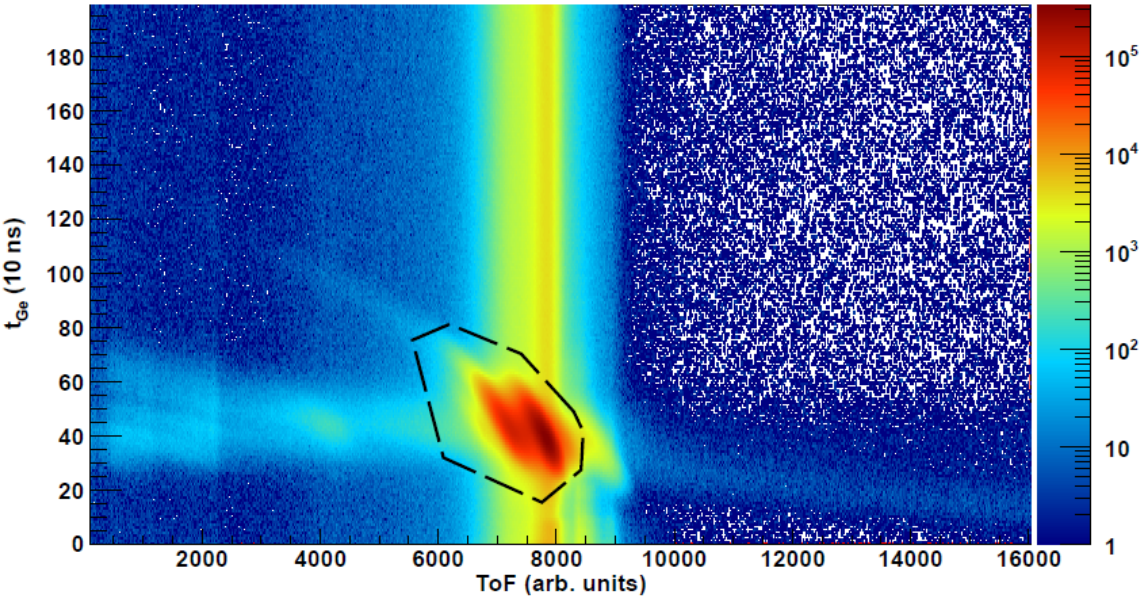

FIGURE 5.7: Ge detection time vs ToF between MWPC and DSSD. Ge detection time is relative to the implantation time in the DSSD. The dashed line indicates the 2D gate used to determine whether a Ge event is beam-prompt.

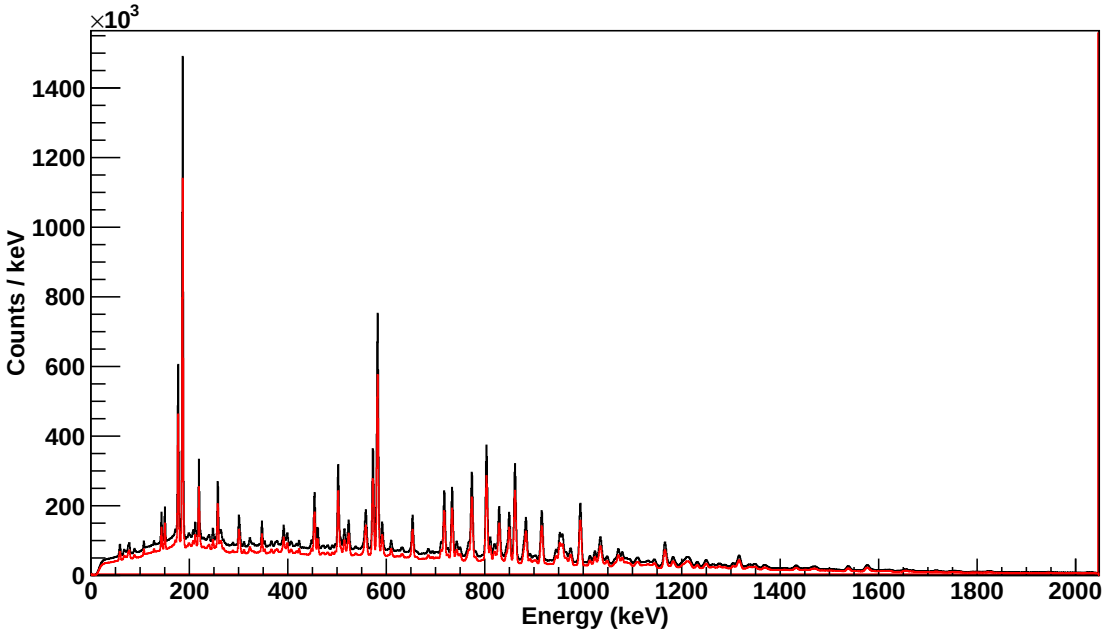

FIGURE 5.8: JUROGAM II spectra, raw (black) and recoil gated (red) on the MWPC and DSSD.

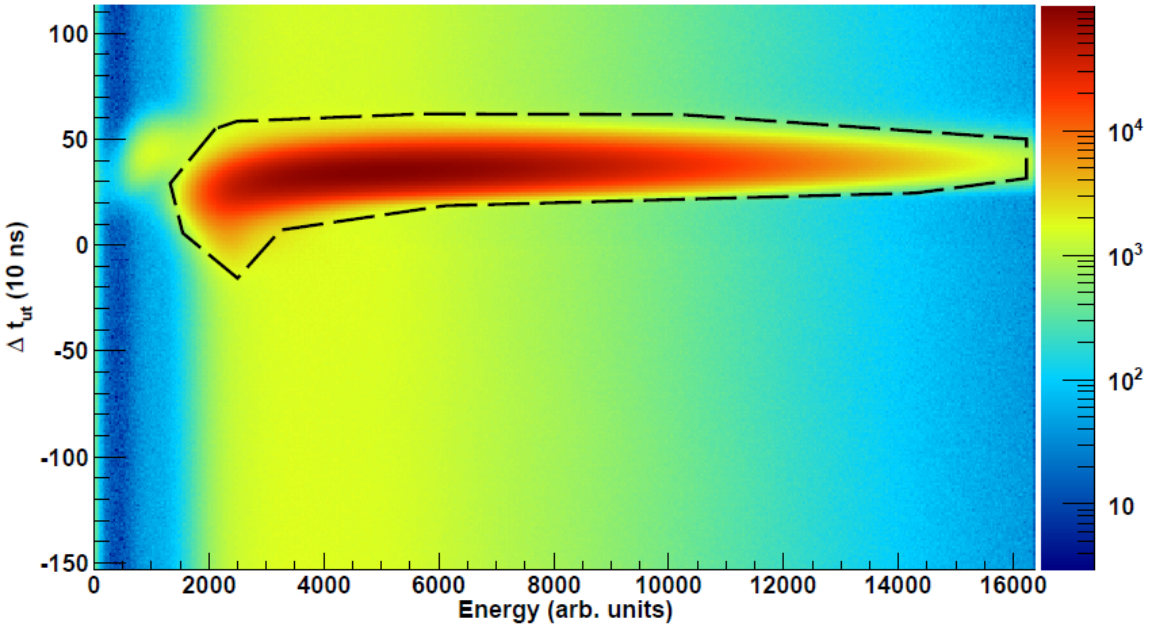

FIGURE 5.9: UoYtube energy vs time, Δt_{ut}. Δt_{ut} is the time difference between the UoYtube detection and the DSSD implantation. The dashed line indicates the 2D gate for the purposes of selection fusion-evaporation particles. The small locus lower in energy is likely due to some punch-through or incomplete charge collection and is a feature in all UoYtube channels.

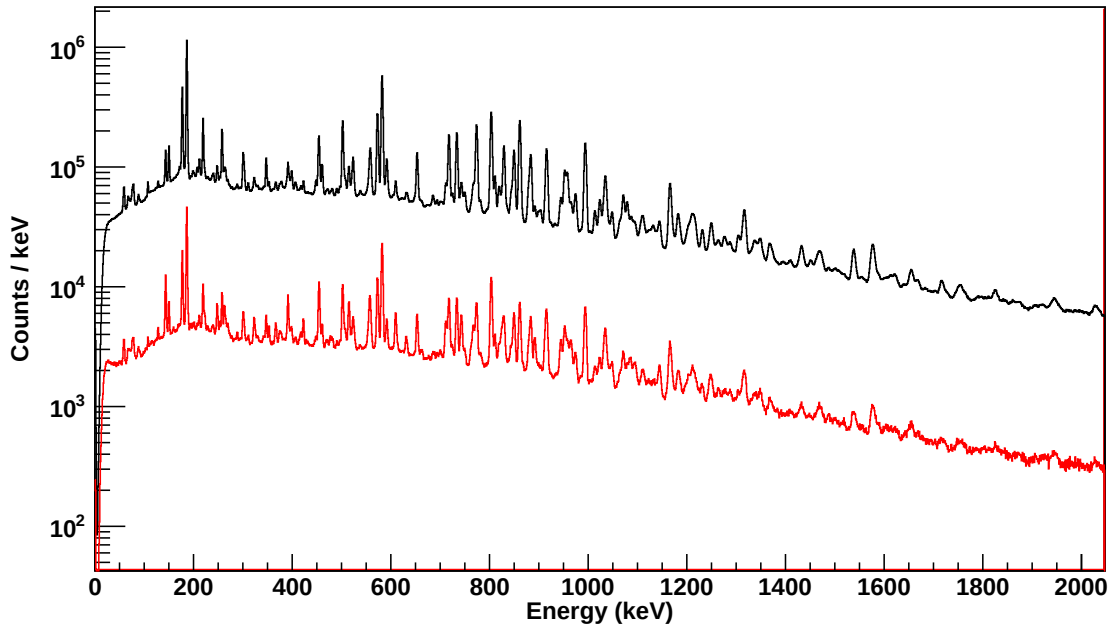

FIGURE 5.10: JUROGAM II spectra with (red) and without (black) veto. A complete charged particle veto is used here with the 2D gate shown in Fig. 5.9. These spectra give a UoYtube single proton detection efficiency of 66%.

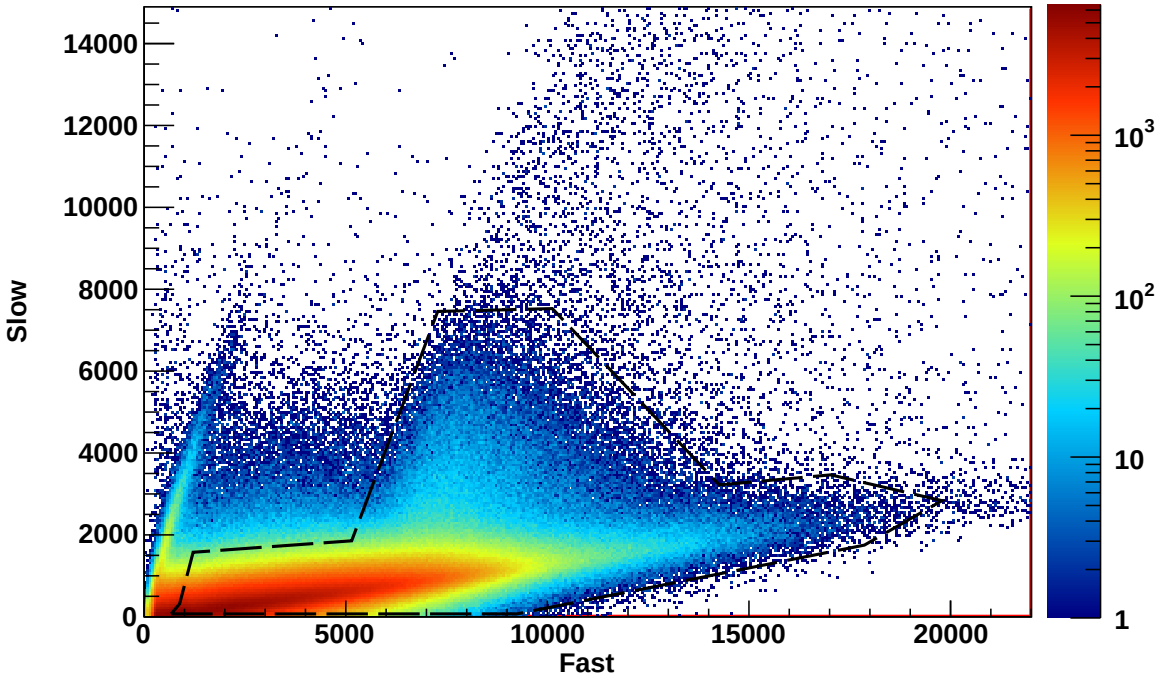

FIGURE 5.11: Phoswich fast signal vs slow signal. The standard β gate is shown, requiring that all candidate β particles have a large fast component.

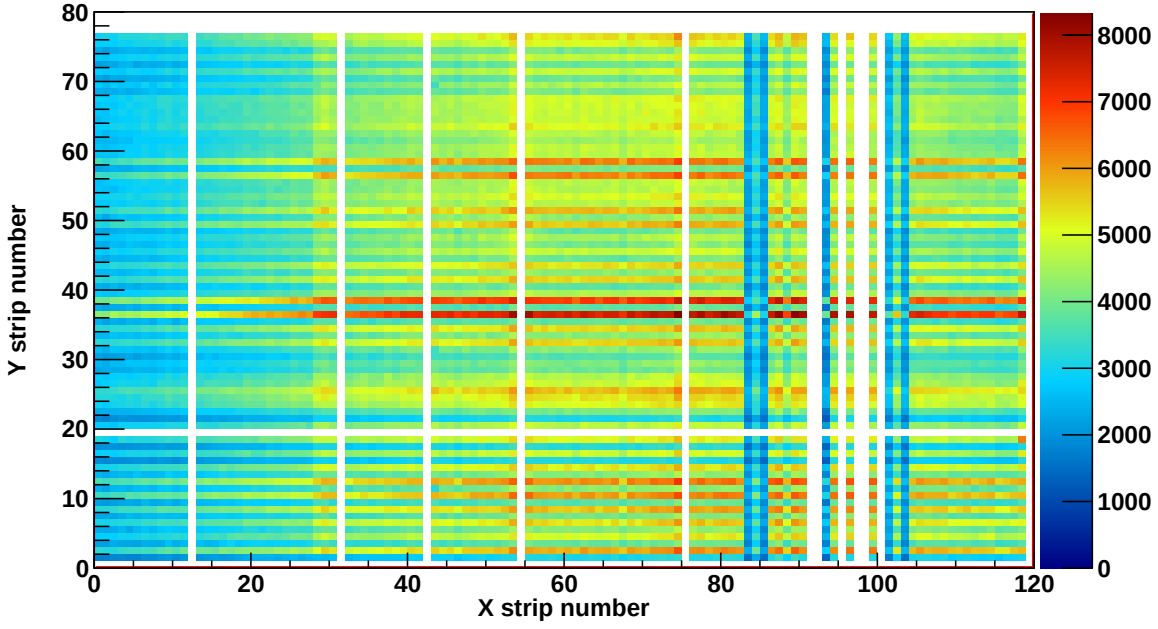

FIGURE 5.12: Recoil map of the DSSD. The left-hand side of the DSSD is lower counting than the right-hand side, making it a more suitable region to search for low cross-section channels.

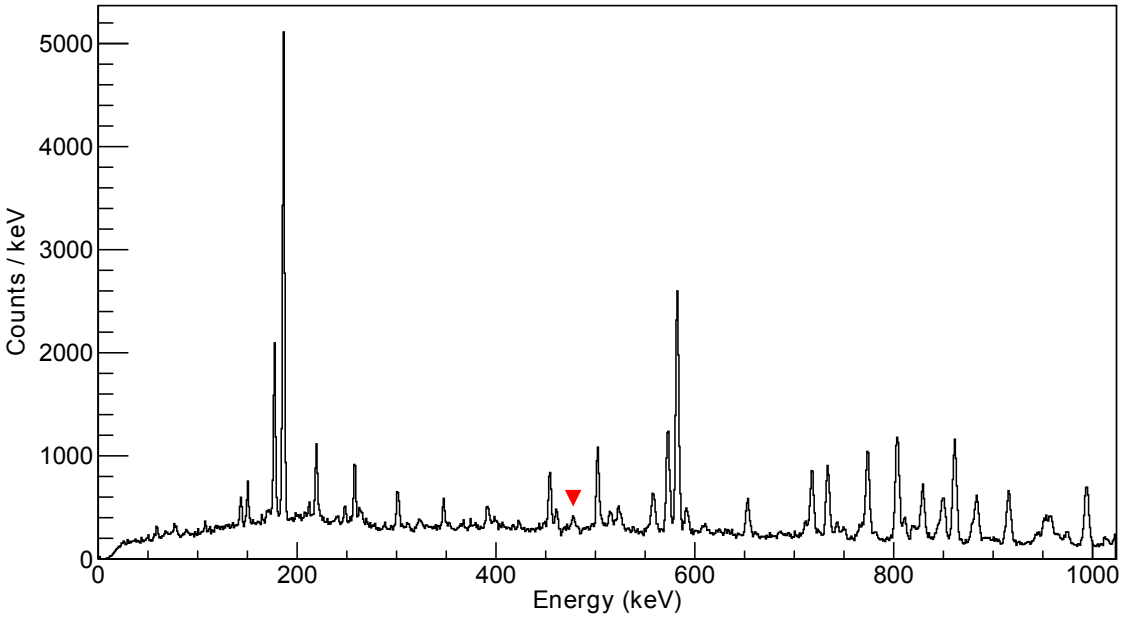

FIGURE 5.13: Gamma-ray spectrum arising from a decay candidate within 200 ms of implantation, and with a phoswich signal consistent with a charged particle interacting with the fast-plastic element. The $2^+ \rightarrow 0^+$ transition in ^{74}Rb is now becoming visible above background, as indicated by the red triangle. The spectrum remains dominated by ^{73}Br.

The RBT technique is very sensitive to DSSD pixel rate (see Section 4.2.3). The DSSD map is shown in Fig. 5.12. One section of the DSSD ($x \lesssim 60$ and $y \lesssim 40$) counts at a lower rate, making this region of the DSSD most sensitive for low cross-section RBT.

5.2.3 ^{74}Sr

The spectra produced during the ^{74}Sr tagging process are shown on a step-by-step basis in Appendix B

Thus far in the analysis, β-tagging has required a fast (< 200 ms), spatially-correlated detection, with a phoswich signal consistent with a charged particle penetrating the fast plastic component. These loose tagging conditions result in the spectrum shown in Fig. 5.13. One can see that the suppression is not yet sufficient to eliminate the primary contaminant ^{73}Br although the conditions are sufficiently stringent to make a peak consistent with the $2^+ \rightarrow 0^+$ transition in ^{74}Rb visible above the background, as indicated by the red triangle.

A more selective tag can be achieved by requiring a larger signal in the phoswich. Fig. 5.14 demonstrates the effect of increasing the demanded phoswich energy whilst maintaining all other tagging requirements. These phoswich signals still comply with the 2D gate shown in Fig. 5.11. Fig. 5.14 (a), (b) and (c) have a requirement for a phoswich signal greater than 2500 ($\sim$ 1.8 MeV), 5000 ($\sim$ 3.7 MeV) and 7500 ($\sim$ 5.5 MeV) units respectively. The transitions in ^{74}Rb become more significant as the phoswich energy requirement increases,

TABLE 5.2: Experimentally derived intensities for transitions in ^{74}Rb and ^{74}Sr. Intensities were calculated on the basis of the JUROGAM II efficiency (see Fig. 5.2). Errors were calculated using the method outlined by Feldman and Cousins in Ref. [101].

Transition	Energy (keV)	Counts	Efficiency (%)	Intensity
$2_1^+ \rightarrow 0_1^+$	471(2)	$6\pm^{3.0}_{2.4}$	5.4	$111\pm^{56}_{45}$
$4_1^+ \rightarrow 2_1^+$	572(2)	$4\pm^{2.4}_{1.9}$	4.8	$83\pm^{51}_{40}$

although this comes at the expense of statistics. The ^{73}Br and ^{74}Kr contaminant lines are not entirely suppressed, even with a β-energy threshold of approximately 5.5 MeV.

Knowledge of the β-decay liftime of the nuclide of interest allows for a more precise β-decay tag to be made. A complementary experiment to the present work was performed at the Radioactive Ion Beam Factory (RIBF) in RIKEN, Japan [98] in order to extract a value for the β-decay lifetime of ^{74}Sr. ^{74}Sr was produced through the fragmentation of ^{124}Xe beam on a beryllium target with nuclides separated using BigRIPS [99]. Nuclei were implanted into the wide-range active silicon strip stopper array for β and ion detection (WAS3ABI) [100] and their subsequent decays detected, allowing for the extraction of lifetimes. A half-life for ^{74}Sr, $t_{1/2} = 30.7(30)$ ms, was extracted in this manner. The lifetime measurement from the experiment performed at RIBF allows for a decay time limit of approximately three half-lives to be placed on the β-tagging conditions.

Using the information provided above, selected steps in the tagging technique used are laid out in Fig. 5.15. Fig. 5.15 (a) has the loose tagging requirements described previously, namely: a decay time of less than 200 ms and a phoswich signal consistent with a charged particle interacting with the fast plastic component. Fig. 5.15 (b) has an additional requirement that a total phoswich signal larger than 6800 units (approximately 5 MeV) was detected. As seen previously in Fig. 5.14, this has the effect of making ^{74}Rb transitions dominate the spectrum. Fig. 5.15 (c) additionally has a UoYtube veto requirement added, which signficantly suppresses all charged-particle channels. Two transitions on the lower energy shoulders of the known ^{74}Rb $2^+ \rightarrow 0^+$ and $4^+ \rightarrow 2^+$ begin to become apparent with this requirement. As previously noted, the lower counting-rate regions of the DSSD have been found to be more sensitive to low cross-section channels. Fig. 5.15 (d) has a final requirement that the implantation occurred in this low counting region. The two previously observed transitions now dominate the spectrum. Before a definitive assignment, a comparison between the spectra corresponding to a UoYtube veto and a one charged-particle requirement is made. This can be seen in Figs. 5.15 (d) and (e). It is clear that the two observed transitions do not appear in the one charged-particle spectrum. As a result, these transitions at 471(2) keV and 572(2) keV are assigned through mirror arguments to the $2^+ \rightarrow 0^+$ and $4^+ \rightarrow 2^+$ transitions in ^{74}Sr, respectively. The relative intensities of these transitions, normalised for JUROGAM II efficiency, are shown in Table 5.2.

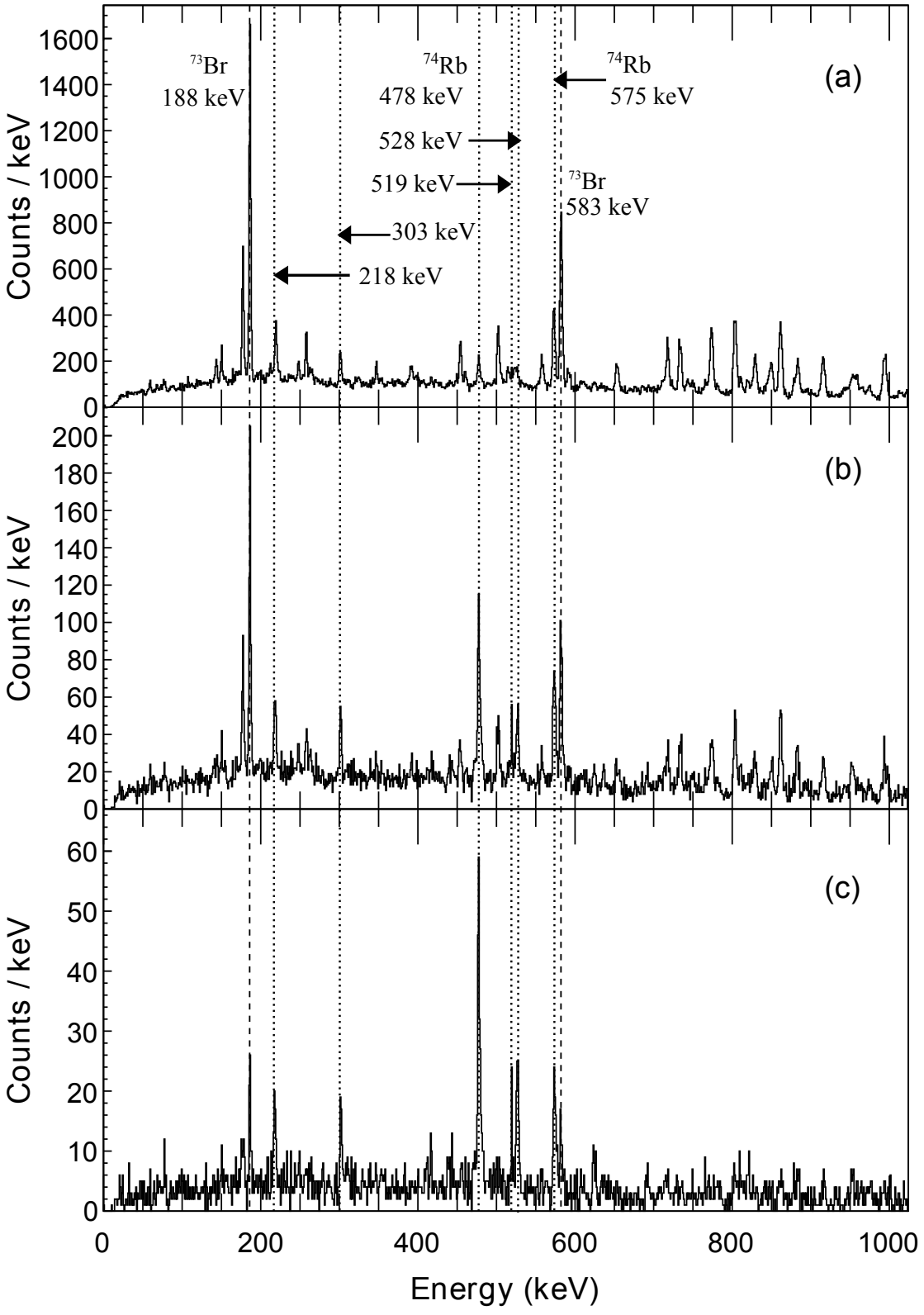

FIGURE 5.14: Gamma-ray spectra with a phoswich energy requirement of (a) 1.8 MeV, (b) 3.7 MeV and (c) 5.5 MeV. ^{74}Rb transitions are indicated by dotted lines, strong ^{73}Br contaminant lines are indicated by dashed lines. The lines corresponding to transitions in ^{74}Rb can be seen to become more significant with increasing phoswich energy, although statistics are lost.

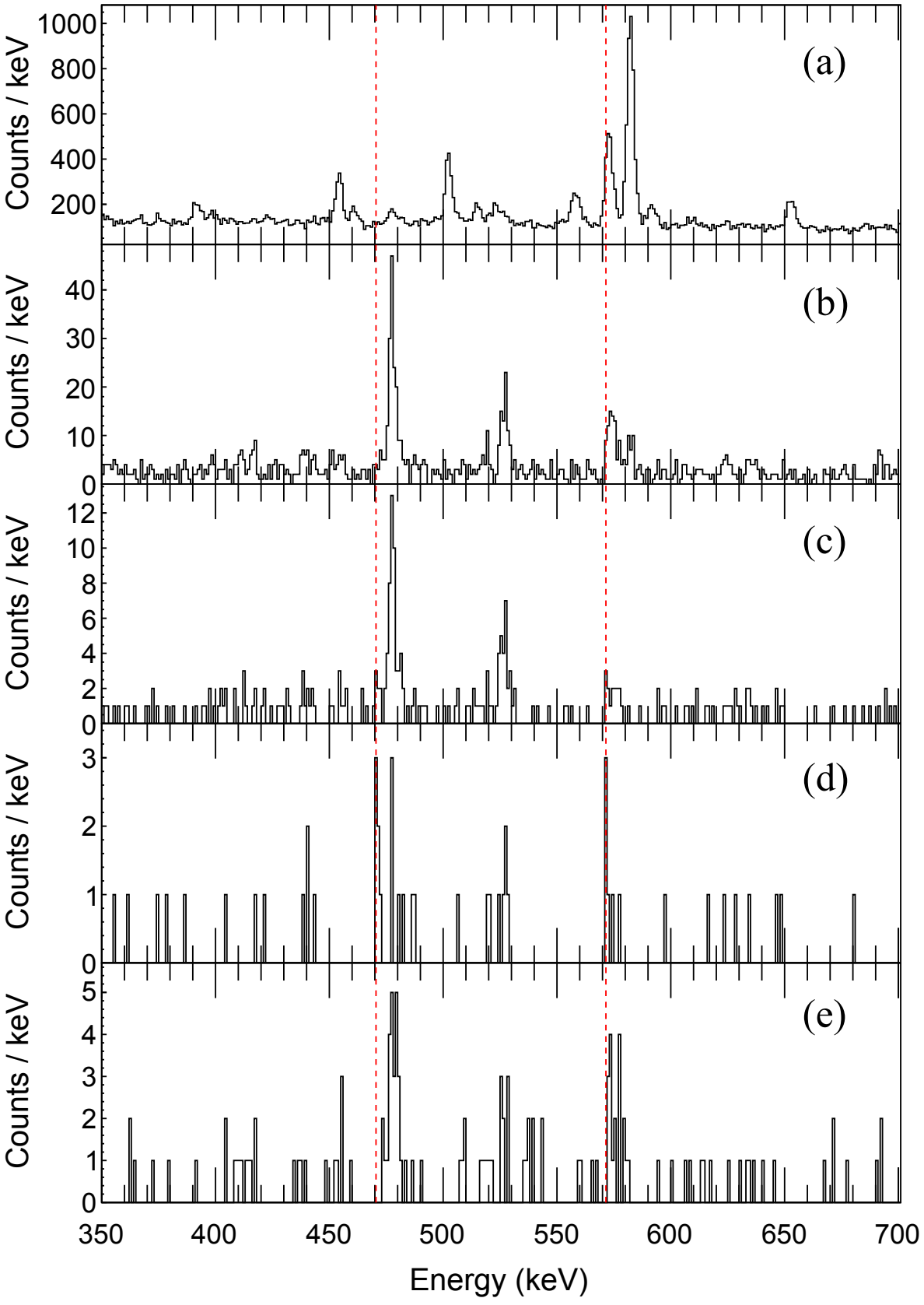

FIGURE 5.15: The RBT process used for ^{74}Sr: (a) Loose tagging requirements. Decay time less than 300 ms and a phoswich signal consistent with a charged-particle interacting with the fast plastic component. (b) Requires additionally that the phoswich signal is greater than 6800 units (about 5 MeV). (c) As (b) but additionally a charged-particle veto is applied. (d) As (c) but also requires that the detection occurred in the low counting region of the DSSD. (e) As (d), except instead requires exactly one charged particle detected in the UoYtube. The dashed lines indicate the transitions assigned to ^{74}Sr.

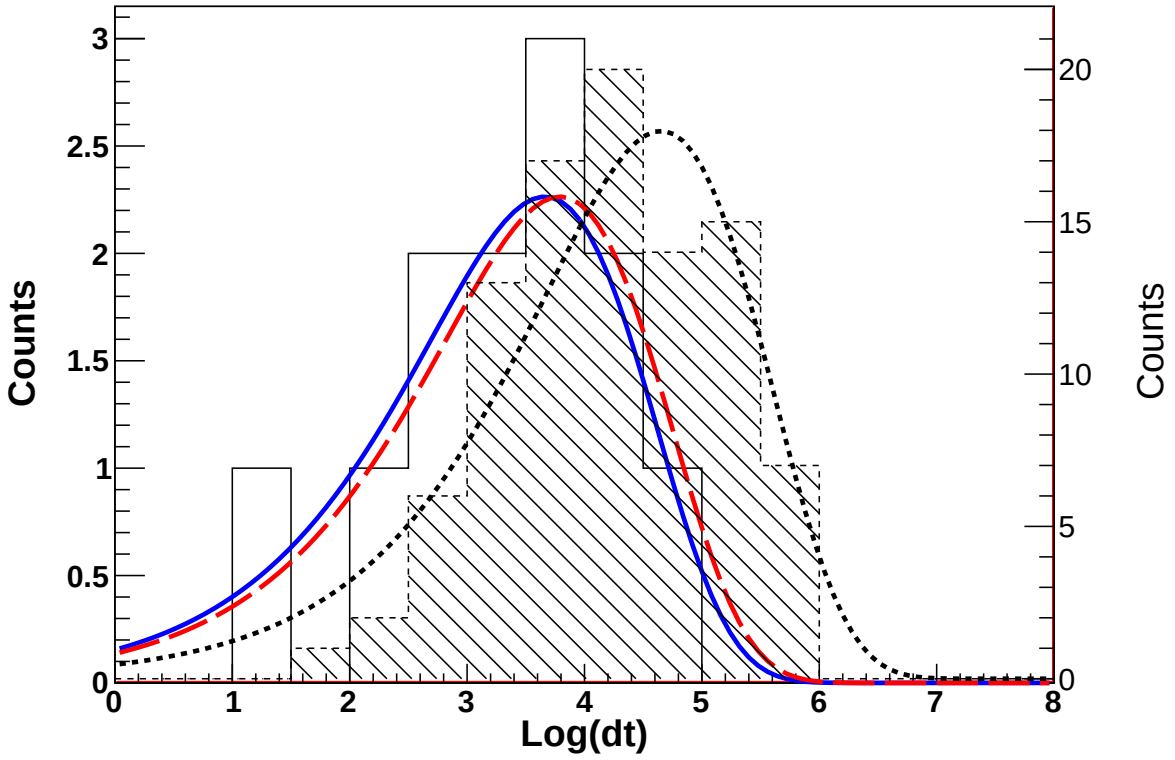

FIGURE 5.16: Natural log(Δt) of decay data gated on the 471-keV transition assigned to ^{74}Sr (unfilled). The solid (blue) line is fitted to the data and corresponds to a half-life of 27(8) ms, while the dashed (red) line corresponds to a half-life of 31(3) ms, as extracted from the complementary RIBF experiment. The filled data is gated on the 478-keV transition in ^{74}Rb and serves as a method comparison, with an extracted half-lives of 73(9) ms, which lies within error of the accepted value.

As discussed in Section 2.3.1, one can extract the lifetime of a nuclide in the case of low statistics using the Schmidt method in which the data is binned evenly with the logarithm of the decay time. In the present work, the 471-keV γ ray was gated on and the lifetime extracted in this manner. The 572-keV γ ray was not used due to the proximity of the known ^{74}Rb transition, which was liable to skew the data and made fitting impractical. The data are shown in Fig. 5.16 (unfilled) and are gated on the 471-keV transition, with a phoswich energy threshold of $>$ 4000 units (approximately 3.2 MeV) and using the entire DSSD in an effort to maximise the available statistics. The data were fitted with the solid (blue) line, resulting in a half-life of 27(8) ms. The dashed (red) line corresponds to the fit expected for a half-life of 31(3) ms, as extracted from the complementary RIBF experiment. The two half-lives lie well within error of one another. As a method comparison, the filled data in Fig. 5.16 are gated on the 478-keV transition in ^{74}Rb. The extracted half-life in this case is 73(9) ms, which lies within error of the accepted value. As mentioned in Section 2.3.1, in Ref. [55] a metric is laid out by which the validity of a decay time distribution can be assessed. The present data lie within the 90% confidence limit of belonging to the decay of a single radioactive species.

5.3 β-delayed protons

In this section, the analysis used to attempt to identify β-delayed proton decays will be outlined. Firstly however, a comment should be made on the nature of the recoil implantation in the present work. Where in higher energy studies, high-Z recoils might well be implanted in the middle of a detector,[3] at the energies used in the present work, recoils are implanted at the surface of the DSSD. As a result of this, any decays resulting in the emission of ionising radiation at backwards angles relative to the implantation trajectory will likely not be detected due to passing through only a small volume of active detector. For this reason, one would expect a β-delayed proton spectrum to look something like that depicted in Fig. 5.17. Here, one observes a narrow distribution corresponding to the proton being detected and the β particle being emitted at backwards angles, as well as a distribution of the familiar β-decay form built on top of that, corresponding to both charged particles being detected. There will additionally be a β-decay distribution at low energies corresponding to only the β particle being detected, but this is likely to lie under considerable background and not be readily identifiable. Assuming that the detection probability is related only to the emission angle[4] the number of detections in the proton-only distribution should be the same as that in the proton and β particle distribution. Given the discrete energy of the proton-only distribution and the fact that the β-particle distribution is seen to range across energy values of about 1 MeV, for low statistics it is likely that only the proton-only distribution will be observable, with the β-plus-proton distribution obscured by background events.

β-delayed protons were identified in a similar manner to the β-tagged ^{74}Sr nucleus, with a requirement that a fast decay event occurred within the same pixel as an implantation with again the lowest counting region of the DSSD being used. In the event that the proton was not detected, the β-particle distribution would be entirely obscured by other events, so the search was limited to the situation where the proton was detected with, or without, the coincident β detection. Since the proton would be required to overcome the nucleus's Coulomb barrier, the search was also limited to higher energies, between 1 and 2 MeV, with energy information taken from the x-side of the DSSD, recalibrated for lower energies as described previously in this chapter. Due to the recalibration being imperfect as one moved away from the region in which the y-side was calibrated, events with energies higher than about 2 MeV were considered to be unreliable. Fig. 5.18 shows the β-delayed proton spectrum extracted. Events were required to be in the energy overflow of the y-side DSSD (i.e. $E > 1$ MeV) and in coincidence with a target position γ ray. Due to the low statistics, it proved impossible to accurately identify these γ rays. This was due to the fact that the presumed nuclide, ^{73}Sr, is the mirrror of the primary contaminant, ^{73}Br.

[3] As was the case with the RIBF data described earlier

[4] i.e. Assuming detector thresholds and other effects are negligible

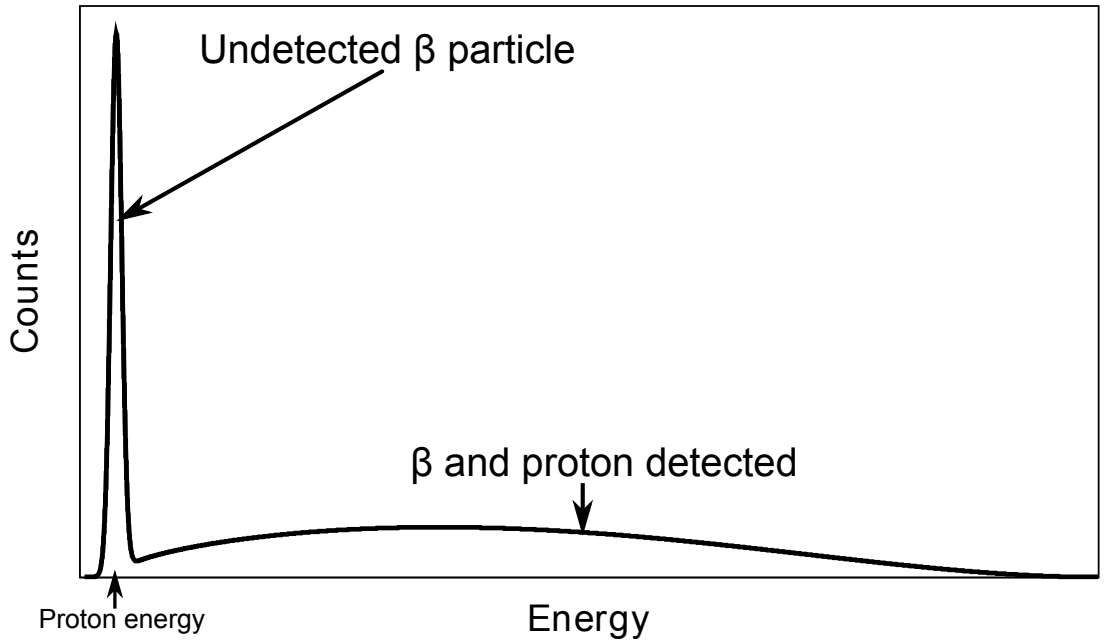

FIGURE 5.17: The form of distribution expected for a β-delayed proton decay occurring near the surface of an implantation detector, not to scale. As indicated, the proton peak corresponds to the non-observation of the β particle and the distribution above it corresponds to both particles being detected. An additional distribution, corresponding to the non-observation of the proton will exist at low energies but is not shown here.

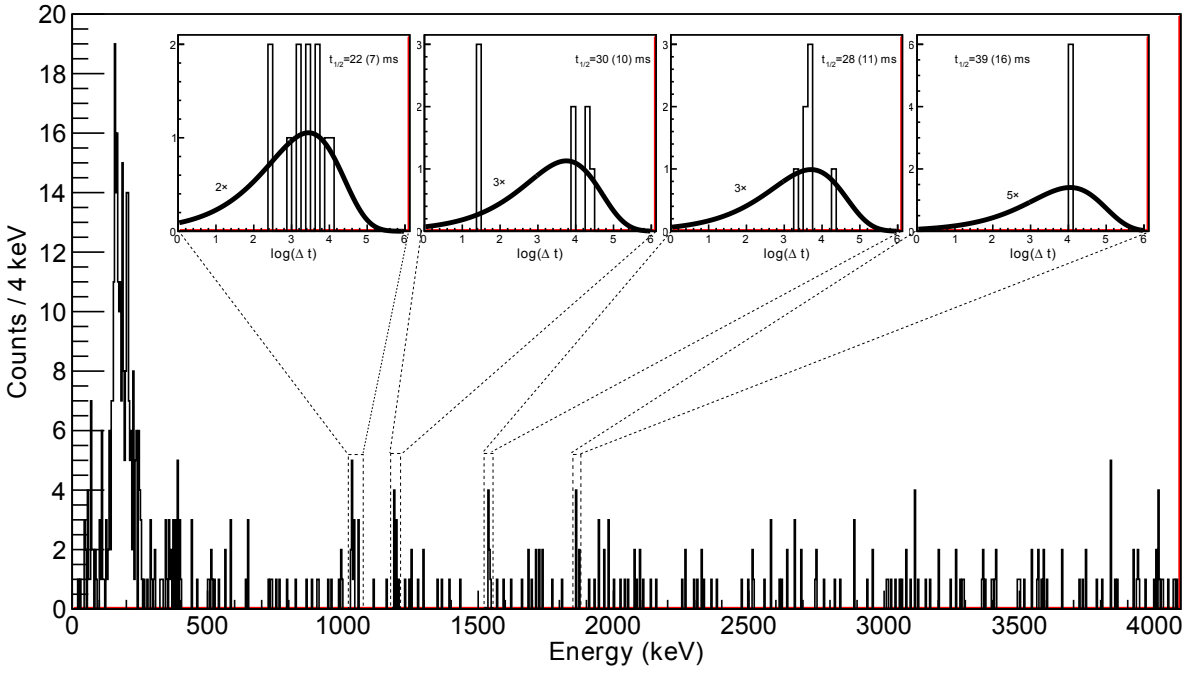

FIGURE 5.18: β-delayed protons, thought to originate from the β decay of ^{73}Sr and the subsequent proton decay of ^{73}Rb. The spectrum shown corresponds to the x-side energy values of the DSSD, recalibrated relative to the y-side as described previously. Events were identified on the basis of being in the DSSD y-side overflow ($E < 1$ MeV), being in the low counting region of the DSSD, occuring within 100 ms of implantation, with a UoYtube veto and being in coincidence with a target position γ ray. Shown in the insets are the lifetimes extracted using the Schmidt log(Δt) method.

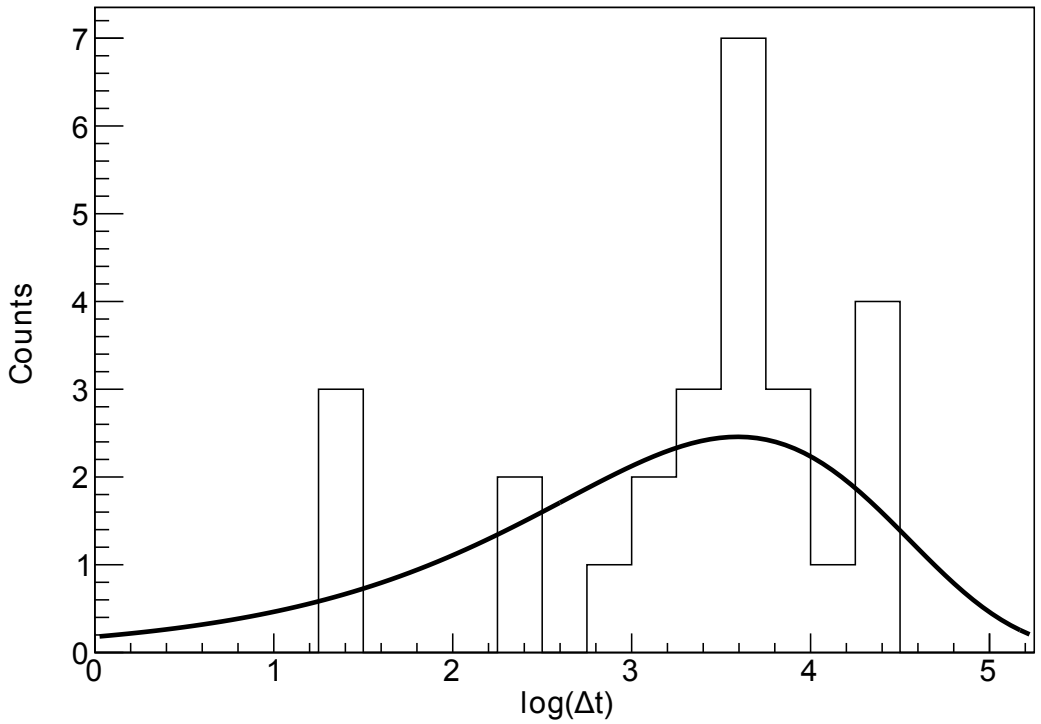

FIGURE 5.19: Lifetime data for β-delayed proton decay of ^{73}Sr, gated on the candidate transitions at 1035 keV, 1187 keV and 1532 keV. The fit corresponds to a half-life of 25(5) ms.

Shown in the insets to Fig. 5.18 are the logarithms of the decay times associated with the four candidate transitions. The three lower energy transitions at 1035 keV, 1187 keV and 1532 keV have consistent lifetimes and distributions. The fourth candidate at 1859 keV has a distribution inconsistent with that expected for a radioactive decay using the Schmidt method outlined in Section 2.3.1 and is consistent with a statistical fluctuation. Note that the fitted distributions are multiplied in order to make them easily visible. The combined lifetime data for the first three candidate proton decays are shown in Fig. 5.19. From the fit to the data, a half-life of 25(5) ms is extracted. These data also lie within the 90% confidence limit of belonging to the decay of a single radioactive species as laid out by Schmidt in Ref. [55].

Chapter 6

Results and interpretation

> In mathematics you don't understand things. You just get used to them.
>
> Johann von Neumann

In this chapter, discussion of the results described in Chapter 5 will be presented. This discussion will, where appropriate, be presented in the context of the theory and motivation outlined in Chapters 1 and 2.

6.1 ^{74}Sr lifetime

The 27(8) ms half-life of ^{74}Sr extracted in the present work is in good agreement with that measured at RIBF, RIKEN [98]. Both values imply that ^{74}Sr is about half as long lived as predicted in Ref. [31]. Given the significant uncertainty on the Q-value of the ^{74}Sr β-decay, it is instructive to consider the Q-value that would correspond to the observed lifetime of the decay. The dependence of the Q_{EC} value on the half-life of the decay is plotted in Fig. 6.1. The observed 30.7(30) ms half-life taken from the RIBF experiment is indicated - due to its superior accuracy - in addition to the dependences for the β-decays of the three calculated minima (see Fig. 6.2).

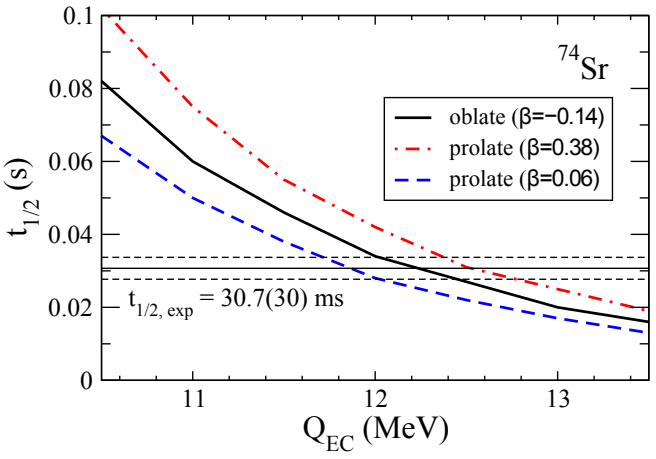

FIGURE 6.1: The dependence of the Q_{EC} value on the β-decay half-life of ^{74}Sr.

The Q-value of 12.2 MeV taken from Fig. 6.1 can then be compared to the Q-value of 11.2 MeV assumed from systematics. This interpretation implies that ^{74}Sr is 1 MeV less bound than

previously supposed, in good agreement with the value calculated by Kaneko *et al.* [23], from CDE data complete with the INC interaction.

It should be noted that the result illustrated in Fig. 6.1 assumes a ground state in ^{74}Sr with an oblate deformation. This is not an uncontroversial result, with considerable evidence pointing to the fact that its mirror, ^{74}Kr, has significant prolate ground-state deformation. Its β deformaqtion parameter is ~ 0.4, which is similar to the second minimum indicated in Fig. 6.2, indicated by the dashed-red line in Fig. 6.1.

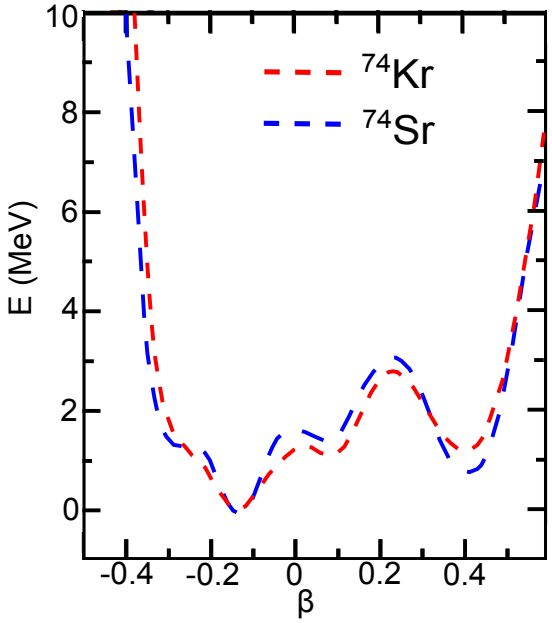

FIGURE 6.2: Potential surfaces for ^{74}Kr and ^{74}Sr extracted from a deformed Skyrme Hartree-Fock + BCS [31].

It can be seen from Fig. 6.1 that, even if the ground-state deformation is highly prolate rather than the assumed oblate, a considerably higher Q_{EC}-value is still required in order to account for the observed half-life. Assuming no changes in the absolute energy of the prolate-deformed minimum at $\beta \sim 0.4$, one would require a Q_{EC}-value 1.4 MeV higher than that assumed from systematics, rather than the 1 MeV required under the assumption of an oblate ground-state.

Given the above considerations, and the S_p and S_{2p} values calculated in Ref. [23] using the JUN45 + INC interaction, it is reasonable to assume that ^{74}Sr is $\gtrsim$1 MeV less bound than extracted from systematics. This introduces the possibility that both the $J^\pi = 2_1^+$ and $J^\pi = 4_1^+$ excited states in the nuclide are two-proton unbound. The consequences of this conclusion will be discussed later in this chapter.

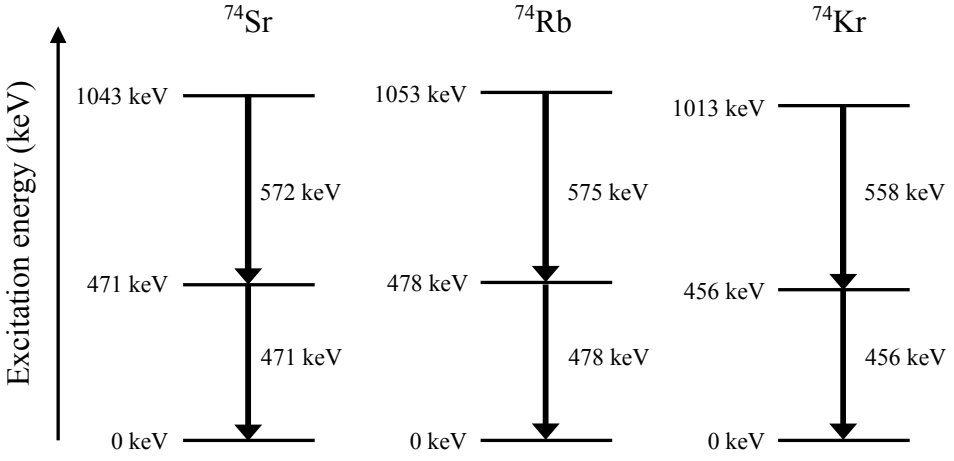

FIGURE 6.3: Isobaric analogue states in the $A = 74$ isobar.

6.2 Energy differences

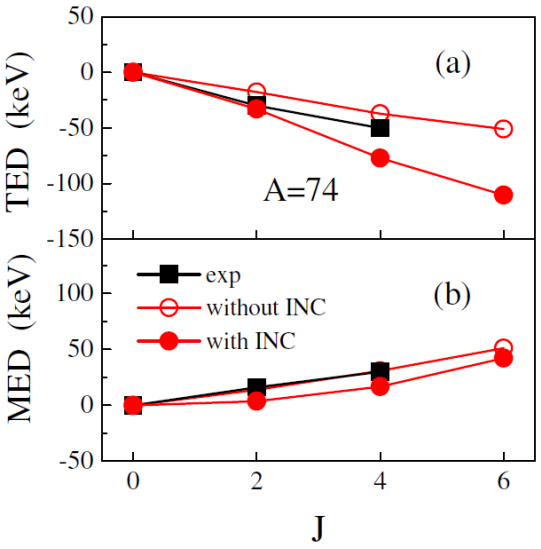

FIGURE 6.4: Observed and calculated TEDs (a) and MEDs (b) for the $A = 74$ isobar.

The level scheme for ^{74}Sr observed in the present work is shown in Fig. 6.3 along with the relevant IAS across the $A = 74$ isobar. The resulting MEDs and TEDs are shown in Fig. 6.4, with the calculated [20] values with and without an INC component. It should again be noted that the MEDs are not sensitive to the INC component, with considerable contribution from single-particle and other structure effects. In particular, as will be discussed later, the shell model is unable to reproduce the collectivity of nuclides in the upper *fpg* shell. The TED however should remain sensitive only to the INC component for the reasons outline in Chapter 1.

For $J = 2$, the experimental TED data is reproduced extremely well by the JUN45 interaction with the inclusion of an additional INC component. This would imply that, as with lower mass regions of the nuclear landscape, an INC component is required in the nuclear interaction. The $J = 4$ case is by no means as clear cut however, with - if anything - the data best reproduced *without* the the INC component.

Whilst the failure to theoretically reproduce the $J = 4$ TED with an INC component might appear to invalidate the conclusion that the INC component is mandated across the nuclear landscape, it is likely that other effects are conspiring to affect the experimental result. As concluded previously, ^{74}Sr may be considerably less bound that was previously assumed and, as a result, it is likely that both the $J = 2$ and $J = 4$ states are, at the very least, two-proton unbound.

6.2.1 The Thomas-Ehrman shift and coupling to the continuum

Two related phenomena which may contribute to an isospin-dependent energy shift in unbound nuclei are coupling to the continuum [102] and the Thomas-Erhman (TE) shift [103, 104].

In the unbound case, the Schrödinger equation has an infinity of solutions, which results in a continuum of states. As one probes unbound or near-unbound nuclei, coupling occurs between this continuum of states and the discrete, bound states. This coupling of states results in an energy shift which is trivially isospin dependent due to the asymmetry of the

drip-lines. The coupling of loosely bound states to the continuum is beyond the prescription of the standard nuclear shell model, which assumes a closed quantum system and limited valence space.

The TE shift results from a shift in the spatial wavefunction due to the state of interest being unbound, which results in a breakdown of the analogue nature of the wavefunctions across the isobar[1]. This effect is again trivially isotensor, due to the asymmetry of the drip-lines about $N = Z$. The TE shift was originally discussed in the context of the energy levels of excited states in the mirror nuclei, ^{13}C and ^{13}N, shown in Fig. 6.5. The asymmetry of the proton and neutron dissociation energies is apparent, which results in the TE shift in the state energies.

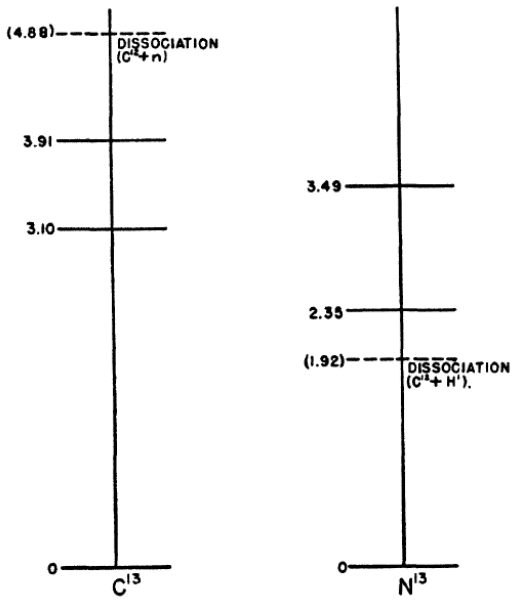

FIGURE 6.5: The level schemes of the mirror nuclei, ^{13}C and ^{13}N. The neutron and proton dissociation energies are indicated. It is the asymmetry of these dissociation energies which introduces an isotensor energy difference. Figure taken from [104].

A systematic study of the TE shift by Comay *et al.* [105] investigated the shift in the ground-state masses of a number of unbound nuclei, with a maximum shift of ~ 1 MeV. The systematics are shown in Fig. 6.6. This is significantly higher than the ~ 100 keV shift typically seen to arise from other Coulomb-related isotensor effects. It should be noted that Wapstra and Audi [106] predict that this shift - observed in relatively low mass data - is considerably larger than should be expected at higher masses. Nonetheless, given that TEDs are sensitive to isotensor effects of the order of ~ 10 keV, it is possible that such an effect would result in the shift seen for the $J = 4$ case.

6.2.2 Shell-model considerations

An important consideration in the $A > 70$, $N \sim Z$ mass region is the ability of the shell model to accurately reproduce the deformation and collectivity of the nuclides. In the shell model, deformation is accounted for by the coupling to so-called deformation-driving orbitals which lie in close proximity to those orbitals occupied by the valence nucleons. Even a very weak coupling to such orbitals is sufficient to introduce significant deformation to the nucleus.

In the JUN45 effective interaction, the model space is limited to the fpg shells, excluding the important $2d_{5/2}$ deformation-driving orbital. As a result such effective interactions are not

[1]There is some inconsistency in the published literature regarding the exact definition of the TE shift. In the present work the TE shift refers only to the specific case of a "boundary condition energy difference" [104] resulting from the Coulomb wavefunction distortion.

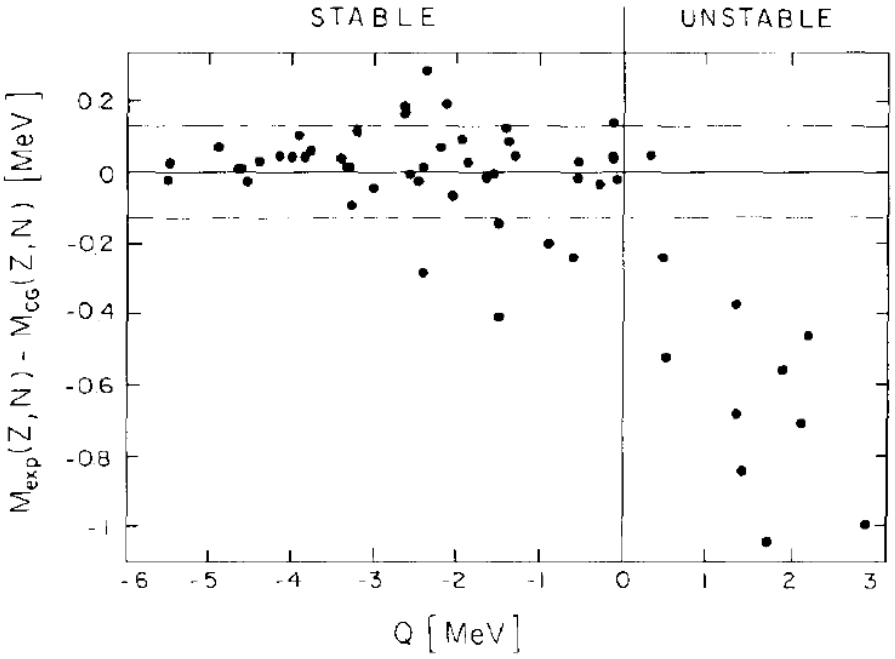

FIGURE 6.6: Systematics of the Thomas-Ehrman shift in ground-state masses [105]. The difference between expected mass and experimental mass is plotted against the Q_p value. It can be seen that the masses begin to deviate as one approaches positive Q-values, with a maximum deviation of ~ 1 MeV.

capable of reproducing the highly collective nature of the nuclei in the $70 < A < 100$ mass region.[2] It is for this reason that MEDs in the *fpg* shell are thought to be a poor measure of the INC, as they are isovector in nature and are therefore sensitive to the deformation of the nuclide. While the analogue description of the states in an isobar holds, this failure to reproduce deformation is not likely to manifest itself in the TED, which is independent of isovector effects.

If the Thomas-Ehrman shift or coupling to the continuum effects in the present work result in a breakdown of the analagous nature of the wavefunctions for the $J = 4$ states, the TED might no longer be truly independent of isovector effects. With the failure of the shell model to accurately replicate the isovector deformation and collective effects, this is a possible explanation of the deviation from the INC requirement seen for the $J = 4$ case.

6.3 β-delayed protons from ^{73}Rb

Candidates for three new β-delayed proton-decays from ^{73}Rb were observed in the present work at 1035 keV, 1187 keV and 1532 keV, with similar energy spacing as seen in the three low-lying states in Fig. 1.15. Due to the technique employed, it was not possible to identify any proton-decay peaks below ~ 1 MeV. As such it is not possible to determine whether the

[2]This is a property of all effective interactions in the region and is not unique to the JUN45.

observed decays originate from the ground state of ^{73}Rb or from excited states. DSSD calibrations above ~ 2 MeV were not reliable, resulting in the failure to reproduce the 3.75 MeV proton decay of the $T = 3/2$ IAS observed by Batchelder *et al.* [29].

It has previously been commented [107] that isomeric "shadowing" of the ground-state - in which reaction mechanisms populate a $9/2^+$ isomeric state which promptly proton decays, rather than the longer lived ground state - may account for the apparent short-lived nature of ^{73}Rb. It would not be expected for such a state to be populated in the β-decay of the ground state of ^{73}Sr, which is presumed from mirror arguments to be of a $1/2^-$ configuration. It is possible that isovector effects may result in an interchange between the low-lying first-excited $5/2^+$ state in the mirror nuclide, ^{73}Br and the $1/2^-$ ground state, however this would still require a first-forbidden Gamow-Teller decay to populate a $9/2^+$ state and is therefore unlikely.

With the aforementioned considerations, it therefore seems likely that the observed proton-decays originate from the low-lying states in ^{73}Rb. The fact that the three candidate transitions have a similar energy distribution to three low-lying excited states in the mirror nucleus, ^{73}Kr, might be taken as an indication that these three states are being populated. Given that the first and second excited states are expected to be of $5/2^-$ and $5/2^+$ configuration, respectively, this might imply that there has indeed been an interchange between the ground- and first-excited states in ^{73}Sr compared to its mirror.

If one considers the proton decay at 1035(50) keV to be originating from the ground state of ^{73}Rb it provides a direct measurement of $S_p \simeq -1.04$ MeV. This compares to calculated single-proton separation energies of -0.59(55) MeV and -0.55(32) MeV calculated by Brown *et al.* [108] with an Audi-Wapstra extrapolation (AWE) and Skyrme-Hartree-Fock model, respectively. Alternatively, Rodríguez *et al.* [109] used Coulomb shifts in concert with precision mass measurements of the ^{73}Rb mirror, ^{73}Kr, to calculate an S_p value of $-0.71(10)$ MeV.

It appears then that the value of $S_p = 1.04$ MeV is in conflict with that calculated. It is worth noting however that the calculations also disagree with the previously determined S_{2p} value for ^{74}Sr. On the other hand, shell-model calculations by Kaneko *et al.* have been performed, utilising the JUN45 effective interaction and including the same INC component as used for the TED measurements. These calculations result in a value of $S_p = -1.1$ MeV, in good agreement with the observed decay. It seems plausible that the proton decay observed in the present work corresponds to the decay of the ground state in ^{73}Rb.

Chapter 7

Conclusions and future work

> Sometimes a scream is better than a thesis.
>
> Manfred Eigen

7.1 Conclusions

In the present work, further developments to the recoil-beta tagging (RBT) technique have been implemented. A phosphor-sandwich (phoswich) detector has been installed at the University of Jyväskylä (JYFL) in order to discriminate β particles. A charged-particle veto detector, the University of York tube (UoYtube) has been characterised and further developed, with an increase in single-proton detection efficiency from $\sim 60\%$ to $\sim 75\%$. A finely segmented double-sided silicon strip detector (DSSD) has also been installed, reducing contributions from false decay correlations. In concert, these changes have dramatically improved the selectivity of the RBT technique, allowing for the observation of excited states in very weakly populated ($\sim$ 10-nb) reaction channels.

Using the JYFL facility, augmented with the aforementioned detectors, an experiment was performed to observe excited states in the $N = Z - 2$ nuclide, ^{74}Sr. The $2^+ \rightarrow 0^+$ and $4^+ \rightarrow 2^+$ transitions were observed. This makes ^{74}Sr the highest mass $T_z = -1$ nuclide for which such spectroscopic information is available. Alongside the γ-ray spectroscopy, a lifetime measurement was also performed. This measurement is in good agreement with a complementary measurement performed at the Radioactive Ion Beam Factory (RIBF) in RIKEN, Japan [98].

Through comparison with ^{74}Rb and ^{74}Kr, the TED for the $A = 74$ triplet was extracted. Comparison with state-of-the-art shell model calculations [20] implies that the inclusion of an additional 100-keV isospin non-conserving (INC) component is required in the $A = 74$ triplet, consistent with that required in lower mass regions. This implies that the INC component

is mandated throughout the nuclear landscape, regardless of local structure considerations, such as shell closures and which orbitals are active.

Further to spectroscopy of ^{74}Sr, candidates for the β-delayed proton decay of ^{73}Rb were observed. Again, a lifetime measurement was extracted, in good agreement with a measurement performed at RIKEN. From the pure-proton detection peaks, a proton-separation energy (S_p) of ~ 1 MeV was extracted, a result which has considerable astrophysical implications.

7.2 Further work

7.2.1 Future experiments

With the completion of this work there are now two cases in the fpg shell for which the TED has been extracted. It is of great interest to perform measurements on the remaining suitable cases in the shell. Above $A = 78$ reaching the $T_z = -1$ nuclide with stable-beam facilities is complicated by the lack of a stable $N = Z$ nuclide above $A = 40$. For $A = 78$ and below however, there are three isobaric triplets centered on an odd-odd nuclide for which TED have not yet been extracted, presenting an obvious avenue for progression from the present work.

The three suitable cases are the $A = 62$, $A = 70$ and $A = 78$ isobaric triplets. For the latter two cases, spectroscopy of the $T_z = -1$ nuclide is required in order to extract the TED and indeed, a proposal to perform a RBT experiment on the $T_z = -1$ nuclide ^{70}Kr has been approved by JYFL and is scheduled to be performed in the Autumn of 2014 [110]. The $A = 62$ case is more complicated, with no definitive observation of the $T = 1$, 2^+ state made in the $T_z = 0$ nuclide, ^{62}Ga and confirmation yet to be provided on the proposed 2^+ state in the $T_z = -1$ nuclide, ^{62}Ge.

A further interesting extension to the present work would be the extraction of reduced transition probabilities ($B(E2)$s) for the transitions in ^{74}Sr to probe any wavefunction change. This could best be achieved through the CoulEx of the nuclide, although such a measurement is (as mentioned in Section 2.5.2) reliant on the development of a reasonably high intensity ^{74}Sr radioactive-ion beam. At the time of writing, no such beam is available for CoulEx studies.

Further investigation is also required for the β-delayed proton decay of ^{73}Rb. The present work was limited by the fact that no mass resolution was available. A future experiment using a similar setup with a mass-resolving spectrometer, such as an FMA equivalent [69] will allow for an unambiguous identification. In addition, it would provide a proof-of-principle, allowing for further studies of potentially proton emitting nuclides, such as ^{69}Br.

7.2.2 RBT development

While the present work significantly enhanced the sensitivity of the RBT technique, further development and refinement is still possible. As mentioned in Section 4.3, the use of a steel target chamber for the UoYtube was not ideal and enquiries about the production of a new, aluminium chamber are being made at the time of writing. Additionally, if one were able to provide θ resolution in the UoYtube, it might be possible to improve the Doppler correction in the JUROGAM II array which would enhance the resolution. This might be achieved using lateral CsI(Tl) strips of constant angular size in the place of the 7x2, square CsI(Tl) elements of the present design.

The possibility of using a novel scintillator array at the focal plane of the RITU and MARA separators is also intruiging. Using the PSA techniques developed for the UoYtube, one might (for example) be able to perform accurate particle identification at considerably lower energies than can be achieved using the present phoswich detector, increasing the β-identification efficiency. Alternatively, a reduction in the thickness of the phoswich fast element would have a similar effect.

Finally, a characterisation of the performance of the RBT technique with the MARA separator will be of high interest. The reduced transmission of the primary reaction contaminants should significantly reduce the false-correlation rate. How this impacts on the sensitivity and, in particular, the efficiency of RBT remains to be seen. Currently, the technique is limited by its efficiency, making the use of double-RBT impractical. In the case where false correlations cease to be an issue, looser gates might allow the use of double-RBT to obtain an unambiguous tag.

Appendix A

Pulse-shape analysis algorithm

Given below is the pulse-shape analysis (PSA) algorithm developed in VHDL intended for use with the UoYtube and Phoswich detectors to be implemented in the JYFL field-programmable gate arrays (FPGAs) of the total data readout (TDR) system.

```
library ieee;
use ieee.std_logic_1164.all;
use ieee.math_real.all;
use ieee.numeric_std.all;
use ieee.std_logic_arith.all;
library std;
use std.textio.all;

entity data_sampler is
  port(Trigger,clk,clear : in STD_LOGIC; -- trigger is 50ns wide from
    trigger-accepted-pulse and clk is 10ns adac_clk, clear is clear_mwd_rdout_logic
   fast_start : in STD_LOGIC_VECTOR(15 downto 0); -- Time after trigger that the
    fast window begins (could probably be dropped and set to zero in the code)
   slow_start : in STD_LOGIC_VECTOR(15 downto 0); -- Time after trigger that the
    slow window begins
   fast_length : in STD_LOGIC_VECTOR(15 downto 0); -- Width of fast sampling window
   slow_length : in STD_LOGIC_VECTOR(15 downto 0); -- Width of slow sampling window
    (window inputs could probably be combined)
   baseline : in STD_LOGIC_VECTOR(15 downto 0); -- Baseline taken from MWDC
   Data : in STD_LOGIC_VECTOR(15 downto 0); -- Data stream
   Data_ready : out STD_LOGIC; -- Flag letting the system know whether the integral
    data is ready
   slow_integral : out STD_LOGIC_VECTOR(15 downto 0); -- Slow integral output
   fast_integral : out STD_LOGIC_VECTOR(15 downto 0) ); -- Fast integral output
end entity data_sampler;

architecture behav of data_sampler is

begin
  process(clk)
   variable event_flag : boolean; -- Flag telling system when to sample
   variable i : integer range 0 to 2048 := 0; -- Maximum sampling range
```

```
 variable baseline_val,fast,slow : integer; -- Integer form of baseline (from
  input) and fast and slow values to be incremented
 variable slow_length_val,fast_length_val,total_length_val : integer; -- Integer
  forms of slow, fast and total window lengths
begin
  -- (Not sure where this section should go):
 fast_length_val := to_integer(unsigned(fast_length)); -- Put fast window into
  integer form for manipulation
 slow_length_val := to_integer(unsigned(slow_length)); -- Put slow window into
  integer form manipulation
 fast_start_val := to_integer(unsigned(fast_start)); -- Put fast start into
  integer form manipulation
 slow_start_val := to_integer(unsigned(slow_start)); -- Put slow start into
  integer form manipulation
 baseline_val := to_integer(unsigned(baseline)); -- Put baseline into integer
  form manipulation
 if slow_length_val = 0 then
    total_length_val = fast_length_val + fast_start_val; -- If slow length is
  zero, total sampling goes until the end of the fast window
 else
    total_length_val = slow_length_val + slow_start_val; -- Otherwise total
  sampling goes until the end of the slow window
 end if;

 if clk'event and clk = '1' then -- For every tick
    if clear = '1' then -- If input clear is on
       event_flag := false; -- Set event_flag to false (i.e. stop sampling)
       data_ready <= '0'; -- Set data_ready to zero (i.e. don't read out data)
    end if;
    if event_flag = true and i <= total_length_val then -- If event_flag is good
  and the sampling range limit hasn't been reached
       i := i + 1; -- Increment sample point (i)
    end if;
    if event_flag = false and Trigger = '1' and clear = '0' then -- When the
  trigger turns on
       i := 0; -- reset incremental sample point counter
       fast := 0;
       slow := 0; -- reset fast and slow sums
       event_flag := true ; -- Turn the event flag to true to start sampling
    end if;
    if event_flag then -- If sampling flag is true
       if (i >= fast_start_val and i <= (fast_start_val + fast_length_val)) then
  -- If sampling point (i) lies within the fast sample window
          fast := fast + (to_integer(unsigned(data))) - baseline_val; -- Increase
  fast sum by (Data-Baseline)
```

```
        end if;
        if (i >= slow_start_val and i <= (slow_start_val + slow_length_val) and
    slow_length_val > 0) then -- If sampling point (u) lies within slow sample
    window (and slow sample window is non-zero)
            slow := slow + (to_integer(unsigned(data))) - baseline_val; -- Increase
    slow sum by (Data-Baseline)
        end if;
        if i > total_length_val then -- If sample point (i) is beyond the total
    window
            data_ready <= '1'; -- Set data_ready to 1 so system knows it can read
    outputs
            slow_integral <= std_logic_vector(to_signed((slow),16));
            fast_integral <= std_logic_vector(to_signed((fast),16)); -- Put fast
    and slow sums into std_logic_vector format to be read out
        end if;
      end if;
   end if;
  end process;
end behav;
```

Appendix B

The ^{74}Sr tagging process

Over the following pages the γ-ray spectra produced with various gates in the RBT process will be provided, beginning with loose tagging conditions in Fig. B.1. It is hoped that this will provide the reader with a clearer understanding of the power of the technique and the tuning of the gates required to produce the optimum spectrum. Significant transitions associated with ^{73}Br, ^{74}Rb and ^{74}Sr are indicated by dotted, dashed and dotted-dashed lines respectively. The gates applied will be as follows:

- Fig. B.1: Light tagging conditions - $\Delta t < 200$ ms, with the requirement for a large phoswich component. The suppression provided by these gates is sufficient to make the $2^+ \rightarrow 0^+$ transition in ^{74}Rb visible above background, but contaminants remain dominant.
- Fig. B.2: A shorter timing requirement ($\Delta t < 100$ ms) is applied, further suppression of contaminants is acheived, with the ^{74}Rb transition slightly enhanced (note that this timing condition is not ideal for ^{74}Rb).
- Fig. B.3 to Fig. B.7 have increasing β-particle energy requirements, from ~ 2.2 MeV up to ~ 5 MeV in steps of ~ 700 keV. The ^{74}Rb transitions begin to dominate the spectra as the energy requirement increases.
- Fig. B.8 includes a charged-particle veto. ^{74}Rb is heavily suppressed, but continues to dominate the spectrum.
- Finally, Fig. B.9 requires that the implantation was in a low-counting region of the DSSD. The two transitions assigned to ^{74}Sr at 471 keV and 572 keV dominate, with some remaining ^{74}Rb contamination.

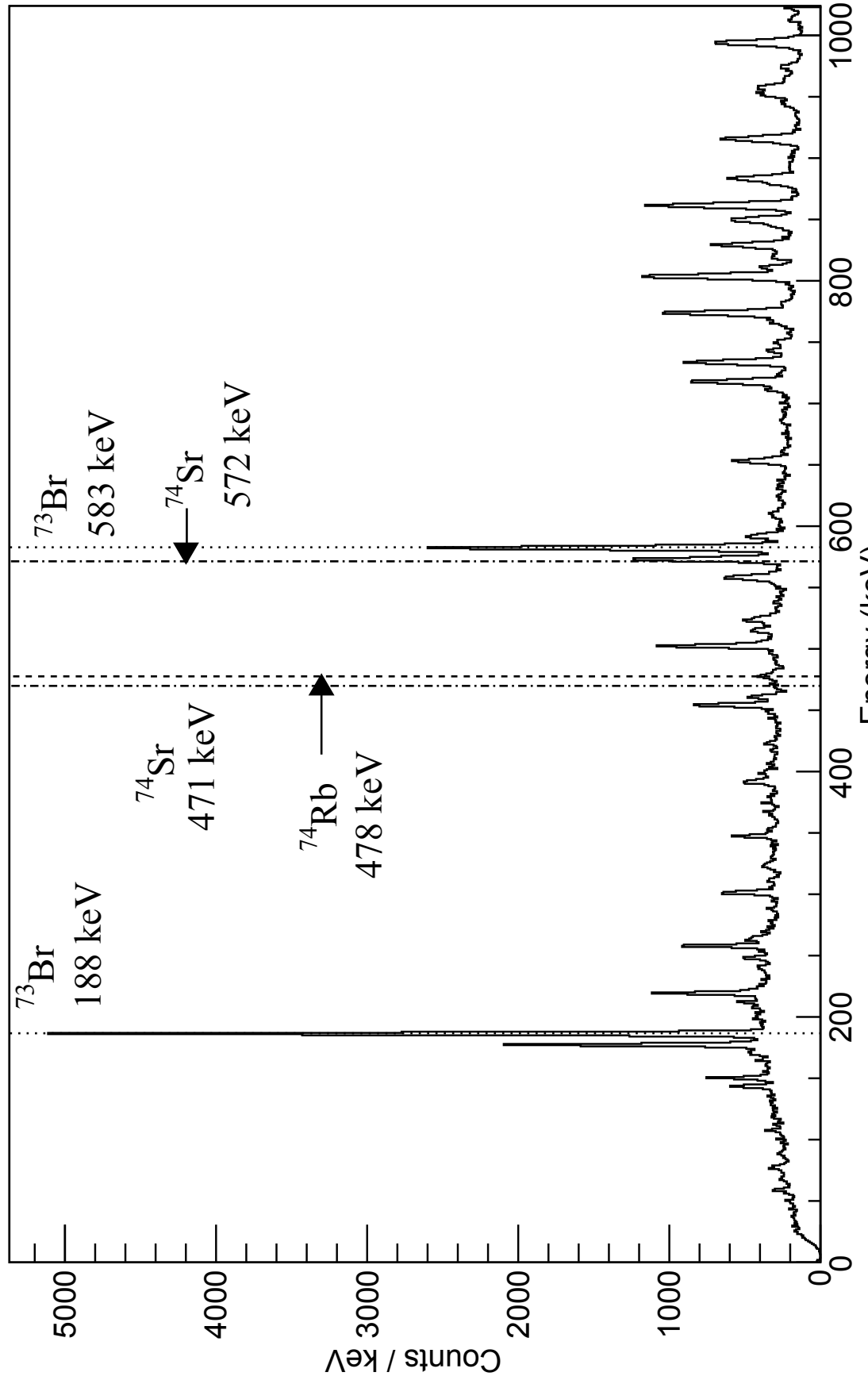

FIGURE B.1: Light tagging conditions: $\Delta t < 200$ ms, large fast component as shown in Fig. 5.11

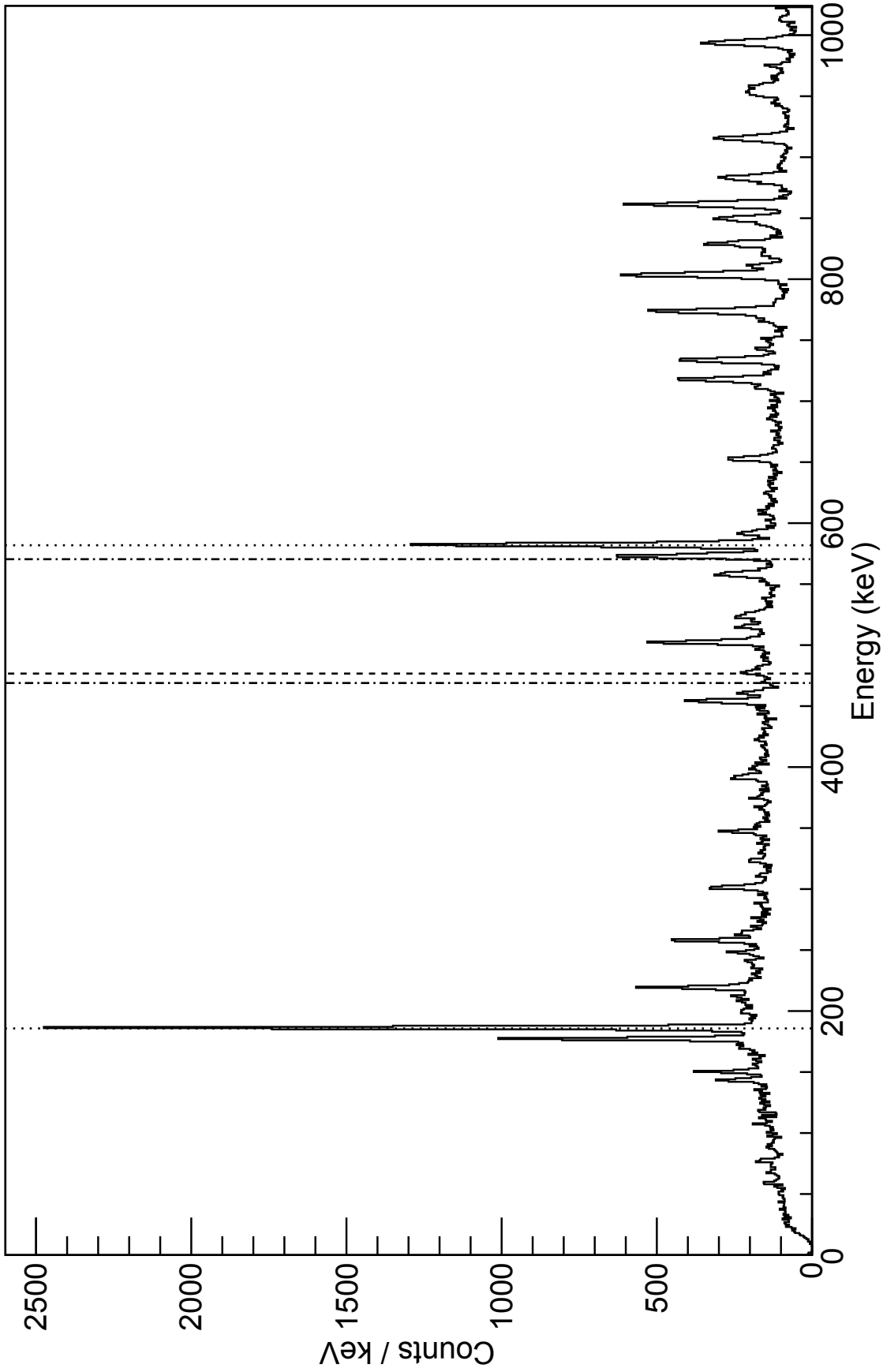

FIGURE B.2: As Fig. B.1 but with a $\Delta t < 100$ ms requirement.

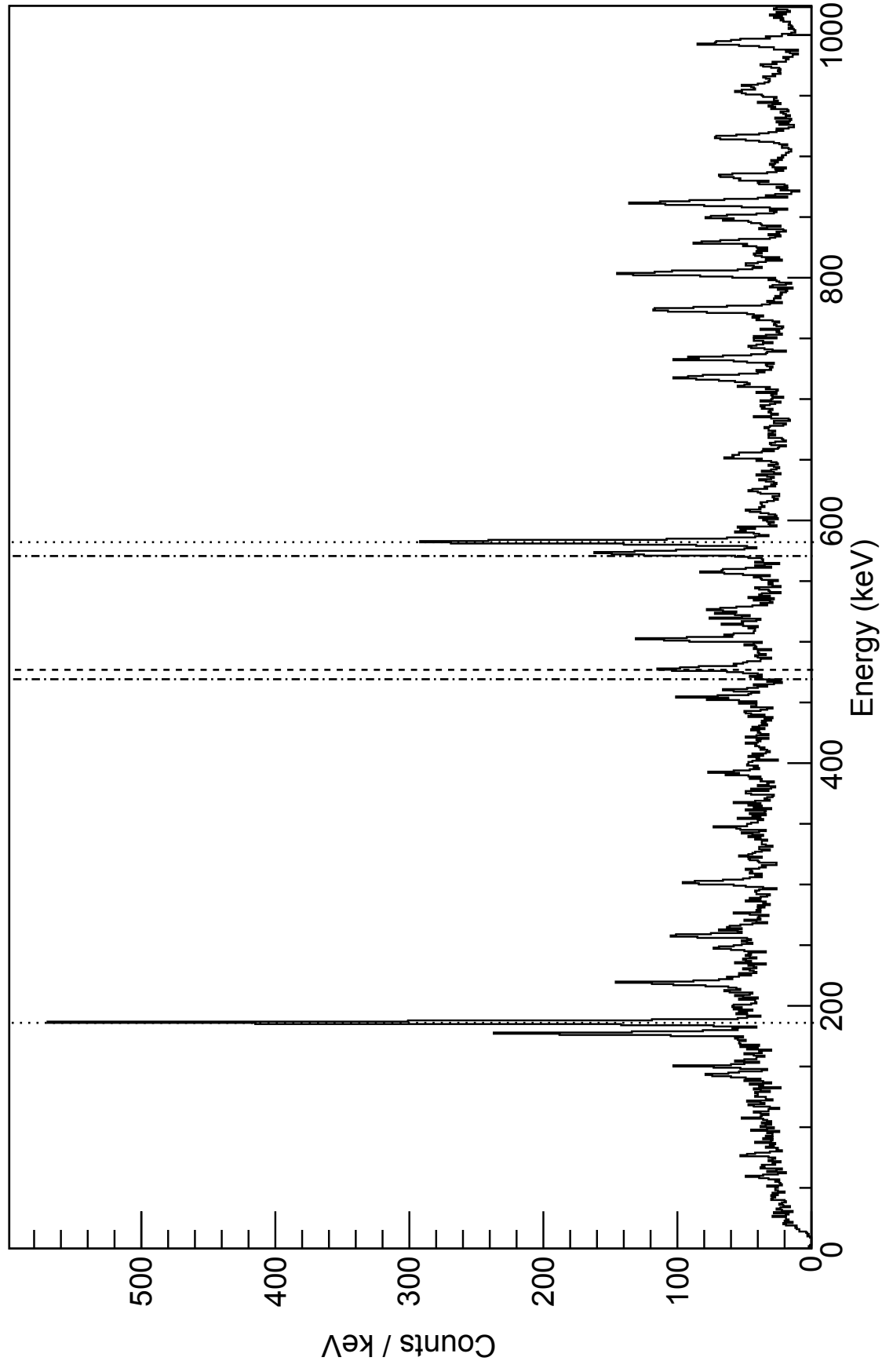

FIGURE B.3: As Fig. B.2 but with a requirement that the total phoswich energy is greater than ∼2.2 MeV.

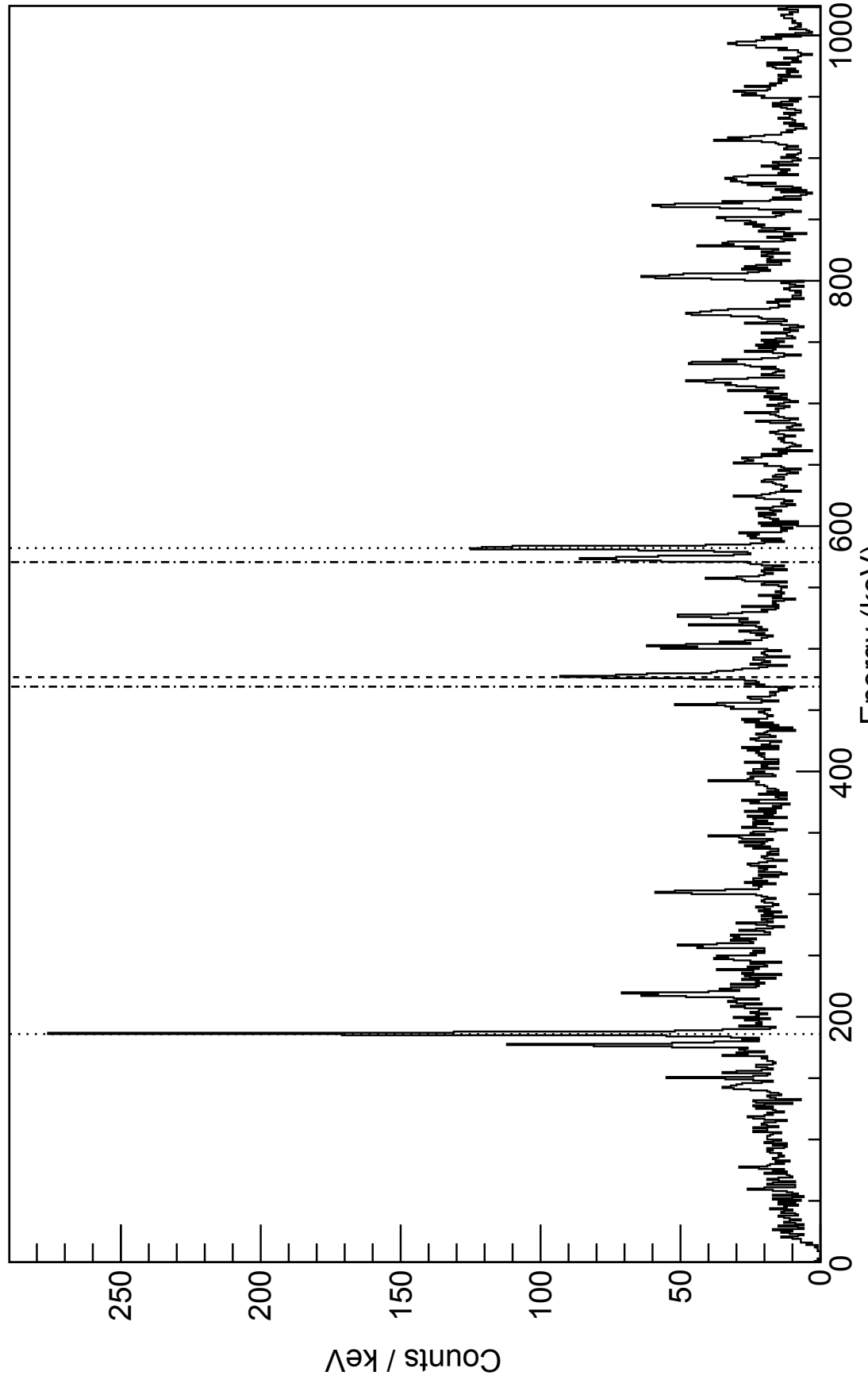

FIGURE B.4: As Fig. B.3 but with a requirement that the total phoswich energy is greater than ∼2.9 MeV.

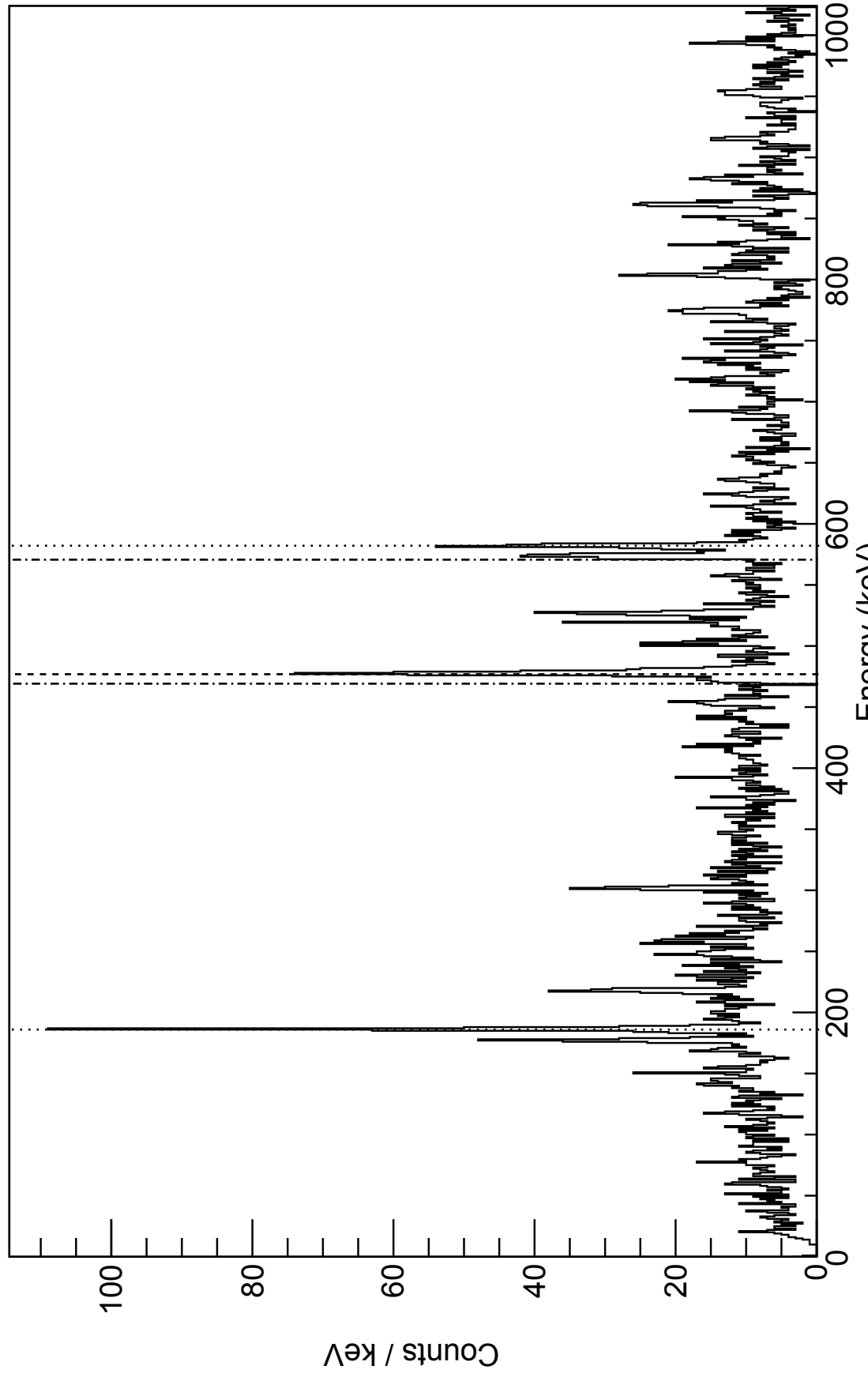

FIGURE B.5: As Fig. B.4 but with a requirement that the total phoswich energy is greater than ∼3.7 MeV.

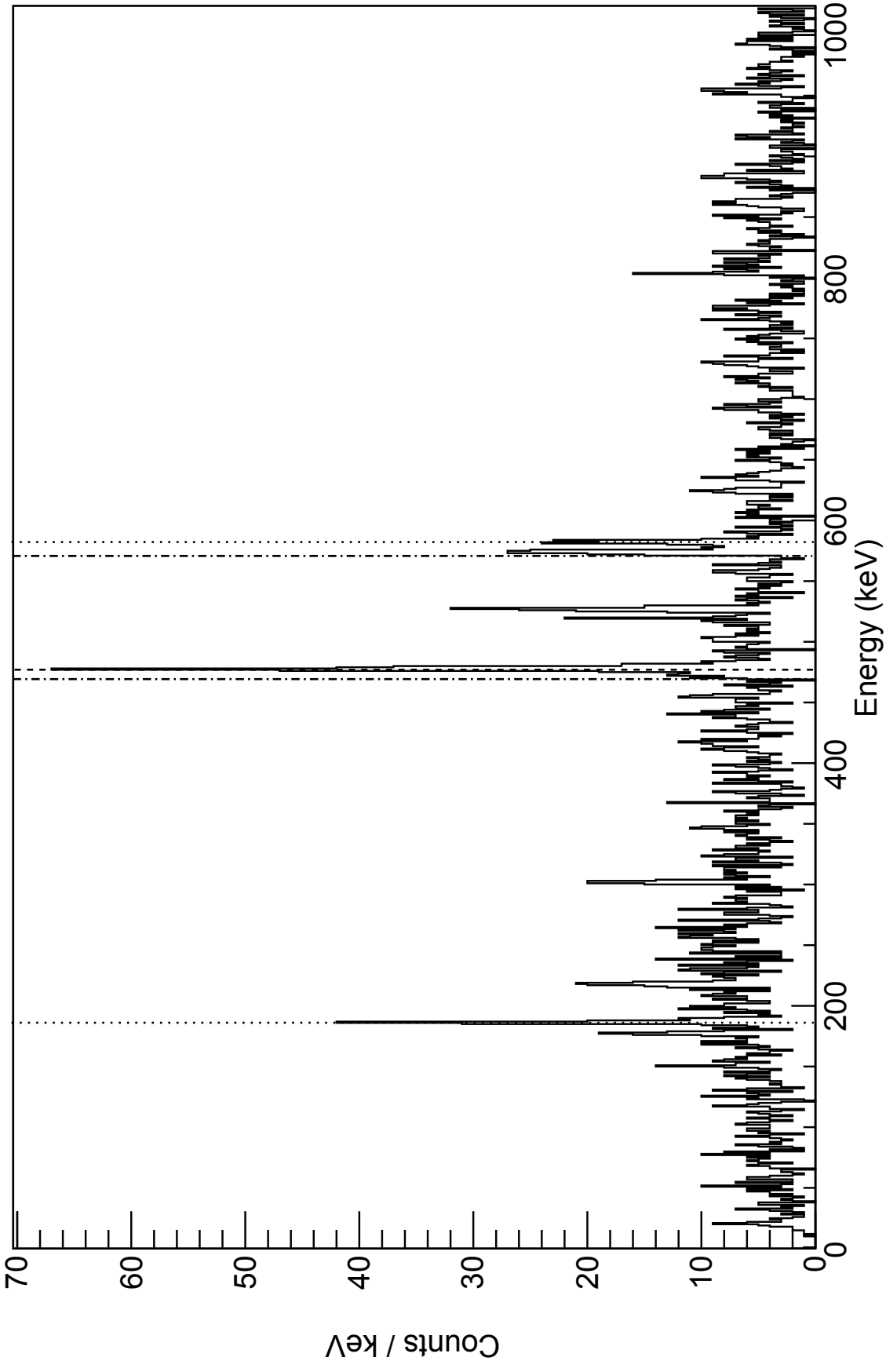

FIGURE B.6: As Fig. B.5 but with a requirement that the total phoswich energy is greater than ∼4.4 MeV.

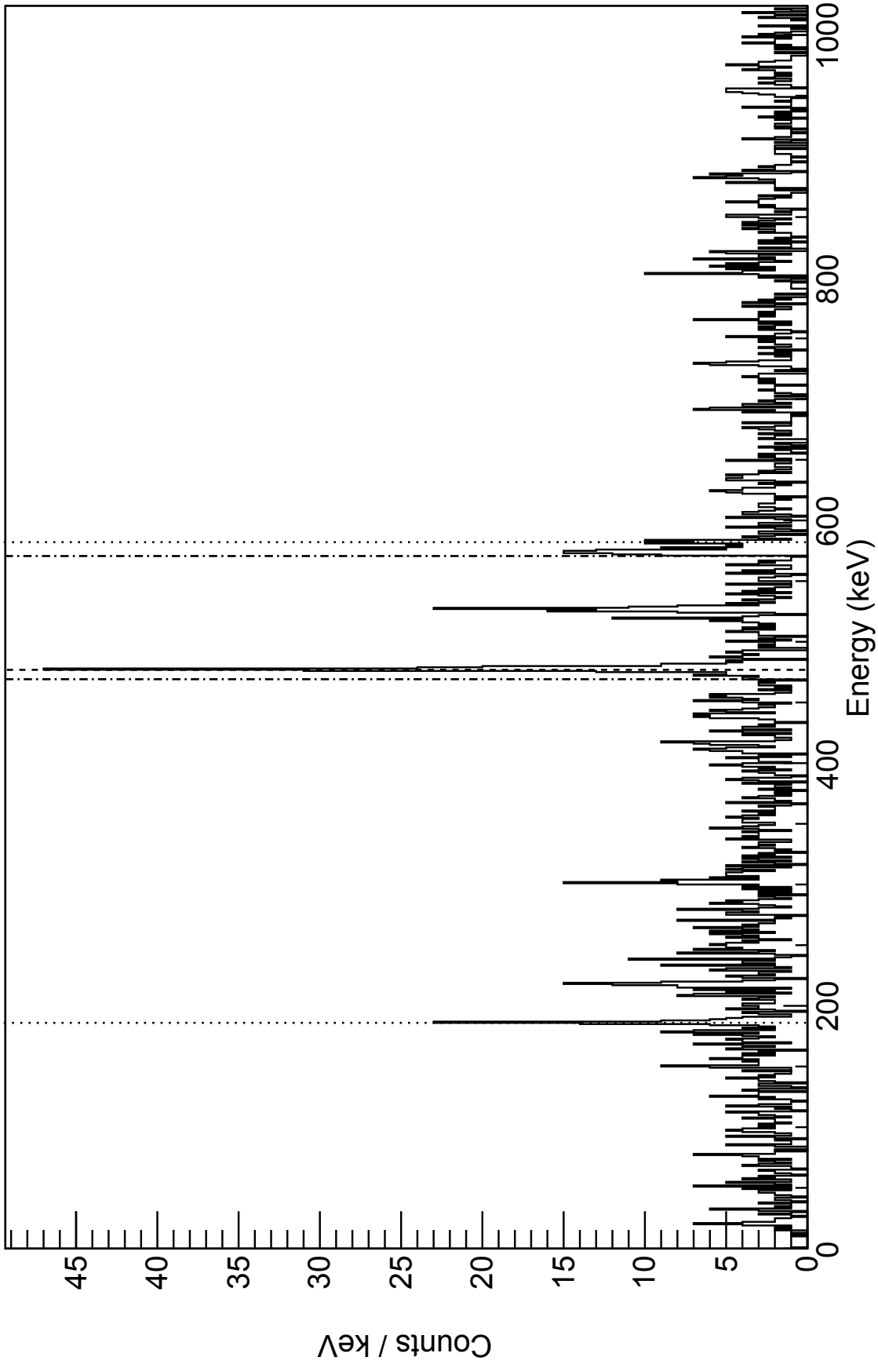

FIGURE B.7: As Fig. B.6 but with a requirement that the total phoswich energy is greater than ∼5 MeV.

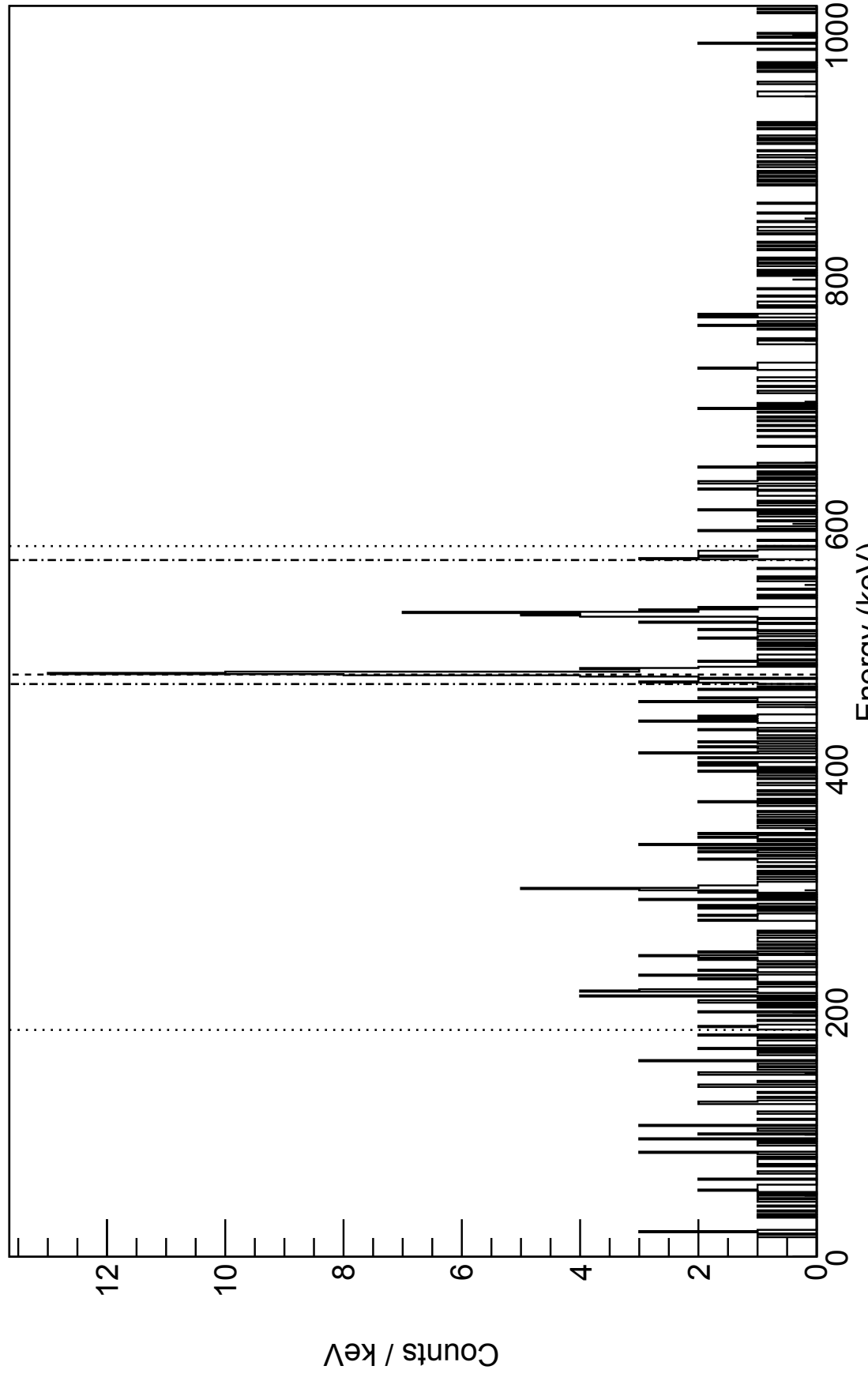

FIGURE B.8: As Fig. B.7 but with a UoYtube charged-particle veto.

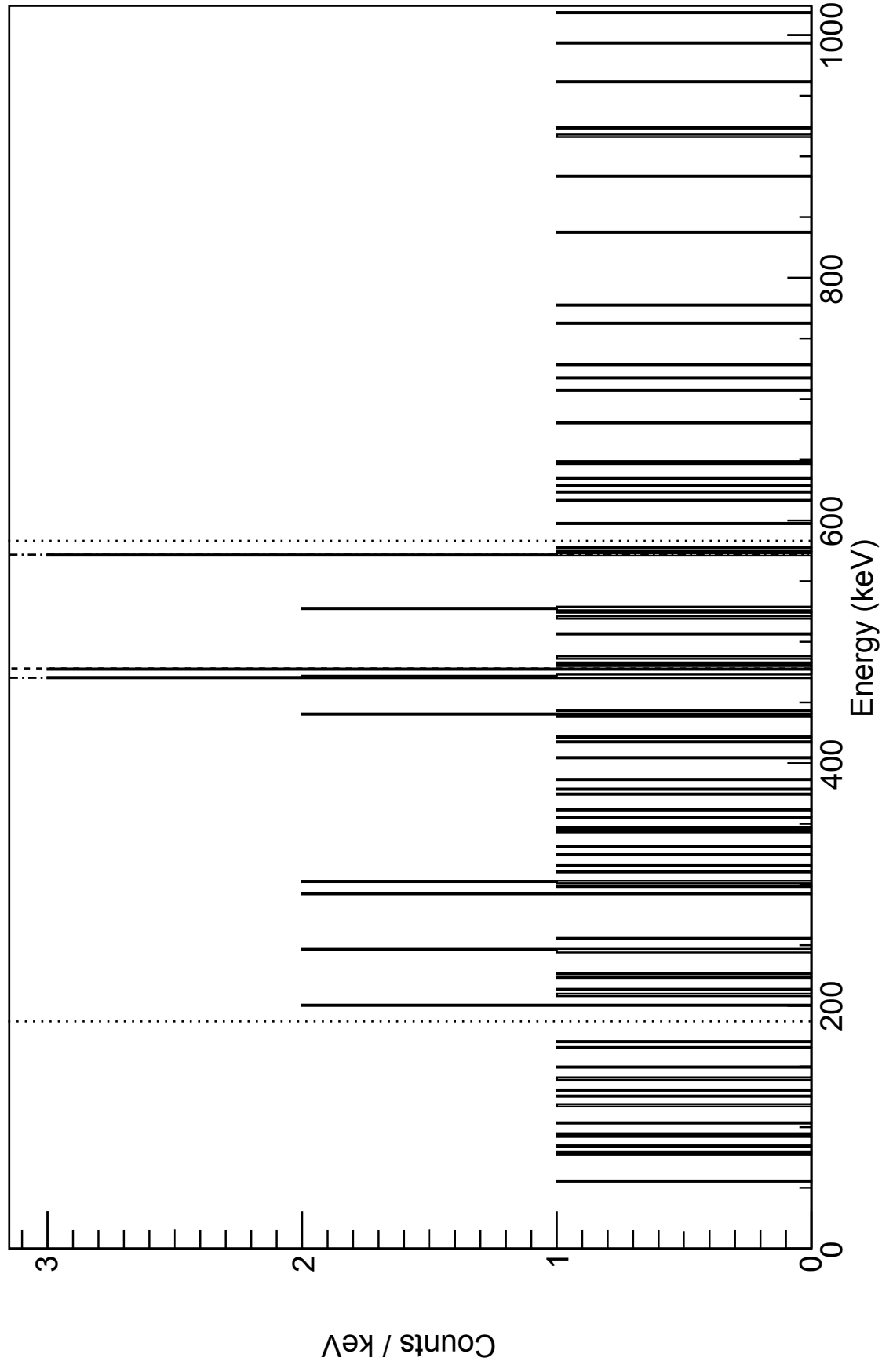

FIGURE B.9: As Fig. B.8 but with a requirement that the implantation was in the low-counting region of the DSSD ($x \lesssim 60 \& xy \lesssim 40$).

Bibliography

[1] A. N. Steer et al. Recoil-beta tagging: A novel technique for studying proton-drip-line nuclei. *Nuclear Instruments and Methods in Physics Research A*, **565**, 630, 2006.

[2] W. Heisenberg. Uber den Bau der Atomkerne. *Zeitschrift f ur Physik*, 1932.

[3] E. Wigner. On the Consequences of the symmetry of the Nuclear Hamiltonian on the Spectroscopy of Nuclei. *Physical Review*, **51**, 106, 1936.

[4] O. Haxel, J. Hans. D. Jensen & H. E. Seuss. On the "Magic Numbers" in Nuclear Structure. *Physical Review*, **75**, 1766, 1949.

[5] M. Goeppert Mayer. Nuclear Configurations in the Spin-Orbit Coupling Model. I. Empirical Evidence. *Physical Review*, **78**, 16, 1950.

[6] R. D. Woods and D. S. Saxon. Diffuse Surface Optical Modelling for Nucleon-Nuclei Scattering. *Physical Review*, **95**, 577, 1954.

[7] K. S. Krane. *Introductory Nuclear Physics*. Wiley, Oregon State University, 2nd edition, 1988.

[8] M. Honma et al. New effective interaction for f_5pg_9-shell nuclei. *Physical Review C*, **80**, 064323, 2009.

[9] J. Duflo and A. P. Zuker. Mirror displacement energies and neutron skins. *Physical Review C*, **66**, 051304(R), 2002.

[10] S. M. Lenzi et al. Couloumb Energy Differences in $T = 1$ Mirror Rotational Bands in ^{50}Fe and ^{50}Cr. *Physical Review Letters*, **87**, 122501, 2001.

[11] D. R. Inglis. Spin-Orbit Coupling in Li^7 and Be^7. *Physical Review*, **82**, 1951.

[12] J. A. Nolen and J. P. Schiffer. Coulomb Energies. *Annual Review of Nuclear Science*, **19**, 471, 1969.

[13] D. D. Warner, M. A. Bentley and P. Van Isacker. The role of isospin symmetry in collective nuclear structure. *Nature Physics*, **2**, 311, 2006.

[14] A. P. Zuker et al. Isobaric Multiplet Yrast Energies and Isospin Nonconserving Forces. *Physical Review Letters*, **89**, 142502, 2002.

[15] P. J. Davies et al. Mirror Energy Differences at Large Isospin Studied through Direct Two-Nucleon Knockout. *Physical Review Letters*, **111**, 072501, 2013.

[16] S. J. Williams et al. Anomalous Coulomb matrix elements in the $f_{7/2}$ shell. *Physical Review C*, **68**, 011301(R), 2003.

[17] A. Gadea et al. Observation of ^{54}Ni: Cross-Conjugate Symmetry in $f_{7/2}$ Mirror Energy Differences. *Physical Review Letters*, **97**, 152501, 2006.

[18] P. Ruotsalainen et al. Spectroscopy of proton-rich ^{66}Se up to $J^{\pi} = 6^{+}$: isospin-breaking effect in the $A = 66$ isobaric triplet. *Physical Review C*, **88**, 041308, 2013.

[19] A. Obertelli et al. First spectroscopy of ^{66}Se and ^{65}As: Investigating shape coexistence beyond the N=Z line. *Physics Letters B*, **701**, 417, 2011.

[20] K. Kaneko et al. Isospin nonconserving interaction in the T=1 analogue states of mass-70 region. *Physical Review C*, **89**, 031302(R), 2014.

[21] T. Mizusaki, K. Kaneko, M. Honma and T.Sakurai. Filter diagonalization of shell-model calculations. *Physical Review C*, **82**, 024310, 2010.

[22] T. Mizusaki, K. Kaneko, M. Honma and T.Sakurai. Filter Diagonalization: A New Method for Large-scale Shell-model Calculations. *Acta Physica Polonica B*, **42**, 447, 2011.

[23] K. Kaneko et al. Variation in Displacement Energies due to Isospin-Nonconserving Forces. *Physical Review Letters*, **110**, 172505, 2013.

[24] H. Iwasaki et al. Evolution of Collectivity in ^{72}Kr: Evidence for Rapid Shape Transition. *Physical Review Letters*, **112**, 142502, 2014.

[25] D. A. Hardy. `http://astroart.org`. Accessed: 09-07-2014.

[26] C. Iliadis. *Nuclear Physics of Stars*. Wiley, 2007.

[27] W. H. G. Lewin, J. van Paradijs and R. E. Taam. X-ray Bursts. *Space Science Reviews*, **62**, 223, 1993.

[28] A.M. Rogers et al. ^{69}Kr β-delayed proton emission: A Trojan horse for studying states in proton-unbound ^{69}Br. *Physical Review C*, **84**, 051306, 2011.

[29] J. C. Batchelder et al. Beta-delayed proton decay of ^{73}Sr. *Physical Review C*, **48**, 2593, 1993.

[30] D. G. Jenkins. Private communication, 2014.

[31] P. Sarriguren. Stellar weak decay rates in neutron-deficient medium-mass nuclei. *Physical Review C*, **83**, 025801, 2011.

[32] T. H. R. Skyrme. The nuclear surface. *Philosophical Magazine*, **1**, 1043, 1956.

[33] T. H. R. Skyrme. The effective nuclear potential. *Nuclear Physics*, **9**, 615, 1959.

[34] P. Ring and P. Schuck. *The Nuclear Many-Body Problem.* Springer-Verlag, 1980.

[35] D. Vautherin and D. M. Brink. Hartree-Fock Calculations with Skyrme's Interaction. I. Spherical Nuclei. *Physical Review C*, **5**, 626, 1972.

[36] D. Vautherin. Hartree-Fock Calculations with Skyrme's Interaction. II. Axially Deformed Nuclei. *Physical Review C*, **7**, 296, 1973.

[37] N. N. Bogolyubov. *Soviet Physics JETP*, **7**, 41, 1958.

[38] J. G. Valatin. Comments on the Theory of Superconductivity. *Nuovo Cimento*, **7**, 843, 1958.

[39] N. N. Bogolyubov. *Soviet Physics JETP*, **34**, 41, 1958.

[40] J. Bardeen, L. N. Cooper and J. R. Schreiffer. Theory of superconductivity. *Physical Review*, **108**, 1175, 1957.

[41] E. Chabanat et al. A Skyrme parameterization from subnucleon to neutron star densities Part II. Nuclei far from stabilities. **635**, 231, 1998.

[42] Nguyen Van Giai and H. Sagawa. Spin-isospin and pairing properties of modified Skyrme interactions. *Physical Letters B*, **106**, 379, 1981.

[43] P. Sarriguren. Personal Communication.

[44] H. Geiger and J. M. Nuttall. The ranges of the α particles from various radioactive substances and a relationship between range and period of transformation. *Philosophical Magazine Series 6*, 1911.

[45] D. C. Camp and L. M. Langer. Shape of the $0^+ \rightarrow 0^+$ Positron Spectrum in ^{66}Ga. *Physical Review*, **129**, 1782, 1963.

[46] C. B. Hinke et al. Superallowed Gamow-Teller decay of the double magic nucleus ^{100}Sn. *Nature*, **486**, 341, 2012.

[47] K. Heyde. *Basic Ideas and Concepts in Nuclear Physics: An Introductory Approach.* Institute of Physics, 3rd edition, 2004.

[48] N. Severijns et al. Isospin mixing in the $T = 5/2$ ground state of ^{71}As. *Physical Review C*, **71**, 064310, 2005.

[49] E. Rutherford and A. B. Wood. Long-range Alpha Particles from Thorium. *Philosophical Magazine*, **31**, 379, 1916.

[50] I. Martel et al. A shell-model analysis of the proton emission from ^{31}Cl using Gamow wave functions. *Nuclear Physics A*, **694**, 424, 2001.

[51] R. S. Simon et al. Evidence for Nuclear Shape Coexistence in ^{180}Hg. *Zeitschrift fur Physik A*, **325**, 197, 1986.

[52] D.M. Cullen et al. Identification of the $K^{\pi}=8^{-}$ rotational band in ^{138}Gd. *Physical Review C*, **58**, 846, 1998.

[53] P. T. Greenlees et al. Shell-Structure and Pairing Interaction in Superheavy Nuclei: Rotational Properties of the Z=104 Nucleus ^{256}Rf. *Physical Review Letters*, **109**, 012501, 2012.

[54] K-H. Schmidt, C.-C. Sahm, K. Pielenz & H.-G. Clerc. Some remarks on the error analysis in the case of poor statistics. *Zeitschrift fur Physik A*, **316**, 19, 1984.

[55] K-H. Schmidt. A new test for random events of an exponential distribution. *European Physical Journal A*, **8**, 141, 2000.

[56] B. S. Nara Singh et al. Coulomb shifts and shape changes in the mass 70 region. *Physical Review C*, **75**, 061301(R), 2007.

[57] P. Ruotsalainen et al. Recoil-β tagging of the N=Z nucleus ^{66}As. *Physical Review C*, **88**, 024320, 2013.

[58] H. M. David et al. Low-lying T=0 states in the odd-odd N=Z nuclude ^{62}Ga. *Physics Letters B*, **726**, 665, 2013.

[59] J. B. Birks. *The Theory and Practice of Scintillation Counting.* Pergamon Press, Ltd., 1964.

[60] G. F. Knoll. *Radiation Detection and Measurement.* Wiley, Ann Harbour, Michigan, 4th edition, 2010.

[61] G. Nelson and D. Reilly. *Passive Nondestructive Analysis of Nuclear Materials.* Los Alamos National Laboratory, 1991.

[62] P. J. Nolan, D. W. Gifford and P. J. Twin. The Performance of a Bismuth Germanate Escape Suppressed Spectrometer. *Nuclear Instruments and Methods in Physics Research A*, **236**, 95, 1985.

[63] W. F. Mueller et al. Thirty-two-fold segmented germanium detectors to identify γ-rays from intermediate energy exotic beams. *Nuclear Instruments and Methods in Physics Research A*, **466**, 492, 2001.

[64] S. Akkoyun et al. AGATA - Advanced Tracking Gamma Array. *Nuclear Instruments and Methods in Physics Research A*, **668**, 26, 2012.

[65] I. Y. Lee et al. GRETINA: A gamma-ray tracking array. *Nuclear Physics A*, **746**, 2004.

[66] C. W. Beausang et al. Measurements on prototype Ge and BGO detectors for the Eurogam array. *Nuclear Instruments and Methods in Physics Research A*, **313**, 37, 1992.

[67] C. Rossi Alvarez et al. The GASP Array. *Nuclear Physics News*, **3**, 1993.

[68] G. Duchêne et al. The Clover: a new generation of composite Ge detectors. *Nucl. Instr. and Meth. A*, **432**, 90, 1999.

[69] C. N. Davids et al. The Argonne Fragment Mass Analyser. *Nuclear Instruments and Methods in Physics Research B*, **40/41**, 1224, 1989.

[70] M. Leino et al. Gas-filled recoil separator for studies of heavy elements. *Nuclear Instruments and Methods in Physics Research B*, **99**, 653–656, 1995.

[71] M. Leino. In-flight separation with gas-filled systems. *Nuclear Instruments and Methods in Physics Research B*, **126**, 320–328, 1997.

[72] J. Sarén et al. Absolute transmission and separation properties of the gas-filled recoil separator RITU. *Nuclear Instruments and Methods in Physics Research A*, **654**, 508–521, 2011.

[73] N. Bohr. Scattering and Stopping of Fission Fragments. *Physical Review*, **58**, 654, 1940.

[74] J. Sarén. *The ion optical design of the MARA seperator and absolute transmission measurements of the RITU gas-filled recoil seperator.* PhD thesis, University of Jyv askyl a, 2011.

[75] J. Uusitalo et al. In-beam spectroscopy using the JYFL gas-filled magnetic recoil separator. *Nuclear Instruments and Methods in Physics Research B*, **204**, 638–643, 2003.

[76] J. Sarén et al. The new vacuum-mode recoil separator MARA at JYFL. *Nuclear Instruments and Methods in Physics Research B*, **266**, 4196, 2008.

[77] R.D. Page et al. The GREAT Spectrometer. 2003.

[78] I. Lazarus et al. The GREAT triggerless total data readout method. *IEEE Trans. on Nucl. Sci.*, **48**, 567, 2001.

[79] J. Henderson et al. Enhancing the sensitivity of recoil-beta tagging. *Journal of Instrumentation*, **8**, P04025, 2012.

[80] P. Ruotsalainen. *Development of the recoil-beta tagging method and recoil-beta tagging studies of* ^{66}As *and* ^{66}Se. PhD thesis, University of Jyväskylä, 2013.

[81] F. Liden et al. Identification of charged particles using plastic phoswich detectors. *Nuclear Instruments and Methods A*, **253**, 305, 1987.

[82] M. Bantel et al. A two-dimensional position-sensitive phoswich detector. *Nuclear Instruments and Methods*, **226**, 394, 1984.

[83] Saint Gobain Crystals. *Organics Brochure*, 2012.

[84] Micron Semiconductor Ltd. *2013 Catalogue*, 2013.

[85] A. Georgiev, W. Gast, R. M. Lieder. An Analog-to-Digital Conversion Based on a Moving Window Deconvolution. *IEEE Transactions on Nuclear Science*, **41**, 1116, 1994.

[86] A. Gavron. Statistical model calculations in heavy ion reactions. *Phys. Rev. C*, **21**, 230–236, 1980.

[87] D. O'Donell. Light Ion Spectrometer Array. `http://ns.ph.liv.ac.uk/~dod/LISA/home.html`.

[88] P. Rahkila. Grain - A Java data analysis system for Total Data Readout. *Nuclear Instruments and Methods in Physics Research A*, **595**, 637–642, 2008.

[89] K-H. Schmidt et al. Some remarks on the error analysis in the case of poor statistics. *Z. Phys. A*, **316**, 19, 1984.

[90] E. Browne and J. K. Tuli. Nuclear Data Sheets for A = 66. *Nuclear Data Sheets*, **111**, 1093, 2010.

[91] B. Hide. Private communication, 2014.

[92] A. Girka. Master's thesis.

[93] O. Nevodov. Master's thesis.

[94] R. S. Storey, W. Jack and A. Ward. The Flourescent Decay of CsI(Tl) for Particles of Different Ionization Density. *Proceeds of the Physical Society*, **72**, 463, 1958.

[95] D. G. Sarantites et al. "The Microball" Design, instrumentation and response characteristics of a 4π-multidetector exit channel-selection device for spectroscopic and reaction mechanism studies with Gammasphere. *Nuclear Instruments and Methods in Physics Research A*, **381**, 418, 1996.

[96] M. Alderighi et al. Particle identification method in the CsI(Tl) scintillator used for the CHIMERA 4π detector. *Nuclear Instruments and Methods in Physics Research A*, **489**, 257, 2002.

[97] D. W. Stracener et al. Dwarfball and Dwarfwall: Design Instrumentation and response characteristics of a 4π CsI(Tl) plastic phoswich multidetector system for light charged particle and intermediate mass fragment spectrometry. *Nuclear Instruments and Methods in Physics Research A*, **294**, 485, 1990.

[98] L. Sinclair et al. Decay spectroscopy in the A∼74 region. *In preparation*, 2014.

[99] T. Kubo. In-flight RI beam separator BigRIPS at RIKEN and elsewhere in Japan. 2003.

[100] S. Nishimura et al. WAS3ABI: The beta-counting system for the EURICA project. *RIKEN Accelerator Progress Reports*, **46**, 182, 2013.

[101] G. J. Feldman and R. D. Cousins. Unified approach to the classical statistical analysis of small signals. *Phys. Rev. D*, **57**, 3873, 1998.

[102] N. Michel, W. Nazarewicz and M. Ploszajczak. Isospin mixing and the continuum coupling in weakly bound nuclei. *Physical Review C*, **82**, 044315, 2010.

[103] R. G. Thomas. An Analysis of the Energy Levels of the Mirror Nuclei, C^{13} and N^{13}. *Physical Review*, **88**, 1109, 1952.

[104] J. B. Ehrman. On the Displacement of Corresponding Energy Levels of C^{13} and N^{13}. *Physical Review*, **81**, 412, 1951.

[105] E. Comay, I. Kelson and A. Zidon. The Thomas-Ehrman shift across the proton dripline. *Physics Letters B*, **210**, 31, 1988.

[106] A. H. Wapstra and G. Audi. Present knowledge of atomic masses. *European Physical Journal A*, **15**, 1, 2002.

[107] D. G. Jenkins. Waiting points in the astrophysical rp process: How unbound are ^{69}Br and ^{73}Rb? *Physical Review C*, **78**, 012801(R), 2008.

[108] B. A. Brown et al. Proton drip-line calculations and the *rp* process. *Physical Review C*, **65**, 045802, 2002.

[109] D. Rodríguez et al. Mass Measurement on the *rp*-Process Waiting Point ^{72}Kr. *Physical Review Letters*, **93**, 161104, 2004.

[110] R. Wadsworth. Personal communication.